Towards a better understanding and modeling of catalyst and catalyst layer operation in Proton Exchange Membrane Fuel Cell

Florent Vandenberghe

To cite this version:

Florent Vandenberghe. Towards a better understanding and modeling of catalyst and catalyst layer operation in Proton Exchange Membrane Fuel Cell. Material chemistry. Université Grenoble Alpes [2020-..], 2022. English. NNT : 2022GRALI102 . tel-04137000

HAL Id: tel-04137000
https://theses.hal.science/tel-04137000v1

Submitted on 22 Jun 2023

THÈSE

Pour obtenir le grade de

DOCTEUR DE L'UNIVERSITÉ GRENOBLE ALPES

École doctorale : I-MEP2 - Ingénierie - Matériaux, Mécanique, Environnement, Energétique, Procédés, Production
Spécialité : 2MGE : Matériaux, Mécanique, Génie civil,
Electrochimie Unité de recherche : CEA Grenoble / LITEN

Vers une meilleure compréhension et modélisation du fonctionnement du catalyseur et de la couche catalytique dans la pile à combustible à membrane échangeuse de protons

Towards a better understanding and modeling of catalyst and catalyst layer operation in Proton Exchange Membrane Fuel Cell

Présentée par :

Florent VANDENBERGHE

Direction de thèse :

Marian CHATENET Professeur INP, Université Grenoble Alpes	Directeur de thèse
Fabrice MICOUD Ingénieur Chercheur, CEA	Co-encadrant de thèse
Pascal SCHOTT Ingénieur Chercheur, CEA	Co-encadrant de thèse

Rapporteurs :

Elena SAVINOVA
PROFESSEUR DES UNIVERSITES, Université de Strasbourg
Marc SECANELL
PROFESSEUR DES UNIVERSITES, University of Alberta

Thèse soutenue publiquement le **20 décembre 2022**, devant le jury composé de :

Marian CHATENET PROFESSEUR DES UNIVERSITES, Université Grenoble Alpes	Directeur de thèse
Elena SAVINOVA PROFESSEUR DES UNIVERSITES, Université de Strasbourg	Rapportrice
Marc SECANELL PROFESSEUR DES UNIVERSITES, University of Alberta	Rapporteur
Stéphane COTTE INGENIEUR DOCTEUR, Toyota Motor Europe	Examinateur
Yann BULTEL PROFESSEUR DES UNIVERSITES, Université Grenoble Alpes	Président

Invités :

Fabrice MICOUD
INGENIEUR CHERCHEUR, CEA LITEN, Université Grenoble Alpes
Pascal SCHOTT
INGENIEUR CHERCHEUR, CEA LITEN, Université Grenoble Alpes

Acknowledgments

I would like to thank all the people who have contributed in any way to this thesis: co-workers, friends and family.

I first want to thank my thesis committee, Marc Secanell and Elena Savinova for reviewing the manuscript and the feedback you gave me, as well as for the very interesting discussion. I would like to also thank Yann Bultel for having chaired the thesis defense and Stephane Cotte for the interesting discussion.

A special thanks to my supervisors: Fabrice who always has an answer or an explanation to my numerous questions, for your availability and wise advice as soon as I had doubts. Pascal, for your wise advice and for having accompanied me in the joys and difficulties of numerical simulations. Marian, for believing in me and for giving me this PhD opportunity and the chance to work on this topic.

Here I thank all my work colleagues for the exchanges we were able to have with a particular thank to Laure for the discussions about microscopy and Arnaud for the time you spent answering my questions as thoroughly as possible. A special thanks to Camille for the discussions we had, about work or about the life. Clémence and Clémence for your very important help in manufacturing and characterizing MEA, as well as for taking care of my cat! I would like to warmly thank Clémence Lafforgue for your precious advice on life but also on work. Finally, I thank Florian for all the human or scientific thoughts, your numerous anecdotes, your discussions with Arnaud through the office windows. Thank you for having accompanied me during these 3 years.

A huge thank you to my group of friends: Zoé, Lucie, Nada, Léo, Mathilde, Cyprien and Lohan with whom I have been blossoming for almost 7 years in Grenoble. I know that I can always count on you and your benevolence and I do not forget it. A special thanks to Juliette, without whom the writing and the end of this thesis would have been much more difficult. Thank you for everything you did so that I could devote myself fully to writing, for your daily support and the long discussions about my lack of confidence.

I would like to finally thank my mother. She is the one who always pushed me to study and I certainly wouldn't be graduated without her. I love you.

LIST OF ACRONYMS **6**

INTRODUCTION **9**

CHAPTER I CONTEXT AND STATE-OF-ART OF THE PEMFC TECHNOLOGY **11**

I.1 ENERGETIC CONTEXT AND HYDROGEN AS AN ATTRACTIVE ENERGETIC VECTOR 11
I.1.1 Hydrogen: a promising fuel 11
I.1.2 Fuel cell technologies 13
I.1.3 PEMFC in transportation applications 14
I.2 PEMFC TECHNOLOGY AND ITS OPERATING PRINCIPLE 15
I.2.1 PEMFC design and components 15
I.2.1.1 PEMFC Overview 15
I.2.1.2 Monopolar Plates (MPs) 17
I.2.1.3 Gas diffusion Layer (GDL) and Micro-Porous Layer (MPL) 18
I.2.1.4 Proton Exchange Membrane (PEM) 19
I.2.1.5 Catalyst Layers (CLs) 20
I.2.2 Contributions and limitations of PEMFC during operation 22
I.2.2.1 Cell voltage calculation 22
I.2.2.2 Overpotential and loss contributions 23
I.2.2.3 Open Circuit Voltage and mixed potential 25
I.2.2.4 H_2-crossover 26
I.3 PEMFC DEGRADATION MECHANISMS 26
I.3.1 Irreversible degradations 27
I.3.1.1 Membrane degradation 27
I.3.1.2 Catalyst layer degradation 28
I.3.2 Reversible degradation 30
I.3.2.1 Water management 30
I.3.2.2 Platinum oxides formation/reduction 32
I.4 CONCLUSION 34

REFERENCES OF CHAPTER I **36**

CHAPTER II EXPERIMENTAL METHODS AND CHARACTERIZATION TECHNIQUES **45**

II.1 ELECTROCATALYSTS STUDIED 45
II.2 ROTATING DISK ELECTRODE SETUP 47
II.2.1 Electrochemical setup description 47
II.2.2 Ink formulation and CL manufacturing 48
II.2.3 RDE electrochemical characterizations 49
II.3 DIFFERENTIAL CELL (DC) CHARACTERIZATION SETUP 53
II.3.1 Electrochemical setup and test bench description 53
II.3.1.1 Differential cell and cell assembly description 53
II.3.1.2 Test bench description and operation 55
II.3.2 Ink formulation and MEA manufacturing 56
II.3.2.1 Ink formulation and anodic CL manufacturing for DC using blade coating method 57
II.3.2.2 Cathodic CL manufacturing for DC using spray coating method 58
II.3.2.3 Catalyst layers characterization and quality control 60
II.3.3 MEA manufacturing process 62
II.3.3.1 Catalyst-Coated Substrate method 62
II.3.3.2 Catalyst-Coated Membrane method 63
II.3.3.3 Decal Transfer Method (DTM) 64
II.3.3.4 CCM characterization by cross-section imaging 66
II.3.4 Electrochemical techniques and MEA characterizations 67
II.4 CONCLUSION 74

REFERENCES OF CHAPTER II **75**

CHAPTER III EXPERIMENTAL RESULTS AND DATABASE FOR MODELING **79**

III.1 ELECTROCATALYSTS INTRINSIC PROPERTIES 79
III.1.1 CO-stripping measurements and ECSA assessment 80
III.1.1.1 Impact of temperature on the ECSA assessed by CO oxidation 80
III.1.1.2 Impact of temperature on the ECSA assessed by proton desorption 82
III.1.2 ORR polarization curve measurements 85
III.1.2.1 Electrocatalyst activity measurements at 25°C 85
III.1.2.2 Impact of temperature on electrocatalyst activity measurements 86
III.2 FURTHER-FC MEA 91
III.2.1 Reproducibility study on FURTHER-FC MEA 92
III.2.2 Impact of the cell temperature 96
III.2.3 Impact of the relative humidity 100
III.2.4 Impact of P_{O_2} 104
III.3 VERY LOW LOADED MEA (20 $\mu G_{PT}.CM_{GEO}^{-2}$) 106
III.3.1 Definition of components and operating conditions 106
III.3.1.1 Thin membrane vs. thick membrane 107
III.3.1.2 H_2/Air vs. H_2/O_2 configuration 112
III.3.1.3 Performance measurements and ohmic drop correction method 115
III.3.2 Electrocatalytic features comparison at 25 and 60°C between the electrochemical setups 119
III.3.2.1 ECSA comparison 119
III.3.2.2 Activity comparison 121
III.4 FOCUS ON PT/VC AND PT/HSAC ELECTROCATALYSTS – VERY LOW LOADED CATALYST LAYERS 126
III.4.1 Under inert atmsophere 126
III.4.1.1 Impact of operating conditions on the ECSA value 126
III.4.1.2 Qualitative coverage ratio of Pt surface oxides evolution during CV under H_2/N_2 configuration 127
III.4.1.3 Impact of temperature and relative humidity on coverage ratio Pt surface oxides evolution 128
III.4.1.4 Impact of sweeping rate on coverage ratio Pt surface oxides evolution 130
III.4.2 Under oxygen atmosphere 131
III.4.2.1 Performance measurements at 80°C, 80% RH 131
III.4.2.2 Performance evolution with temperature and relative humidity 132
III.5 IMPACT OF CATALYST LAYER LOADING 135
III.5.1 Impact of loading increase on ECSA and coverage ratio of Pt surface oxides evolution 135
III.5.2 Impact of loading on global performance and R_{HF} evolution 138
III.6 CONCLUSIONS 139

REFERENCES OF CHAPTER III 141

CHAPTER IV PEMFC MODELING AND IMPROVEMENTS OF ELECTROCHEMICAL AND PHYSICO-CHEMICAL PROCESSES DESCRIPTION AT THE CATHODE CATALYST LAYER 145

IV.1 MODELING IN THE LITERATURE 145
IV.2 SIMULATION FRAMEWORK AND GENERAL DESCRIPTION OF THE MODEL 146
IV.2.1 EUROPIUM platform 147
IV.2.2 Geometry and domains 148
IV.2.3 Physics taken into account 149
IV.2.3.1 Transport modeling for gases in porous media 149
IV.2.3.2 Transport modeling for gases in electrolyte phase 150
IV.2.3.3 Water motion in the electrolyte phase 152
IV.2.3.4 Electronic transport 153
IV.2.3.5 Ionic transport 154
IV.2.3.6 Thermal modeling 154
IV.2.3.7 Electrochemistry 155
IV.3 IMPROVEMENT OF THE ELECTROCATALYST DESCRIPTION BY THE IMPLEMENTATION OF PT SURFACE STATES 158
IV.3.1 Multi-step mechanism implemented at the cathode 158
IV.3.1.1 Pt oxides formation/reduction mechanism 158
IV.3.1.2 Proton adsorption/desorption on Pt 161
IV.3.1.3 Parameter fitting process 162
IV.3.2 Very low loaded MEA simulation 163

IV.3.2.1 Overall presentation of modeling results 163
IV.3.2.2 Calculation of Pt coverage ratio: investigated scenario under H_2/O_2 configuration 168
IV.3.2.3 Calculation of Pt coverage ratio: investigated scenario under H_2/N_2 configuration 174
IV.4 PARAMETRIC STUDIES 177
IV.4.1 Impact of sweeping rate 178
IV.4.2 Impact of temperature 181
IV.4.2.1 Under H_2/O_2 configuration 181
IV.4.2.2 Under H_2/N_2 configuration 185
IV.4.3 Impact of relative humidity 189
IV.4.3.1 Under H_2/O_2 configuration 189
IV.4.3.2 Under H_2/N_2 configuration 193
IV.4.4 Potentiostatic study under H_2/N_2 configuration 196
IV.5 SIMULATIONS OF THICKER CATALYST LAYER 197
IV.5.1.1 Under H_2/O_2 configuration 198
IV.5.1.2 Under H_2/N_2 configuration 201
IV.6 CONCLUSION 204

REFERENCES OF CHAPTER IV 205

CONCLUSION & PERSPECTIVES 209

ABSTRACT........ 212

RESUME........ 213

List of Acronyms

AEMFC	Anion Exchange Membrane Fuel Cell
AFC	Alkaline Fuel Cell
BP	Bipolar Plate
BET	Brunauer, Emmett and Teller theory
BEV	Battery Electrical Vehicle
CCM	Catalyst-Coated Membrane
CCS	Catalyst-Coated Substrate
CE	Counter Electrode
CL	Catalyst layer
CV	Cyclic voltammetry
DC	Differential Cell
DTM	Decal Transfer Method
ECSA	ElectroChemical active Surface Area
EuROPIUM	ElectRochemistry OPtImization Understanding Modeling
FCEV	Fuel Cell Electrical Vehicle
GC	Graphitized Carbon
GDE	Gas Diffusion Electrode
GDL	Gas Diffusion Layer
HER	Hydrogen Evolution Reaction
HOR	Hydrogen Oxidation Reaction
HSAC	High Surface Area Carbon
HUPD	Hydrogen Under Potential Deposition
IPA	IsoPropyl Alcohol
MB	Membrane
MCFC	Molten Carbonate Fuel Cell
MEA	Membrane Electrode Assembly
MP	Monopolar Plate

MPL	Micro Porous Layer
MUSES	Multi-Scale Simulation of Electrochemical Systems
OCV	Open Circuit Value
OER	Oxygen Evolution Reaction
ORR	Oxygen Reduction Reaction
PAFC	Phosphoric Acid Fuel Cell
(P)EIS	(Potentiostatic) Electrochemical Impedance Spectroscopy
PEM	Proton Exchange Membrane
(PEM)FC	(Proton Exchange Membrane) Fuel Cell
(PEM)WE	(Proton Exchange Membrane) Water Electrolysis
PET	PolyEthylene Terephthalate
PFSA	PerFluoroSulfonic Acid
PGM	Platinum Group Metal
PTFE	PolyTetraFluoroEthylene
RDE	Rotating Disk Electrode
RE	Reference Electrode
RH	Relative Humidity
RHE	Reversible Hydrogen Electrode
SEM	Scanning Electron Microscopy
SOFC	Solid Oxide Fuel-Cell
SHE	Standard Hydrogen Electrode
TKK	TANAKA Kikinzoku Kogyo
(HR)TEM	(High-Resolution) Transmission Electron Microscopy
VC	Vulcan Carbon
WE	Working Electrode
XEDS	Energy-Dispersive X-ray Spectroscopy
XPS	X-Ray Photoelectron Spectroscopy
XRD	X-Ray Diffraction

XRF	X-Ray Fluorescence

Introduction

The recent extreme climate events have shown that the global warming is alarming. The combustion of fossil fuel such as coal, oil and fossil natural gas, as well as some agricultural and industrial practices release tremendous amounts of greenhouse gases in the atmosphere. These greenhouse gases emissions are slowly increasing (but in an accelerating manner) the global temperature of the planet, resulting in multiple irreversible consequences: extinction of various plant and animal species and more frequent and more extreme climate events, which significantly affect the food and human safety. As a result, a near-world-wide-shared and real willingness recently arose to find appropriate energy production means (and human behaviours) that can reduce the greenhouse gases emissions. Among these solutions, deploying at large scale hydrogen as an energy (and chemical) vector appears to be a viable and an essential way to reach a decarbonised energy mix and lead to successful energy transition.

Proton-exchange membrane fuel cells (PEMFCs) are devices that will take part in this effort; PEMFCs convert hydrogen and oxygen into electricity at low operating temperature, thanks to well-chosen hydrogen oxidation and oxygen reduction catalysts. Present state-of-the-art catalysts are based on platinum group metal (PGM) nanoparticles supported on high-surface area carbon substrates, and their optimal use in well-designed catalytic layers enables high power density and high efficiency for today‘s PEMFCs. While these performances render PEMFCs compatible with automotive applications, their initial cost and too-short lifetime in operation still have to be improved in order to allow the wide-commercialization of the technology (not to speak of the complex hydrogen distribution and storage). The cathode catalyst layer is probably the most limiting component of a PEMFC, mainly due to the complex interplay of the different physico-chemical and electrochemical phenomena occurring concomitantly in this component. These complex phenomena are coupled and the fact that the properties aforementioned cannot be decorrelated from one another, makes difficult the identification and quantification of what is limiting the catalyst layer operation.

This thesis work aims to improve our understanding of the cathode catalyst layer in PEMFCs. It has been carried out at the CEA in Grenoble within the Laboratory of Innovation for New Energy Technologies (LITEN) in collaboration with the Laboratory of Electrochemistry and Physical Chemistry of Materials and Interfaces (LEPMI), for its expertise in electrocatalysis. The idea is to develop and/or exploit electrochemical measurements based on both rotating disk electrode and differential cell setups, under various conventional operating conditions, in order to better understand the cathode active layer operation and limitations. As the catalyst layer structure and therefore operation depends on many parameters related to the manufacturing process, this work aims to manufacture ‘model’ active layers, which will be extensively characterized to establish a reliable baseline and experimental datasets for initial performances. This data shall enable to understand what is at stake when a catalyst layer is operated under nominal conditions. Because of the multiple couplings, the better understanding of how the catalyst operates in catalyst layer can also be addressed by the development and use of a numerical model. Several models have already been developed so far, to simulate and predict the performance of PEMFC, as well as to identify the limiting phenomena at different scales. Based on the reliable and specific dataset, this work aims at improving the description of the physico-chemical and electrochemical phenomena that occur at the cathode catalyst layer and at the membrane electrode assembly levels, by implementing a multi-steps mechanism instead of a single one-step reaction for the ORR description. If successfully implemented, this more accurate understanding and description of the ORR should lead to a predictive tool that better captures the catalyst layer evolution during operation, which is relevant to support the development and optimization of the composition and the structure of cathode catalyst layer, as well as to take into account further degradation mechanisms.

This work is divided into 4 chapters:

- This first chapter introduces the global energetic context and gives some insights into why hydrogen has received increasing attention regarding the energy transition. The PEMFC technology will be fully described, from its operation principle to degradation mechanisms relevant for transport application;
- The second chapter focuses on the presentation of the different experimental setups (Rotating Disk Electrode and Differential Cell setups) and characterizations (performance measurements, impedance spectroscopy and potential cycling under nitrogen atmosphere) performed on four state-of-art carbon-supported Pt-based materials, from the raw materials to their integration and utilization in PEMFC catalyst layers;
- The third chapter presents the different experimental results obtained thanks to Rotating Disk Electrode and Differential Cell measurements performed on the commercial electrocatalysts. These experiments were conducted in order to better understand the electrocatalytic properties of the materials. It notably aims to make the link between their physico-chemical properties and their electrochemical features. In addition, the relevance of the electrochemical setups including the choice of operating conditions, the electrochemical techniques, the materials used for the electrochemical characterizations in fuel cell configuration (DC), but also the way to process data will be discussed. Finally, ‘model’ catalyst layers are characterized to build a reliable dataset to help improving the model description;
- The fourth and last chapter presents the one-dimensional through thickness PEMFC model used in this work to better understand the catalyst layer operation and predict its performance. Compared to the initial simplistic version of the electrochemical description, the ORR mechanism description has been improved by including the participation of surface intermediates species, which is linked to the Pt oxides formation and reduction reactions. The improvements are initially made considering catalyst layers as an interface (0 dimension, 0D) to facilitate the implementation of the multi-steps ORR mechanism. Comparison with the experimental data is done to investigate the operating conditions window in which the improvements are valid. The transition to 1D catalyst layer is also investigated to be representative of realistic active layers by taking into account transport phenomena.

Chapter I Context and state-of-art of the PEMFC technology

This chapter introduces the global energetic context and gives some insights into why hydrogen has received increasing attention regarding the energy transition. Some fuel cell technologies will be presented, with emphasis on the Proton Exchange Membrane Fuel Cell; the PEMFC technology is the one investigated in this work, especially in view of its use for transportation applications. Thus, the PEMFC will be fully described, from its operation principle to degradation mechanisms.

I.1 Energetic context and hydrogen as an attractive energetic vector

The combustion of fossil fuel, greenhouse gases emitter, results in an increase of global temperature of the planet as shown on Figure I-1. This is worrying as it multiplies the number of extreme climate events and the extinction of various ecosystem, affecting significantly the food and human safety in an irreversible manner. The different Representative Concentration Pathways (RCP) scenarios (from Figure I-1) are detailed in the work of Moss *et al.* [1]. It is possible to limit the global temperature increase if only some scenarios and efforts are respected. As a result, appropriate energy production means (and human behaviours) must be found in order to reduce the greenhouse gases emissions. Among these solutions, deploying at large scale hydrogen as an energy vector (and chemical) appears to be a viable and an essential way to reach a decarbonised energy mix and lead to successful energy transition [2].

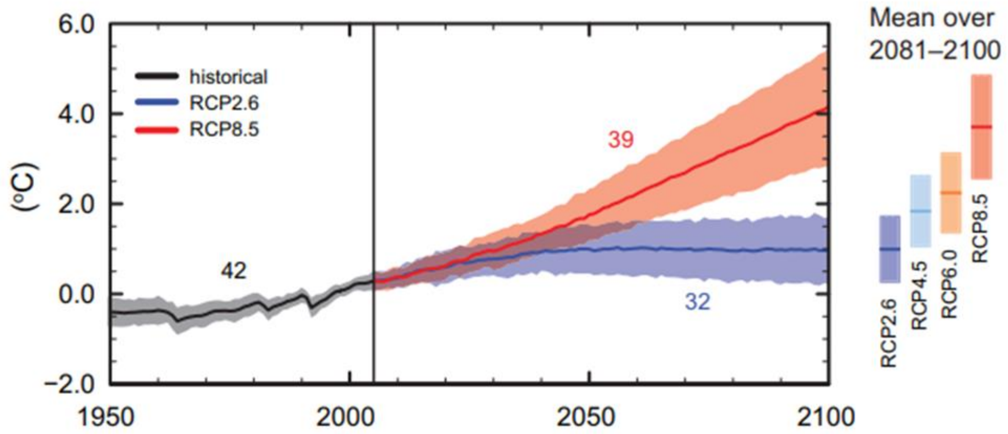

Figure I-1 : Global average surface temperature change according to four different RCP scenarios [3]. The different numbers indicated on the graph correspond to the number of model used to calculate the mean of the scenarios.

I.1.1 Hydrogen: a promising fuel

Hydrogen is one of the most abundant chemical element on the planet; however, in its natural state, hydrogen is mainly combined with other chemical elements; this means that molecular dihydrogen must be produced. The calorific value of molecular dihydrogen (H_2), hereafter simply denoted as “hydrogen” is almost three times higher than the fossil fuel (141 000 kJ.kg^{-1} compared to 48 000 kJ.kg^{-1} for petrol) and its catalytic combustion almost only releases water and heat as by-products, which is mainly why it is such an attractive candidate as decarbonized energetic vector. The use of hydrogen implies its production, storage, transportation, distribution and conversion into electricity. As a matter of fact, the excess of renewable energy, that would be lost if not stored (this is essentially the present case, as renewable systems produce electrical peaks which are de-phased compared to the consumption peak of the electrical grid), can be stored by producing hydrogen (the power-to-hydrogen strategy). Among the hydrogen production methods, there are the water electrolysis and the steam reforming. Table I-1 shows the power or the electricity sources and the carbon footprint associated for both production methods. It is clear that the production of hydrogen must be done using decarbonated power or electricity sources, and the cleanest mean to do so is water electrolysis using renewable electricity [4]. In fact, the steam reforming of natural gas method is CO_2 emitter. Please note that the major part of hydrogen production comes today from CO_2 emitter production methods (~ 95%) [5] since they are up to 5 times cheaper than water electrolysis. Even if temporary solutions, such as CO_2 capture are possible, it is necessary to keep developing the water electrolysis technology in order to reduce its costs and to be attractive for large-scale production of hydrogen with lowered CO_2 emissions [6].

Table I-1 : Examples of hydrogen production method and the power/electricity source required, including their carbon footprint [6].

Production method	Power/electricity source	Carbon footprint
Water Electrolysis	Renewable / Nuclear / electrical network	$< 2\text{-}3\ kg_{CO_2}eq.kg_{H_2}^{-1}$ (low CO_2 emission)
Steam reforming	Biomethane	$< 3\ kg_{CO_2}eq.kg_{H_2}^{-1}$ (low CO_2 emission)
	Natural/fossil gas	$\sim 11\ kg_{CO_2}eq.kg_{H_2}^{-1}$ (High CO_2 emission)

Regarding the storage of hydrogen, it is commonly done in either compressed gas (for most of terrestrial applications) or cryogenic liquid form (essentially for space/specific applications). Another method is the hydrogen adsorption on solid materials (*e.g.* nanostructured carbon powder), or the hydridation of metals (*e.g.* nanostructured magnesium-based hydrides) or the use of complex/chemical hydrides (*e.g.* borohydrides). Each method has its proper benefits and drawbacks and finds an interest depending on the transport method and distance, and the application needs [7]. Speaking of hydrogen transport, the distribution network is not enough mature at the moment to have a viable hydrogen infrastructure. It is usually transported from the point it is produced, to the point of use thanks to pipelines (for sustained and significant demands) or tank trucks (for small/rising demands). As example, for vehicle transportation, the hydrogen is dispensed in refilling stations, with by the end of 2018, 369 operational hydrogen stations in the world [8]. To produce electricity thanks to hydrogen, fuel cells are required. The next section presents the different fuel cell technologies that exist, their main specificities and the application associated.

I.1.2 Fuel cell technologies

Fuel cells ensure the chemical energy conversion of a fuel into electrical energy thanks to electrochemical reactions. The fuel is supplied to the anode, where it is oxidized and the oxidant at the cathode, where it is reduced. The anode and cathode are separated by an electrolyte, which allows the ionic conduction, and prevents the electronic conduction between the two electrodes. The fuel cells are open electrochemical reactors which can deliver electrical energy and heat as long as reactants are supplied. This allows to generate power (linked to the fuel cell size) and energy (linked to the autonomy, *e.g.* reactant storage capacity), which is one of the benefits of the use of fuel cells compared to batteries. The fuel cell technologies, which are summarized in the Table I-2, can be distinguished mainly by the nature of their electrolyte and their operating temperature, from which they generally take their names [9]. The Solid-Oxide Fuel Cell (SOFC) and Molten Carbonate Fuel Cell (MCFC) technologies are mainly used for stationary applications as they both operates at very high temperature, which render very awkward start-stop cycles (hence, they cannot be directly coupled with renewable electricity sources, which are inherently intermittent). MCFCs are suitable for distributed power generation and SOFCs can be used to produce a large amount of energy, usually in stationary plants which are coupled to a stable electricity and heat sources [10], [11]. Phosphoric Acid Fuel Cells (PAFCs) are generally found in stationary power generators, but they can also be used in transport application in large vehicles such as buses; they are however limited by their very large consumption of Pt-based catalysts and are in clear industrial decline presently. For all these reasons, the other fuel cell technologies have been more attractive in the recent years [12]. The PEMFC and AEMFC are commonly used/envisaged in light and heavy-duty applications, from bikes to trains, and stationary application such as emergency, domestic or industrial energy supply. The following section will focus on the PEMFC, as it is the fuel cell technology investigated in this work, and its application in transport sector.

Table I-2 : Fuel cell technologies and some of their features [9].

Fuel Cell	Fuel	Electrolyte	Charge carrier	Operating temperature (°C)	Catalyst	Applications
PEMFC	H_2	Proton Exchange Membrane	H^+	20-180	Pt	Light and heavy-duty vehicles, small stationary
PAFC	H_2	Phosphoric acid	H^+	150-200	Pt	Stationary
A(EM)FC	H_2	Anion Exchange Membrane (KOH for AFC)	OH^-	20-100	Pt/non-noble metal	Undersea vehicles, spacecraft
MCFC	H_2, CO, CH_4	Molten carbonate salt	CO_3^{2-}	600-700	Non-noble metal	Stationary
SOFC	H_2, CO, CH_4	Solid oxide	O^{2-}	700-1000	Non-noble metal	Stationary

I.1.3 PEMFC in transportation applications

Proton Exchange Membrane Fuel Cells tend to be a relevant technology for clean and efficient energy conversion for transport applications: they convert the chemical energy of hydrogen (H_2) into electricity and heat, water being the only chemical by-product. This technology is attractive to reduce as much as possible the CO_2 emissions in the mobility sector. In competition with battery to power electrical vehicles (EV), the main difference between the B-EV and PEMFC-EV technologies relies in their energy storage. Batteries have lower density and specific energies than PEMFC and H_2 storage, resulting in a lower autonomy of the vehicle at a given weight of generator (+ storage). Figure I-2 shows the major components of a fuel cell vehicle; for example, the Mirai from Toyota or the Nexo from Hyundai, have already been (successfully) commercialized since several years. The PEMFC-EV technology is more attractive for long journeys that require a large amount of energy, such as heavy-duty transportation. However, to reach a complete deployment of PEMFC-EV, inherent limitations of the technology still need to be overcome, not to speak about the hydrogen production, storage and delivery infrastructures. The first main technological limitation is the cost of the technology, mainly linked to the different materials needed in the PEMFC; this is especially the case regarding the catalyst layer (~40% of the total cost, considering 500 000 systems per year) [13]. PEMFC catalyst layers use platinum, a noble, rare and expensive metal, as catalyst for the electrochemical reactions. Thus, it is mandatory to reduce the Pt quantity used in catalyst layers. However, the performance of PEMFC, mainly driven by the cathode catalyst layer efficiency, is very platinum-dependant, meaning that, until recently, the highest performance was only obtained with high Pt loaded cathode catalyst layers under nominal operating conditions. Reducing the Pt-loading in catalyst layers keeping high performance is very challenging, which constitutes the second technological limitation. Finally, the durability of PEMFC still needs to be improved as the third technological limitation; the different degradation mechanisms of PEMFC will be presented in the sections I.3.1 and I.3.2. The PEMFC technology and especially the Low-Temperature PEMFC working up to 90-100°C (using perfluoro-sulfonated membrane) will be considered in this work and detailed in the next sections.

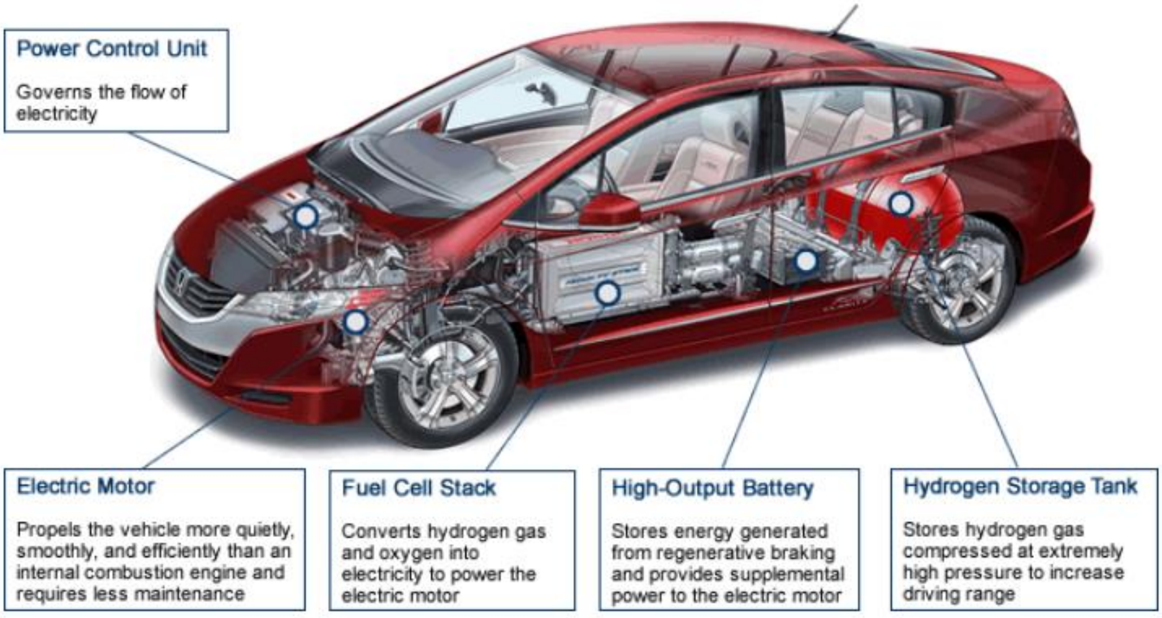

Figure I-2 : Fuel cell vehicle description (Honda FCX Clarity) [14].

I.2 PEMFC technology and its operating principle

I.2.1 PEMFC design and components

I.2.1.1 PEMFC Overview

The PEMFC is an electrochemical system that converts molecular dihydrogen (H_2) and dioxygen (O_2) into electricity, heat and water via electrochemical reactions. A unit of PEMFC is made up of a PEM electrolyte, on which are deposited two catalyst layers, an anode and a cathode, on both sides to form a Catalyst Coated Membrane (CCM); Gas Diffusion Layers (GDLs) and Monopolar Plates (MPs) complete the elementary cell. In real PEMFC systems, the elementary cells are usually stacked in series, two neighbouring single cells being electronically connected by the Bipolar Plates (BP) (standing for “two connected MPs”), which supply each cell with H_2 on one side and O_2 on the other side. The chemical energy conversion into electricity is achieved by the Hydrogen Oxidation Reaction (HOR) at the anode and the Oxygen Reduction Reaction (ORR) at the cathode. Table I-3 summarizes the electrochemical reactions that take place at the anode and the cathode, as well as the overall electrochemical reaction responsible for the energy conversion.

I.2 PEMFC technology and its operating principle

Table I-3 : Electrochemical reactions involved during PEMFC operation.

Electrochemical reaction	**Chemical equation**	**Standard potential (25°C – 1 bar abs.)**
HOR	$H_{2(g)} \rightarrow 2H^+ + 2e^-$	0 V *vs.* SHE
ORR	$½\ O_{2(g)} + 2H^+ + 2e^- \rightarrow H_2O_{(liq)}$	1.23 V *vs.* SHE
Global	$½\ O_{2(g)} + H_{2(g)} \rightarrow H_2O_{(liq)}$	1.23 V

The PEMFC single cell operation with the different reactants/products fluxes is described by the Figure I-3. The fuel, H_2 in this case, is fed to the anode via supply channels, formed on the monopolar plate. The gas diffuses through the GDL to the active sites of the catalyst layer, which contains platinum. At the anode, the HOR releases protons and electrons: the protons migrate through the PEM and the electrons are collected by the carbon in the catalyst layer and transported in the GDL, the monopolar plates and an external circuit, resulting in an electrical work, to the cathode catalyst layer. At the cathode, the oxygen, usually harvested from the ambient air using a compressor, is combined with protons and electrons at the active sites and reduced into water. The water produced and the excess of reactive gas are evacuated through the GDL and the channels, while the GDL and the monopolar plates evacuate the heat released.

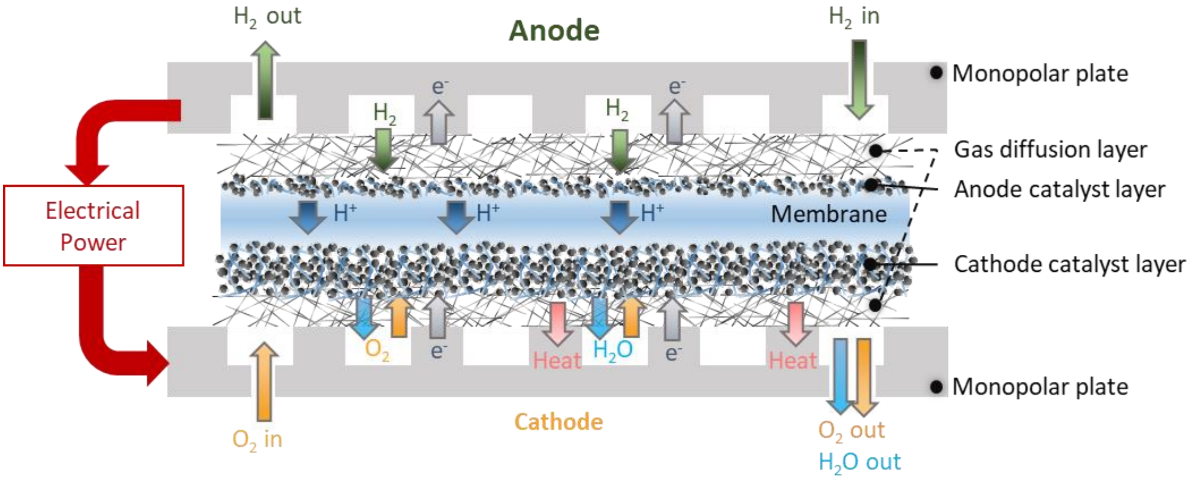

Figure I-3 : PEMFC single cell operation (reproduced from [15]).

In order to increase the power, single cells can be joined together and connected electrically in serial. This assembly is the so-called PEMFC stack, whose voltage (and therefore power) is proportional to the number of elementary cells that compose the stack. An example of such a stack is shown on Figure I-4.

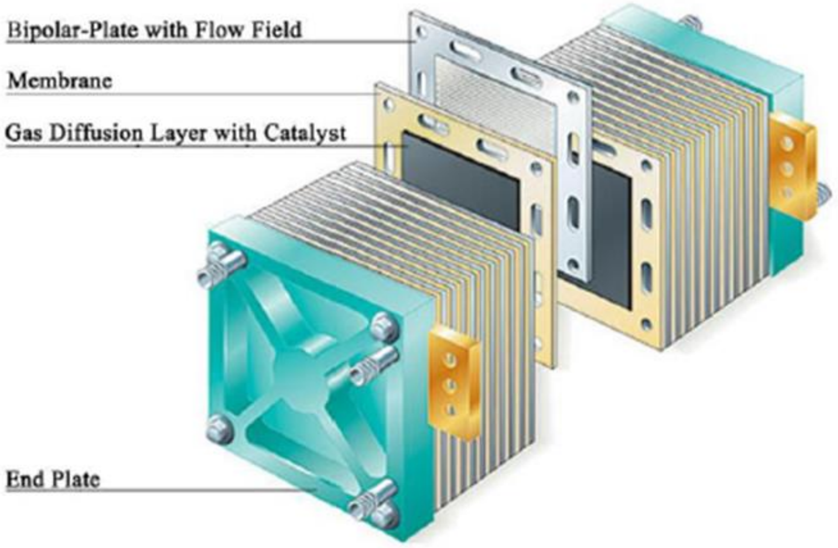

Figure I-4 : Example of PEMFC stack (reproduced from[16]).

The following sections detail the role of each component within a PEMFC and their main properties to reach efficient operation.

I.2.1.2 Monopolar Plates (MPs)

Monopolar plates ensure several important functions in a PEMFC. First, the monopolar plates ensure the reactive gases supply and the products evacuation, thanks to supply channels, usually etched (or stamped) on the monopolar plate material. Second, the MP conducts the current, by collecting the electrons, and the heat. To ensure these two functions as efficiently as possible, specific flow field rib/channel designs have been developed. The flow field rib/channel geometry (length, width, and pattern) is really important in order to supply homogeneously the reactive gases within the cell and between each cell of the stack and enable adequate pressure drop between the inlet and the outlet. The rib/channel design is also crucial to ensure the electrons collection and the evacuation of water, heat and exhaust gases [17]. If one of these functions is not correctly ensured, it may lead to heterogeneous operation of the PEMFC, which can result in lower performances and premature and local degradation. The most common rib/channel designs are serpentine and parallel, which are displayed on Figure I-5 (a) and (b), respectively. In this work, a small surface area single cell (1.8 cm^2) with a thin parallel rib/channel design (250 µm/250 µm rib/channel width and 400 µm depth) is used to perform electrochemical measurements.

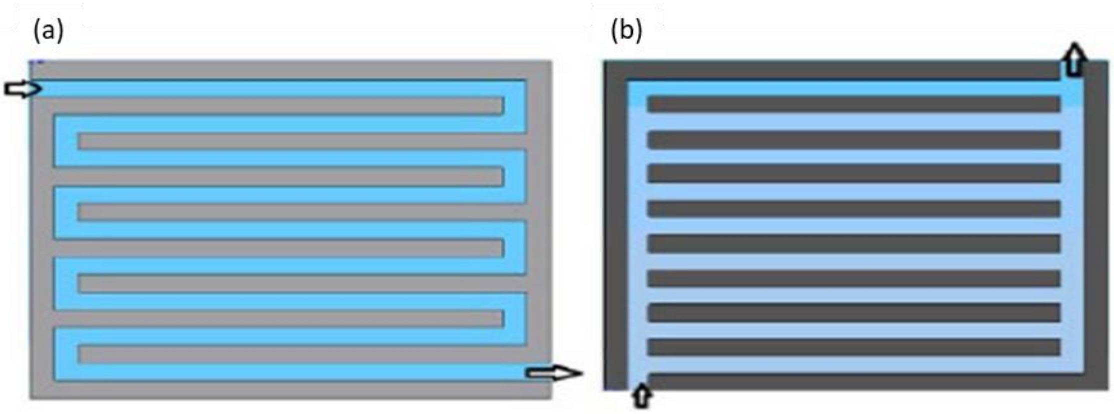

Figure I-5 : (a) Serpentine and (b) parallel flow field rib/channel designs (reproduced from [18]).

Finally, the monopolar plates are usually made of graphite composites or metal such as stainless steel, titanium or aluminium for their good electrical and thermal conductivity, as well as their good mechanical properties. These metallic materials must be treated against corrosion in order to be durable/stable in operation [19], [20] and to reach low interfacial contact resistance (< 10 mΩ.cm²). The monopolar plates of the single cell used in this work are made of aluminium with a gold coating. More details on the single cell used will be provided in the Chapter II.

I.2.1.3 Gas diffusion Layer (GDL) and Micro-Porous Layer (MPL)

Another key component of the PEMFC is the GDL. The GDLs are arranged between the catalyst layer and MP. This assembly is called the Membrane Electrode Assembly (MEA). The GDL aims at diffusing homogeneously the reactive gases to the surface of the catalyst layers, conducting the electrons, and heat to the monopolar plate's ribs. They are usually made of carbon fibres, a good electrical and thermal conductive material, coated with PTFE, which is a hydrophobic material. They ensure the evacuation of vapour and excess (liquid) water, produced at the cathode catalyst layer, avoiding any flooding phenomenon, which is an extreme case of water accumulation hindering the reactive gases transport to the active sites. Towards the catalyst layers, the GDL consists of a so-called Micro Porous Layer (MPL). The MPL is also made of carbon (in that case particles) coated with PTFE. In addition, the porosity of the MPL is lower than the GDL (around 35% *vs.* 75% respectively) to improve the water management and the fine distribution of the reactive gases to the catalyst layer (the MPL has more or less the same pore size as the catalyst layer). The MPL allows keeping a sufficient quantity of water at the catalyst layer surface, in order to ensure a good protonic conduction inside the catalyst layer and inside the membrane, while evacuating the excess water towards the GDL and monopolar plate. Finally, the GDL also ensure a good mechanical stability of the MEA. Figure I-6 shows a schematic description of the 22 BB GDL from Sigracet® (with MPL) including SEM images of these materials.

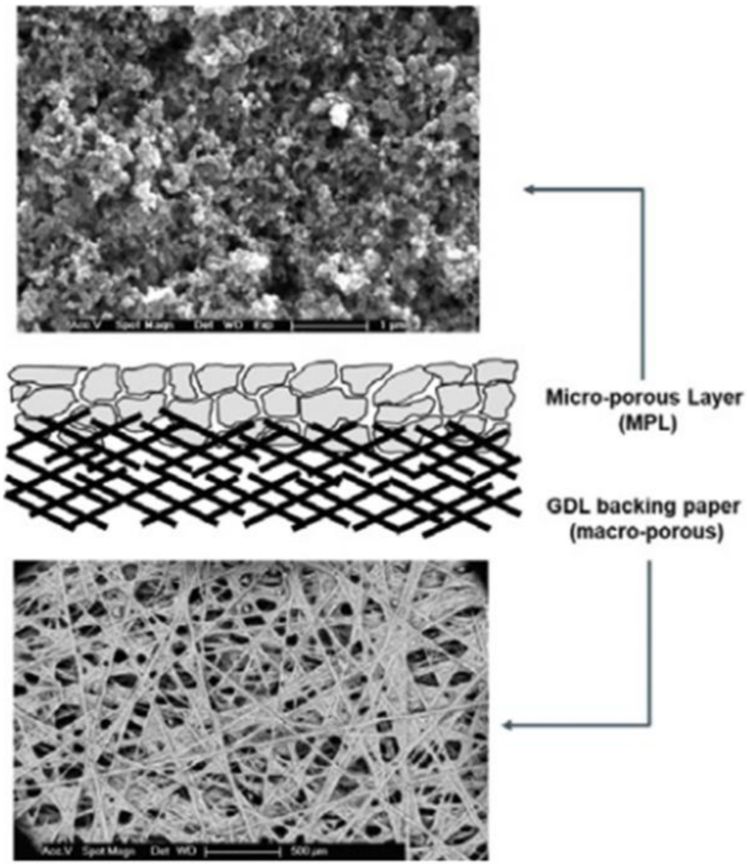

Figure I-6 : SEM images of the GDL and the MPL of the 22 BB material reference from Sigracet® datasheet [21].

I.2.1.4 Proton Exchange Membrane (PEM)

The PEM stands for the electrolyte, which electrically isolates the two electrodes and also forms a barrier that limits the diffusion/permeation of the two reactive gases, inhibiting the direct combustion reaction between them, that would result in a performance loss of the cell. The protons, produced by the HOR, migrate from the anode to the cathode through this material; thus, it must have a good protonic conduction. Nafion®, a perfluorosulfonic acid (PFSA) polymer, is the most commonly used material for PEM and a lot of research has been done on this material [22]. To reach an efficient protonic conduction, the PEM has to be hydrated. Indeed, PFSAs are made of PTFE polymer backbone with pendant side chains terminated by sulfonic acid groups as shown on Figure I-7.

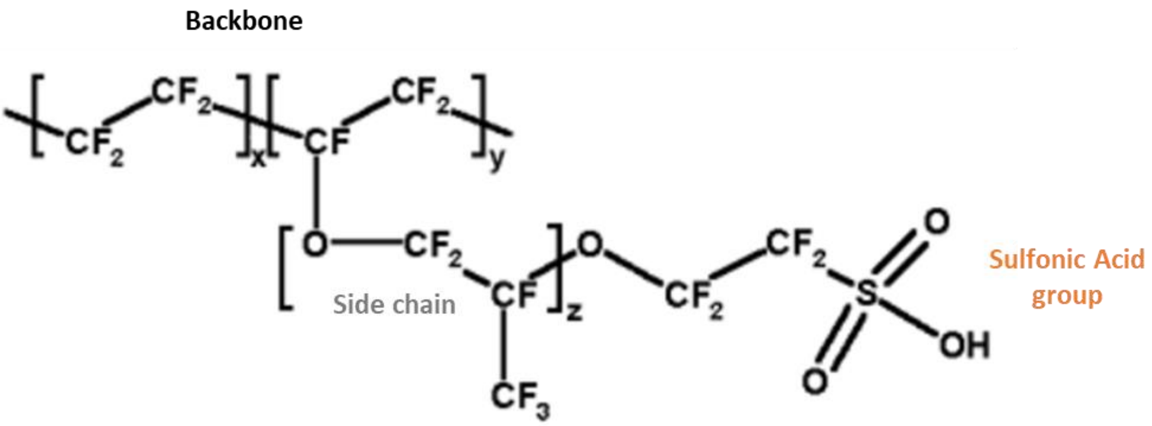

Figure I-7 : Chemical structure of PFSA Nafion® based material [22].

The hydration of the membrane leads to a phase separation between the backbones, which are hydrophobic, and the sulfonic acid groups, which are hydrophilic and where the water is located. The protons are transported in these hydrophilic regions thanks to water: high hydration level of the PEM is required to optimize proton conductivity.

I.2.1.5 Catalyst Layers (CLs)

The electrodes, or catalyst layers, are usually deposited on both sides of the membrane. It is where the electrochemical half-reactions take place. Catalyst layers are made of Pt nanoparticles (2 to 5 nm) dispersed onto a carbon support (particles diameter between 10 to 40 nm) and a protonic conductive polymer, called ionomer (usually of the same chemical nature as the PEM, but made of shorter macromolecules). The catalyst layer has a porous structure that ensures the reactive gases transport through porosity, the electrons conduction thanks to carbon connection network and proton migration via the ionomer. Electrochemical reactions take place on Pt nanoparticles as illustrated schematically for ORR on Figure I-8, where the connection between protons, electrons and the reactive gases, called triple phase interface, is necessary for the reaction to occur. Both anode and cathode catalyst layers contain Pt. The kinetics of the ORR is much more sluggish than the HOR on Pt, so higher Pt loadings are needed for the cathode catalyst layer (between usually 0.1 - 0.5 $mg_{Pt}.cm_{geo}^{-2}$) than for the anode catalyst layer (lower than 0.1 $mg_{Pt}.cm_{geo}^{-2}$).

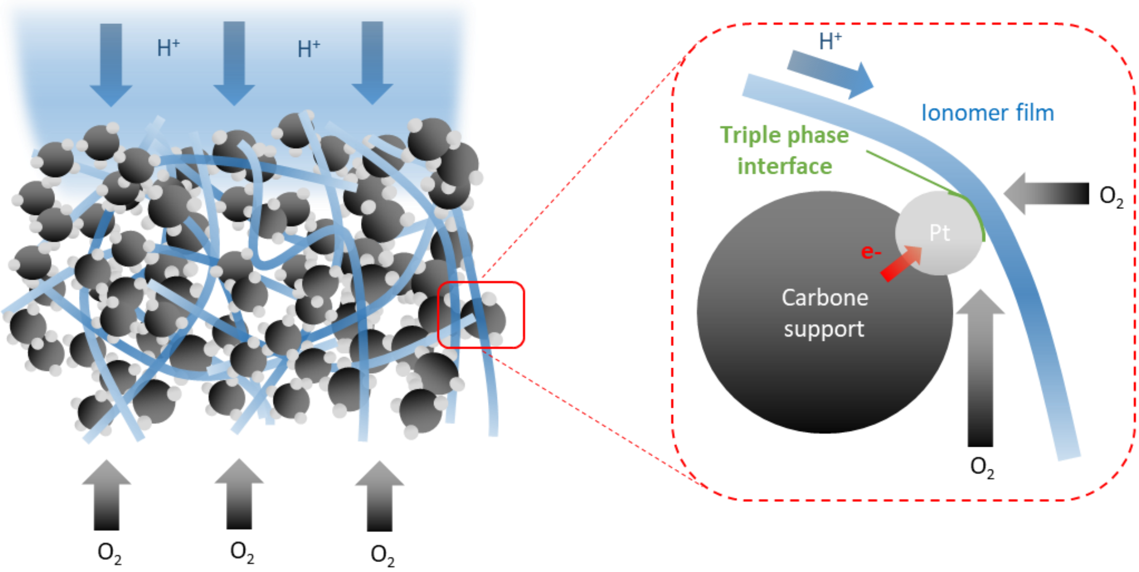

Figure I-8 : Cathode catalyst layer representation including the triple phase interface description (reproduced from [15]).

In order to operate well, catalyst layers, especially the cathode, must ensure several properties such as: reactive gases transport, proton and electronic conduction, water management and reaction catalysis. All these characteristics are mandatory to reach the highest efficiency of the PEMFC. In fact, the cathode catalyst layer is probably the most limiting component of PEMFC, mainly due to the complex interplay of the different physico-chemical and electrochemical phenomena occurring concomitantly in that component. These complex phenomena are coupled and the fact that the properties aforementioned cannot be decorrelated one from the other, makes difficult the identification and quantification of what is limiting during catalyst layer operation. In that extent, more and more work focus on the understanding of catalyst layer operation and performance limitation, at low Pt loadings, in order to make the link between the catalyst layer local properties, its structure and the performance. For instance, on-going European projects (FURTHER-FC and CAMELOT), including many actors, focus on the understanding of cathode catalyst layer performance and limitations [23], [24]. Classical and more advanced experimental characterizations are required to unravel the complex interplay of the physico-chemical and electrochemical phenomena. The experimental data may be used as input for models to validate and help describing relevant properties/behaviour of the catalyst layer that are neither fully understood nor enough accurately described; the modelling of the cathode active layer is precisely one of the main targets of this work (see Chapter IV).

I.2.2 Contributions and limitations of PEMFC during operation

I.2.2.1 Cell voltage calculation

The theoretical reversible cell voltage of the PEMFC (U°_{rev}) can be calculated, in standard operating conditions (25°C and 1 bar abs.) according to the potentials at its two electrodes (E°_{rev}), according to Equation I-1:

Equation I-1 :

$$U^\circ_{\mathrm{rev}} = -\frac{\Delta G^\circ}{nF}$$

With ΔG° the reaction free enthalpy, F the Faraday constant and n the number of electrons exchanged in the overall reaction from Table I-3. As PEMFC usually operates at various temperature, the reaction free enthalpy must be temperature dependant and can be expressed as:

Equation I-2 :

$$\Delta G(T) = \Delta H(T) - T \cdot \Delta S(T)$$

With ΔH and ΔS the enthalpy and entropy of the global reaction, whose values are given in Table I-4 for water production for both liquid and vapour state under standard operating conditions.

Table I-4 : Thermodynamic value for water production reaction in both liquid and vapour state in standard operating conditions [25].

Thermodynamic quantity	Liquid water	Vapor water
ΔG (kJ)	-237	-229
ΔH (kJ)	-285	-242
ΔS (J.K^{-1})	-162	-44

PEMFC usually operates at higher pressure than the atmospheric pressure and not with pure oxygen, thus the reversible cell voltage can be calculated thanks to the Nernst equation, described by Equation I-3:

Equation I-3 :

$$U_{\mathrm{rev}}(T,P) = -\frac{\Delta G(T)}{nF} - \frac{RT}{nF}\ln\left(\frac{a_{\mathrm{H_2O}}}{a_{\mathrm{H_2}} \cdot \sqrt{a_{\mathrm{O_2}}}}\right)$$

With R the universal gas constant and $a_{\mathrm{H_2O}}$ the activity of water, which is equal to the relative humidity defined by $\frac{P_{\mathrm{vap}}}{P_{\mathrm{sat}}(T)}$. $a_{\mathrm{H_2}}$ and $a_{\mathrm{O_2}}$ are the activity of hydrogen and oxygen respectively. Under standard operating conditions and considering a liquid water production, the theoretical reversible cell voltage is equal to 1.23 V. In the case of vapour water production (at 1 bar abs.), the reversible cell voltage is equal to 1.18 V. However, these values are calculated considering the equilibrium in standard operating conditions, without any kind of kinetic losses or limitations, which is not the case during real fuel cell operation. Figure I-9 shows a schematic illustration of the impact of the different limitations on the PEMFC global performance during classical PEMFC operation. Three main loss mechanisms can be observed, leading to a drop in potential on the global current range, which is why they are called overpotential. One should be aware that the different losses are not simply cumulative but coupled between each other.

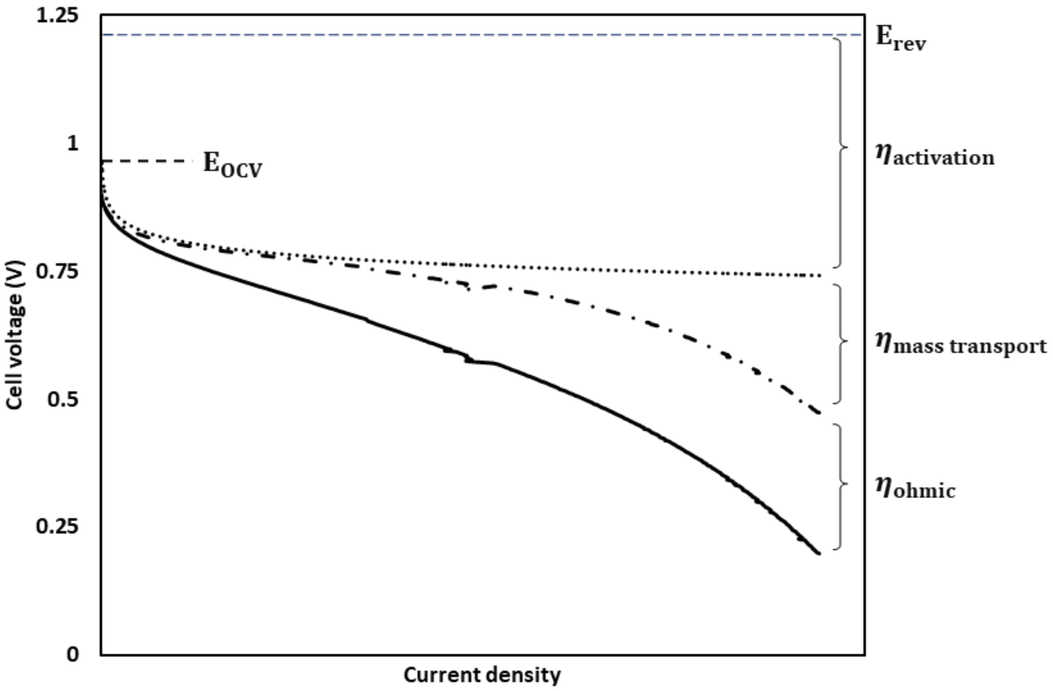

Figure I-9 : Schematic illustration of the different loss contributions impact on the PEMFC global performance.

I.2.2.2 Overpotential and loss contributions

The activation overpotential is related to the kinetics of the ORR and HOR. In the present case (in a PEMFC in general), the activation overpotential of the anode is negligible compared to the cathode ($\eta_{\mathrm{HOR}} \ll |\eta_{\mathrm{ORR}}|$) due to the fast kinetics of HOR on Pt. Thus, the activation overpotential are approximated to the losses due to the sluggish kinetics of ORR ($\eta_{\mathrm{activation}} \simeq \eta_{\mathrm{ORR}}$). The losses are increasing rapidly as soon as current density is produced, which corresponds to the very low current density region. In all the other current density regions, the activation overpotential is still present (and dominant) but other losses (ohmic and from mass-transport) start to be significant. This means that at very low current density, which corresponds to very low overpotential region of the cell voltage, the activation overpotential is predominant and mass transport limitations are usually negligible. In a first approach, considering that the ORR is driven only by an electrochemical kinetic step, with a single electrochemical step to convert O_2 into H_2O (a very hypothetical case), the current density can be expressed as a function of the overpotential according to the Butler-Volmer law:

Equation I-4 :

$$j = j_0 \left[e^{\frac{\alpha F}{RT}\eta_{\mathrm{ORR}}} - e^{\frac{-(1-\alpha)F}{RT}\eta_{\mathrm{ORR}}} \right]$$

With j_0 the exchange current density, the fictive reaction current at equilibrium for both the oxidation and reduction directions (when there is no overpotential) and α the charge transfer coefficient. The oxidation component of the Butler-Volmer law may be negligible in the case of sufficient cell overpotential ($\eta_{\mathrm{ORR}} > 90\ \mathrm{mV}$) resulting in the approximation of Tafel described by Equation I-5, which allows to express the ORR overpotential as a function of the current density.

Equation I-5 :

$$j = j_0\, e^{\frac{-\alpha F}{RT}\eta_{\mathrm{ORR}}}$$

The mass transport overpotential includes all the limitations related to the depletion of reactants at the surface of the catalyst. Such an interfacial lack of the reactive gases leads to a decrease of their respective partial pressure, resulting in a cell potential drop according to Equation I-3 and affecting the exchange current density j_0, which depends of the reactant activities. During real operation of the PEMFC, when current density is produced, the reactive gases must be channelled to the active site. Thus, concentration gradients appear in the catalyst layer and the GDL thicknesses and pressure drop along the channel: the higher the current density at fixed stoichiometry, the bigger the flowrates of the reactants, which results in more important pressure drop. This is why the different components of the PEMFC must be optimized in order to well manage the reactants supply and the products evacuation. For instance, (liquid) water accumulation hinders the oxygen transport to the active sites. Note that the mass transport overpotential is not only affected by the transport of reactants in the components of the PEMFC. In fact, kinetic phenomena related to the catalyst utilization effectiveness and the reactants concentration, cannot be separated from mass transport limitations through the components. Indeed, operating heterogeneities result in heterogeneous operating conditions in the plane or through thickness of the catalyst layer, which exacerbates the concentration gradients through the components and also creates concentration gradients in the plane of the catalyst layer (rib/channel effect for instance). All these phenomena worsen the cell potential drop related to mass transport overpotential ($\eta_{\mathrm{mass\ transport}}$).

Finally, an ohmic overpotential (η_{ohmic}) is induced by the electronic and ionic resistances of the different materials that compose the cell. The ionic resistance is ascribed to the proton resistance in the ionomer in the catalyst layer and in the membrane. This ionic resistance depends on the thickness of the ionomer and its humidification level and temperature. The resistance decreases with hydration and temperature and it increases with the thickness [26], [27]. The electronic resistance is ascribed to the transport of electrons to the active site. To reach the active sites, the electrons are passing by many cell component interfaces. A non-negligible part of the electronic resistance is ascribed to the quality of these interfaces and thus the compression level applied to the components [26]. This electronic resistance decreases with the applied mechanical pressure, with a limit not to exceed, because it may be incompatible with a stack assembly and because the porosity is decreasing with the compression level, hindering the water and gas transport management. The ohmic overpotential, which is current density dependant, can be estimated according to an ohmic law thanks to Equation I-6:

Equation I-6 :

$$\eta_{\mathrm{ohmic}} = i \cdot (R_{\mathrm{electronic}} + R_{\mathrm{ionic,MB}})$$

These resistances can be estimated thanks to Electrochemical Impedance Spectroscopy (EIS) measurements at high frequency [26]. EIS measurements consists of monitoring the response of an electrochemical system (in that case the fuel cell) when a current or potential disturbance, whose features are a stationary working point, the amplitude and the range of frequency applied. The EIS measurements applied to our PEMFC single cell will be more detailed in the Chapter II. The sum of the electronic resistance of the electrodes/BPs and ionic resistance of the membrane is often associated to the high frequency resistance (R_{HF}) estimated with the aforementioned EIS measurements. Assuming the invariance of $R_{\mathrm{electronic}}$ during PEMFC operation [26], the EIS measurements can be done in order to capture the hydration state of the ionomer of the membrane, as $R_{\mathrm{ionic,MB}}$ is water content dependant. At the end, considering all the loss contributions, the cell potential is estimated according to Equation I-7:

Equation I-7 :

$$U_{\mathrm{cell}} = E_{rev} - \eta_{\mathrm{activation}} - \eta_{\mathrm{mass\ transport}} - \eta_{\mathrm{ohmic}} - \eta_{\mathrm{other}}$$

With η_{other} the overpotential due to other phenomena leading to a cell voltage drop, such as parasitic reactions originating from the presence of other electroactive species than O_2 at the cathode (*e.g.* H_2 crossover through the membrane, or contaminants). These phenomena are presented and discussed in the following sections. Here again, note that the Equation I-7 gives an idea of the calculation of the cell potential value considering that the losses are cumulative, which is strictly not the case.

I.2.2.3 Open Circuit Voltage and mixed potential

On Figure I-9, the voltage at which no current density is produced is called the Open Circuit Voltage (OCV). It corresponds to a cathode potential (as the anode potential is close to 0 V *vs.* RHE) where the catalyst is simply in contact with the reactant and the ionomer. Theoretically, this potential would be an “equilibrium”, that could be calculated according to the Nernst equation. The same could be done at the anode and, if hydrogen and oxygen are the only electroactive species in presence at the anode and cathode respectively, the OCV should be equal to U_{rev}. This is not the case in PEMFC. Indeed, the ORR is a slow reaction, that cannot proceed close to its equilibrium potential. Also, the composition of catalyst layer (Pt, carbon and ionomer), as well as, the operating conditions (temperature and hygrometry) induce the presence of other electroactive species, thus other electrochemical couples with their specific reversible potentials. For instance, platinum in presence of oxygen and water will be oxidized, leading to species such as PtOH or PtO, which are the oxidized form of Pt at a degree 1 (Pt^{+I}) and 2 (Pt^{+II}) respectively. The reversible potential of Pt/PtOH and Pt/PtO is often estimated under 1 V *vs.* RHE [28]. The Pt oxides formation/reduction will be more detailed in the section I.3.2.2. These redox couple impose their potential to the cathode, precisely owing to the slow ORR kinetics. Another example is that the carbon in presence of water and oxygen leads to the presence of quinone/hydroquinone species, which electrochemically respond around 0.6 V *vs*. RHE [29]. All in all, the hindrance of these electrochemical redox couples in the catalyst layer decreases the U_{rev} value until the so-called mixed potential in open circuit, not to speak from impurities at the catalyst surface that may also decrease the OCV.

I.2.2.4 H_2-crossover

Another contribution to the OCV drop is the H_2-crossover. The membrane is not completely gas tight and a small flux of hydrogen from the anode is crossing the membrane to reach the cathode. This H_2 flux leads to an oxidation current density production at the positive electrode (from the HOR at the cathode potential), the permeation current. Symmetrically, the oxygen from the cathode can also cross the membrane to reach the anode, where it is reduced. These two contributions result in drop of the OCV value [30]. In this work, as cathode catalyst layer are characterized, only the hydrogen crossover will be considered and discussed (it is the most prevalent anyways in real PEMFCs): the oxygen crossover does not have a significant impact on the OCV value, as it does not lead to significant variation of the anode potential [31]. Due to the fast oxidation of hydrogen on platinum, Vilekar and Datta estimated the permeation current according to Equation I-8 [31]:

Equation I-8 :

$$i_{H_2-crossover} = \frac{Fk_{\mathrm{m}}}{e_m}P$$

With e_{m} and k_{m} the membrane thickness and permeability, respectively. From this equation, the hydrogen flux that reaches the cathode, thus the permeation current produced, increases with the hydrogen gas partial pressure P and the permeability of the membrane, which depends on its temperature and humidification (it increases with hydration [32]) and thickness (it decreases with the membrane thickness). The permeation of the membrane drastically increases upon degradation, resulting in large potential drop of the OCV. Thus, the OCV may be used as a good indicator of the state of health of the membrane [30].

As shown above, the OCV depends on the different species in presence at the cathode catalyst layer (materials used and hydrogen that crosses the membrane). These contributions are many parameters dependant. Both the temperature and relative humidity (water activity) impact the species in presence and the calculation of reversible potential (Nernst equation), but may also affect the membrane hydration and thus its permeability to gases. Thus, it is difficult to quantify the different contributions due to their complex interplay, not to speak about the nature and structure of the different components that may lead to different local environments.

I.3 PEMFC degradation mechanisms

PEMFC degradation mechanisms, causing performance losses and ultimately the end of life of the stack, are extremely critical for the deployment of the technology in mass markets, like the automotive applications; they are therefore under intensive focus in the research community since *ca*. 20 years. PEMFC degradations can be classified into two main categories: the irreversible degradations and the reversible degradations. The irreversible degradations include all the mechanisms that lead to a performance loss that is not reversible or recoverable; they are usually connected to a non-negligible alteration of the PEMFC materials (MEA and BPs) [33], [34]. On the contrary, the reversible degradations deal with phenomena that contribute to a performance loss that may be recoverable under specific operation of the PEMFC, and are usually not connected to deep materials changes [35]. The following sections will present the different degradation mechanisms related to the fuel cell core (MEA) components, the membrane and the catalyst layers. The mitigation strategies regarding these degradation mechanisms are not presented here.

I.3.1 Irreversible degradations

Each component of the PEMFC is prone to irreversible (materials') degradations. The degradation mechanisms of the bipolar plates are the corrosion, due to the acidic and humid environment of the PEMFC and mechanical deformation due to compressive force applied to ensure the good electrical interface and the sealing of the PEMFC [35]. Only few studies were made on the durability of GDL [36]–[38]; most of them are converging towards modifications of physico-chemical properties due to PTFE degradation/carbon corrosion, during mainly *ex situ* ageing procedure to avoid any controversy regarding the other component degradation consequences [35]. The following will focus on the membrane and catalyst layers degradation mechanisms.

I.3.1.1 Membrane degradation

The membrane degradation can occur according to three main categories: mechanical, thermal and chemical or electrochemical mechanisms. Mechanical degradation mechanisms may come from excessive or non-uniform compression resulting in cracks, tears or pinholes formation [39], these processes likely being emphasized after chemical attack of the ionomer, *e.g.* by peroxide radicals [40]. Such degradations affect directly the performance of the PEMFC as the barrier property for reactive gases that must ensure the PEM is not effective anymore, resulting in a significant and irreversible drop of the cell voltage [35]. These degradation phenomena may also be caused by repetitive volume changes of the membrane, mainly due to hygrometry cycles at high temperature that induce swelling and shrinkage of the membrane [41]. Depending on its applications, transport or stationary, the PEMFC may be subject to thermal cycling, as well as extreme temperature, especially freezing and/or close to water boiling temperature. Some studies showed that thermal cycling result in impaired mechanical and physico-chemical membrane properties, but not serious physical or chemical damage [42]. However, these modifications of the membrane properties may induce local physical defects on the membrane that may result in other degradation mechanisms [43]. Chemical degradation is the last but not least mechanism that leads to irreversible failure of the membrane. It consists of polymer end groups attacked by radicals, $HOO^{\bullet}$ and $HO^{\bullet}$ [44], radicals that are formed from hydrogen peroxide H_2O_2, which is produced either at the cathode during the ORR or at the anode due to O_2 crossover through the membrane [45], [46]. The radical formation from H_2O_2 requires the presence of metal cations such as Fe^{2+} or Pt^{2+}, which usually come from contamination due to corrosion of the bipolar plates or of the catalyst, and is generally accelerated at the OCV under dry operating conditions [47]. There is another pathway that leads to the radical formation, which does not require the initial formation of hydrogen peroxide. During PEMFC operation, the simple presence of H_2, O_2 and Pt can directly result in the radical formation. In addition to catalyst layers, the radical formation can also occur in the membrane where Pt can deposit due to the electrode degradation and catalyst dissolution/redeposition mechanism [43], [48], which will be presented in the next section.

I.3.1.2 Catalyst layer degradation

Catalyst layers are an assembly of several materials (carbon, platinum and ionomer) in a complex porous structure. Under real and long-term operation of PEMFC, catalyst layers are prone to different degradation mechanisms. The cathode catalyst layer is the most concerned (compared to the anode) due to its more stressed environment (oxidative, hygrometry and thermal cycles, wide potential range) [48]. In addition, the cathode catalyst layer operation is usually heterogeneous, resulting in heterogeneous degradation [34]. Thus, the optimization of the catalyst layer structure, as well as the other components is mandatory to avoid these local and heterogeneous degradations, due to various local operating conditions. There are four main degradation mechanisms of the catalyst layer, which are presented on Figure I-10 [34].

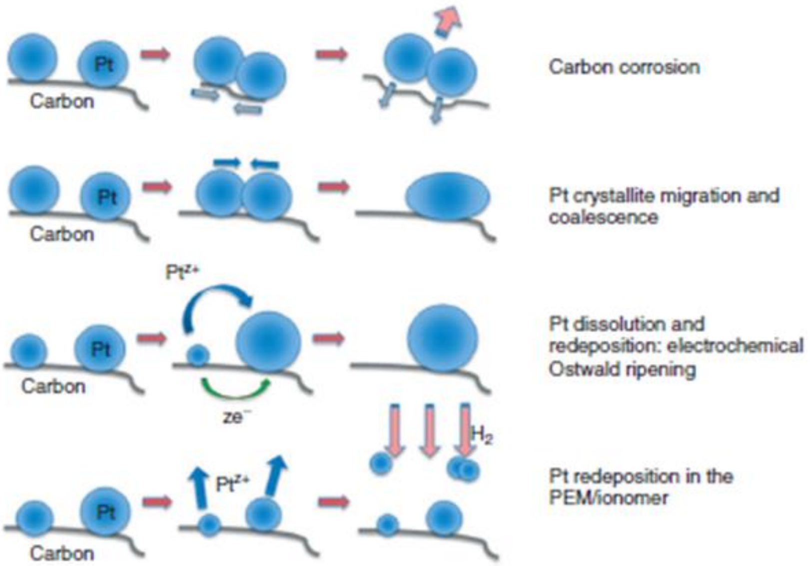

Figure I-10 : Degradation mechanisms related to the Pt/C electrode (taken from [34]).

Equation I-9 describes the carbon corrosion phenomena, which is thermodynamically possible at potential above 0.207 V *vs.* SHE, the standard potential of the carbon corrosion at 25 °C ($E^{\circ}_{\mathrm{C/CO_2}} = 0.207\ \mathrm{V}\ vs.\mathrm{SHE}\ @\ 25\ °\mathrm{C}$). Thus, this degradation mechanism occurs at usual cathodic potential [49]. Nevertheless, the reaction is slow and becomes usually significant only at high potential, generally encountered during fuel cell startup.

Equation I-9 :

$$C + 2H_2O \rightarrow CO_2 + 4H^+ + 4e^-$$

The carbon corrosion is impaired by many parameters such as the potential, the temperature, the hydration and the nature of the carbon material (structure/morphology and surface properties) [50]–[52]. In addition, the presence of Pt nanoparticles supported on the carbon enhances its corrosion [53]. The carbon corrosion mechanism in presence of Pt is described by Equation I-10 and Equation I-11:

Equation I-10 : $$Pt + CO_{ad} \rightarrow PtCO_{ad}$$

Equation I-11 : $$PtCO_{ad} + H_2O \rightarrow CO_2 + 2H^+ + 2e^-$$

The carbon corrosion mechanism is generally evidenced by accelerated stress tests, which consist of potential cycling between high/low potential values, inducing the repeated Pt oxides formation/reduction and carbon surfaces groups formation/reduction, unavoidable during PEMFC operation and start/stop and at OCV [29], [52], [54]. The carbon corrosion results in Pt nanoparticles detachment that leads to a loss of the Electrochemical active Surface Area (ECSA) and thus a drop of PEMFC performance. In extreme cases, carbon corrosion leads to a collapse of the porous structure and a thinning of the catalyst layer (amorphization) [55]. This results in irreversible mass transports losses, as it is more difficult for reactive gases to reach the active sites due to the lower porosity and enhanced hydrophilicity of the active layer (that induces flooding) [34].

Platinum degradation mechanism can take place in three different ways: (i) the Pt coalescence upon Pt crystallite migration, resulting in Pt agglomerates, (ii) the Pt dissolution and redeposition upon the Ostwald ripening mechanism and (iii) the Pt dissolution and redeposition in the PEM or in the ionomer of the catalyst layer (all lower the ECSA) [34]. The Pt crystallites migration is enhanced in the presence of surface oxygenated carbon groups, while hydrogen crossover (and reducing potential values) promotes coalescence. All the Pt degradation mechanisms are accelerated upon potential cycling, in particular the Pt crystallites migration in presence of reducing species [56]. In addition, the nature of carbon may have a non-negligible impact on this degradation mechanism, as for carbon corrosion [52]. Then, platinum is prone to corrosion, especially in an acidic environment and in presence of water (*e.g.* the environment of a PEMFC cathode). The corrosion mechanism may occur via the formation of Pt oxides or their reduction Equation I-12 [57], but also via chemical dissolution of Pt oxides Equation I-13 [58].

Equation I-12 : $$Pt + H_2O \leftrightarrow PtO + 2H^+ + 2e^-$$

Equation I-13 : $$PtO + 2H^+ \leftrightarrow Pt^{2+} + H_2$$

Platinum corrosion may also occur via a single electrochemical step described by Equation I-14 [48], [59].

Equation I-14 : $$Pt \leftrightarrow Pt^{2+} + 2e^-$$

In any case, the platinum corrosion leads to the formation of dissolved Pt^{2+} ions. According to the Gibbs-Thomson equation and many studies in literature, smaller platinum nanoparticles are preferentially corroded compared to bigger nanoparticles, which are more stable (low surface energy) [60]–[62]. Thus, the Pt corrosion depends on many parameters such as the Pt size distribution, the pH, the potential range and the operating conditions. In summary, Pt corrosion leads to the dissolution of the smallest nanoparticles and the redeposition on the largest, during potential cycling or through the electrochemical Ostwald Ripening (Figure I-10), which can take place naturally (selective corrosion between particles). It results in an irreversible loss of ECSA, as the smallest nanoparticles develop the highest surface, but not to a significant activity loss [63], owing to the well-known particles size effect [64]. Moreover, the dissolved Pt^{2+} ions can be chemically reduced according to Equation I-15:

Equation I-15 :

$$Pt^{2+} + H_2 \rightarrow Pt + 2H^+$$

The dissolved Pt^{2+} ions can be transported via water flow pathway (electro-osmotic drag from the cathode to the anode through the membrane or water transport in the cathode catalyst layer). The chemical reduction of Pt^{2+}, due to the H_2-crossover, results in the presence of Pt nanoparticles inside the ionomer of the catalyst layer or inside the membrane, inducing the formation of a Pt band in the membrane [48]. The Pt nanoparticles may not be connected electrically anymore to ensure the ORR, which leads to a significant and irreversible loss in ECSA and of the global performance of the PEMFC [34], [48], [58].

Regarding the ionomer component inside the active layer, its degradation mechanisms are substantially similar to the chemical degradation of the membrane [65], [66]. However, the impact of ionomer degradation on the performance remains unclear and is still an open question [67]–[69].

I.3.2 Reversible degradation

As said previously, the reversible degradation mechanisms reflect a performance loss that can be recoverable. A typical example of reversible degradation is the hysteresis phenomenon, which indicates a dynamic behaviour in the cell, observed experimentally on PEMFC performance measurements, between the increase (forward) and decrease (backward) current density sweeps [70]. It may also happen during a stationary operation, resulting in a performance loss over time [63]. Globally, these phenomena are related to mass transport limitations and/or abnormal (transient) local operating conditions, which can appear under specific operating condition of the PEMFC. Among the phenomena that lead to reversible degradations, the most known are related to the water management, the Pt oxidation and the presence of impurities at the catalyst surface [71]. The case of airborne pollutants (SO_x, NO_x, NH_3, etc) and specific contaminants in H_2 will not be detailed or considered here [72]. However, Decoopman et *al.* highlighted that the presence of CO even under pure H_2, due to the carbon support corrosion at the anode catalyst layer which poisons the catalyst, results in a cell voltage loss. This performance loss is recovered thanks to potential cycling at the anode or the addition of air, resulting in the carbon monoxide oxidation [73]. Air impurities can also alter the cathode operation (in a reversible manner – or in some cases in a rather irreversible manner) [74]. The water management and the Pt oxidation phenomena are presented in the following sections.

I.3.2.1 Water management

Water management plays a crucial role on the efficiency of PEMFC operation in order to reach the highest performance, as it affects significantly the protons and oxygen mass transport. Indeed, on the one hand, the ionomer inside the catalyst layer and the membrane must be enough hydrated to ensure a good proton conduction, as protons migrate through the hydrated regions (more hydrophilic) of the ionomer. On the other hand, accumulation of liquid water in the porosity of the catalyst layer or the GDL and in the channels in the bipolar plate must be avoided in order to prevent flooding events and ensure an efficient reactive gases transport to the active sites [75]. Flooding events are often observed at high current densities, where the water production become so significant that the removal rate is not enough, resulting in a significant mass transport overvoltage. However, depending on the operating conditions, flooding events may occur at lower current density regions [75]. Flooding may be avoided with short time operation with dry gases [76]. Water distribution in PEMFC is a complex mechanism, as it is affected by the global operating conditions, but also by the local operating conditions, possibly arising from heterogeneous operation of the PEMFC (especially in large cells). In fact, the current density distribution depends on many parameters, such as the reactants distribution, the bipolar plate design (flow field rib/channel design and cooling channel design) and the operating conditions (hygrometry, temperature, pressure). In his thesis, Nandjou highlighted that an heterogeneous current density distribution is often a consequence of an heterogeneous distribution of water and the appearance of local hot spots, even though this is a retroactive effect (which can amplify or mitigate the heterogeneities) [77]. In addition, heat and water management were found closely related and coupled, local hot spots having a significant impact on the membrane properties (proton conductivity and water content), these phenomena being exacerbated at high current densities [77]. Considering these observations, it is clear that a poor water management induces a non-optimized PEMFC operation, resulting in performance loss, but not necessarily in irreversible damage of the components (if it does not happen during a long period).

Many studies in literature agree on the fact that water management (flooding events and water distribution), which depends on the GDL nature, flow rates, temperature and relative humidity, explains the hysteresis observed experimentally on polarization curves. Under dry operating conditions at the cathode, Hou found that the high frequency resistance (R_{HF}) decreases on the forward sweep of the polarization curve, due to the increase water generation (as the current density is increasing), and increases on the backward sweep of the polarization curve, due to the decreasing current density, so water generation. In his work, he also discusses water accumulation in the diffusion media, that may explain the initial worst performance of the backward sweep compared to the forward sweep at low potential [78]. The different R_{HF} values between the two sweeps of the polarization curve indicate in part changes of the hydration state of the membrane between the two sweeps, and account for the hysteresis observed experimentally on the polarization curve. The fact that different water quantity production has an impact on the hydration state of the membrane, and thus results in a decrease of the high frequency resistance was also mentioned in the study of Santarelli and Torchio. However, they did not show their high frequency measurement results [79]. In fact, if a quantitative estimation of the ohmic loss is done, related to different R_{HF} between the forward and the backward sweeps of the polarization curve, it is not sufficient to explain the different performance observed on the experimental polarization curve. For instance, in the work of Hou, on the first polarization curve at 0.4 A.cm^{-2}, there is a gap of 50 mV between the forward and the backward sweep of the polarization curve. Considering the ΔR_{HF} 0.4 A.cm^{-2}, it leads to a rough ohmic loss estimation of 32 mV, which is not sufficient to explain the gap of 50 mV they observe [78]. An ohmic drop correction from the R_{HF} value should lead to a polarization curve corrected from the losses due to the different hydration state of the membrane and reveal if the hysteresis is still observed or not. In addition, the ionic resistance of the catalyst layer ($R_{\mathrm{ionic,CL}}$), which accounts for the hydration state of the ionomer inside the catalyst layer, was not taken into account in their work and its evolution along, and between the two sweeps of the polarization may be similar to R_{HF}. Thus, there must be other contributions accounting for this hysteresis phenomenon. In the work of Jomori *et al.*, the hysteresis was ascribed to phenomena occurring at the ionomer/Pt interface due to ionomer adsorption: the high frequency resistance change with water uptake of the membrane or catalyst layer have only minor contributions according to their observations [80]. For He *et al.*, the hysteresis observed on the polarization curve is ascribed to the hysteresis observed from the capillary pressure and liquid saturation level in porous media [81].

I.3.2.2 Platinum oxides formation/reduction

The platinum oxidation was also identified as a phenomenon inducing activity decrease regarding the ORR at the cathode and performance loss. On the one hand, Pt oxides formation and reduction upon potential cycling result in Pt corrosion and irreversible performance loss, as it was said previously. On the other hand, a constant operation at high potential of the PEMFC, induces the formation of Pt oxides, resulting in Pt activity loss for ORR [63], [71], [76], [82]. The progressive activity loss during long period at high potential, such as at the OCV, can be recovered under specific operating conditions. Uribe *et al.* showed that the recovery of the activity could be achieved by forcing the cell voltage to drop down to 0.2 V, potential at which the Pt oxides are reduced into Pt [82].

Even though the different degradation mechanisms involving Pt oxidation are now well identified, the impact of Pt oxidation on the ORR mechanism is not entirely understood. In fact, the ORR mechanism consists of a complex multi-step reactions, which involves several surface reaction intermediates [63], [83]–[85]. Previous studies notably mentioned the formation of PtOH, PtO [86], [87], PtOOH [88] and PtO_2 [89] species depending on the operating conditions and the pathway the ORR can proceed: associative [102], dissociative [101] or peroxide pathways [103] (see Figure I-11). The main difference between the associative and dissociative pathways is whether oxygen adsorbs during hydrogenation or before it happens. The peroxide pathway leads to the formation of peroxide species due to incomplete reduction. However, there is no mutual agreement on the real description and there are still issues that need to be overcome to unravel the complex ORR mechanism (Tafel slope doubling, the impact of intermediate species formation, etc.).

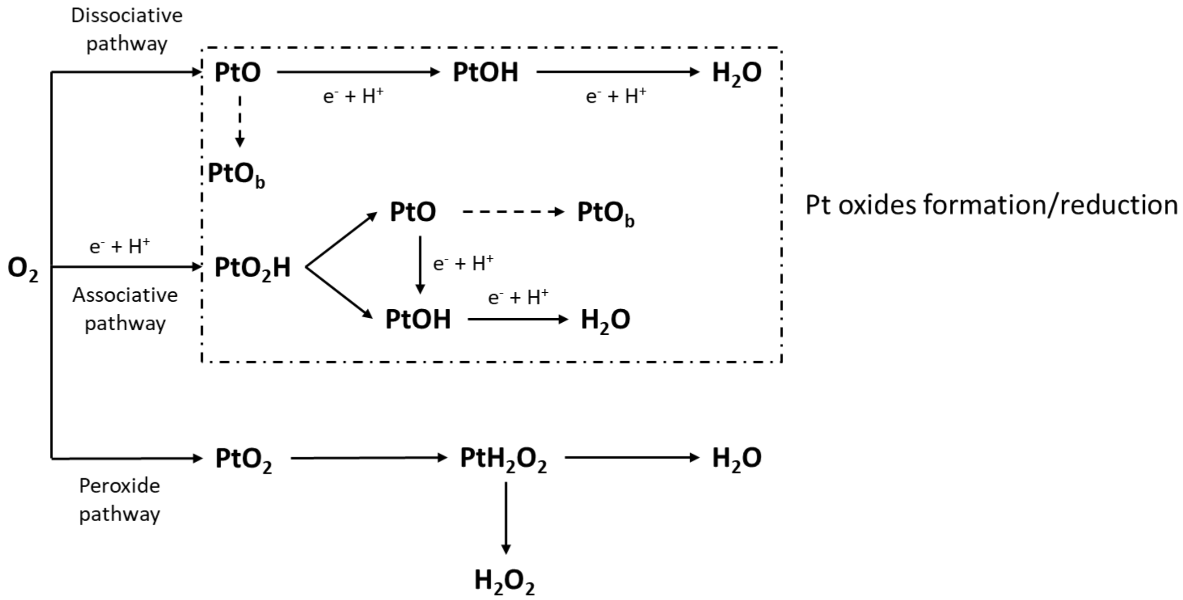

Figure I-11 : Pathways through which the ORR can proceed (reproduced from [95]). The 'b' subscript denotes the sub lattice Pt oxides

Conway *et al.* and Jerkiewicz *et al.* agree on the fact that surface oxygenated adsorbed species come from water interaction with metal at potential below 0.85 V *vs.* RHE [87], [90]. This surface oxidation can be described by Equation I-16.

Equation I-16 :
$$Pt + H_2O \rightarrow PtOH + H^+ + e^-$$

Further oxidation occurs in potential range *E* = 0.85 – 1.15 V *vs*. RHE, corresponding to the formation of PtO oxides according Equation I-17 [90], [91].

Equation I-17 :
$$PtOH \rightarrow PtO + H^+ + e^-$$

Regarding the kinetics of surface oxides growth, it was found that it follows a logarithmic law with time [92], [93]. At higher electrode potential, typically above 1.2 V *vs.* RHE, a slow chemical place exchange phenomenon occurs, allowing OH and O species to move under the Pt surface through structural transformation to form a sub lattice [93], [94]. However, all these observations were mostly done without the presence of gaseous oxygen. The effect of oxygen on the Pt oxidation is a relevant question, which is not fully understood yet. In the work of Jerkiewicz *et al.*, a significant increase of the oxidation coulometry was observed in one of their experiment at a cell voltage of 1.5 V *vs*. RHE [90]. They assigned this significant oxidation coulometry increase to the possible presence of oxygen, which is due to the oxygen evolution reaction at the operating conditions considered. Thus, it seems that the gaseous oxygen has a non-negligible impact on the Pt oxidation. More research on the oxygen electrochemistry, especially on the impact of Pt oxidation on ORR, needs to be done in this direction as the impact of oxygen concentration on Pt oxidation is not necessarily mentioned in the literature. Jayasankar and Karan proposed a multi-step model for oxygen electrochemistry on Pt to describe as accurately as possible (i) the ORR mechanism, (ii) the platinum oxides formation/reduction under inert atmosphere through potential cycling and (iii) the Pt oxides growth during potentiostatic holds [95]. Advanced characterizations are also considered to better understand the Pt surface oxidation and structural evolution. For instance, Martens *et al.* used in situ X-ray diffraction to probe the Pt oxides formation and reduction processes [96]. In their study, they obtained information on these processes thanks to structural parameters: the lattice strain, which gives information on the adsorption of surface electro-active species, the refined peak area and the particle size, which give information on the place exchange phenomenon. They found that the slow place exchange phenomenon somewhat hinders the surface oxide formation. They also highlight kinetic asymmetry between oxidation and reduction sweeps, which may be ascribed to the place exchange phenomenon, resulting in significant variation of oxide coverage during potential cycling. Thus, the hysteresis phenomenon is affected by both the potential scan rate and the upper potential limit. In addition, the hysteresis observed during dynamic Pt oxides formation/reduction, due to change of surface state of the catalyst, is consistent with the work of Conway *et al.* [93]. Finally, Martens *et al.* observed evolution of the peak area and the particle size at cell voltage above 1 V *vs*. RHE, which agrees with the onset potential of the place-exchange phenomenon referenced in the literature ($E > 1.10$ V *vs*. RHE).

From the different studies, it is relevant to consider that the Pt oxidation plays a crucial role on the Pt surface state and its activity regarding the ORR. The slow place-exchange phenomena seem to have an impact on surface structural change, resulting in a hysteresis between oxidation and reduction sweeps during potential cycling without oxygen. Thus, one may consider that Pt oxides formation/reduction may have a non-negligible impact on the hysteresis observed experimentally on the polarization curve. In order to confirm this assumption, the impact of oxygen concentration on the Pt oxidation mechanisms still needs to be unraveled. All these coupled phenomena are sometimes difficult to estimate in experiments, thus a modeling approach may be required to add some qualitative and quantitative insights to the interpretation of the different studies on the topic [95], [97]–[100].

I.4 Conclusion

This chapter exposed the energetic context and why hydrogen, thanks to its properties, seems to be a viable and efficient energetic vector. However, there is still a lot to do regarding the whole infrastructure: hydrogen production, transport, distribution and utilization, and their related technologies. Regarding the utilization of hydrogen in transportation applications, the PEMFC technology is considered with increasing interest, *e.g*. by big companies like Toyota and Hyundai (which are present commercially on the segment since *ca*. 5 years), but also other actors like Plug Power, Stellantis and Symbio (this list not being exhaustive). It still suffers from technological limitations, though, which are the cost, the performance and the durability of the PEMFC. In that extent, much effort is devoted to further improve the performance (to reduce the number of components and thus the cost) and to overcome the insufficient operational durability of PEMFCs (higher durability meaning also lower cost in the end for the technology deployment). The guiding idea is the better understanding of the limiting phenomena of the PEMFC, presented in sections I.2.2 and I.3, with classical or advanced characterizations, as well as thanks to modeling. Both experimental and modeling research are important as they can support each other to describe as accurately as possible the complex phenomena, their limitations and their interplay involved during PEMFC operation.

This thesis precisely follows this direction: experiments, presented in Chapter II and Chapter III, are conducted on catalyst layers with different composition (catalyst, loadings, etc.) in order to better understand the behaviour of the catalyst and catalyst layer during PEMFC operation; in addition, the Chapter IV deals with numerical simulation, thanks to a 1D model through MEA thickness. Due to specific needs regarding modeling and the understanding of catalyst layer operation, all the experiments in this work were designed to lead to a reliable and controlled dataset, which is relevant to improve the physico-chemical and electrochemical description of catalyst layer in our models. There is a need to develop a predictive model, which will describe as accurately as possible the catalyst layer operation and limitation. The main idea is to improve the description of the ORR mechanism and develop a performance model in order to accurately simulate the operation of the cathode catalyst layers with different composition, and to capture the reversible degradations that are frequently disregarded in PEMFC models. Modeling can then become a powerful tool to simulate one or combined physico-chemical/electrochemical processes, to get insights on their complex interplay and to make the link between the materials, the operating conditions and limiting processes ruling the cell performance. In addition, detailed models can take into account the evolution of the active layer from a sustainability perspective. On the whole, this study shall support and accelerate R&D work to design high performances and durable catalyst layers for the next generations of PEMFC.

References of Chapter I

[1] R. H. Moss, J. A. Edmonds, K. A. Hibbard, M. R. Manning, S. K. Rose, D. P. van Vuuren, T. R. Carter, S. Emori, M. Kainuma, T. Kram, G. A. Meehl, J. F. B. Mitchell, N. Nakicenovic, K. Riahi, S. J. Smith, R. J. Stouffer, A. M. Thomson, J. P. Weyant and T. J. Wilbanks, "The next generation of scenarios for climate change research and assessment," *Nature*, vol. 463, no. 7282, pp. 747–756, Feb. 2010, doi: 10.1038/nature08823.

[2] "Hydrogen as an Energy Vector," *LITEN CEA tech - Hydrogen as an Energy Vector*. https://liten.cea.fr/cea-tech/liten/english/Pages/Strategic-research/Grid-flexibility-solutions/Hydrogen-Vector.aspx

[3] "Climate Change 2013: The Physical Science Basis. Contribution of Working Group I to the Fifth Assessment Report of the Intergovernmental Panel on Climate Change," IPCC, United Kingdom and USA, 2013.

[4] A. F. Ghoniem, "Needs, resources and climate change: Clean and efficient conversion technologies," *Progress in Energy and Combustion Science*, vol. 37, no. 1, pp. 15–51, Feb. 2011, doi: 10.1016/j.pecs.2010.02.006.

[5] M. Balat, "Potential importance of hydrogen as a future solution to environmental and transportation problems," *International Journal of Hydrogen Energy*, vol. 33, no. 15, pp. 4013–4029, Aug. 2008, doi: 10.1016/j.ijhydene.2008.05.047.

[6] France Hydrogène, "Parlons Hydrogène," https://www.france-hydrogene.org/publication/parlons-hydrogene/, 2022.

[7] C. Tarhan and M. A. Çil, "A study on hydrogen, the clean energy of the future: Hydrogen storage methods," *Journal of Energy Storage*, vol. 40, p. 102676, Aug. 2021, doi: 10.1016/j.est.2021.102676.

[8] P. Malbrunot, "La distribution de l'hydrogène pour les véhicules automobiles," https://s3.production.france-hydrogene.org, 2021.

[9] P. Stevens, F. Novel-Cattin, A. Hammou, C. Lamy and M. Cassir, "Piles à combustible," Techniques de l'Ingénieur p. 31, 2000.

[10] I. Rexed, "Applications for Molten Carbonate Fuel Cells," Thèse, KTH Royal Institute of Technology, School of Chemical Science and Engineering Department of Chemical Engineering and Technology Applied Electrochemistry p. 75 ,2014.

[11] S. H. Jensen, C. Graves, M. Mogensen, C. Wendel, R. Braun, G. Hughes, Z. Gaoc and S. A. Barnettc, "Large-scale electricity storage utilizing reversible solid oxide cells combined with underground storage of CO_2 and CH_4," *Energy Environ. Sci.*, vol. 8, no. 8, pp. 2471–2479, 2015, doi: 10.1039/C5EE01485A.

[12] N. P. Brandon and D. Thompsett, Eds., *Fuel cells compendium*, Transferred to digital printing. Amsterdam: Elsevier, 2006.

[13] “Fuel Cell System Cost - 2017,” Department of Energy, 17007, 2017.

[14] “Fuel Cell Vehicles,” *fueleconomy.gov*. https://www.fueleconomy.gov/feg/fuelcell.shtml

[15] O. Marconot, “Croissance confinée de nanofils/nanotubes métalliques : élaboration et intégration dans les cathodes des PEMFC,” Thèse, Université Grenoble Alpes, CEA Grenoble, 2016.

[16] T. Gaumont, “Résistance protonique d’électrodes de piles à combustible à membrane (PEMFC): effets de l’humidité et des dégradations,” Thèse, Université de Lorraine, Laboratoire d’´Energétique et de Mécanique théorique et Appliquée, 2017. [Online]. Available: https://tel.archives-ouvertes.fr/tel-01546366

[17] T. D. Tran, S. Huang, D. H. Vu and V. N. Duy, “Effects of Gas Channel Design on Water Management and on the Performance of Polymer Electrolyte Membrane Fuel Cells: A Review,” *Int. J. Electrochem. Sci.*, pp. 10480–10495, Nov. 2018, doi: 10.20964/2018.11.22.

[18] M. Fontana, “Tapis de nanotubes de carbone structurés comme nouveau microporeux pour couche de diffusion de gaz des piles à combustible,” Thèse, Université Grenoble Alpes, CEA Grenoble, 2021. [Online]. Available: https://tel.archives-ouvertes.fr/tel-03256127

[19] S. Wang, J. Peng, W. Lui and J. Zhang, “Performance of the gold-plated titanium bipolar plates for the light weight PEM fuel cells,” *Journal of Power Sources*, vol. 162, no. 1, pp. 486–491, Nov. 2006, doi: 10.1016/j.jpowsour.2006.06.084.

[20] W. Yoon, X. Huanga*,* P. Fazzino, K. L. Reifsnider and M. A. Akkaoui, “Evaluation of coated metallic bipolar plates for polymer electrolyte membrane fuel cells,” *Journal of Power Sources*, vol. 179, no. 1, pp. 265–273, Apr. 2008, doi: 10.1016/j.jpowsour.2007.12.034.

[21] Sigracet®, “Sigracet® GDL property sheet.”, https://www.fuelcellstore.com/sigracet-22-bb.

[22] A. Kusoglu and A. Z. Weber , “New Insights into Perfluorinated Sulfonic-Acid Ionomers,” *Chem. Rev.*, vol. 117, no. 3, pp. 987–1104, Feb. 2017, doi: 10.1021/acs.chemrev.6b00159.

[23] “FURTHER-FC project - Objectives.” https://further-fc.eu/ABOUT-FURTHER-FC/OBJECTIVES/

[24] “CAMELOT - Overview.” https://www.camelot-fuelcell.eu/index.php/about-camelot/overview

[25] L. J. M. J. Blomen and M. N. Mugerwa, *Fuel Cell Systems*, Plenum Press. 1993.

[26] B. S. Pivovar and Y. S. Kim, “The Membrane–Electrode Interface in PEFCs I. A Method for Quantifying Membrane–Electrode Interfacial Resistance,” *Journal of The Electrochemical Society*, p. 6.

[27] Y. S. Kim, M. Einsla, J. E. McGrath and B. S. Pivovar, “The Membrane–Electrode Interface in PEFCs II. Impact on Fuel Cell Durability,” *Journal of The Electrochemical Society*, p. 7.

[28] J. P. Hoare, “Rest Potentials in the Platinum-Oxygen-Acid System,” *J. Electrochem. Soc.*, vol. 109, no. 9, p. 858, 1962, doi: 10.1149/1.2425569.

[29] L. Castanheira, L. Dubau, M. Mermoux, G. Berthomé, N. Caqué, E. Rossinot, M. Chatenet and F. Maillard, “Carbon Corrosion in Proton-Exchange Membrane Fuel Cells: From Model Experiments to Real-Life Operation in Membrane Electrode Assemblies,” *ACS Catal.*, vol. 4, no. 7, pp. 2258–2267, Jul. 2014, doi: 10.1021/cs500449q.

[30] Q. Tang, B. Li, D. Yang, P. Ming, C. Zhang and Y. Wang, “Review of hydrogen crossover through the polymer electrolyte membrane,” *International Journal of Hydrogen Energy*, vol. 46, no. 42, pp. 22040–22061, Jun. 2021, doi: 10.1016/j.ijhydene.2021.04.050.

[31] S. A. Vilekar and R. Datta, “The effect of hydrogen crossover on open-circuit voltage in polymer electrolyte membrane fuel cells,” *Journal of Power Sources*, vol. 195, no. 8, pp. 2241–2247, Apr. 2010, doi: 10.1016/j.jpowsour.2009.10.023.

[32] K. Broka and P. Ekdunge, “Oxygen and hydrogen permeation properties and water uptake of Nafion 117 membrane and recast film for PEM fuel cell.pdf,” *Journal of Applied Electrochemistry*, vol. 27, pp. 117–123, 1997.

[33] L. Dubau, L. Castanheira, M. Chatenet, F. Maillard, J. Dillet, G. Maranzana, S. Abbou, O. Lottin, G. De Moor, A. El Kaddouri, C. Bas, L. Flandin, E. Rossinot and N. Caqué, “Carbon corrosion induced by membrane failure: The weak link of PEMFC long-term performance,” *International Journal of Hydrogen Energy*, vol. 39, no. 36, pp. 21902–21914, Dec. 2014, doi: 10.1016/j.ijhydene.2014.07.099.

[34] L. Dubau, L. Castanheira, F. Maillard, M. Chatenet, O. Lottin, G. Maranzana, J. Dillet, A. Lamibrac, J. Perrin, E. Moukheiber, A. ElKaddouri, G. De Moor, C. Bas, L. Flandin and N. Caqué, “A review of PEM fuel cell durability: materials degradation, local heterogeneities of aging and possible mitigation strategies: A review of PEM fuel cell durability,” *WIREs Energy Environ*, vol. 3, no. 6, pp. 540–560, Nov. 2014, doi: 10.1002/wene.113.

[35] J. Wu, X. Z. Yuan, J. J. Martin, H. Wang, J. Zhang, J. Shen, S. Wu and W. Merida, “A review of PEM fuel cell durability: Degradation mechanisms and mitigation strategies,” *Journal of Power Sources*, vol. 184, no. 1, pp. 104–119, Sep. 2008, doi: 10.1016/j.jpowsour.2008.06.006.

[36] Q. Yan, H. Toghiani, Y. Lee, K. Liang and H. Causey, “Effect of sub-freezing temperatures on a PEM fuel cell performance, startup and fuel cell components,” *Journal of Power Sources*, vol. 160, no. 2, pp. 1242–1250, Oct. 2006, doi: 10.1016/j.jpowsour.2006.02.075.

[37] A. Bazylak, D. Sinton, Z.-S. Liu and N. Djilali, “Effect of compression on liquid water transport and microstructure of PEMFC gas diffusion layers,” *Journal of Power Sources*, vol. 163, no. 2, pp. 784–792, Jan. 2007, doi: 10.1016/j.jpowsour.2006.09.045.

[38] M. Balakrishnan, P. Shrestha, C. Lee, N. Ge, K. F. Fahy, M. Messerschmidt, J. Scholta, L. Eifert, J. Maibach, R. Zeis, B. D. Hatto, and A. Bazylak, “Degradation Characteristics of Electrospun Gas Diffusion Layers with Custom Pore Structures for Polymer Electrolyte Membrane Fuel Cells,” *ACS Appl. Mater. Interfaces*, vol. 13, no. 2, pp. 2414–2427, Jan. 2021, doi: 10.1021/acsami.0c15324.

[39] G. De Moor, C. Bas, N. Charvin, J. Dillet, G. Maranzana, O. Lottin, N. Caqué, E. Rossinot and L. Flandin, “Perfluorosulfonic acid membrane degradation in the hydrogen inlet region: A macroscopic approach,” *International Journal of Hydrogen Energy*, vol. 41, no. 1, pp. 483–496, Jan. 2016, doi: 10.1016/j.ijhydene.2015.10.066.

[40] M. Inaba, T. Kinumoto, M. Kiriake, R. Umebayashi, A. Tasaka and Z. Ogumib, “Gas crossover and membrane degradation in polymer electrolyte fuel cells,” *Electrochimica Acta*, vol. 51, no. 26, pp. 5746–5753, Aug. 2006, doi: 10.1016/j.electacta.2006.03.008.

[41] S. R. Choi, D. Y. Kim, W. Y. An, S. Choi, K. Park, S.-D. Yim and J.-Y. Park, “Assessing the degradation pattern and mechanism of membranes in polymer electrolyte membrane fuel cells using open-circuit voltage hold and humidity cycle test protocols,” *Materials Science for Energy Technologies*, vol. 5, pp. 66–73, 2022, doi: 10.1016/j.mset.2021.12.001.

[42] R. C. McDonald, C. K. Mittelsteadt and E. L. Thompson , “Effects of Deep Temperature Cycling on Nafion® 112 Membranes and Membrane Electrode Assemblies,” *Fuel Cells*, vol. 4, no. 3, pp. 208–213, Aug. 2004, doi: 10.1002/fuce.200400015.

[43] F. A. de Bruijn , V. A. T. Dam and G. J. M. Janssen, “Review: Durability and Degradation Issues of PEM Fuel Cell Components,” *Fuel Cells*, vol. 8, no. 1, pp. 3–22, Feb. 2008, doi: 10.1002/fuce.200700053.

[44] C. Iojoiu, E. Guilminot, F. Maillard, M. Chatenet, J.-Y. Sanchez, E. Claude and E. Rossinot, “Membrane and Active Layer Degradation Following PEMFC Steady-State Operation,” *J. Electrochem. Soc.*, vol. 154, no. 11, p. B1115, 2007, doi: 10.1149/1.2775282.

[45] A. B. LaConti, M. Hamdan and R. C. McDonald, *Handbook of Fuel Cells*, vol. 3. Chichester: Wiley, 2003.

[46] A. Panchenko, H. Dilger, J. Kerres, M. Hein, A. Ullrich, T. Kazc and E. Roduner, “In-situ spin trap electron paramagnetic resonance study of fuel cell processes,” *Phys. Chem. Chem. Phys.*, vol. 6, no. 11, p. 2891, 2004, doi: 10.1039/b404253k.

[47] E. Endoh, S. Terazono, H. Widjaja and Y. Takimoto, “Degradation Study of MEA for PEMFCs under Low Humidity Conditions,” *Electrochem. Solid-State Lett.*, vol. 7, no. 7, p. A209, 2004, doi: 10.1149/1.1739314.

[48] E. Guilminot, A. Corcella, F. Charlot, F. Maillard and M. Chatenet, “Detection of Ptz+ Ions and Pt Nanoparticles Inside the Membrane of a Used PEMFC,” *Journal of The Electrochemical Society*, p. 10.

[49] L. Castanheira, W. O. Silva, F. H.B. Lima, A. Crisci, L. Dubau and F. Maillard, “Carbon Corrosion in Proton-Exchange Membrane Fuel Cells: Effect of the Carbon Structure, the Degradation Protocol, and the Gas Atmosphere,” *ACS Catal.*, vol. 5, no. 4, pp. 2184–2194, Apr. 2015, doi: 10.1021/cs501973j.

[50] S. C. Ball, S.L. Hudson, D. Thompsett and B. Theobald, “An investigation into factors affecting the stability of carbons and carbon supported platinum and platinum/cobalt alloy catalysts during 1.2V potentiostatic hold regimes at a range of temperatures,” *Journal of Power Sources*, vol. 171, no. 1, pp. 18–25, Sep. 2007, doi: 10.1016/j.jpowsour.2006.11.004.

[51] O.V. Cherstiouk, A.N. Simonov, N.S. Moseva, S.V. Cherepanova, P.A. Simonov, V.I. Zaikovskii and E.R. Savinova, “Microstructure effects on the electrochemical corrosion of carbon materials and carbon-supported Pt catalysts,” *Electrochimica Acta*, vol. 55, no. 28, pp. 8453–8460, Dec. 2010, doi: 10.1016/j.electacta.2010.07.047.

[52] L. F. R. Castanheira, “Corrosion of high surface area carbon supports used in proton-exchange membrane fuel cell electrodes,” Thèse, Université Grenoble Alpes, LEPMI Grenoble, 2014. [Online]. Available: https://tel.archives-ouvertes.fr/tel-01303814

[53] F. Maillard, A. Bonnefont and F. Micoud, “An EC-FTIR study on the catalytic role of Pt in carbon corrosion,” *Electrochemistry Communications*, vol. 13, no. 10, pp. 1109–1111, Oct. 2011, doi: 10.1016/j.elecom.2011.07.011.

[54] A. Lamibrac, G. Maranzana, J. Dilleta, O. Lottin, S. Didierjean, J. Durst, L. Dubau, F. Maillard and M. Chatenet, “Local Degradations Resulting from Repeated Start-ups and Shut-downs in Proton Exchange Membrane Fuel Cell (PEMFC),” *Energy Procedia*, vol. 29, pp. 318–324, 2012, doi: 10.1016/j.egypro.2012.09.038.

[55] K.L. More, R. Borup and K.S. Reeves, “Identifying Contributing Degradation Phenomena in PEM Fuel Cell Membrane Electride Assemblies Via Electron Microscopy,” *ECS Trans.*, vol. 3, no. 1, pp. 717–733, Oct. 2006, doi: 10.1149/1.2356192.

[56] Z. Zhao, L. Dubau and F. Maillard, “Evidences of the migration of Pt crystallites on high surface area carbon supports in the presence of reducing molecules,” *Journal of Power Sources*, vol. 217, pp. 449–458, Nov. 2012, doi: 10.1016/j.jpowsour.2012.06.016.

[57] S. Cherevko, G. P. Keeley, S. Geiger, A. R. Zeradjanin, N. Hodnik, N. Kulyk and K. J. J. Mayrhofer, “Dissolution of Platinum in the Operational Range of Fuel Cells,” *ChemElectroChem*, vol. 2, no. 10, pp. 1471–1478, Oct. 2015, doi: 10.1002/celc.201500098.

[58] E. Guilminot, A. Corcella, M. Chatenet, F. Maillard, F. Charlot, G. Berthomé, C. Iojoiu, J.-Y. Sanchez, E. Rossinot and E. Claude, “Membrane and Active Layer Degradation upon PEMFC Steady-State Operation,” *J. Electrochem. Soc.*, vol. 154, no. 11, p. B1106, 2007, doi: 10.1149/1.2775218.

[59] X. Wang, R. Kumar, and D. J. Myers, “Effect of Voltage on Platinum Dissolution,” *Electrochem. Solid-State Lett.*, vol. 9, no. 5, p. A225, 2006, doi: 10.1149/1.2180536.

[60] Y. Shao-Horn, W. C. Sheng, S. Chen, P. J. Ferreira, E. F. Holby and D. Morgan, “Instability of Supported Platinum Nanoparticles in Low-Temperature Fuel Cells,” *Top Catal*, vol. 46, no. 3–4, pp. 285–305, Dec. 2007, doi: 10.1007/s11244-007-9000-0.

[61] M. Prokop, R. Kodym, T. Bystron*, M. Drakselova, M. Paidar and K. Bouzek, “Degradation kinetics of Pt during high-temperature PEM fuel cell operation part II: Dissolution kinetics of Pt incorporated in a catalyst layer of a gas-diffusion electrode,” *Electrochimica Acta*, vol. 333, p. 135509, Feb. 2020, doi: 10.1016/j.electacta.2019.135509.

[62] M. Prokop, T. Bystron, P. Belsky, O. Tucek, R. Kodym, M. Paidar and K. Bouzek, “Degradation kinetics of Pt during high-temperature PEM fuel cell operation Part III: Voltage-dependent Pt degradation rate in single-cell experiments,” *Electrochimica Acta*, vol. 363, p. 137165, Dec. 2020, doi: 10.1016/j.electacta.2020.137165.

[63] M. Zago, A. Baricci, A. Bisello, T. Jahnke, H. Yu, R. Maric, P. Zelenay and A. Casalegno, “Experimental analysis of recoverable performance loss induced by platinum oxide formation at the polymer electrolyte membrane fuel cell cathode,” *Journal of Power Sources*, vol. 455, p. 227990, Apr. 2020, doi: 10.1016/j.jpowsour.2020.227990.

[64] Y. Takasu, N. Ohashi, X.-G. Zhang, Y. Murakami, H. Minagawa, S. Sato and K. Yahikozawa, “Size effects of platinum particles on the electroreduction of oxygen,” *Electrochimica Acta*, vol. 41, no. 16, pp. 2595–2600, Jan. 1996, doi: 10.1016/0013-4686(96)00081-3.

[65] N. Martinez, G. Gebel, N. Blanc, N. Boudet, J.-S. Micha, S. Lyonnard and A. Morin, “Heterogeneous Nanostructural Aging of Fuel Cell Ionomer Revealed by Operando SAXS,” *ACS Appl. Energy Mater.*, vol. 2, no. 5, pp. 3071–3080, May 2019, doi: 10.1021/acsaem.8b02004.

[66] C. Bas, L. Flandin, A.-S. Danerol, E. Claude, E. Rossinot and N. D. Alberola, “Changes in the chemical structure and properties of a perfluorosulfonated acid membrane induced by fuel-cell operation,” *J. Appl. Polym. Sci.*, vol. 117, no. 4, pp. 2121–2132, Aug. 2010, doi: 10.1002/app.31386.

[67] A. El Kaddouri, L. Flandin and C. Bas, “Chemical degradation of PFSA ionomer binder in PEMFC’s catalyst layer,” *International Journal of Hydrogen Energy*, vol. 43, no. 32, pp. 15386–15397, Aug. 2018, doi: 10.1016/j.ijhydene.2018.06.049.

[68] R. Sharma and S. Ma Andersen, “Quantification on Degradation Mechanisms of Polymer Electrolyte Membrane Fuel Cell Catalyst Layers during an Accelerated Stress Test,” *ACS Catal.*, vol. 8, no. 4, pp. 3424–3434, Apr. 2018, doi: 10.1021/acscatal.8b00002.

[69] T. Gaumont, G. Maranzana, O. Lottin, J. Dillet, S. Didierjean, J. Pauchet and L. Guétaz, “Measurement of protonic resistance of catalyst layers as a tool for degradation monitoring,” *International Journal of Hydrogen Energy*, vol. 42, no. 3, pp. 1800–1812, Jan. 2017, doi: 10.1016/j.ijhydene.2016.10.035.

[70] C. Zhang, Z. Liu, W. Zhou, S. H. Chan and Y. Wang, “Dynamic performance of a high-temperature PEM fuel cell – An experimental study,” *Energy*, vol. 90, pp. 1949–1955, Oct. 2015, doi: 10.1016/j.energy.2015.07.026.

[71] T. Chu, Q. Wang, M. Xie, B. Wang, D. Yang, B. Li, P. Ming and C. Zhang, “Investigation of the reversible performance degradation mechanism of the PEMFC stack during long-term durability test,” *Energy*, vol. 258, p. 124747, Nov. 2022, doi: 10.1016/j.energy.2022.124747.

[72] B. Shabani, M. Hafttananian, Sh. Khamani, A. Ramiar and A.A. Ranjbar, “Poisoning of proton exchange membrane fuel cells by contaminants and impurities: Review of mechanisms, effects, and mitigation strategies,” *Journal of Power Sources*, vol. 427, pp. 21–48, Jul. 2019, doi: 10.1016/j.jpowsour.2019.03.097.

[73] B. Decoopman, R. Vincent, S. Rosini, G. Paganelli and P.-X. Thivel, “Proton exchange membrane fuel cell reversible performance loss induced by carbon monoxide produced during operation,” *Journal of Power Sources*, vol. 324, pp. 492–498, Aug. 2016, doi: 10.1016/j.jpowsour.2016.05.113.

[74] T. Reshetenko, A. Serov, K. Artyushkova, I. Matanovic, S. Stariha and P. Atanassov, “Tolerance of non-platinum group metals cathodes proton exchange membrane fuel cells to air contaminants,” *Journal of Power Sources*, vol. 324, pp. 556–571, Aug. 2016, doi: 10.1016/j.jpowsour.2016.05.090.

[75] M. Ji and Z. Wei, “A Review of Water Management in Polymer Electrolyte Membrane Fuel Cells,” *Energies*, vol. 2, no. 4, pp. 1057–1106, Nov. 2009, doi: 10.3390/en20401057.

[76] P. Gazdzick, J. Mitzel, D. Garcia Sanchez, M. Schulze and K. A. Friedrich, “Evaluation of reversible and irreversible degradation rates of polymer electrolyte membrane fuel cells tested in automotive conditions,” *Journal of Power Sources*, vol. 327, pp. 86–95, Sep. 2016, doi: 10.1016/j.jpowsour.2016.07.049.

[77] F. Nandjou, “Etude locale de la thermique dans les piles à combustibles pour application automobile. Corrélation à la durée de vie,” Thèse, Université Grenoble Alpes, CEA Grenoble, 2015. [Online]. Available: https://tel.archives-ouvertes.fr/tel-01267255

[78] J. Hou, “A study on polarization hysteresis in PEM fuel cells by galvanostatic step sweep,” *International Journal of Hydrogen Energy*, vol. 36, no. 12, pp. 7199–7206, Jun. 2011, doi: 10.1016/j.ijhydene.2011.03.059.

[79] M. G. Santarelli and M.F. Torchio, “Experimental analysis of the effects of the operating variables on the performance of a single PEMFC,” *Energy Conversion and Management*, vol. 48, no. 1, pp. 40–51, Jan. 2007, doi: 10.1016/j.enconman.2006.05.013.

[80] S. Jomori, K. Komatsubara, N. Nonoyama, M. Kato and T. Yoshida, “An Experimental Study of the Effects of Operational History on Activity Changes in a PEMFC,” *J. Electrochem. Soc.*, vol. 160, no. 9, pp. F1067–F1073, 2013, doi: 10.1149/2.103309jes.

[81] W. He, G. Lin and T. Van Nguyen, “Diagnostic tool to detect electrode flooding in proton-exchange-membrane fuel cells,” pp. 3221–3228, 2003.

[82] F. A. Uribe and T. A. Zawodzinski Jr., “A study of polymer electrolyte fuel cell performance at high voltages. Dependence on cathode catalyst layer composition and on voltage conditioning,” *Electrochimica Acta*, vol. 47, no. 22–23, pp. 3799–3806, Aug. 2002, doi: 10.1016/S0013-4686(02)00350-X.

[83] A. Damjanovic, M. A. Genshaw and J. O'M. Bockris, “The Mechanism of Oxygen Reduction at Platinum in Alkaline Solutions with Special Reference to H2O2,” J. Electrochem. Soc. **114** 1107, 1967.

[84] A. Damjanovic and V. Brusic, “Electrode kinetics of oxygen reduction on oxide-free platinum electrodes,” *Electrochimica Acta*, vol. 12, no. 6, pp. 615–628, Jun. 1967, doi: 10.1016/0013-4686(67)85030-8.

[85] A. Damjanovic, D. B. SEPA and M. V. Vojnovic, “New evidence supports the proposed mechanism for O2, reduction at oxide free platinum electrodes,” *Electrochimica Acta, vol 24, pp. 887-889*.

[86] H. Xu, R. Kunz and J. M. Fentonb, “Investigation of Platinum Oxidation in PEM Fuel Cells at Various Relative Humidities,” *Electrochem. Solid-State Lett.*, vol. 10, no. 1, p. B1, 2007, doi: 10.1149/1.2372230.

[87] B. V. Tilak, B. E. Conway and H. Angerstein-Kozlowska, “The real condition of oxidized pt electrodes: Part III. Kinetic theory of formation and reduction of surface oxides,” *Journal of Electroanalytical Chemistry and Interfacial Electrochemistry*, vol. 48, no. 1, pp. 1–23, Nov. 1973, doi: 10.1016/S0022-0728(73)80290-6.

[88] D. E. Ramaker, A. Korovina, V. Croze, J. Melke and C. Roth, “Following ORR intermediates adsorbed on a Pt cathode catalyst during break-in of a PEM fuel cell by in operando X-ray absorption spectroscopy,” *Phys. Chem. Chem. Phys.*, vol. 16, no. 27, pp. 13645–13653, 2014, doi: 10.1039/C4CP00192C.

[89] E. L. Redmond, B. P. Setzler, F. M. Alamgir and T. F. Fuller, “Elucidating the oxide growth mechanism on platinum at the cathode in PEM fuel cells,” *Phys. Chem. Chem. Phys.*, vol. 16, no. 11, pp. 5301–5311, Feb. 2014, doi: 10.1039/C3CP54740J.

[90] A. A. McMath, J. van Drunen, J. Kim and G. Jerkiewicz, “Identification and Analysis of Electrochemical Instrumentation Limitations through the Study of Platinum Surface Oxide Formation and Reduction,” *Anal. Chem.*, vol. 88, no. 6, pp. 3136–3143, Mar. 2016, doi: 10.1021/acs.analchem.5b04239.

[91] H. Angerstein-Kozlowska *et al.*, “The real condition of electrochemically oxidized platinum surfaces: Part I. Resolution of component processes,” *Journal of Electroanalytical Chemistry and Interfacial Electrochemistry*, vol. 43, no. 1, pp. 9–36, Apr. 1973, doi: 10.1016/S0022-0728(73)80307-9.

[92] B. E. Conway, B. E. Conway and W. B. A. Sharp, “A surface-electrochemical basis for the direct logarithmic growth law for initial stages of extension of anodic oxide films formed at noble metals,” *J. Chem. Phys.*, vol. 93, no. 11, pp. 8361–8373, Dec. 1990, doi: 10.1063/1.459319.

[93] B. E. Conway, “Electrochemical oxide film formation at noble metals as a surface-chemical process,” *Progress in Surface Science*, vol. 49, no. 4, pp. 331–452, Aug. 1995, doi: 10.1016/0079-6816(95)00040-6.

[94] G. Jerkiewicz, G. Vatankhah, J. Lessard, M. P. Soriaga and Y.-S. Park; “Surface-oxide growth at platinum electrodes in aqueous H2SO4,” *Electrochimica Acta*, vol. 49, no. 9–10, pp. 1451–1459, Apr. 2004, doi: 10.1016/j.electacta.2003.11.008.

[95] B. Jayasankar and K. Karan, “O2 electrochemistry on Pt: A unified multi-step model for oxygen reduction and oxide growth,” *Electrochimica Acta*, vol. 273, pp. 367–378, May 2018, doi: 10.1016/j.electacta.2018.03.191.

[96] I. Martens, R. Chattot, M. Rasola, M. Valeria Blanco, V. Honkimäki, D. Bizzotto, D. P. Wilkinson and J. Drnec, “Probing the Dynamics of Platinum Surface Oxides in Fuel Cell Catalyst Layers Using in Situ X-ray Diffraction,” *ACS Appl. Energy Mater.*, vol. 2, no. 11, pp. 7772–7780, Nov. 2019, doi: 10.1021/acsaem.9b00982.

[97] T. Jahnke, G. A. Futter, A. Baricci, C. Rabissi and A. Casalegno, “Physical Modeling of Catalyst Degradation in Low Temperature Fuel Cells: Platinum Oxidation, Dissolution, Particle Growth and Platinum Band Formation,” *J. Electrochem. Soc.*, vol. 167, no. 1, p. 013523, Nov. 2019, doi: 10.1149/2.0232001JES.

[98] G. Maranzana, A. Lamibrac, J. Dillet, S. Abbou, S. Didierjean and O. Lottin, “Startup (and Shutdown) Model for Polymer Electrolyte Membrane Fuel Cells,” *J. Electrochem. Soc.*, vol. 162, no. 7, pp. F694–F706, 2015, doi: 10.1149/2.0451507jes.

[99] S. Arisett, Y. Liu, W. Gu and M. F. Mathias, “Modeling Platinum Oxide Growth of PEMFC Cathode Catalysts,” *ECS Trans.*, vol. 69, no. 17, pp. 273–289, Sep. 2015, doi: 10.1149/06917.0273ecst.

[100] B. Andreaus, F. Maillard, J. Kocylo, E. R. Savinova and M. Eikerling, “Kinetic Modeling of COad Monolayer Oxidation on Carbon-Supported Platinum Nanoparticles,” J. Phys. Chem. B, vol. 110, no. 42, pp. 21028–21040, Oct. 2006, doi: 10.1021/jp063856k.

[101] J. K. Nørskov, J. Rossmeisl, A. Logadottir, L. Lindqvist, J. R. Kitchin, T. Bligaard and H. Jonsson, “Origin of the Overpotential for Oxygen Reduction at a Fuel-Cell Cathode,” J. Phys. Chem. B, vol. 108, no. 46, pp. 17886–17892, Nov. 2004, doi: 10.1021/jp047349j.

[102] M. Moore, A. Putz and M. Secanell, “Investigation of the ORR Using the Double-Trap Intrinsic Kinetic Model,” J. Electrochem. Soc., vol. 160, no. 6, pp. F670-F681, Apr. 2013, doi: 10.1149/2.123306jes.

[103] H. S. Wroblowa, Y.-C. Pan and G. Razumney, “Electroreduction of oxygen A new mechanistic criterion,” J. Electroanal. Chem., vol. 69, no. 2, pp.195-201, Apr. 1976, doi: 10.1016/S0022-0728(76)80250-1.

Chapter II Experimental methods and characterization techniques

This chapter focuses on the different experimental characterizations performed on the electrocatalysts studied, from the raw materials to their integration and utilization in PEMFC catalyst layers. First, the raw materials (carbon-supported Pt-based nanoparticles) will be presented as well as the Transmission Electronic Microscopy (TEM) characterizations performed to gather information on the Pt particle size distribution and the nano and microstructure of the electrocatalysts. Then, physico-chemical and electrochemical characterizations were performed on catalyst layers using different electrochemical setups. The different electrochemical techniques used as well as the ink formulation and Membrane Electrode Assembly (MEA) manufacturing for each setup will be presented. The purpose of all the experimental characterizations is to gather information on the electrocatalysts as well as their utilization/effectiveness in catalyst layer during real PEMFC operation: Pt electrochemical surface area (ECSA), electrocatalyst activity/performance, impact of operating conditions on physico-chemical and electrochemical properties. These data will be used to establish a reliable baseline and experimental datasets for initial performances, which depends on MEA formulations in order to understand what is at stake when a catalyst layer is operated under nominal conditions.

II.1 Electrocatalysts studied

The first part of this section present the different materials studied in this work. Four state-of-art ORR carbon-supported Pt-based electrocatalysts from Tanaka Kikinzoku Kogyo (TKK) have been characterized (Table II-1).

Table II-1 : Presentation of the electrocatalysts studied from TKK.

Electrocatalyst reference	**Carbon support**	**Metal loading**	**Designation**
TEC10V50E	**Vulcan XC72**	**47.7 wt% Pt**	**Pt/VC**
TEC36V52	**Vulcan XC72**	**47.0 wt% Pt & 6.4 wt% Co**	**Pt_3Co/VC**
TEC10EA30E-HT	**Graphitized Carbon black**	**30.1 wt% Pt**	**Pt/GC**
TEC10E50E	**High Surface Area Carbon**	**46.9 wt% Pt**	**Pt/HSAC**

To have a better understanding of the catalyst layer operation and more specifically to get information about the correlation between microstructure of the CL and the performances obtained, TEM imaging was carried out. TEM micrographs are used to gather morphological and micro/nano-structural information about the materials (particles size, homogeneity of the catalyst). The Pt/VC, Pt_3Co/VC and the Pt/GC images were obtained using the TEM JEOL 2010 operating at 200 kV equipped for XEDS analyses (INCA®). The Pt/HSAC images were obtained in the frame of the FURTHER-FC European project using a FEI-Titan Ultimate microscope operating at 200 kV and equipped with an image aberration corrector in a HRTEM (High Resolution TEM) mode. Figure II-1 shows the different TEM images of the four catalysts. First, the presence of many Pt-based nanoparticles supported on their respective supportive carbons can be observed. Their high Pt loadings lead to non-negligible extent of Pt agglomeration for all the electrocatalysts. Some of Pt aggregates are circled in yellow on the Figure II-1 (as a non-quantitative guide for the eyes); these aggregates account for the non-homogeneous distribution of Pt nanoparticles on the carbon substrate. More aggregates are observed for Pt/VC versus Pt/HSAC, which is ascribed to the smaller BET area (available carbon surface) of the Vulcan XC72 support; the Pt_3Co/VC and Pt/GC materials do not show dramatic extent of agglomeration of the catalysts particles, but instead, these are of larger average size (Figure II-1), the average diameter having been calculated considering only the isolated nanoparticles from the images. Around 100 particles were considered for each electrocatalyst among all the images obtained by TEM to have a relevant Pt particles average diameter of the total particle size distribution. The Pt_3Co/VC and Pt/GC samples exhibit larger particle sizes than for the other two materials.

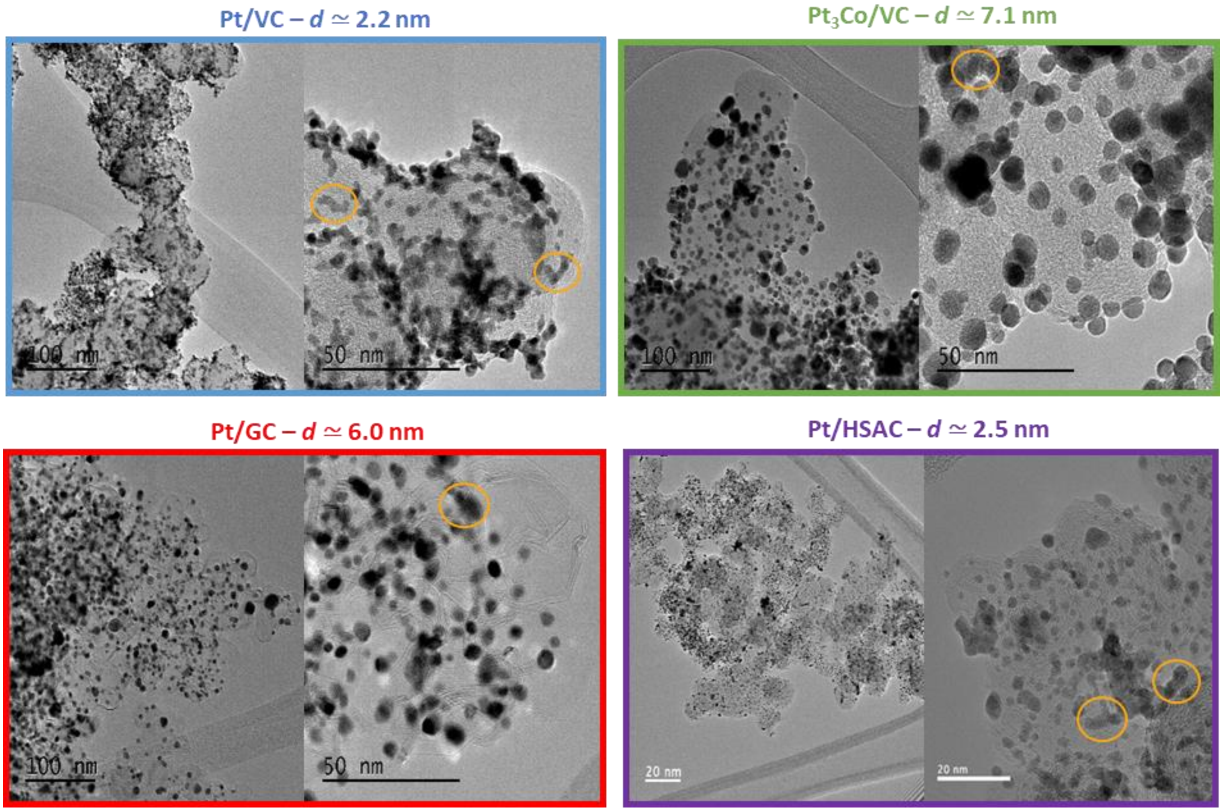

Figure II-1 : TEM images and corresponding average particles diameters for the four electrocatalysts studied.

In the following, the different electrochemical setup and techniques used to characterize the different materials will be detailed. Three electrochemical setups are considered in this work. For each of them, a focus on the catalyst ink preparation and the MEA manufacturing processes will be done. These steps are really important and even crucial in the experimental part. In fact, they ensure the good reproducibility of the different measurements and allow to control the microstructure and the composition of the catalyst layers that need to be studied. Indeed, depending on the amount of materials used for the ink, the dispersion method and the fabrication process, MEA manufactured can lead to a wide range of performance [1]–[3]. Thus, it is mandatory to be aware of all the factors that affect the catalyst layer microstructure to make consistent, reliable and reproducible measurements for the understanding and modeling. The idea behind the use of these setups is to have a complete characterization of the electrocatalysts, from raw materials to their utilization in real catalyst layers, to gather as much information as possible on their utilization/effectiveness in various environments for the ORR. In addition, new electrocatalysts designs recently developed such as bimetallic, core-shell catalyst and shape-controlled nanocrystal exhibit really promising performance using RDE setup but still show poor activity in MEA configuration [4]–[7]. Thus, confronting the different electrochemical setups between them and highlighting the limitations of each (physical processes, operating conditions, materials used, etc) for classical electrocatalysts is a point of interest, that will be investigated herein. Beyond that, all these measurements are conducted to better understand the electrocatalyst and catalyst layer operation by building a reliable dataset for ORR, and to help developing/improving the description and the reliability and performance of models studied in this thesis.

II.2 Rotating Disk Electrode setup

The first setup considered is the very well-known and well established Rotating Disk Electrode (RDE) [8]–[10]. The RDE is a classical measurement method in electrochemistry to quantify ORR intrinsic electrocatalytic properties. This characterization setup is a three-electrode cell methodology that can be used for a fast and reliable benchmarking of different electrocatalysts activities [10]. It is a cheap method, because it only requires a little amount of catalyst material to make thin and ideal catalyst layers in a reproducible manner, which is really convenient when novel and promising high active electrocatalysts are produced in a small amount. It allows an analytical approach in liquid electrolyte in contrast with MEA in fuel cell configuration, and enables accessing “intrinsic” parameters of the electrocatalysts (mass-transport and Ohmic drop can be corrected, while the effect of the counter-electrode is transparent in the three-electrode cell configuration).

II.2.1 Electrochemical setup description

A three-electrode glass cell was used to perform experiments: the Counter Electrode (CE) is a Pt grid, the Reference Electrode (RE) is a homemade Reversible Hydrogen Electrode (RHE) and the Working Electrode (WE) is a RDE equipped with a glassy carbon tip (5 mm diameter) embedded in Teflon, where 10 µL of the catalyst ink is deposited to reach 20 $\mu g_{Pt}.cm^{-2}$ loading. All the electrodes are immersed in a 0.1 M $HClO_4$ solution, a non-specifically-adsorbing liquid electrolyte. Figure II-2 shows a picture of the three-electrode glass cell and a global view of RDE measurements. Before any measurements, the glassware is rigorously cleaned by overnight soaking in Caro’s acid then rinsed thoroughly with ultra-pure water and finally boiled to remove any impurities or any anions that could adsorb on Pt and lead to bad/inaccurate measurements. The temperature of the cell is regulated via an external water circuit allowing measurements at 25°C and 60°C.

II.2 Rotating Disk Electrode setup

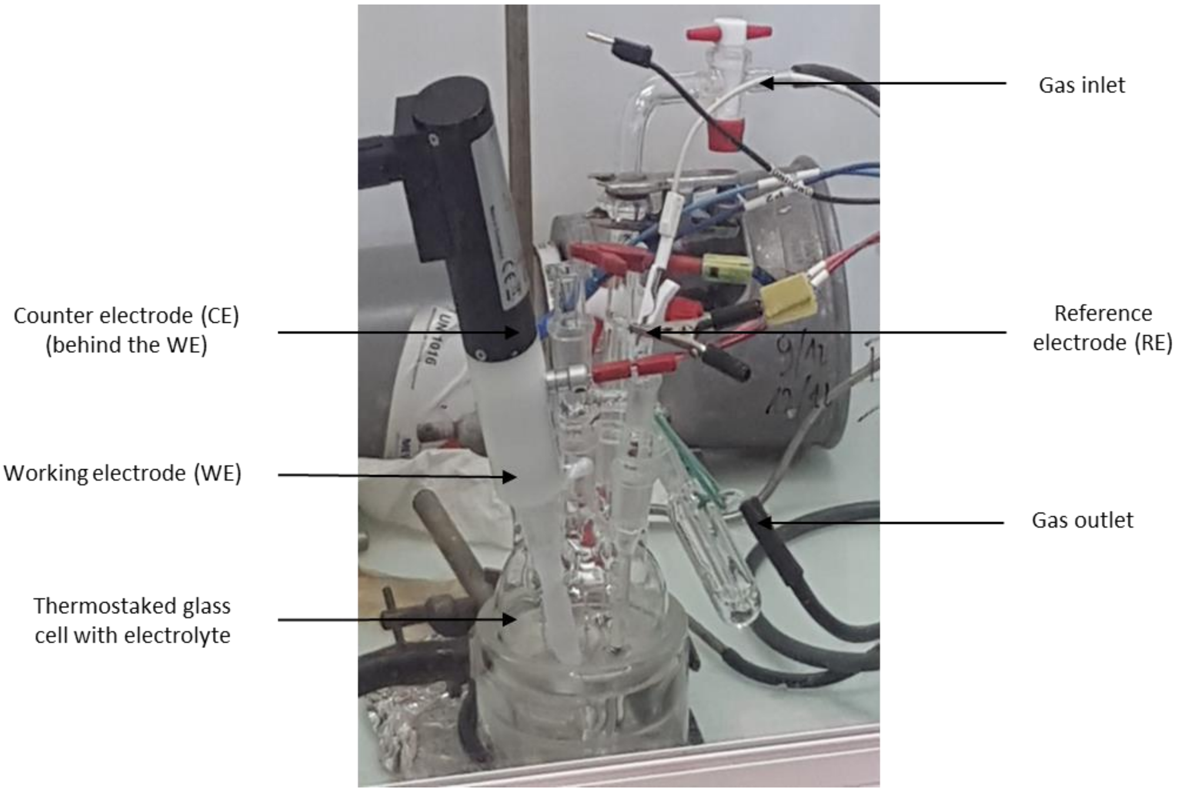

Figure II-2 : Picture of the three-electrode glass cell used for RDE measurements.

II.2.2 Ink formulation and CL manufacturing

Catalytic inks are made of electrocatalyst powder, deionized water and solvent. An ionomer is added to the mixture acting as a binding agent. The electrocatalysts (10 mg) are dispersed in an IPA/water/Nafion^{TM} D2020 mixture, the volumes of IPA, water and ionomer added being calculated to reach a loading of 20 $\mu g_{Pt}.cm_{geo}^{-2}$ when 10 µL of the catalyst ink is deposited on a glassy carbon tip with a surface of 0.196 cm^2. Once formulated, the ink is dispersed using an ultrasonic bath for 30 min twice, with fresh water each time. For stability, the ink is stored in a fridge for one day and the measurement in RDE are performed the next day. Before each deposit, the ink is re-dispersed during 10 min using the ultrasonic bath. The respective amounts of each component are summarized in the Table II-2.

Table II-2 : Summary of the component and respective amounts used for ink formulation for RDE.

Formulation	**Pt/VC**	**Pt_3Co/VC**	**Pt/HSAC**	**Pt/GC**
Mass of electrocatalyst (mg)	10	10	10	10
Volume of Nafion^{TM} D2020 (µL)	127.4	125.6	125.8	40.85
Volume of IPA (µL)	3413	3361	3369	3053
Volume of deionized water (µL)	8486	8370	8388	4581

The procedure to obtain a thin-film for RDE measurements in liquid electrolyte is based on the work of Garsany *et al.* [8]. The procedure consists of depositing 10 µL of catalytic ink on the glassy carbon tip (5 mm diameter), which has been polished and cleaned previously, embedded in Teflon and mounted on an inverted rotator. The revolution of the rotating electrode (spin coating) under a flow of hot air (using a hair dryer) leads to more homogeneous and reproducible catalytic thin-film than a stationary drying method. With such a procedure, effects such as 'coffee-ring' presented in the work of Garsany *et al.* can be avoided. Thus, this catalyst layer manufacturing procedure also leads to better and more reliable RDE measurements [8].

II.2.3 RDE electrochemical characterizations

Regarding electrochemical characterizations, all the techniques performed include a dynamic ohmic drop correction in order to capture more accurately and reliably the behaviour of each electrocatalyst. Before each measurement, an impedance measurement is done at Open Circuit Voltage (OCV) at 100 kHz frequency and a correction of 85% of the resistance value obtained from this measurement is applied to all the next measurements. A 100% ohmic drop correction is not advised by Biologic® manufacturer for the stability of the measurement. Thus, a correction with the last 15% can be done manually during post-processing. In the following and in the Chapter III of the thesis, the ORR measurements are 100% ohmic drop corrected, while the other electrochemical measurements in RDE are only 85% ohmic drop corrected. The procedure used for the electrochemical measurements consists of:

1) An activation step (Figure II-3 (a)) which consists of 20 min Ar bubbling in the electrolyte to remove any trace of oxygen, followed by 50 potential cycles performed between 0.05 and 1.23 V *vs.* RHE at a scan rate of 500 $mV.s^{-1}$, in order to remove impurities from the catalyst.

2) CO-stripping measurement is then performed to assess the value of the Pt ECSA (Figure II-3 (b)). The first step is CO bubbling at 0.1 V *vs.* RHE in the electrolyte for 6 min and then Ar bubbling for 39 min maintaining potential at 0.1 V *vs.* RHE to remove any trace of CO from the electrolyte and only keep a monolayer of CO adsorbed on the platinum active sites. To oxidise the monolayer of CO into CO_2, three CVs are then performed between 0.05 and 1.23 V *vs.* RHE at a scan rate of 20 $mV.s^{-1}$. The ECSA value is obtained using the CO oxidation peak coulometry (considering 420 $\mu C.cm_{Pt}^{-2}$), which is precisely determined by subtracting the 1st cycle of the CV (CO-stripping) from the 3rd one (baseline CV) on the Figure II-3 (b).

3) A blank CV is performed between 0.2 and 1.05 V *vs.* RHE at a scan rate of 5 $mV.s^{-1}$ with a rotation speed of the WE of 1600 rpm to correct the ORR data also obtained at 1600 rpm from capacitive current under Ar-saturated electrolyte. Basically, this blank CV is subtracted to the ORR data.

4) Before ORR measurements, O_2 is bubbled during 20 minutes to saturate the electrolyte. Then, a cycle is performed between 0.2 and 1.05 V *vs.* RHE at a scan rate of

5 mV.s^{-1} for different rotation speeds of the WE: 400, 400, 900, 1600, 2500, and back to 400 rpm. The measurement at a rotation speed of 1600 rpm is used to get the specific activity and mass activity of the electrocatalyst at 0.95, 0.90 and 0.85 V *vs.* RHE after capacitive current and mass-transport correction. After the capacitive correction explained in 3), the total current density can be expressed following Equation II-1:

Equation II-1 :

$$\frac{1}{j_f} = \frac{1}{j_t} + \frac{1}{j_{lim}}$$

With j_{f} the faradic current density, j_{t} the charge-transfer current density and j_{lim} the diffusion limiting current density captured in the region 0.2 – 0.5 V *vs.* RHE. The mass-transport corrected current density used to get the specific and mass activity is then calculated according to Equation II-2:

Equation II-2 :

$$j_t = \frac{j_{lim} \cdot j_f}{j_{lim} - j_f}$$

This electrochemical procedure is performed in the exact same way for all the electrocatalysts and using the software EC-lab® that drives the Biologic® VSP 300 and VMP 3 potentiostats. Figure II-3 shows the different electrochemical measurements performed on the Pt/VC electrocatalyst at 25°C in a 0.1 M $HClO_4$ liquid electrolyte. Figure II-3 (a) illustrates the effect of the activation step between the first, the 40th and the final 50th cycle. Removing impurities with potential cycling leads to more defined electrochemical profile of the Pt electrode, with well-defined characteristic regions of H_{UPD} (low potential) double layer (middle potential) and Pt-oxides (high potential). The peaks monitored in the H_{UPD} and Pt-oxides regions are also more pronounced, meaning that extra active sites are available for the electrochemical reactions at the end of this activation step. The stability of this procedure is also exhibited as there are almost no differences between the 40th and the 50th cycle. The Figure II-3 (b) shows an example of the CO-stripping measurement. The first sweep (full line) shows the peak related to the CO_{ad} oxidation into CO_2 on isolated Pt nanoparticles around 0.8 V *vs.* RHE. A pre-peak at 0.7 V *vs.* RHE is also observed, corresponding to the oxidation of CO that is absorbed on agglomerates or close to surface defects that are more active [11], [12]. The following sweeps 2 and 3 (dashed lines) are superposed and no current coming from further CO oxidation is observed, which means that the entire CO-monolayer adsorbed on Pt has been oxidized (and also validates the proper Ar-purge of the cell). Thus, by considering the coulometry of the CO peak using the second scan as a baseline (dashed area), it is possible to calculate the Pt ECSA thanks to the Equation II-3:

Equation II-3 :

$$\mathrm{ECSA} = \frac{Q_{\mathrm{CO}}}{C \cdot S_{\mathrm{geo}}} L_{\mathrm{Pt}}$$

with Q_{CO} the coulometry of the CO_{ad} oxidation peak, C = 420 µC.cm$_{\mathrm{Pt}}^{-2}$ corresponding to the specific coulometry of CO on bulk Pt (25°C/liquid electrolyte) but also assumed for nanoparticles, S_{geo} the geometric surface of the working electrode and L_{Pt} the platinum loading of the catalyst layer (mg.cm^{-2}). The sweep 2 and 3 from CO-stripping measurements can also be used to assess the

ECSA value via the proton adsorption/desorption coulometry. The dashed area in Figure II-3 (c) corresponds to the desorption of protons. The same formula as for CO-coulometry is used by taking C equal to 210 µC.cm$_{Pt}^{-2}$ as the specific coulometry of proton for bulk Pt platinum (25°C/liquid electrolyte) and taking Q_{H} the coulometry of proton desorption area. However, CO$_{ad}$ is more strongly adsorbed on Pt than protons and the CO$_{ad}$ oxidation peak is well defined, plus the possible H_2 formation that can disturb the ECSA measurements in the H$_{UPD}$ region, imply that ECSA values assessed by considering the coulometry of CO$_{ad}$ oxidation are more reliable. Figure II-3 (d) displays an example of ORR measurements for 400 rpm and 1600 rpm. One should note that two measurements performed at 400 rpm are displayed: the second and the last of the ORR measurements in the procedure (cross and circle markers). This shows the good reproducibility and stability during the protocol. Such measurements are done to assess the intrinsic activity of the electrocatalyst: the specific activity (in µA.cm$_{Pt}^{-2}$) and the mass activity (in A.mg$_{Pt}^{-1}$) at potential around 0.9 V *vs.* RHE. These activities are obtained from the 1600 rpm measurement. Depending on the WE rotation speed, below typically 0.8 V *vs.* RHE, a diffusion limiting current is reached, which corresponds to mass transport limitation by diffusion of dissolved O_2 in liquid electrolyte. Thus, the activity measurement is only reliable for a short range of potential around 0.9 V *vs.* RHE, which is significantly different from real active layer potential range of operation. The ORR measurements performed at the different WE rotation speeds also lead to the so-called Levich plot: the diffusion limiting current captured in the region 0.2 – 0.5 V *vs.* RHE during ORR measurements is plotted versus the square root of the WE rotation speed in rad.s^{-1} according to Levich equation (Equation II-4):

Equation II-4 :

$$j_{lim} = 0.620 \cdot n \cdot F \cdot A \cdot D^{2/3} \cdot \nu^{-1/6} \cdot \omega^{1/2} \cdot C$$

With n the number of electron exchanged, F the Faraday constant, A the geometric electrode area, D the diffusion coefficient of the oxidizer/reductant, ν the kinematic viscosity of the electrolyte, ω the angular rotation rate of the WE and C the concentration of the oxidizer/reductant. The limiting current increases linearly with the square root of the WE rotation speed according to Equation II-4. Figure II-3 (e) shows the Levich plot for the electrocatalysts studied including the linear regression coefficients ranging from 0 to 1 for the trend curves (dashed lines). The coefficient values are all above 0.99, which accounts for the agreement of the experimental data with the Levich equation. The differences on the limiting current densities between the electrocatalysts for each WE rotation speed come from geometrical effects: each deposit does not necessarily cover perfectly the glassy carbon tip. However, the agreement with the Levich equation validates the ORR measurements protocol and its stability for all the Pt-based materials. The electrochemical characterization results for the four electrocatalysts will be shown in the next chapter dedicated to the experimental results.

II.2 Rotating Disk Electrode setup

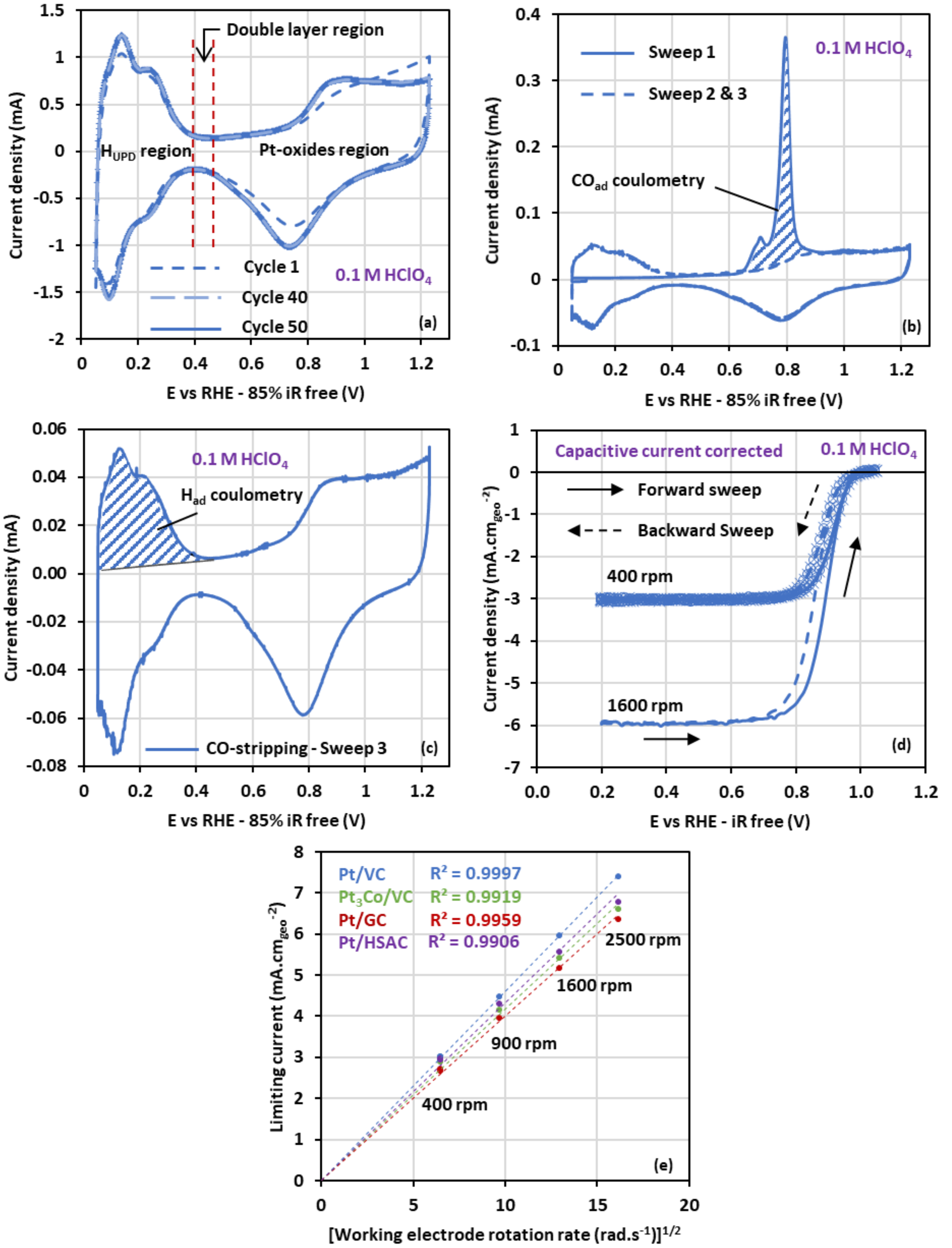

Figure II-3 : (a) Activation step for Pt/VC electrocatalyst from 0.05 to 1.23 vs. RHE at 500 mV.s^{-1} (Only cycle 1, 40 and 50 are displayed) (b) CO stripping measurement performed on Pt/VC electrocatalyst from 0.05 to 1.23 V vs. RHE (c) Third cycle of the CO stripping measurement for Pt/VC electrocatalyst (d) ORR measurements performed on Pt/VC electrocatalyst from 0.2 to 1.05 V vs. RHE (e) Levich plot for all electrocatalysts.

The last observation that can be made from ORR measurement is the existence of a hysteresis phenomenon: the current of the forward sweep (from 0.2 up to 1.05 V *vs*. RHE, dashed line) differs from that on the backward sweep (from 1.05 down to 0.2 V *vs*. RHE continuous line) in the potential region above 0.7 V *vs.* RHE. This hysteresis is also measured in fuel cell configuration and is ascribed to: i) the variation of hydration state of the ionomer in the catalyst layer, which is here unlikely in liquid electrolyte measurement, and ii) the change of Pt surface state as a function of the electrode potential and "history". The latter is probably the main reason here, because the phenomenon happens in the Pt oxides potential region. Thus, the asymmetry of the Pt oxides formation and reduction reactions kinetic may explain the hysteresis observed on experimental RDE ORR measurements. On the whole, if RDE is widely used to evaluate the intrinsic ORR activity of Pt-based electrocatalysts, the RDE electrochemical setup suffers from reactant mass transport limitation due to the very low solubility of the gas reactant in the liquid electrolyte (witnessed by the well-defined limiting current observed on Figure II-3 (d)), and does not enable ORR activity measurements in the low potential (E < 0.8 V *vs*. RHE) domain, which is of interest for the PEMFC application. Therefore to have insights into the real effectiveness of the electrocatalyst in proper experimental conditions, characterization in fuel cell configuration must be preferred.

II.3 Differential Cell (DC) characterization setup

The second setup considered is the Differential Cell, a small active surface single cell that gives insights/data on catalyst layers under various operating conditions that are the most representative of fuel cell system operation [13]. A focus on the DC description and why such a cell has been chosen to perform the different electrochemical characterizations presented hereafter. The assembly method of the cell is also covered as well as the test bench description.

II.3.1 Electrochemical setup and test bench description

II.3.1.1 Differential cell and cell assembly description

Electrochemical characterizations in fuel cell configuration may be performed using single cells with various active surface areas, from 1 cm^2 up to 500 cm^2. The main issue when performing electrochemical characterisations is the intrinsic heterogeneous operation of the cell in the plane (e.g. along the fluidic channels), due to transport of the reactant and the current in the GDL, and through-plane in the thickness of the catalyst layer. These heterogeneities come from the progressive consumption of reactant along the cell, the pressure drop due to the flow-field design and the presence of liquid water that hinders the homogeneous distribution of gas reactant in the catalyst layer as well as from heterogeneous proton transport within each catalyst layer, which may proceed via ionomer and/or liquid water paths. The compression of the assembly may also lead to heterogeneous operation of the cell, as it impacts the porosity of the GDL/MPL and the rib/GDL interface (with strong heterogeneities in electrical contact resistance) [14]–[17]. All these phenomena have a significant impact on the local and global performance of the PEMFC as well as on the degradation mechanisms that will heterogeneously occur and are specifically at stake for large cells. The PEMFC Differential Cell setup is mainly used to characterize the electrocatalyst in MEA configuration under ideal and well-controlled operating conditions. Such cell is attractive because it allows operation under homogeneous conditions in the plane without any significant reactant heterogeneities between the inlet and the outlet using very high reactant stoichiometries (e.g. 50 @ 1 A.cm^{-2}). Electrochemical measurements were conducted in a 1.8 cm^2 active area cell using a fine flow-field design (250 µm/250 µm rib/channel width and 400 µm depth) at both anode and cathode sides. Thus, it makes sense that the manufacturing of CCM shall be meticulously controlled in this work since a small active surface cell is used for electrochemical characterizations and local processes investigation.

The cell assembly consists of stacking consecutively the different components of the MEA and the DC parts. First, a PTFE wedge (150 µm thick) is deposited on the monopolar plate. It ensures the cell tightness and the GDL compression level. Then, a commercial GDL with MPL (22 BB from SGL) is put between the flow field and the 3-layers CCM. A PET layer support (25 µm thick) is added to delimit the active area of 1.8 cm^2 and reinforce the membrane towards the compression. The PTFE wedge and the PET layer thicknesses ensure the GDL compression advised by the manufacturer (around 20% compression) for efficient mass transport and electronic conductivity. The CCM is placed in such a way that the electrodes entirely cover the area delimited by the support in PET. The rest of the components is put together symmetrically to finish the assembly. The Figure II-4 shows a picture of the differential cell design used for electrochemical characterizations and a MEA and the Table II-3 summarizes the different CCM composition characterized in differential cell. Note that, the Pt/HSAC electrocatalyst is also characterized in DC using MEA coming from a European project, FURTHER-FC project [18] (FURTHER-FC project funded by Fuel Cells and Hydrogen 2 Joint Undertaking (now Clean Hydrogen Partnership) under grant agreement No. 875025), dedicated to improve the understanding of performance limitations (related to transport and electrochemical properties) and the optimization of the design and durability of MEA. Detailed information on the ink formulation and dispersion method as well as the CCM manufacturing process cannot be disclosed here for this MEA.

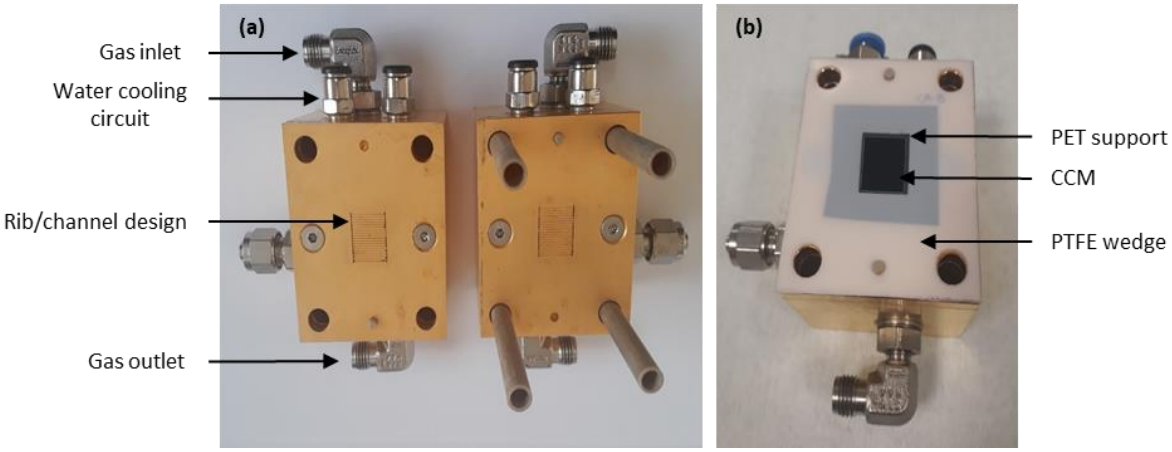

Figure II-4 : Picture of the differential cell flow-field design (a) and the assembly of a MEA and the DC (b) (Note that a GDL is missing for better displaying).

Table II-3 : Summary of the different CCM composition tested in DC.

CCM tested	Anode electrocatalyst	Anode loading	Membrane	Cathode electrocatalyst	Cathode loading
FURTHER-FC	Pt/HSAC	100 $\mu g_{Pt}.cm_{geo}^{-2}$	Thin 15 µm Chemours membrane	Pt/HSAC	200 $\mu g_{Pt}.cm_{geo}^{-2}$
Very low loaded	Pt/VC	100 $\mu g_{Pt}.cm_{geo}^{-2}$	Nafion®115	Pt/VC Pt_3Co/VC Pt/GC Pt/HSAC	20 $\mu g_{Pt}.cm_{geo}^{-2}$
Low loaded	Pt/VC	100 $\mu g_{Pt}.cm_{geo}^{-2}$	Nafion®115	Pt/VC Pt/HSAC	100 $\mu g_{Pt}.cm_{geo}^{-2}$

II.3.1.2 Test bench description and operation

To perform the different measurements, the cell is mounted on a test bench. The test bench is a commercial FuelCon evaluator-C 70350, which can supply gases such as nitrogen, oxygen, air and hydrogen. Reactant pressures and flow rates are controlled via a software on the bench. Each connection and pipe is heated up between 10°C and 30°C above the temperature of the cell to avoid water condensation before the cell inlets. A DI water circuit goes through the monopolar plates to regulate the cell temperature via a thermostatically controlled bath. Temperature sensors are placed into the flow-field plate to check the cell temperature as well as on the bench to measure the temperature of the connections/pipes. The Figure II-5 displays pictures of the commercial test bench used and the DC mounted on this test bench. The cell is connected to a Biologic® VMP2 potentiostat equipped with a 10 A/20 V booster VMP3B-10. In this case, the negative electrode stands for both the reference and counter electrode (blue and white connections) and the positive electrode is the working electrode (red connection). The cell is fed with dry or humidified gases thanks to bubblers filled with deionized water. The relative humidity of the gases is calculated according to the dew point, which is controlled by the temperature of the bubblers.

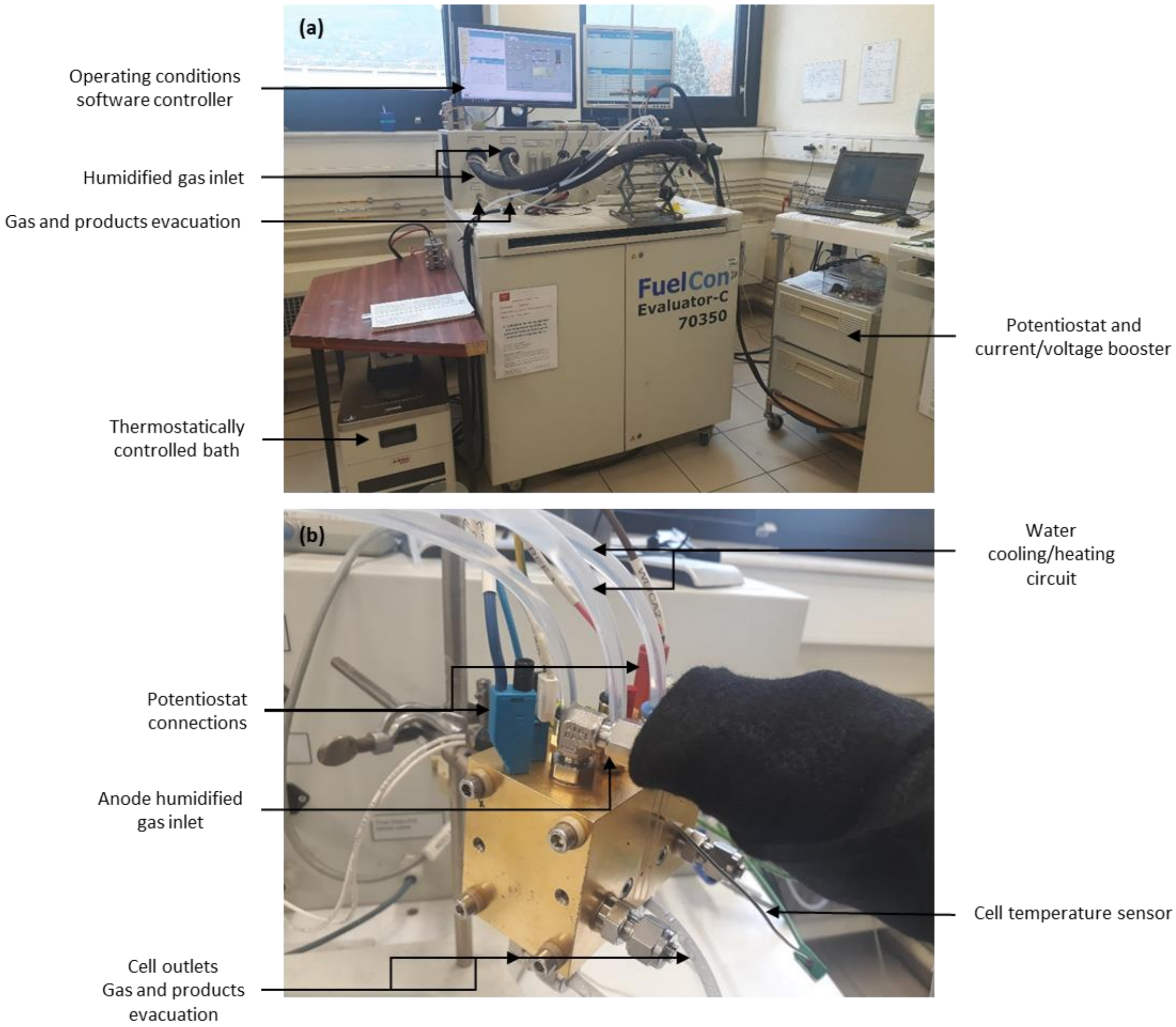

Figure II-5 : (a) Picture of the commercial test bench used for electrochemical characterizations and (b) the DC mounted on the test bench.

II.3.2 Ink formulation and MEA manufacturing

The ink formulation and catalyst layers manufacturing are very important steps to ensure the homogeneity of the catalyst layer and a reproducible operation in PEMFC. In this section, two types of ink are formulated: the first one is used to manufacture anodic catalyst layers via a blade coating method and the second one is used to manufacture cathodic catalyst layers using a spray coating machine. The spray coating method is used to reach Pt loadings below 100 $\mu g_{Pt}.cm_{geo}^{-2}$, that may be hard to reach in an accurate manner via the blade coating method and/or would lead to inhomogeneous catalyst layers. In this work, two catalyst layer loadings are considered: 100 $\mu g_{Pt}.cm_{geo}^{-2}$ and 20 $\mu g_{Pt}.cm_{geo}^{-2}$. Catalyst layers with 100 $\mu g_{Pt}.cm_{geo}^{-2}$ loading are manufactured either using the blade coating method or the spray coating method and catalyst layers with 20 $\mu g_{Pt}.cm_{geo}^{-2}$ loading are only manufactured using the spray coating method. Here again, catalytic inks are made of electrocatalyst powder, deionized water, solvent and ionomer. In addition to its role of binding agent, the ionomer in catalyst layer helps ensuring a good proton transport to the active sites, a pivotal role. There are many parameters that need to be considered when formulating the inks such as, the nature of solvent and electrocatalyst used, the quantity of each component (ionomer to carbon ratio I/C, water to solvent ratio, etc.), the dispersion method and even the order of introduction of the components. All these parameters have an impact on the catalytic ink, thus the catalyst layer and, ultimately, the performance of the cell. In the recent years, research on ink formulation and catalyst layer manufacturing has been extensive, which shows the importance of these steps [19]–[24].

II.3.2.1 Ink formulation and anodic CL manufacturing for DC using blade coating method

Anodic catalytic inks were prepared with the Pt/VC electrocatalyst for differential cell measurements. The Table II-4 gives information on the material and the quantities used to make the anodic catalytic ink.

Table II-4 : Summary of the components and their quantities used for Pt/VC ink formulation for blade coating method.

Formulation	**Weight (g)**	**Dry extract wt.**		**Ionomer/Carbon wt.**	**Water/alcohol wt.**	**Water/alcohol vol.**
Pt/VC	2.00	**Dry matter Ink**	17.7%	0.68	4.8	3.8
Nafion™ D2020	3.20	**Pt**	35.2%			
Ethanol	0.75	**Carbon**	38.6%			
Deionized water	9.25	**Nafion™**	26.2%			
TOTAL	15.20					

The ink formulation protocol for the Pt/VC electrocatalysts at 100 $\mu g_{Pt}.cm_{geo}^{-2}$ including the dispersion process is composed of multiple steps as follow:

1) The catalyst is mixed with deionized water and pure ethanol in a glove box in a vial;
2) Milling balls in zirconia (3 mm diameter) are added to the mixture, which is left for 24 hours on a roller mixer IKA® ROLLER 10 basic;
3) Nafion™ D2020 is added to the mixture, which is dispersed using the roller mixer for another 24 hours;
4) The ink is ready for deposition and CL layer manufacturing.

The catalyst layer manufacturing process is done in order to manufacture MEA via the Decal Transfer Method, the process considered in this thesis that will be explained in section II.3.3.3. Figure II-6 shows the coating table used for the blade coating method, which consists of five successive steps:

1) A PTFE inert substrate (250 µm thick) is deposited on the pre-heated coating table. This smooth substrate without pattern is chosen to have a homogeneous catalyst layer deposited and to reach a complete decal-transfer process onto the membrane;
2) The coating blade is put on the PTFE substrate;
3) The catalytic ink is deposited on the PTFE substrate near the coating blade;

4) The coating blade is set in motion to spread homogeneously the catalytic ink into a liquid film on the PTFE substrate;
5) The solvent is evaporated thanks to the heating table resulting in a solid catalyst layer with a porous structure on the PTFE substrate.

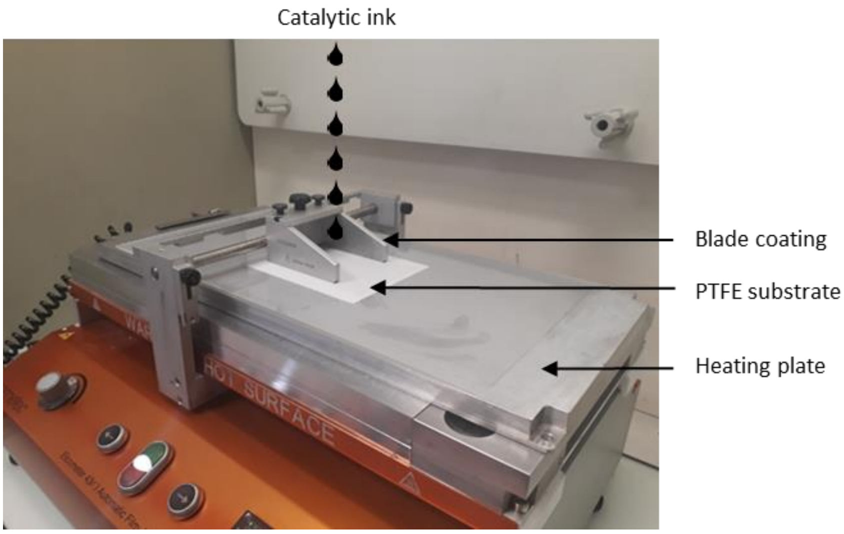

Figure II-6 : Picture of the coating table and hardwares used for the blade coating method.

The different parameters of this process are the temperature of the coating table, the height and the speed of the coating blade. The temperature of the table and the speed of the coating blade will affect the drying time and therefore the homogeneity/microstructure of the catalyst layer. The blade height controls the thickness of the liquid film deposited, which is directly linked to the loading of the solid and dry catalyst layer. These parameters are adjusted to reach loading specifications and to get a layer as homogenous as possible. In this case, the temperature of the table is set at 60°C, the speed of the coating blade is 10 mm.s^{-1} and the height of the coating blade is set at 20 µm. With such parameters and the ink composition of Table II-4, the CL loading obtained is near 100 $\mu g_{Pt}.cm_{geo}^{-2}$.

II.3.2.2 Cathodic CL manufacturing for DC using spray coating method

As it was stated before, cathodic catalyst layers with 20 $\mu g_{Pt}.cm_{geo}^{-2}$ and 100 $\mu g_{Pt}.cm_{geo}^{-2}$ loadings are manufactured using the spray coating method. The fundamental differences between this process and the blade coating process lie in the ink formulation, the mixing and the drying method. Regarding the ink, it is much more diluted than the one used for blade coating. Table II-5 and

Table II-6 give information on the material and the quantities used to make the catalytic ink for the spray coating process. As the type of carbon and method of ink coating (here blade coating) mostly drives the ink formulation, the same formulation is used for the Pt/VC and Pt_3Co/VC electrocatalysts, because they have the same carbon support Vulcan XC72. Regarding the Pt/HSAC electrocatalyst, the quantities are adjusted to reach a I/C ratio of 0.8 and appears in purple in the Table II-5.

The ink formulation protocol for all the electrocatalysts including the dispersion process is as follow:

1) The catalyst is mixed with deionized water and IPA in a glove box;

2) The mixture is dispersed using magnetic stirring for 5 minutes and then an ultrasonic bath 15 minutes, 2 times in a row;
3) Nafion^{TM} D2020 is added to the mixture, which is dispersed using magnetic stirring for 24 hours;
4) The ink is ready for spraying and CL layer manufacturing.

Table II-5 : Summary of the components and their quantities used for Pt/VC, Pt_3Co/VC and Pt/HSAC inks formulation for spray coating method.

Formulation	Weight (g)	Dry extract wt.		Ionomer/Carbon wt.	Water/alcohol wt.	Water/alcohol vol.
Pt/VC Pt_3Co/VC Pt/HSAC	0.50	**Dry matter Ink**	1.5%	0.7 **0.8**	0.5	0.4
Nafion^{TM} D2020	0.80 **0.95**	**Pt**	35.2% **33%**			
IPA	29.0	**Carbon**	38.6% **37.3%**			
Deionized water	13.85	**Nafion^{TM}**	26.2% **29.7%**			
TOTAL	44.15 **44.30**					

Table II-6 : Summary of the components and their quantities used for Pt/GC ink formulation for spray coating method.

Formulation	Weight (g)	Dry extract wt.		Ionomer/Carbon wt.	Water/alcohol wt.	Water/alcohol vol.
Pt/GC	0.20	**Dry matter Ink**	0.6%	0.5	0.5	0.4
Nafion^{TM} D2020	0.32	**Pt**	22.4%			
IPA	29.0	**Carbon**	51.4%			
Deionized water	13.85	**Nafion^{TM}**	26.2%			
TOTAL	43.37					

For Vulcan and HSA carbon-based materials, the coating is made on the same inert PTFE substrate as for blade coating. On the contrary, the electrocatalyst ink with Pt/GC is directly sprayed onto the membrane, with the support plate heated at 40°C, and not onto an inert substrate for MEA manufacturing. This is explained by the fact that at such low loadings, the decal-transfer process is not completely achieved for this electrocatalyst. The spray coating is done using a Sono-tek machine, which is presented on the Figure II-7. The catalytic ink goes through an ultrasonic nozzle that vibrates at a frequency of 120 kHz thanks to a piezoelectric ceramic, which creates a cloud of very thin droplets that are pulverised on the inert PTFE substrate (or the membrane for Pt/GC). The PTFE substrate is fixed on a plate pre-heated at 80°C. The nozzle is moving above the substrate through x and y-axis, the height being fixed. The flow of catalytic ink sprayed, the speed of the nozzle, the number of passes and the surface of coated CL are fixed and set respectively equal to 0.1 mL.min^{-1}, 30 mm.s^{-1}, 4 passes and 15 cm² (being delimited by a dedicated mask). All these parameters are inputs for command and are set to reach the target Pt loading of 20 µg$_{Pt}$.cm$_{geo}^{-2}$, the process being entirely automatized. For catalyst layers 5 times more loaded, the number of passes is 5 times higher and the surface of the CL is equal to 49 cm².

Figure II-7 : Picture of the Sono-tek machine used for spray coating method.

II.3.2.3 Catalyst layers characterization and quality control

The homogeneity and the loading of each catalyst layer are then controlled and checked. To have information on the catalyst layer loadings, X-Ray Fluorescence (XRF) measurements are carried out using a FISCHERSCOPE® X-RAY XDV®-SDD equipment. This technique is non-destructive and gives information on the local elemental composition of materials. X-rays with high energy are first sent by an X-ray tube on the sample leading to excited atoms. Then, excited atoms return to a stable energy state by releasing a fluorescent X-ray that is analysed. Each atom has its characteristic response at a specific energy that can be graphically represented as X-ray intensity peaks versus energy. The position of the peak gives information on the element and its intensity on the concentration of the corresponding element, Pt here, in the sample. In this work, the samples are catalyst layers of 49 cm² (7 cm x 7 cm) coated on PTFE substrate for 100 µg$_{Pt}$.cm$_{geo}^{-2}$ loading and catalyst layers of 15 cm² (5 cm x 3 cm) coated on PTFE substrate for 20 µg$_{Pt}$.cm$_{geo}^{-2}$ loading. To have insights on the catalyst loading homogeneity of the catalyst layers, 64 and 24 points are analysed for 100 µg$_{Pt}$.cm$_{geo}^{-2}$ and 20 µg$_{Pt}$.cm$_{geo}^{-2}$ loadings respectively. Each point is exposed to X-ray for 30 seconds with a 3 mm diameter collimator. All the measurements are done with the catalyst layers always in the same position.

Figure II-8 shows results after post-processing of the loading mapping of the catalyst layers manufactured with Pt/VC via the spray coating process. The same method is applied for the other electrocatalysts and the catalyst layers manufactered via the blade coating process. For catalyst layer made of Pt/VC, the average loading obtained is equal to 90 ± 9 $\mu g_{Pt}.cm_{geo}^{-2}$, with a loading in range of 40 to 120 $\mu g_{Pt}.cm_{geo}^{-2}$ for the whole 49 cm² surface as seen on Figure II-8 (a). The edges of the surface of the catalyst layer are not taken to manufacture the MEA, as the loading is more heterogeneous in these areas. For the very low loaded catalyst layer made of Pt/VC, the average loading obtained is equal to 20 ± 1 $\mu g_{Pt}.cm_{geo}^{-2}$, with a loading in range of 16 to 24 $\mu g_{Pt}.cm_{geo}^{-2}$ for the whole 15 cm² surface as seen on Figure II-8 (b). The average loading is close to the target values of 100 $\mu g_{Pt}.cm_{geo}^{-2}$ and 20 $\mu g_{Pt}.cm_{geo}^{-2}$, with a reasonable average dispersion over the CL geometric surface area (5% to 10%). The loading of CL can also be measured using UV spectrophotometry and by weighing. The other techniques give the same average loading as the XRF. However, it was decided to prefer and keep the XRF measurement technique, as it also gives information on local loadings which may be important when local electrochemical measurements are performed with the DC setup at such low loadings.

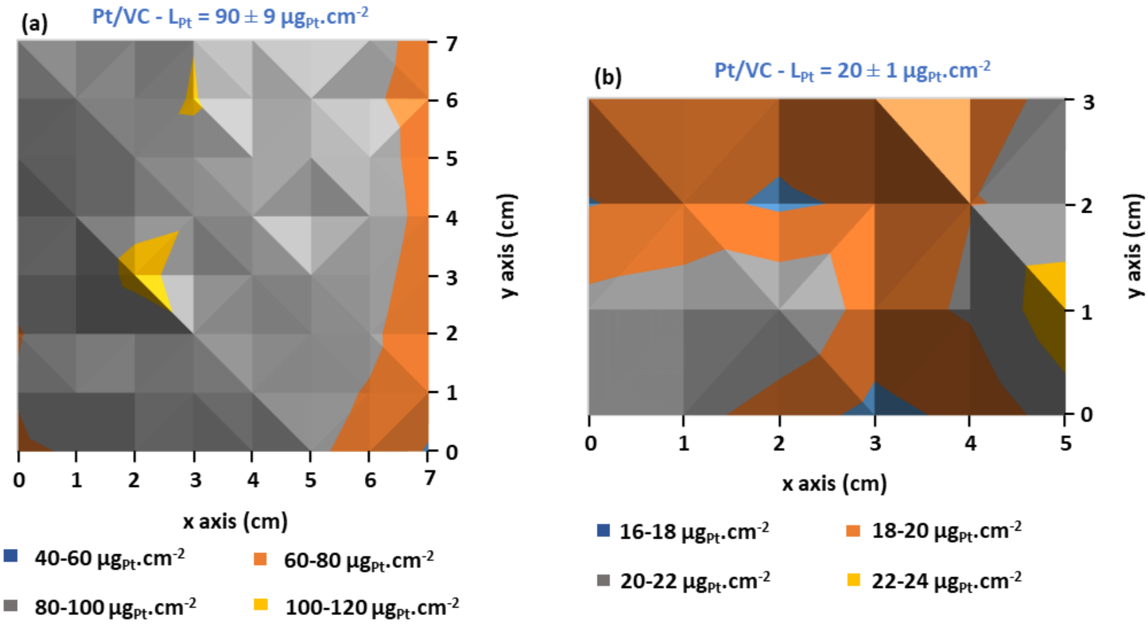

Figure II-8 : Example of cartographies with XRF measurements to control the loading homogeneity of the CL made of Pt/VC manufactured with (a) 100 $\mu g_{Pt}.cm_{geo}^{-2}$ and (b) 20 $\mu g_{Pt}.cm_{geo}^{-2}$ targeted loadings.

The structural homogeneity of the catalysts layers is then additionally checked by making surface Scanning Electron Microscopy (SEM) with the FEG-SEM LEO 1530 from Zeiss. Four small squares are chosen randomly within the catalyst layer, these samples accounting for a statistical description of the whole surface. They are deposited on a conductive support which is placed in a vacuum chamber. Electrons are sent on the sample with an accelerating voltage 5 kV. The secondary electrons are analysed by a detector above the sample in InLens mode, which allow a topographic contrast of the CL surface. The Figure II-9 displays SEM images of Pt/VC catalyst layers loaded at 100 $\mu g_{Pt}.cm_{geo}^{-2}$ manufactured by blade coating method and spray coating method. The images show the good homogeneity of the CL manufactured by the coating blade method. Neither surface cracks nor agglomerates are observed. In the case of spray coated catalyst layer, the topographic surface obtained is quite different than with the blade coating method. A more porous and levelled structure is observed. The differences mainly come from the drying method: the catalyst layer is deposited and dried layer by layer with the spray coating method due to the different passes, whereas the catalyst layer is entirely deposited and then dried all at once with the blade coating method. Another explanation may be the nature of the catalytic ink, which is less viscous in the case of spray coating than in blade coating process. Surface SEM images were not realised on $20\ \mu g_{Pt}.cm_{geo}^{-2}$ catalyst layers because almost nothing could be seen at such low Pt loadings. Cross-section microscopy has also been done on the MEA manufactured to gather information on the CL|Membrane interface. These images will be shown in the section dedicated to the MEA manufacturing. All the physico-chemical characterizations demonstrate that the composition/microstructure of the CL layers manufactured are rather homogeneous and well controlled, which is mandatory to obtain electrochemical characterizations as reproducible and reliable as possible.

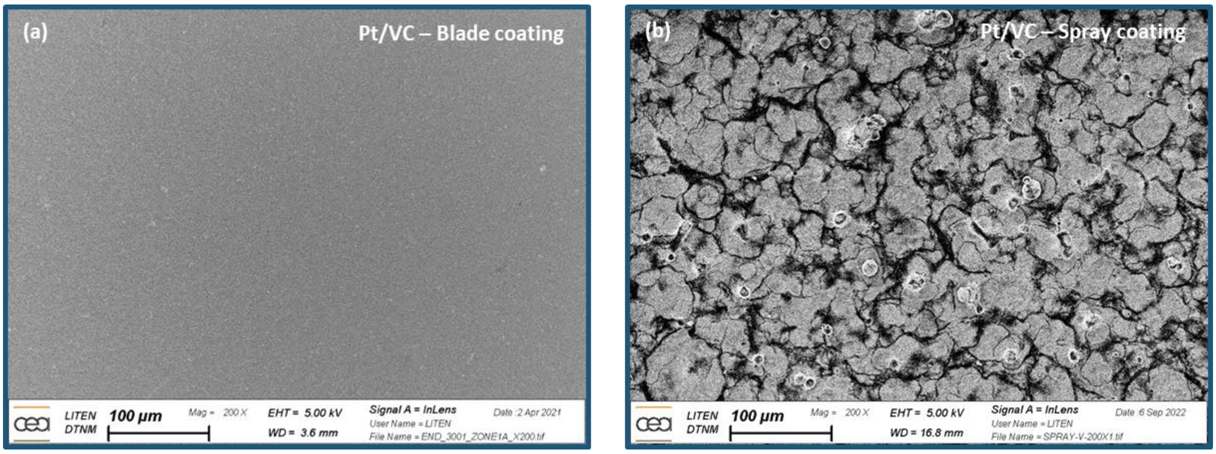

Figure II-9 : Surface SEM images of the Pt/VC catalyst layers manufactured by (a) Blade coating method and (b) spray coating method.

II.3.3 MEA manufacturing process

The MEA manufacturing process to perform electrochemical characterizations in fuel cell configuration can be done using different methods. The most common are the Catalyst-Coated Substrate (CCS), the Catalyst-Coated Membrane (CCM) and the Decal Transfer Method (DTM). The main difference between these methods is the type of substrate used to deposit the catalyst layers. These methods will be quickly presented with a focus on the DTM method used for most of MEA manufacturing in this work. All these methods have pros and cons that will be quickly discussed.

II.3.3.1 Catalyst-Coated Substrate method

The first step of the CCS method is the coating of the catalyst layers onto pre-existing (e.g. commercial) GDL. Then, the assemblies CL-GDL (also known as GDE for Gas Diffusion Electrode) are hot pressed with a membrane. The Figure II-10 illustrates the CCS process for the MEA manufacturing.

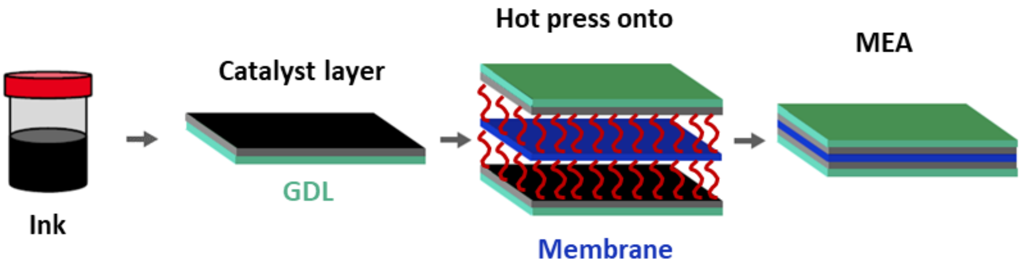

Figure II-10 : Illustration of the CCS method (reproduced from [25]).

This CCS method is quite convenient for commercial/industrial purposes as it is a quite reliable/reproducible method to manufacture many MEA in a reasonable amount of time. In addition, whatever the solvent used for the catalytic ink, the membrane will not be damaged (unlike when direct coating on membrane is done) at least if the hot pressing parameters are properly chosen. However, such procedure often leads to unclearly defined interface between the catalyst layers and the membrane. This can result in a bad protonic conduction in some areas of the interface CL|PEM and thus to uneven local current density production on the MEA active surface area. Such uneven current density distribution leads to higher ohmic losses, thus worse performance and even favours inhomogeneous degradation [26].

II.3.3.2 Catalyst-Coated Membrane method

The CCM method consists of the coating of the catalysts layers directly onto the proton exchange membrane, leading to the so-called CCM. Then GDL are hot pressed onto the CCM. The Figure II-11 illustrates the CCM process for the MEA manufacturing.

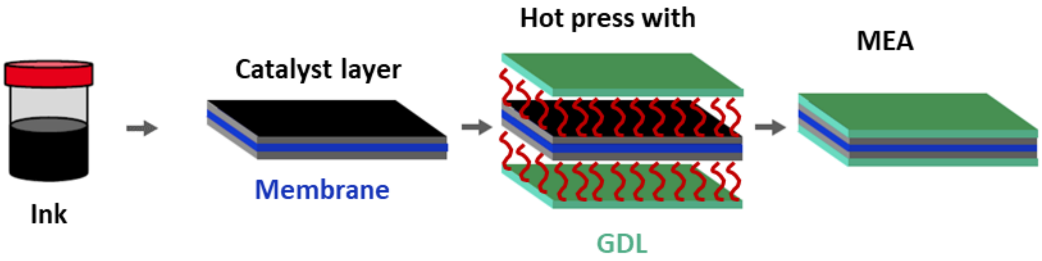

Figure II-11 : Illustration of the CCM method (reproduced from [25]).

The major inconvenience in this method is that some solvent composing catalytic ink may damage (or contaminate) the membrane through dissolution process and mechanical deformation of the membrane can occur during the coating. However, the ionic connections between the catalyst layers and the membrane are better defined than with the CCS procedure. This leads to a better use of the electrocatalyst, as the protonic conduction is ensured in a more optimized manner at the CL|PEM interface. As a result, the performance of the CL can be improved with a more uniformly distribution of the current density generated [27], [28].

II.3.3.3 Decal Transfer Method (DTM)

The last method is the DTM which consists of coating the catalyst layer onto an inert substrate (a sheet of PTFE is commonly used) that must fulfil specific conditions for the hot decal-process [29]. A thin liquid film of the catalyst layer is deposited onto the PTFE sheet (by blade coating for instance) and after evaporation of the solvent, it leads to a solid and porous catalyst layer. The next step is a decal-process to transfer the catalyst layers from the substrates to the membrane, leading to a CCM. The CCM is then assembled with GDL when preparing the cell for electrochemical measurements with or without a hot-pressing step to get the complete MEA. The Figure II-12 illustrates the DTM process for the MEA manufacturing and the Figure II-13 shows pictures of the different tools/materials used to operate the decal-transfer step. This process is done using a 3R SYNTAX 100 hot press machine.

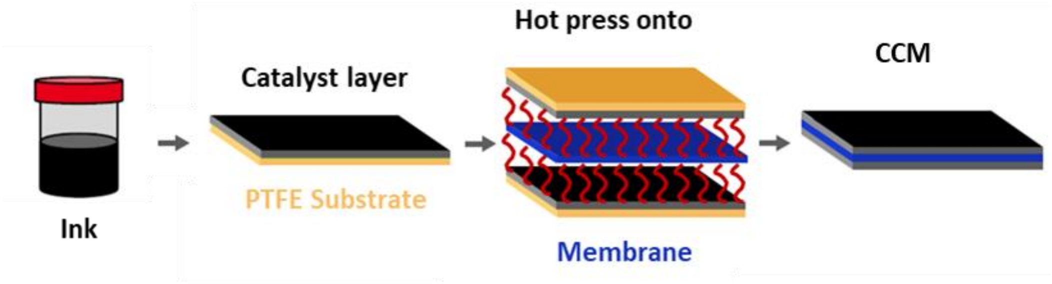

Figure II-12 : Illustration of the DTM method (reproduced from [25]).

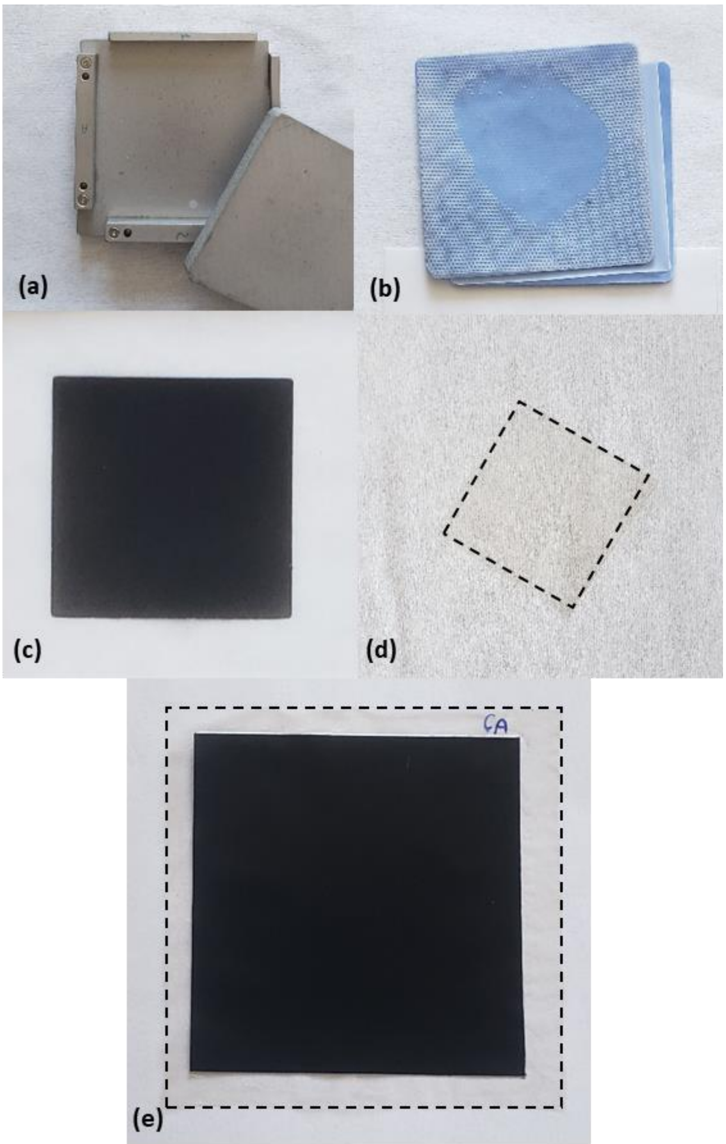

Figure II-13 : (a)-(b) Mould and kit used to transfer the CL from the substrate to the membrane (c) CL coated on PTFE substrate (d) Membrane Nafion® 115 (e) CCM without GDL obtained after decal-process.

The DTM method gathers all the pros from the previous processes possible at the lab scale, while avoiding the inconveniences except one: it is hardly transferable to the industrial scale. This is why, the DTM was preferred and selected for CCM manufacturing in this work. Let us stress that three parameters drive the efficiency of the hot pressing for the decal step: the mechanical stress *P*, the stress time *t* and the temperature *T*. The idea is to find the optimal combination of these parameters to transfer entirely the catalysts layers from the substrate onto the membrane, without degrading neither the catalyst layer microstructure nor the membrane. Even though the increase of the three parameters benefits to transfer effectiveness, it may also lead to a negative effect on the CL: the higher the mechanical stress and/or stress time, the more compact the catalyst layer. This could lead to mass transport limitations especially at high current densities. Using a too high temperature may lead to irreversible damages of catalyst layer (delamination with membrane, not to speak from possible damages to the membrane). In that case, catalyst layers may be less efficient regarding water management, for instance [27], [28], [30]. The Table II-7 summarizes the hot decal-process parameters and materials used for CCM manufacturing for each electrocatalyst for both cathode loadings of 20 $\mu g_{Pt}.cm_{geo}^{-2}$ and 100 $\mu g_{Pt}.cm_{geo}^{-2}$. Note that for 20 $\mu g_{Pt}.cm_{geo}^{-2}$, the Pt/GC has been directly sprayed onto the membrane but there is still a hot decal-process to transfer the anode onto the other side of the membrane. Regarding the PEM considered for these CCM, a thicker Nafion®115 (127 µm thick) has been chosen (compared to thinner membranes in state-of-the-art MEAs), to limit as much as possible hydrogen crossover, which would perturbate electrochemical characterizations with such low loaded cathode catalyst layers: i) perturbation during cyclic voltammetry measurements under H_2/N_2 configuration and ii) an open circuit value lowered under H_2/O_2 configuration, which is limiting when activity measurements have to be done at high potential. All the details regarding this choice will be provided and discussed in the Chapter III.

Table II-7 : Parameters and materials used for CCM manufacturing for 20 and 100 $\mu g_{Pt}.cm_{geo}^{-2}$ target loadings.

Cathode		**Membrane**	**Anode**		**Parameters**
Electrocatalyst	**Loading ($\mu g_{Pt}.cm_{geo}^{-2}$)**		**Electrocatalyst**	**Loading ($\mu g_{Pt}.cm_{geo}^{-2}$)**	
Pt/VC	20	Nafion®115	Pt/VC	100	*T* = 160°C *P* = 1 MPa *t* = 10 min
Pt_3Co/VC					
Pt/HSAC					
Pt/VC	100				
Pt/HSAC					

These specific hot decal-process parameters were chosen according to previous studies [25], [31] and cross-section SEM characterizations are done, these cross-section SEM measurements being used to check the homogeneity of the catalyst layers as well as the definition of the CL|PEM interface.

II.3.3.4 CCM characterization by cross-section imaging

The Figure II-14 shows some cross-section images performed with the FEG-SEM LEO 1530 from Zeiss for MEA made of Pt/VC and Pt/GC and with a catalyst loading of 90 $\mu g.cm_{geo}^{-2}$. To make the cross-section images, small squares of the CCM were embedded in a resin. After drying, the resin was polished until the CCM cross-sections were directly exposed to the smoothened surface. On this smooth surface, a carbon deposition was made to ensure the electronic conduction. The accelerating voltage was set to 10 kV, and secondary electrons were analysed by a detector above the sample in SE2 mode. On the images, the catalyst layers appear very homogenous and the CL|MB interfaces are well defined, which validates the hot decal-process parameters values.

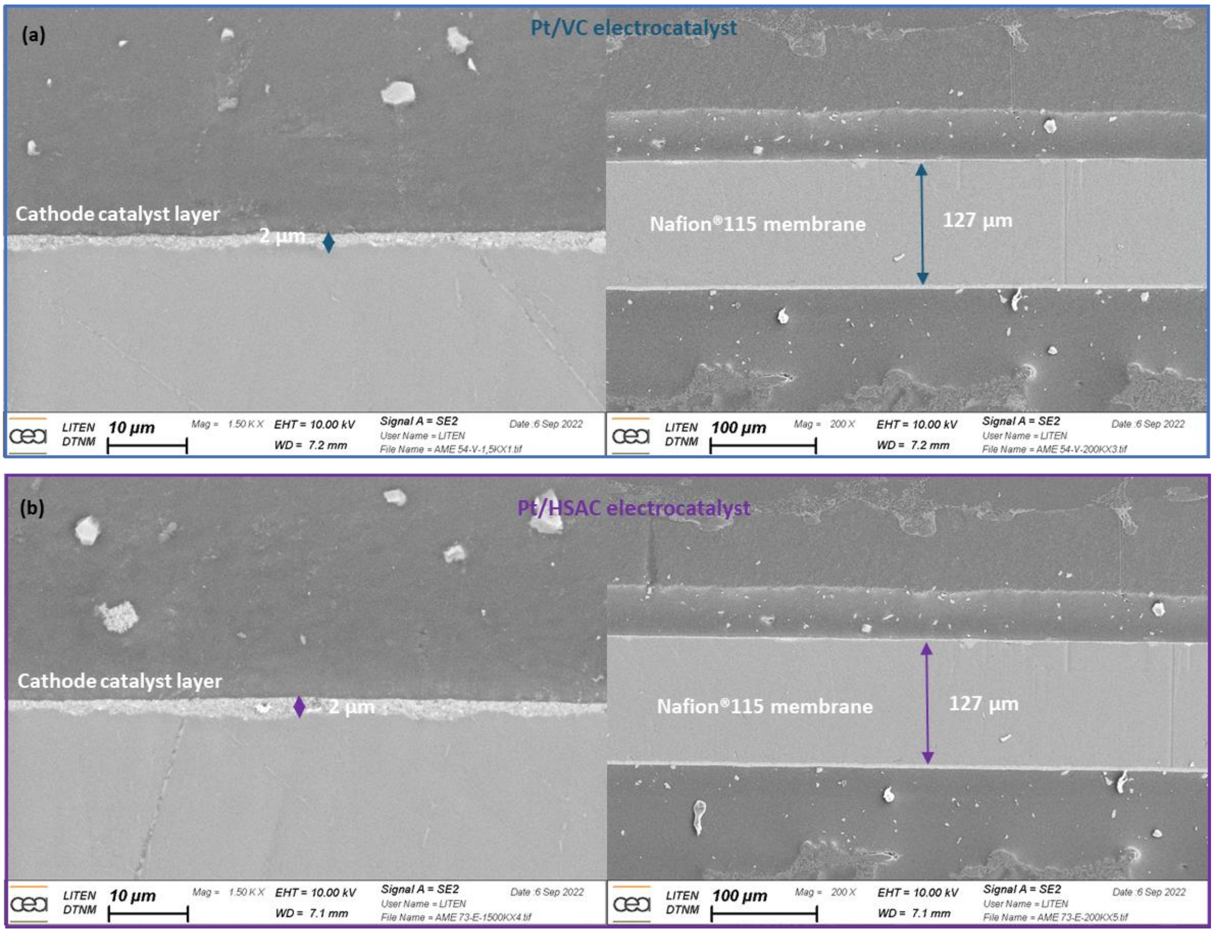

Figure II-14 : Cross-section SEM images of MEA made of (a) Pt/VC and (b) Pt/HSAC catalyst layers, both loaded at 90 $\mu g_{Pt}.cm_{geo}^{-2}$.

II.3.4 Electrochemical techniques and MEA characterizations

In this work, three electrochemical techniques are used to characterize the different MEA using the DC setup. The different electrochemical techniques are performed for the CCM from the FURTHER-FC project under various operating conditions: temperature (*T*), relative humidity (*RH*), and two different partial pressures of O_2 for each condition of *T* and *RH* that were chosen to be relevant for modeling part. As the different operating conditions for the electrochemical characterizations depend on the MEA considered, they will be reminded before each characterization shown in the Chapter III. The electrochemical techniques are performed using the software EC-lab® that drives the potentiostat and consist in:

1) A break-in step performed to reach the nominal performance of the MEA at the operating condition considered. This step is mandatory as it enables the good operation of the MEA and guarantees that the DC assembly was well done. It allows to reach the nominal performances of the MEA and to be sure that almost no evolution of the performance can occur during the characterization measurements, and make them the most relevant and reliable. The break-in step consists of a stationary cell operation at low cell voltage (0.1 V here) under H_2/O_2, for both 20 $\mu g_{Pt}.cm_{geo}^{-2}$ and 100 $\mu g_{Pt}.cm_{geo}^{-2}$ loadings and under H_2/O_2+N_2 (5% oxygen) for the CCM from FURTHER-

FC project, during 45 minutes. Such operation enables to reach the nominal performance of the cell as the production of water and the Pt oxides reduction/contaminant removal are enhanced, which is favourable to an efficient operation and activation of the cell.

2) Polarization curves under H_2/O_2 or H_2/Air configuration from OCV to 0.1 V by Cyclic Voltammetry (CV) to assess the electrochemical performances of the MEA under various operating conditions. Polarization curves are made by applying two consecutive scans the second one is considered and shown/processed in the further results. Indeed, MEA are very sensitive to the history of their characterization, so one must be cautious in the procedures. Thus, systematic conditioning under given operating conditions and the first polarization curve are carried to control their history, which makes the second polarization curve relevant at the operating condition considered.

3) Cyclic voltammetry under H_2/N_2 configuration are plotted to characterize the behaviour of the cathode from around 0.1 V (the actual low limit in voltage depends on the MEA tested) up to 1.2 V. As in RDE, the CV can be divided in three areas depending on the range of cell voltage (cathode potential). From 0.1 to 0.4 V the adsorption ($I < 0$) and desorption ($I > 0$) of protons on Pt nanoparticles occur in the H_{UPD} region. The region between 0.4 and 0.45 V is ascribed to a capacitive region where there is no faradic current generated by electrochemical reactions. In the potential range from 0.45 to 1.2 V, the Pt oxidation ($I > 0$) and Pt oxides reduction ($I < 0$) is described. The main difference with CV in RDE is the global shift of the CV towards positive current due to the H_2-crossover current (even present with a thicker Nafion® membrane). Three CV are carried out in a row at several potential sweep rates. The third scan will always be considered and shown/processed in the results. These characterizations are very similar to the ones performed in RDE configuration.

4) Electrochemical Impedance Spectroscopy (EIS) is performed to gather information about the impedance contributions. It measures the impedance of a system over a range of frequencies that leads to a specific response of the system according to the characteristic time response of the processes at stake. This technique is used to get insights into the proton resistances in the ionomer inside the membrane and the catalyst layer (e.g. Proton transport properties in the ionomer). The EIS measurements are performed at a specific voltage, which is set for 2 minutes, then frequencies from 100 kHz to 0.1 Hz are scanned under H_2/Air configuration and frequencies from 200 kHz to 0.1 Hz are scanned under H_2/N_2 configuration.

These electrochemical techniques are used to characterize all the MEA considered in this work. However, the operating conditions as well as the parameters of the different techniques may be adjusted depending on the MEA characterized. This information will be reminded before each experimental result shown hereafter. The Figure II-15 shows examples of these characterizations performed on the reference MEA from the FURTHER-FC project. This MEA has also been chosen as a reference in this work, which is representative of what can be used in real PEMFC system. In addition, this MEA is deeply characterized in the frame of this European project dedicated to the understanding of the cathode catalyst layer operation and limitation. The Figure II-15 (a) displays a polarization curve performed on this MEA under H_2/Air configuration at 80°C, 80/80% RH, 1.5 bar abs. and 10 mV.s^{-1}. This sweeping rate has been chosen because it has almost no impact on performance measurements between two consecutive sweeps and allows a decent measurement time (A study of the impact of the sweeping rate has been done but is not shown here). A similar hysteresis phenomenon, as in RDE setup, between the forward (in dashed line) and backward (in full line) sweeps is observed. From Figure II-15 (b), it is possible to assess the cathode ECSA value considering the desorption coulometry of proton in the same way as in RDE measurements. With the differential cell setup, CO-stripping measurements could not be achieved due to safety issue and a restricted access of the test bench allowing such measurements. On Figure II-15 (c) and (d), information on the different impedances over a range of frequencies of our system can be obtained by potentiostatic electrochemical impedance spectroscopy (PEIS) measurement under H_2/O_2+N_2 or H_2/N_2 configuration at different potential values. Data obtained via this technique are generally represented graphically in a Nyquist plot (e.g. -Im(Z) *vs.* Re(Z)) and allow to assess: the high frequency resistance of the system R_{HF}, which mainly gives information on the hydration state of the membrane (e.g. the protonic resistance in the membrane), the ohmic resistance of proton inside the catalyst layer $R_{H+,CL}$ and the charge transfer resistance R_{ct} that partly describes the kinetic of the ORR under operating atmosphere. In fact, proton and oxygen mass transport limitations may have an impact on the charge transfer resistance outside the activation potential region, at high potential, where mass transport limitations are negligible. Under H_2/N_2, R_{ct} describes the HOR due to H_2 permeation, but the PEIS is done at 0.4 V, which leads to non-relevant kinetic information due to limiting current (infinite impedance).

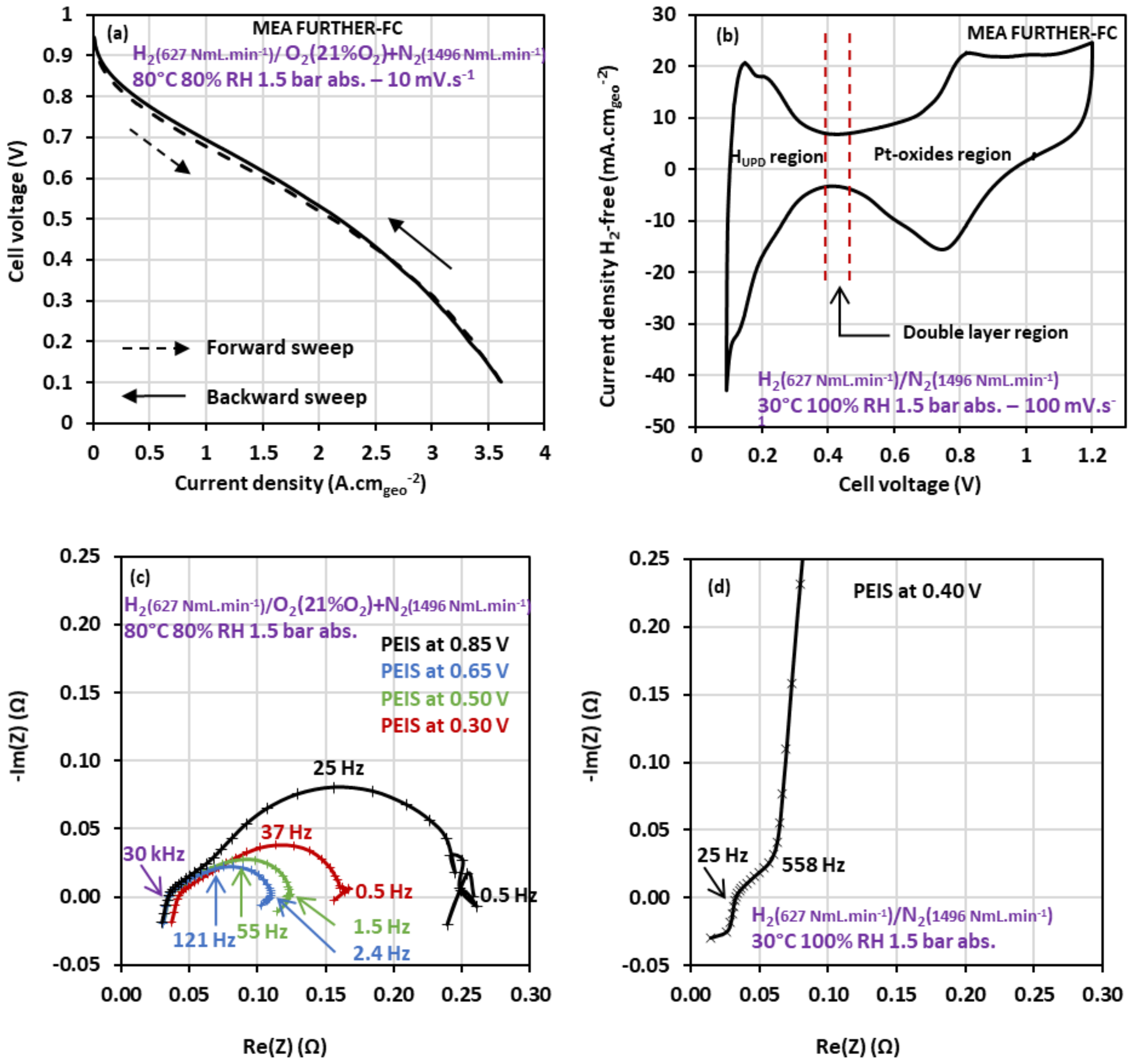

Figure II-15 : (a) Second sweep of polarization curve performed on FURTHER MEA from OCV to 0.1 V (b) Third cycle of cyclic voltammetry performed on FURTHER MEA from 0.09 V to 1.2 V corrected from H_2-crossover current (c) PEIS performed on FURTHER MEA at 0.3 V, 0.5 V, 0.65 V and 0.85 V from 100 kHz to 0.1 Hz (d) PEIS performed on FURTHER MEA at 0.4 V from 200 kHz to 0.1Hz (Only frequencies from 200 kHz to 16 Hz are displayed).

The software EC-lab® offers the possibility to fit the impedance spectra to estimate the values of these resistances, as shown on Figure II-16 (a) and (b). Basically, equivalent electrical circuits are used to describe the electrochemical behaviour of the PEMFC. Equivalent circuits are composed of electrical components (such as resistance, inductance, capacitor) disposed either in serial or in parallel mode. Another component is used to build the electrical circuit: the Warburg element W, that allows modeling the diffusion of electroactive species depending on limiting condition and that helps to describe the protonic transport in the catalyst layer. Depending on the gas configuration to perform the PEIS measurements, the electrical circuit will be modified to describe as well as possible the physical processes involved and to get the most relevant and reliable estimation of the different contributions. Between the two gas configurations, H_2/O_2+N_2 and H_2/N_2, the same components are used for the equivalent electrical circuit. In the case of H_2/O_2+N_2, the Warburg element is set in parallel with the components R_{ct} and C_{dl} (double layer capacity) that are used to describe the ORR. In fact, the ORR happens in the whole volume of the electrode simultaneously as the proton diffusion inside the electrode. These two processes take place at the same time, which is why these components are in parallel. Regarding the H_2/N_2 configuration, the Warburg element is set in serial with the components R_{ct} and C_{dl}. In fact, the proton electrochemical reaction on Pt is really fast, which leads to the assumption that the oxidation of H_2 that crosses the membrane, happens immediately at the membrane|catalyst layer interface. Thus, there is a first oxidation at this interface and then a motion of proton inside the volume of the catalyst layer [13]. The L element stands for the wire inductance at the highest frequencies. This being said, one can notice on the Figure II-16 (a) and (b) that, in both cases, the fits realised with the software EC-lab® and the corresponding electrical circuits agree with the experimental data at the frequencies considered. In fact, only the experimental frequencies that are relevant to make an accurate fit are considered. Under H_2/N_2 configuration, the very low frequencies are not taken into account as they prevent from having an accurate fit of the high frequencies linked to R_{HF} and $R_{H+,CL}$; under H_2/O_2+N_2 configuration, instabilities appear at very low frequencies, linked to slight stationary performance variations, which also hinders the accurate fitting of the high frequency region.

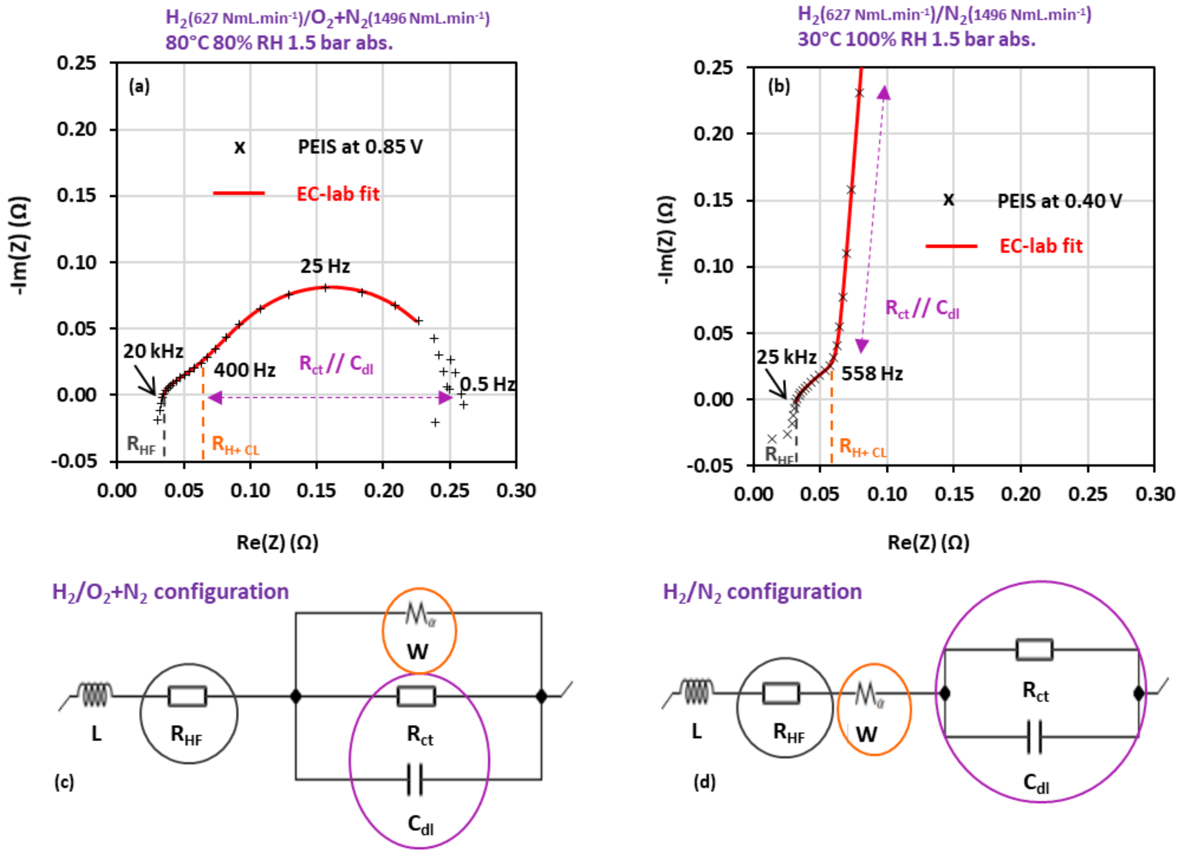

Figure II-16 : (a) Fit of the experimental PEIS performed on FURTHER MEA from 100 kHz to 0.1 Hz under H_2/O_2+N_2 configuration (b) PEIS performed on FURTHER MEA from 200 kHz to 0.1Hz (Only frequencies from 200 kHz to 16 Hz are displayed) (c) Equivalent electrical circuit used to fit the experimental PEIS under H_2/Air configuration (d) Equivalent electrical circuit used to fit the experimental EIS under H_2/N_2 configuration.

II.3 Differential Cell (DC) characterization setup

Cyclic voltammetry measurements under H_2/N_2 configuration can also give information on the Pt oxides formation/reduction reaction. The coulometry of these reactions can be used to have some qualitative insights on the coverage ratio of Pt surface oxides evolution θ_{PtOx_s} with potential during the CV measurement. Figure II-17 (a) shows the raw third cycle of CV performed on FURTHER MEA. This CV is slightly shifted towards positive current densities due to the H_2-crossover current, equal to 1.8 $mA.cm_{geo}^{-2}$ at 0.4 V in this case. The CV can be corrected from this oxidation current, assuming that the H_2-crossover current is constant in the range of potential considered and at such loading (200 $\mu g_{Pt}.cm_{geo}^{-2}$), by subtracting this constant oxidation current to the global CV: this leads to a CV centred around 0 $mA.cm_{geo}^{-2}$ at 0.4 V (Figure II-17 (b)). On the latter, at 0.4 V, two currents are noticeable: a positive double layer current and a negative one. Both of them can be subtracted to the CV corrected from H_2-crossover current, resulting in CV corrected, from the positive and negative double layer current at 0.4 V, as shown on Figure II-17 (c) and (d) respectively. These corrections are done in order to get rid of the capacitive current and have access to the dashed areas that correspond to Pt oxides formation ($I > 0$) and reduction ($I < 0$) coulometries between 0.4 and 1 V. This range of voltage has been chosen because, according to the work of Martens *et al.*, the Pt surface state is considered only covered by surface oxides corresponding to Pt^{+I} or Pt^{+II} as oxidation states, depending on the nature the surface oxides [32]. Indeed, a cell potential (cathode potential) of 1 V is not high enough for the place exchange phenomenon to occur. Moreover, below 0.4 V, the Pt surface is considered entirely reduced (Pt^0 state). By calculating the coulometries at each intermediate potential between 0.4 and 1 V (thanks to a trapeze method), and dividing them by the total coulometry of Pt oxides formation, or reduction, a qualitative coverage ratio of Pt surface oxides evolution with potential between 0.4 and 1 V can be obtained (Figure II-17 (e)). This evolution is qualitative because the nature of the surface oxides remains unknown. Between 0.4 and 0.75 V, the oxidation is quite slow, resulting is a slow increase of θ_{PtOx_s} with potential. From 0.75 to 1 V, the Pt surface is rapidly oxidized as witnessed by the fast increase in current on the CV above 0.75 V. On the reduction sweep, θ_{PtOx_s} exceeds 1, because of the positive dashed area between 1 and 0.9 V that may correspond to further formation of Pt oxides, and thus a delayed Pt oxides reduction reaction. Then θ_{PtOx_s} decreases fast with potential from 0.8 to 0.4 V, potential at which the Pt is entirely metallic. The presence of a hysteresis between the oxidation and reduction scans can be ascribed to the asymmetry of Pt oxides formation and Pt oxides reduction reactions in this range of potential. In other words, this hysteresis implies that Pt surface state is different for a given potential between the oxidation and reduction sweeps. This behaviour can partly contribute to the performance hysteresis observed during polarization curves. With such experimental measurements, it is not possible to have insights into the type and quantity of oxides formed. Thus, modeling Pt oxides formation/reduction is necessary and shall help to unravel the Pt surface state and evolution during fuel cell characterization and operation. This will be detailed in the chapter IV dealing with the modeling improvements.

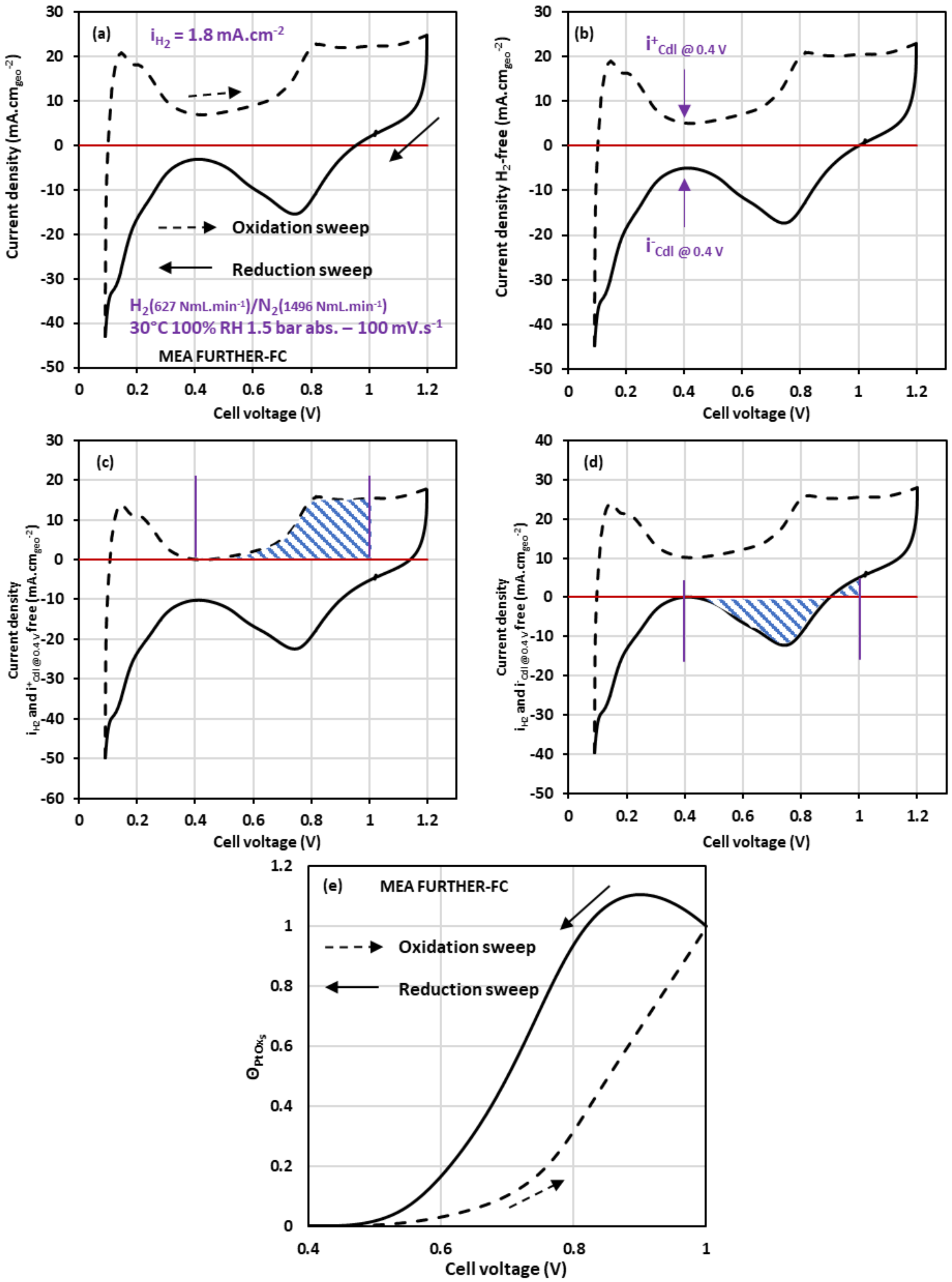

Figure II-17 : (a) Third cycle of cyclic voltammetry performed on FURTHER MEA from 0.09 V to 1.2 V (b) CV corrected from H_2-crossover current (c) CV corrected from H_2-crossover and positive double layer current (d) CV corrected from H_2-crossover and negative double layer current (e) Evolution of the qualitative coverage ratio of Pt surface oxides with cell voltage.

In this experimental study, a third electrochemical setup has been used to conduct the same characterization: the Gas Diffusion Electrode [33]. Basically, the electrode is put at the liquid electrolyte|gas interface, enabling realistic mass transport with triple phase interface of fuel cell configuration while keeping the fundamental aspects of the RDE setup. The Gas Diffusion Electrode setup allows to overcome the mass transport limitation of dissolved O_2 in liquid electrolyte for RDE and to reach much higher current density between *ca.* 0.1 - 1 $A.cm_{geo}^{-2}$. Moreover, GDE setup remains simple and cheap in terms of lab facilities and of quantity of raw catalyst (or catalyst layer) needed. The measurements are also fast and show comparable features to the RDE measurements. The whole comparative electrochemical setup study has been done in collaboration with Raphaël Riasse, who is also a PhD student at LEPMI in Grenoble and Dr. Clémence Lafforgue, a post-doc, who worked with us in the frame of the OPTIPEM project funded by Carnot Institute “Energies du future”. One purpose of this project was to unravel the way to conduct specific experiments with the transition from one electrochemical setup to another and to confront the limitation of the different setups. It is currently in the process of being published, but GDE data will not be presented herein.

II.4 Conclusion

Depending on the electrocatalyst (mostly the type of carbon) considered and the loading targeted, the ink formulation as well as the deposit methods need to be adjusted in order to manufacture in the most reproducible way as homogeneous CL as possible. In this work, we used the hot decal process to manufacture the CCM. The different parameters of the process were determined and optimized thanks to a rigorous quality control work. For each catalyst layer manufactured, Pt loading and layer homogeneity were validated thanks to XRF measurements (and microscopy measurements with relevant for CL|MB interface observation) before electrochemical characterizations. Indeed, it is mandatory to control the CL composition to make the link between the microstructure of CL and the performance measured. On the whole, by coupling optimized coating processes and quality control, we are able to control the composition of our MEA, which is very important for the understanding of the catalyst layer and electrocatalyst operation, as well as for specific needs for experiments/modeling. As this work focuses on the understanding of electrocatalyst and catalyst layer operation, all the characterizations using RDE or DC setup are made in order to gather as much information as possible on electrocatalyst from raw material to their use in catalyst layer in configuration representative of the real PEMFC system. Now that the description of the objects and methods has been done, the different electrochemical results are shown in the next chapter.

References of Chapter II

[1] S. Shahgaldi, I. Alaefour and X. Li, “Impact of manufacturing processes on proton exchange membrane fuel cell performance,” *Appl. Energy*, vol. 225, pp. 1022–1032, Sep. 2018, doi: 10.1016/j.apenergy.2018.05.086.

[2] S. Shahgaldi, I. Alaefour, J. Zhao and X. Li, “Impact of ionomer in the catalyst layers on proton exchange membrane fuel cell performance under different reactant flows and pressures,” *Fuel*, vol. 227, pp. 35–41, Sep. 2018, doi: 10.1016/j.fuel.2018.04.076.

[3] Y. Garsany, J. Ge, J. St-Pierre, R. Rocheleau and K. E. Swider-Lyons, “Analytical Procedure for Accurate Comparison of Rotating Disk Electrode Results for the Oxygen Reduction Activity of Pt/C,” *J. Electrochem. Soc.*, vol. 161, no. 5, pp. F628–F640, 2014, doi: 10.1149/2.036405jes.

[4] D. Banham and S. Ye, “Current Status and Future Development of Catalyst Materials and Catalyst Layers for Proton Exchange Membrane Fuel Cells: An Industrial Perspective,” *ACS Energy Lett.*, vol. 2, no. 3, pp. 629–638, Mar. 2017, doi: 10.1021/acsenergylett.6b00644.

[5] C. Chen, Y. Kang, Z. Huo, Z. Zhu, W. Huang, H. L. Xin, J. D. Snyder, D. Li, J. A. Herron, M. Mavrikakis, M. Chi, K. L. More, Y. Li, N. M.Markovic, G. A. Somorjai, P. Yang and V. R. Stamenkovic, “Highly Crystalline Multimetallic Nanoframes with Three-Dimensional Electrocatalytic Surfaces,” *Science*, vol. 343, no. 6177, pp. 1339–1343, Mar. 2014, doi: 10.1126/science.1249061.

[6] X. Wang, Z. Li, Y. Qu, T. Yuan, W. Wang, Y. Wu and Y. Li, “Review of Metal Catalysts for Oxygen Reduction Reaction: From Nanoscale Engineering to Atomic Design,” *Chem*, vol. 5, no. 6, pp. 1486–1511, Jun. 2019, doi: 10.1016/j.chempr.2019.03.002.

[7] A. Ly, T. Asset and P. Atanassov, “Integrating nanostructured Pt-based electrocatalysts in proton exchange membrane fuel cells,” *J. Power Sources*, vol. 478, p. 228516, Dec. 2020, doi: 10.1016/j.jpowsour.2020.228516.

[8] Y. Garsany, I. L. Singer, K. E. Swider-Lyons, “Impact of film drying procedures on RDE characterization of Pt/VC electrocatalysts,” *J. Electroanal. Chem.*, vol. 662, no. 2, pp. 396–406, Nov. 2011, doi: 10.1016/j.jelechem.2011.09.016.

[9] Y. Garsany, Ol. A. Baturina, K. E. Swider-Lyons and S. S. Kocha, “Experimental Methods for Quantifying the Activity of Platinum Electrocatalysts for the Oxygen Reduction Reaction,” *Anal. Chem.*, vol. 82, no. 15, pp. 6321–6328, Aug. 2010, doi: 10.1021/ac100306c.

[10] H. A. Gasteiger, S. S. Kocha, B. Sompalli and F. T. Wagner, “Activity benchmarks and requirements for Pt, Pt-alloy, and non-Pt oxygen reduction catalysts for PEMFCs,” *Appl. Catal. B Environ.*, vol. 56, no. 1, pp. 9–35, Mar. 2005, doi: 10.1016/j.apcatb.2004.06.021.

[11] F. Maillard, M. Eikerling, O. V. Cherstiouk, S. Schreier, E. Savinova and U. Stimmina, “Size effects on reactivity of Pt nanoparticles in CO monolayer oxidation: The role of surface mobility,” *Faraday Discuss.*, vol. 125, p. 357, 2004, doi: 10.1039/b303911k.

[12] B. Andreaus, F. Maillard, J. Kocylo, E. R. Savinova, and M. Eikerling, "Kinetic Modeling of CO_{ad} Monolayer Oxidation on Carbon-Supported Platinum Nanoparticles," *J. Phys. Chem. B*, vol. 110, no. 42, pp. 21028–21040, Oct. 2006, doi: 10.1021/jp063856k.

[13] M. Fontana, "Tapis de nanotubes de carbone structurés comme nouveau microporeux pour couche de diffusion de gaz des piles à combustible," Thèse, Université Grenoble Alpes, CEA Grenoble, 2021. [Online]. Available: https://tel.archives-ouvertes.fr/tel-03256127

[14] A. C. Olesen, T. Berning and S. K. Kær "The Effect of Inhomogeneous Compression on Water Transport in the Cathode of a Proton Exchange Membrane Fuel Cell," *J. Fuel Cell Sci. Technol.*, vol. 9, no. 3, p. 031010, Jun. 2012, doi: 10.1115/1.4006475.

[15] I. Nitta, S. Karvonen, O. Himanen and M. Mikkola, "Modelling the Effect of Inhomogeneous Compression of GDL on Local Transport Phenomena in a PEM Fuel Cell," *Fuel Cells*, vol. 8, no. 6, pp. 410–421, Dec. 2008, doi: 10.1002/fuce.200700058.

[16] A. Bertei, V. Yufit, F. Tariq and N.P. Brandon, "A novel approach for the quantification of inhomogeneous 3D current distribution in fuel cell electrodes," *J. Power Sources*, vol. 396, pp. 246–256, Aug. 2018, doi: 10.1016/j.jpowsour.2018.06.029.

[17] T. Hottinen and O. Himanen, "PEMFC temperature distribution caused by inhomogeneous compression of GDL," *Electrochem. Commun.*, vol. 9, no. 5, pp. 1047–1052, May 2007, doi: 10.1016/j.elecom.2006.12.018.

[18] "FURTHER-FC project - Objectives." https://further-fc.eu/ABOUT-FURTHER-FC/OBJECTIVES/

[19] T. Carine and C. Nayouze-Coynel, "Improvement of active layers homogeneity for the MEA's (Membrane Electrode Assembly) of PEMFC (Proton Exchange Membrane Fuel Cell): impact of the ink quality formulation," *Nanomater. Sci. Eng.*, pp. 135-143 Páginas, Sep. 2020, doi: 10.34624/NMSE.V2I3.19554.

[20] F. Afsahi, F. Mathieu-Potvin and S. Kaliaguine, "Impact of Ionomer Content on Proton Exchange Membrane Fuel Cell Performance," *Fuel Cells*, vol. 16, no. 1, pp. 107–125, 2016, doi: 10.1002/fuce.201500138.

[21] T. Van Cleve, S. Khandavalli, A. Chowdhury, S. Medina, S. Pylypenko, M. Wang, K. L. More, N. Kariuki, D. J. Myers, A. Z. Weber, S. A. Mauger, M. Ulsh and K. C. Neyerlin, "Dictating Pt-Based Electrocatalyst Performance in Polymer Electrolyte Fuel Cells, from Formulation to Application," *ACS Appl. Mater. Interfaces*, vol. 11, no. 50, pp. 46953–46964, Dec. 2019, doi: 10.1021/acsami.9b17614.

[22] D. Li, Y. T. Pan, X. Wang, C. Wang, Y. S. Kim and J. S. Spendelow, "Effect of the Catalyst Metal Content on PEMFC Durability," *ECS Trans.*, vol. 92, no. 8, p. 589, Jul. 2019, doi: 10.1149/09208.0589ecst.

[23] R. Sharma and S. Ma Andersen, "Zoom in Catalyst/Ionomer Interface in Polymer Electrolyte Membrane Fuel Cell Electrodes: Impact of Catalyst/Ionomer Dispersion Media/Solvent," *ACS Appl. Mater. Interfaces*, vol. 10, no. 44, pp. 38125–38133, Nov. 2018, doi: 10.1021/acsami.8b14622.

[24] M. Chen, C. Zhao, F. Sun, J. Fan, H. Li and H. Wang, “Research progress of catalyst layer and interlayer interface structures in membrane electrode assembly (MEA) for proton exchange membrane fuel cell (PEMFC) system,” *eTransportation*, vol. 5, p. 100075, Aug. 2020, doi: 10.1016/j.etran.2020.100075.

[25] M. Grandjean, “Optimisation du transfert des couches actives pour PEMFC,” ENSCM, CEA Grenoble, Stage, 2020.

[26] S. A. Mauger, J. R. Pfeilsticker, M. Wang, S. Medina, A. C. Yang-Neyerlin, K. C. Neyerlin, C. Stetson, S. Pylypenko and M. Ulsh, “Fabrication of high-performance gas-diffusion-electrode based membrane-electrode assemblies,” *J. Power Sources*, vol. 450, p. 227581, Feb. 2020, doi: 10.1016/j.jpowsour.2019.227581.

[27] Indriyati, Y. Irmawati and B. Prihandoko, “Preparation of catalyst coated membrane by modified decal transfer method for proton exchange membrane fuel cell,” *IOP Conf. Ser. Mater. Sci. Eng.*, vol. 223, p. 012037, Jul. 2017, doi: 10.1088/1757-899X/223/1/012037.

[28] S. Shahgaldi, I. Alaefour, G. Unsworth and X. Li, “Development of a low temperature decal transfer method for the fabrication of proton exchange membrane fuel cells,” *Int. J. Hydrog. Energy*, vol. 42, no. 16, pp. 11813–11822, Apr. 2017, doi: 10.1016/j.ijhydene.2017.02.127.

[29] S. H. Akella, E. D., S. S. R. S., A. Ahire and N. K. Mal, “Studies on structure property relations of efficient decal substrates for industrial grade membrane electrode assembly development in pemfc,” *Sci. Rep.*, vol. 8, no. 1, p. 12082, Dec. 2018, doi: 10.1038/s41598-018-30215-0.

[30] T. Suzuki, H. Tanaka, M. Hayase, S. Tsushima and S. Hirai, “Investigation of porous structure formation of catalyst layers for proton exchange membrane fuel cells and their effect on cell performance,” *Int. J. Hydrog. Energy*, vol. 41, no. 44, pp. 20326–20335, Nov. 2016, doi: 10.1016/j.ijhydene.2016.09.078.

[31] P. Toudret, “Optimisation du procédé de transfert pour électrode de pile à combustible PEMFC,” INSA Lyon, CEA Grenoble, Stage, 2018.

[32] I. Martens, R. Chattot, M. Rasola, M. Valeria Blanco, V. Honkimäki, D. Bizzotto, D. P. Wilkinson and J. Drnec, “Probing the Dynamics of Platinum Surface Oxides in Fuel Cell Catalyst Layers Using in Situ X-ray Diffraction,” *ACS Appl. Energy Mater.*, vol. 2, no. 11, pp. 7772–7780, Nov. 2019, doi: 10.1021/acsaem.9b00982.

[33] M. Inaba, A. W. Jensen, G. W. Sievers, M. Escudero-Escribano, A. Zana and M. Arenz, “Benchmarking high surface area electrocatalysts in a gas diffusion electrode: measurement of oxygen reduction activities under realistic conditions,” *Energy Environ. Sci.*, vol. 11, no. 4, pp. 988–994, 2018, doi: 10.1039/C8EE00019K.

Chapter III Experimental results and database for modeling

This chapter deals with the different experimental results for Rotating Disk Electrode and Differential Cell measurements performed on all the electrocatalysts and MEA considered in this work. These experiments were conducted in order to better understand the electrocatalytic properties of the four state-of-art carbon-supported Pt-based materials presented previously (Chapter II) by making the link between their physico-chemical properties and their electrochemical features. The ECSA, the surface and mass activities were obtained thanks to both electrochemical setups. In addition to comparing these features between all the electrocatalysts, the relevance of the electrochemical setups including the choice of operating conditions, the electrochemical techniques, the materials used for the electrochemical characterizations in fuel cell configuration (DC) but also the way to process data will be discussed. This last point is also investigated in collaboration with Raphaël Riasse, a Ph.D student at LEPMI in Grenoble and Dr. Clémence Lafforgue who is also working on the topic at LEPMI Grenoble. The study includes another electrochemical setup: the Gas Diffusion Electrode (GDE) [1], in which the electrode is put at the liquid electrolyte|gas interface, enabling realistic mass transport with triple-phase interface of fuel cell configuration, while keeping the fundamental aspects of the RDE setup. The will to better understand how the catalyst operates in catalyst layer is also motivated by modeling. The experimental data deserve to feed the model, thereby improving its physico-chemical and electrochemical description of the catalyst layer upon fuel cell operation. In that frame, the impact of operating conditions on the behaviour of the Pt/VC and Pt/HSAC electrocatalysts is particularly evaluated, especially in the Pt oxides region, whose influence on fuel cell performance is not always described (or even captured) in models. It is firstly done on very low loaded catalyst layer (20 $\mu g_{Pt}.cm_{geo}^{-2}$), such low loading being used to (ideally) get rid of mass transport issues (proton and oxygen transport) in the catalyst layer. Then, more realistic catalyst layers loaded at 100 $\mu g_{Pt}.cm_{geo}^{-2}$ are characterized to include mass transport features and to better understand the impact of loading on catalyst layer operation. Finally, in the fourth chapter of the thesis, a performance model will be developed, calibrated and validated by comparing simulation to experiment.

III.1 Electrocatalysts intrinsic properties

This section focuses on the results obtained with the electrochemical RDE setup. For all the electrocatalysts studied, the electrochemical surface area, the mass and specific activities, assessed at room temperature, will be measured and discussed. The fuel cell configuration usually operates with these Pt-based materials at higher temperature (60-80°C). In that frame, a temperature study has been performed to get insights into the (possible) evolution of the catalyst intrinsic properties with temperature in order to be closer to fuel cell configuration operating conditions. Thus, ECSA and electrocatalysts’ activities are also assessed at 60°C.

III.1.1 CO-stripping measurements and ECSA assessment

III.1.1.1 Impact of temperature on the ECSA assessed by CO oxidation

Depending on the electrocatalyst nature (Pt particle size distribution, type of carbon support and nature of metal catalyst) the electrochemical response of the CO_{ad} oxidation monitored can vary. The Figure III-1 shows the CO-stripping measurements for the Pt-based materials performed at 25°C. The first observations will focus on the first sweep of the cyclic voltammetry. The second and third sweeps (dashed lines) being used as baseline to assess the ECSA. The main CO_{ad} oxidation peak is centered around 0.8 V *vs.* RHE for all the electrocatalysts. Slight shifts in this peak potential can be observed; they depend on the particle size, larger sized Pt particles leading to lower peak potential [2], [3]. When the particles are fully isolated (not agglomerated), the nanoparticle size distribution also accounts for the width of the CO_{ad} oxidation peak. The more heterogeneous is the particle size distribution, the wider is the CO_{ad} oxidation peak including 'tailing' effect: the end of the CO_{ad} oxidation occurs at potential above 1 V *vs.* RHE due to very small Pt particles as it is the case for Pt/HSAC electrocatalyst. The presence of Pt agglomeration/surface defects also induces a pre-peak, at lower potential (around 0.65 - 0.70 V *vs.* RHE on Figure III-1), as Pt grain boundaries favour fast CO_{ad} oxidation [4]. It is assumed herein, that the same trends are also valid for Pt alloyed particles, hence for the Pt_3Co/VC catalyst [5].

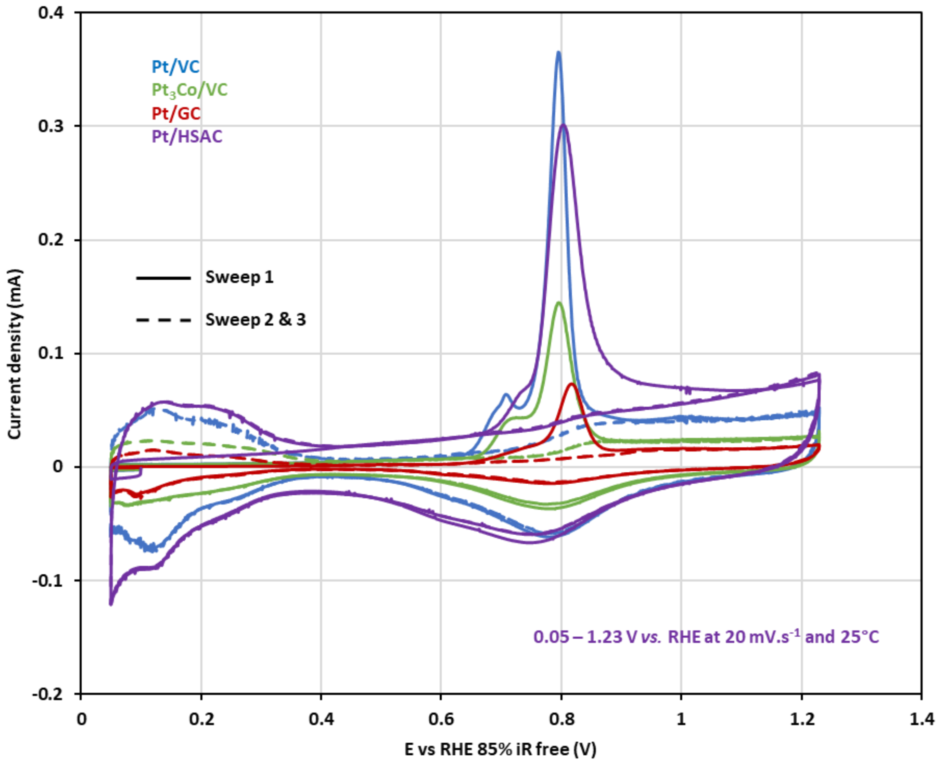

Figure III-1 : CO-stripping measurements performed at room temperature for all the electrocatalysts in $HClO_4$ 0.1 M Ar saturated electrolyte.

CO-stripping measurements were also performed at 60°C in order to investigate the impact of temperature on the ECSA value. Figure III-2 displays the characterizations performed for all the electrocatalysts with the measurements at 60°C plotted in lighter lines. The peak related to CO_{ad} oxidation is shifted towards lower potential, around 0.65 V *vs.* RHE; it is very well defined and thinner than the peak obtained at 25°C; this observation is made for all the electrocatalysts. The shift in potential is ascribed to much faster CO_{ad} oxidation kinetics at 60 than at 25°C, likely owing to easier formation of OH_{ad} species of Pt surfaces at elevated temperatures. In addition, the electrochemical Pt size distribution/Pt agglomeration signature regarding CO_{ad} oxidation is less noticeable at elevated temperature, the beneficial effects of defective sites (agglomeration) or of larger Pt particles being overwhelmed by the larger overall CO_{ad} oxidation kinetics at 60°C.

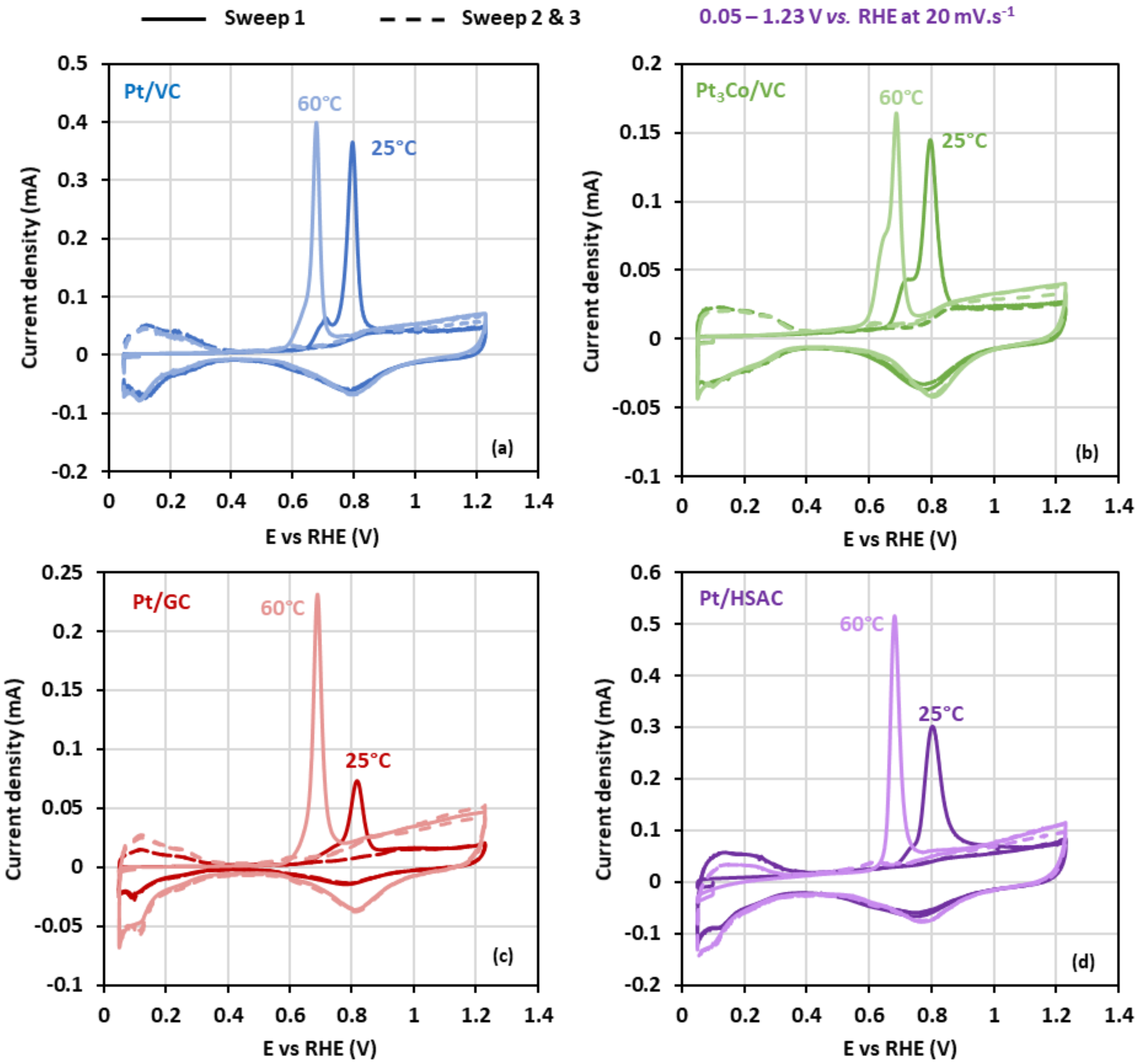

Figure III-2 : CO-stripping measurements performed at 25°C and 60°C for (a) Pt/VC, (b) Pt_3CO/VC, (c) Pt/GC and (d) Pt/HSAC in $HClO_4$ 0.1 M Ar saturated electrolyte.

As detailed in the Chapter II, the coulometry of CO_{ad} oxidation is then used to assess the ECSA of the Pt-based materials at 25 and 60°C, as summarized in the Table III-1.

Table III-1 : ECSA assessed by CO-stripping for the electrocatalysts at 25°C and 60°C

Electrocatalyst	**ECSA CO-stripping ($m^2_{Pt}.g^{-1}_{Pt}$)**	
	25°C	**60°C**
Pt/VC	**49 ± 3**	**47 ± 2**
Pt_3Co/VC	**28 ± 2**	**25 ± 1**
Pt/GC	**16 ± 3**	**22 ± 5**
Pt/HSAC	**67 ± 2**	**58 ± 1**

Table III-1 firstly shows that the values obtained in this work at 25°C are in the same order of magnitude as those obtained by other groups, except for the Pt/GC electrocatalyst [6]–[8]. In fact, the Pt/GC ink is quite difficult to formulate and deposits on the glassy carbon tip were not as controlled as for the other electrocatalysts, which also results in larger dispersion of the results for this catalyst. In addition, graphitized carbon being more hydrophobic, wettability issues may explain the very low ECSA value obtained at 25°C (the active layer of Pt/GC may not be fully wetted, hence accessible, by the electrolyte). For Pt/VC, Pt_3Co/VC and Pt/HSAC, the differences (up to 20% [6], [8]) between literature and this work may come from the ink composition, the ink dispersion protocol, the Pt loading, the operating conditions or the ECSA assessment method. Regarding the temperature impact on ECSA, it seems that an increase of temperature leads to a decrease of ECSA. One likely explanation, could be that at 60°C, owing to the better activity of Pt-based catalysts to oxidize CO_{ad} (see Figure III-2), the monolayer of CO_{ad} normally formed at 0.1 V *vs*. RHE may not be complete (or some of it may be eliminated/desorbed during the 39 min of Ar purge). However, this is not observed for the Pt/GC electrocatalyst; in that case, an increase of temperature could lead to a better wettability of the graphitized carbon with more accessible fraction of the active layer for CO_{ad} formation and thus oxidation. Finally, Pt/GC sets aside, the maximum dispersion for each ECSA values is about 7% for all the electrocatalysts, which demonstrates that CO-stripping measurement is a relevant and reliable technique to assess the ECSA.

III.1.1.2 Impact of temperature on the ECSA assessed by proton desorption

The ECSA can also be assessed via the protons desorption coulometry in the H_{UPD} region. Figure III-3 shows the third sweep of cyclic voltammetries from CO-stripping measurements performed at 25°C, from which the H_{upd} ECSA values were determined. Here again, depending on the electrocatalyst nature, the electrochemical response is different. For instance, the nature of the carbon support of the Pt particles influences the double layer capacity value, as the latter depends on the fraction of the active layer seen by the electrolyte (which may not be complete for Pt/GC) and on the developed area of the carbon support (BET area): the larger the interface Pt/C electrode|electrolyte, the higher the current related to the double layer capacity on Figure III-3. In the H_{UPD} region, the proton desorption coulometry also varies depending on the nature of the Pt/C electrode, leading to different ECSA values; indeed Pt and alloyed Pt do not bind H_{ad} species in a similar manner, the presence of Co (in Pt_3Co/VC) depreciating the affinity of H_{ad} to the catalyst surface [5]. Finally, at higher potential, in the Pt-oxides region, the specific peaks related to Pt oxidation and Pt oxides reduction are monitored at potential around 0.8 V *vs.* RHE. As for CO_{ad} oxidation peak, the position of the peaks can be slightly shifted towards positive or negative potential depending on the Pt size distribution and structure, as well as in the presence of alloying element (in Pt_3Co/VC).

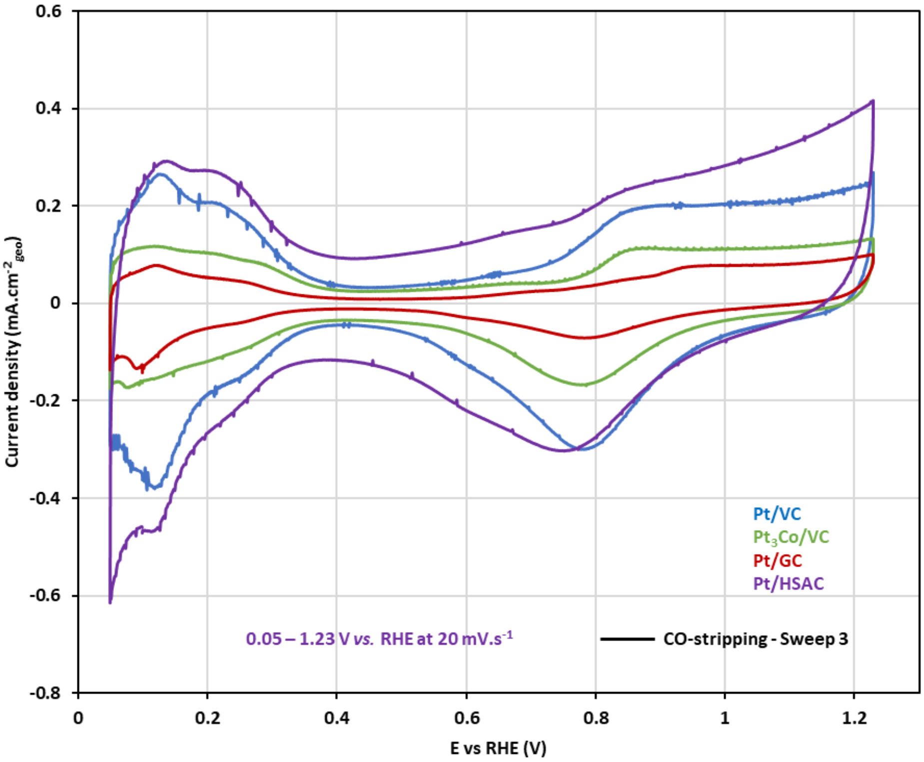

Figure III-3 : Third sweep of CO-stripping measurements for all the electrocatalysts in $HClO_4$ 0.1 M Ar saturated electrolyte.

The Figure III-4 shows the impact of temperature on the third sweep of CO-stripping measurements for the electrocatalysts. On all the graphs, a clear oxidation peak is observed at 0.6 V *vs.* RHE on voltamogramms obtained at 60°C. This peak is ascribed to quinone/hydroquinone groups, relative to the initiation of carbon support oxidation [9]. These groups can also be observed at 25°C around 0.7 V *vs.* RHE as it is the case for the Pt_3Co/VC electrocatalyst, with the presence of an oxidation peak around this potential. An increase of temperature seems to promote the carbon surface oxidation (functionalization), as revealed by the rise of quinone/hydroquinone groups. The presence of such oxygenated species at 60°C is a sign of the faster initial steps of carbon corrosion at elevated temperature and enables to understand the observed CO_{ad} oxidation reaction promotion at 60°C [9]–[11]. A slight shoulder is also observed at 0.7 V *vs.* RHE à 60°C, which is probably due to the oxidation of the CO groups formed, which are oxidised on or near Pt sites [12]. Regarding the H_{UPD} region, for Pt/VC and Pt_3Co/VC electrocatalysts, the temperature increase leads to smaller proton desorption coulometry and thus, a decrease of the ECSA value (keeping 210 $\mu C.cm_{Pt}^{-2}$). The coulometry of proton desorption of the Pt/HSAC electrocatalyst seems to be lowered by the temperature increase. For Pt/GC, the improved wettability of the graphitized carbon due to the increase of temperature leads to more active sites available for electrochemical reactions in the H_{UPD} region but also in the Pt-oxides region. For all the electrocatalysts, the increase of temperature promotes the Pt oxides formation/reduction reactions leading to bigger coulometry monitored in the Pt oxides region at high potential. In addition, the onset Pt oxidation potential is lowered and the Pt oxides reduction peak is shifted towards positive potential.

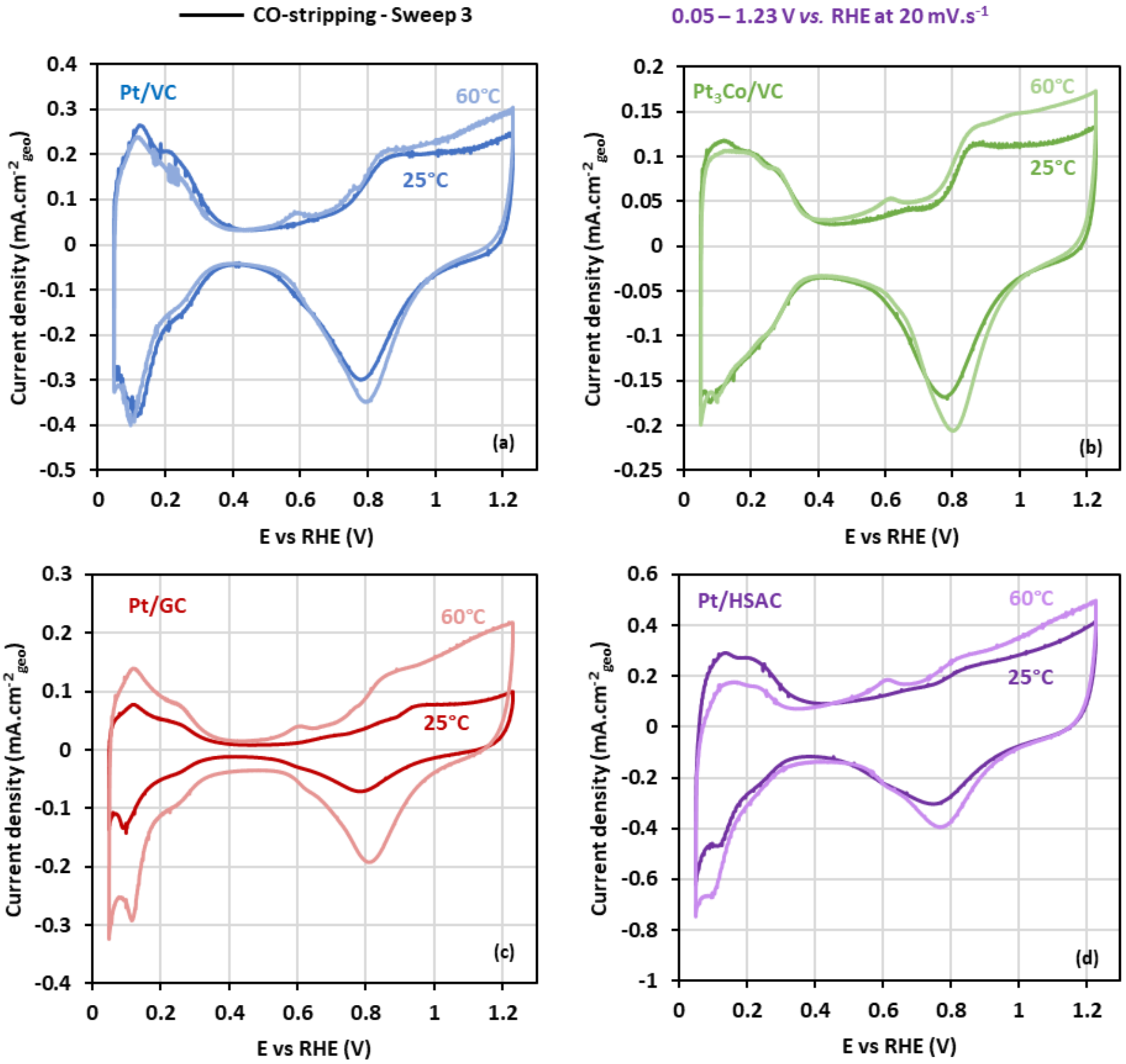

Figure III-4 : Third sweep of CO-stripping measurements performed at 25°C and 60°C for (a) Pt/VC, (b) Pt$_3$CO/VC, (c) Pt/GC and (d) Pt/HSAC in HClO$_4$ 0.1 M Ar saturated electrolyte.

The ECSA values and their dispersion obtained via the proton desorption coulometry at 25 and 60 °C are summarized in the Table III-2. As for the CO-stripping method, the increase of temperature leads to lower ECSA value except for Pt/GC electrocatalyst and the specific coulometry value on bulk Pt (25°C/liquid electrolyte) considered for proton desorption may not be strictly equal to 210 µC.cm_{Pt}^{-2} at 60°C. The values obtained at 25°C are similar to those obtained via CO-stripping measurements. However, Pt/GC sets aside, the minimum dispersion obtained for both temperatures is around 18% with this measurement method. This means that, in liquid electrolyte, using the proton desorption coulometry is less reliable to assess the ECSA value of electrocatalyst than the CO_{ad} oxidation coulometry, as also noted in the work of Dubau *et al.* [5].

Table III-2 : ECSA assessed by H_{UPD} for the electrocatalysts at 25°C and 60°C.

Electrocatalyst	ECSA H_{UPD} ($m^2_{Pt}.g^{-1}_{Pt}$)	
	25°C	60°C
Pt/VC	**54 ± 11**	**37 ± 7**
Pt_3Co/VC	**28 ± 6**	**23 ± 8**
Pt/GC	**14 ± 4**	**24 ± 1**
Pt/HSAC	**66 ± 13**	**48 ± 9**

III.1.2 ORR polarization curve measurements

III.1.2.1 Electrocatalyst activity measurements at 25°C

Figure III-5 displays the ORR polarization curves obtained at a WE rotation speed of 1600 rpm for all the electrocatalysts. All the curves shown are 100% ohmic drop and capacitive current corrected. Both forward (positive sweep, continuous line) and backward (negative sweep, dashed line) sweeps are shown: they highlight that different performances are observed for the electrocatalysts above 0.6 V *vs.* RHE, depending on the potential sweep direction. This range of potential corresponds to the Pt-oxides region, the latter being partly responsible of the hysteresis observed experimentally. The width of the hysteresis appears to be different according to the nature of the electrocatalyst: the width of the hysteresis of the Pt/VC is smaller than the other Pt/C electrodes, meaning that the Pt oxides formation/reduction kinetics must differ depending on the Pt/C electrode nature. At potential lower than 0.5 V *vs.* RHE, a well-defined diffusion limiting current is observed. According to the Levich equation (see Equation II-4), the theoretical value of the diffusion limiting current should be the same regardless the nature of the electrocatalyst, which is not the case here. The differences may come geometrical effects (e.g. an electrode film that not entirely covers the glassy carbon tip). At potential around 0.2 V *vs.* RHE, the reduction current ascribed to the ORR reaction is decreasing for the Pt/GC electrocatalyst. Such potential corresponds to the H_{UPD} region and the proton adsorption on Pt leads to less available Pt sites for the ORR reaction and/or to a change of ORR mechanism from 4 to 2 electron pathway, which is classical for Pt surfaces [13].

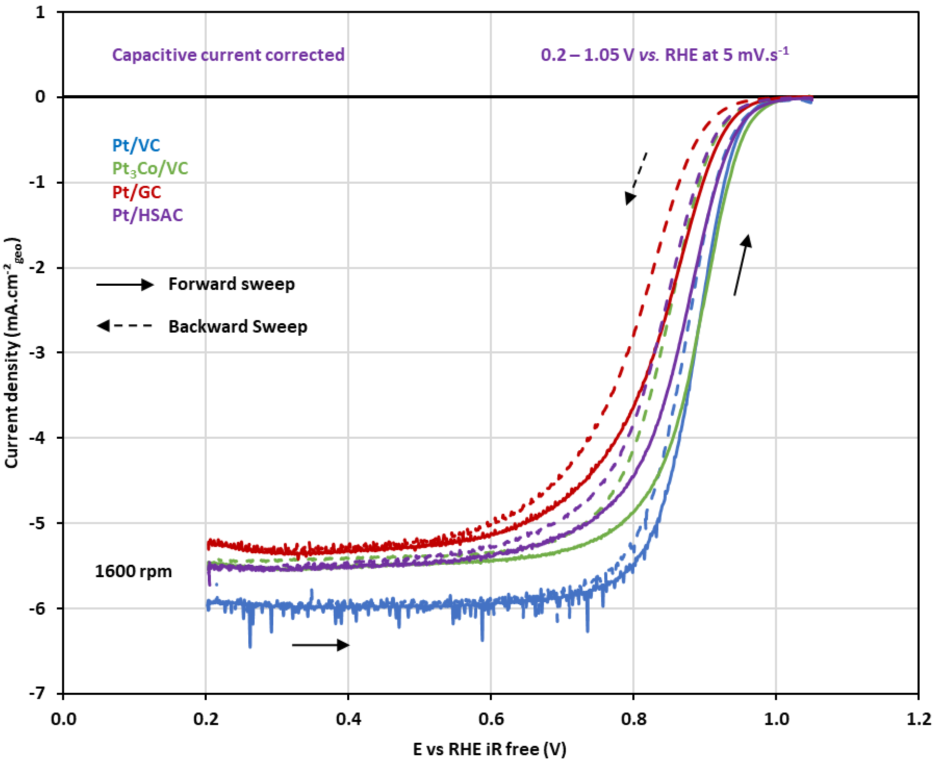

Figure III-5 : ORR polarization curve measurements performed at 25°C for all the electrocatalysts in $HClO_4$ 0.1 M O_2 saturated electrolyte.

III.1.2.2 Impact of temperature on electrocatalyst activity measurements

The impact of the temperature on ORR measurements and electrocatalysts activities was also investigated. Figure III-6 shows the ORR polarization curves performed at 25 and 60°C for all the electrocatalysts. For all materials, the temperature increase enhances the Pt oxides reduction and the Pt oxidation reaction. On all graphs, the hysteresis related to Pt-oxides formation/reduction appears to be thinner in 0.6 – 0.8 V *vs.* RHE potential range at 60°C compared to 25°C, meaning that most of the Pt oxides are reduced at higher potential. Regarding the Pt oxidation reaction, the trend is not so clear but it seems that the onset potential of Pt oxidation is shifted negatively. Nevertheless, these trends are consistent with the negative shift of the onset CO_{ad} oxidation potential observed on Figure III-2, which implies the formation of PtOH species to oxidize the adsorbed CO. It is also consistent with the observations made on the positive shift of the specific peak related to the Pt oxides reduction and the negative shift of the onset Pt oxidation reaction potential during cyclic voltammetries in Ar saturated electrolyte from Figure III-4. Also, the temperature increase leads to better activity for the Pt/GC with a diffusion-limiting current density better defined and of higher absolute value than at 25°C (Figure III-6 (c)). As it was said previously, the temperature increase leads to a better wettability of the graphitized carbon and thus more active site available for the ORR on the whole geometric area of the electrode. More generally, Pt/VC sets aside, the temperature increase leads to a larger absolute value of the diffusion-limiting current density, which is ascribed to a better wetting of the active layer at elevated temperature, this effect being particularly present for Pt/GC.

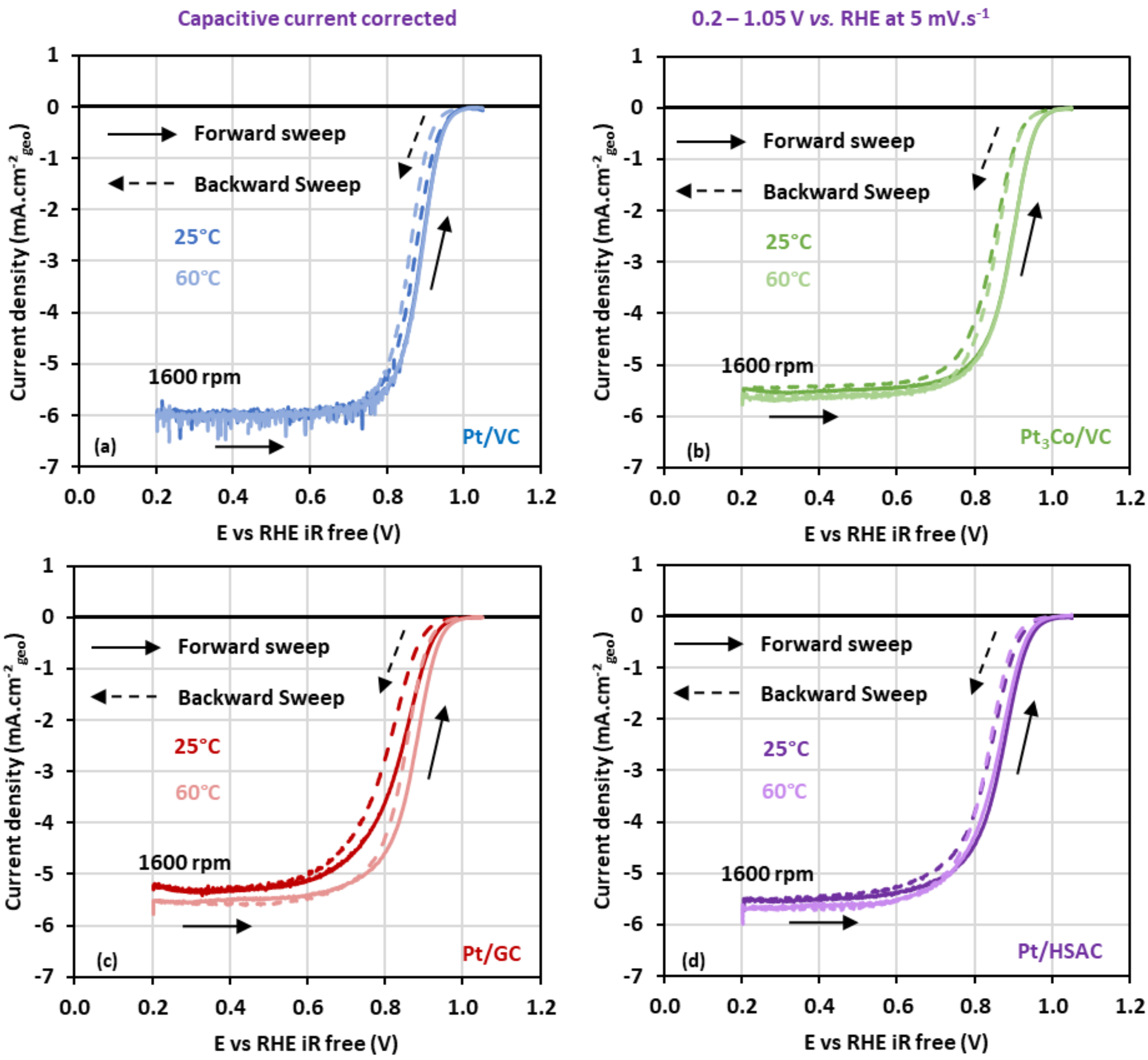

Figure III-6 : ORR polarization curve measurements performed at 25 and 60°C for (a) Pt/VC, (b) Pt_3CO/VC, (c) Pt/GC and (d) Pt/HSAC in $HClO_4$ 0.1 M O_2 saturated electrolyte. In all cases, the lighter colour corresponds to the higher temperature.

The specific and mass activities are obtained by normalizing the geometrical current read at 0.85, 0.9 and 0.95 V *vs.* RHE on the positive sweeps of the ORR polarization curves (after capacitive, ohmic and mass transport corrections), by the Pt electrochemical surface area in $cm^2_{Pt}.cm^{-2}_{geo}$ and the Pt loading of the thin film electrode in $mg_{Pt}.cm^{-2}_{geo}$ respectively. These activities are reported for both 25 and 60°C on Figure III-7 and Figure III-8 in a Tafel representation. For the sake of clarity, the activities reported at 60°C are slightly graphically shifted but were obtained at the same potential than activities at 25°C (0.85, 0.9 and 0.95 V *vs.* RHE). First, one should be aware that all the ORR polarization curve measurements were done at 5 $mV.s^{-1}$. It was reported in the work of Gasteiger et *al.* that measurements performed at this sweeping rate often lead to lower activity than measurements done at 20 $mV.s^{-1}$ due to (i) adsorbed oxygen species on Pt (linked with its oxidation at such potential) that hinder the ORR and (ii) possible contamination by the electrolyte (which is more detrimental at lower potential sweep rates) [6]. Thus, all the activity values shown in this work may be slightly lower than values reported in the literature [6], [14]. Regarding the specific activities on Figure III-7, Pt_3Co/VC outperforms the other electrocatalysts at both 25 and 60°C, with a decreasing gap at 0.9 and 0.85 V *vs.* RHE. Pt/VC and Pt/GC shows similar specific activities at 25°C. At higher temperature, it was seen that the wettability of Pt/GC electrode is improved, which leads to more active sites available for ORR and thus higher activities. The Pt/VC electrocatalyst is also more active at higher temperature except at 0.95 V *vs.* RHE, potential at which the Pt oxidation, promoted by temperature increase, starts to significantly hinder the ORR in a more prevalent manner than the beneficial effect of the temperature on the ORR intrinsic kinetics. This is also the case for Pt_3Co/VC electrocatalyst. Pt/HSAC shows the worst specific activity in liquid electrolyte, while it has the highest ECSA value. In fact, the TEM and CO stripping measurements showed that the Pt/HSAC is composed of very small Pt nanoparticles that leads to higher developed active surface but are poorly active towards ORR, owing to a well-known particle-size effect [15], [16]. In addition, the temperature increase tends to slightly decrease the activity of this electrocatalyst for the ORR, which can again be ascribed to its smaller Pt crystallite/particles size (smaller crystallites are more oxidized at higher temperature, leading to less free surface Pt sites, and this effect is likely prevalent versus the beneficial improvement of the ORR kinetics on Pt sites).

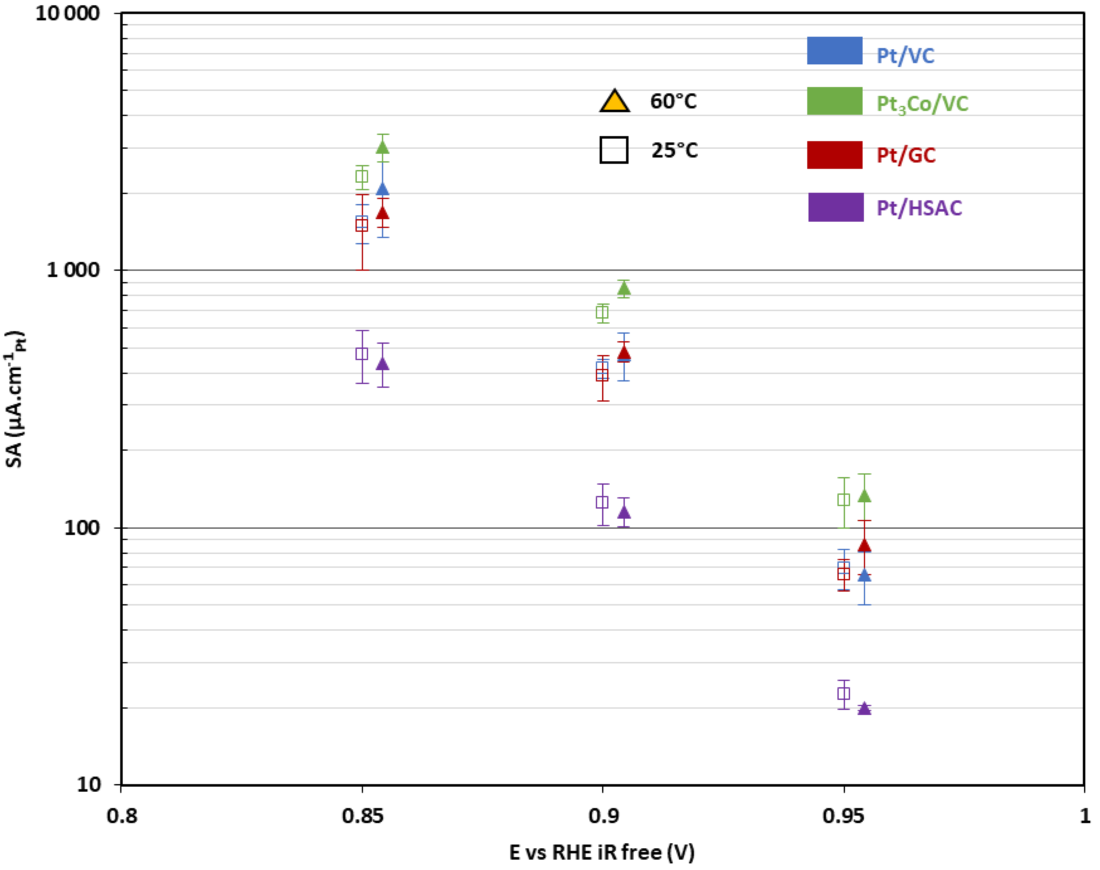

Figure III-7 : Tafel representation of specific activities obtained at 0.85, 0.9 and 0.95 V vs. RHE at 25 and 60°C for all the electrocatalysts.

Regarding the mass activity, Pt/VC and Pt_3Co/VC show similar activity at 25°C; Pt_3Co/VC is not outperforming all the other electrocatalysts anymore in terms of mass activity. This can be ascribed to the detrimental (too large) size of the Pt_3Co/VC particles compared to the Pt/VC ones. The positive effect of temperature increase is also not so clear for both electrocatalysts: the mass activity is lower at 0.95 V *vs.* RHE at 60°C than at 25°C, but this trend is reversed at 0.85 V *vs.* RHE. The hypothesis that can be made is that the increase of temperature, promoting the Pt oxides formation/reduction, leads to a hindrance more or less important depending on the potential, and this once again shows that surface PtO_x formation/reduction has a tremendous importance on the apparent ORR kinetics of the considered catalyst. Regarding the Pt/GC and Pt/HSAC electrocatalysts, the observation made on specific activities can also be made for mass activities for the temperature increase effect. However, Pt/HSAC does not have the worst mass activity anymore at 25°C, owing to the fact that its very small Pt particle size leads to a larger ECSA that, to some extent, counter balances the low specific activity of its small Pt particles. Thus, the observation and trends made regarding the specific activities may not be viable anymore for mass activities. In general, while specific activity tends to praise the electrocatalysts with the smallest ECSA, mass activity (knowing exactly the theoretical mass of Pt inside the thin film electrode), will be more relevant in practical systems (application). In addition, mass activities enable comparing different carbon-based Pt supported materials in a more convincing manner than specific activity, the latter being biased by some uncertainties in ECSA measurements by CO-stripping or H_{UPD}, which are assessed in conditions that might not be representative of the one used for ORR characterizations.

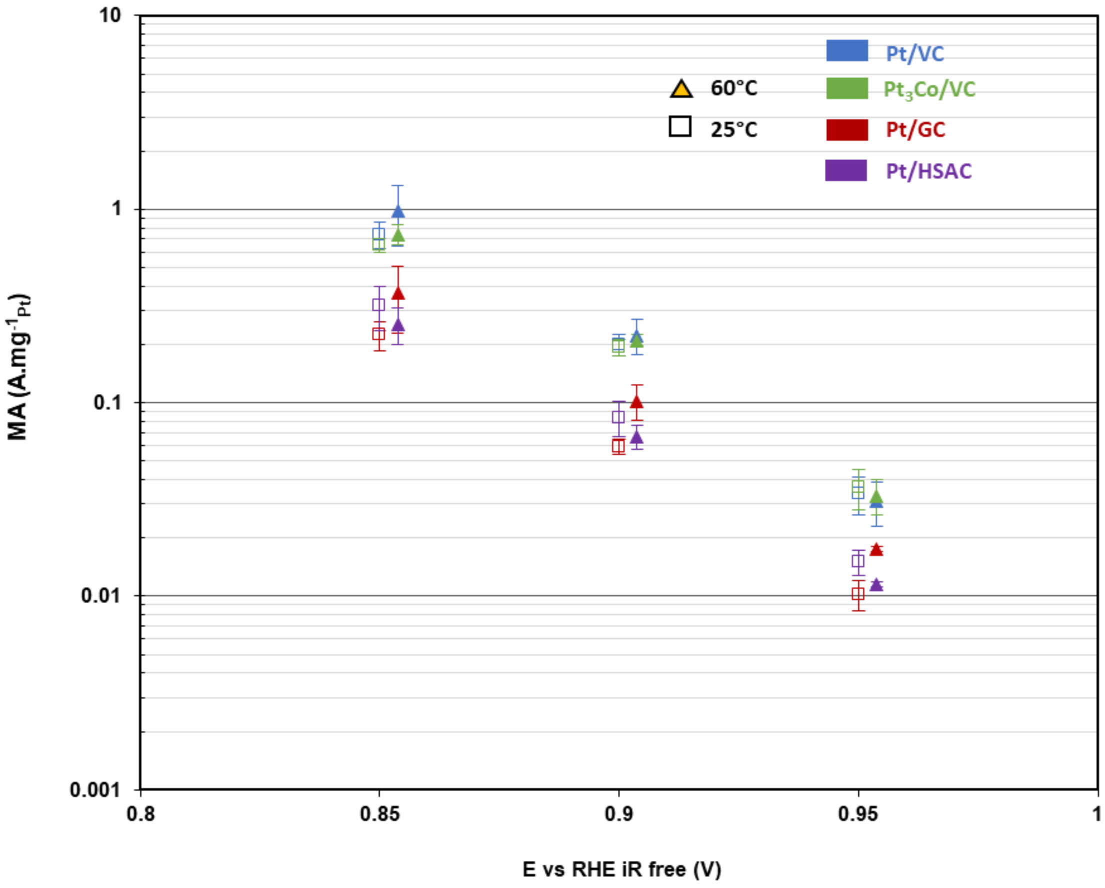

Figure III-8 : Tafel representation of mass activities obtained at 0.85, 0.9 and 0.95 V vs. RHE at 25 and 60°C for all the electrocatalysts.

In this section, four state-of-art carbon-based Pt supported materials were characterized in Rotating Disk Electrode setup in order to gather intrinsic electrocatalytic features and better understand the materials activity/structure/composition relationship. The study showed and confirmed that CO_{ad} oxidation coulometry was more reliable to assess the ECSA of an electrocatalyst than the proton desorption coulometry, especially when considering measurements at 60°C. The specific and mass activities were obtained performing ORR polarization curve measurements. The different activities are in the right order of magnitude compared to the values reported by Gasteiger *et al.* and Garsany *et al.*, even if they are lower (up to 35%) according to our measurements protocol [6], [8]. This shows the consistency/reproducibility of the RDE setup to quantify the electrocatalytic features of Pt/C materials, if experiments are performed in a proper manner. Here, it has to be noted that this study was conducted in collaboration with Raphaël Riasse and Clémence Lafforgue. According to the dispersion of the different results by the three operators and the small error bars obtained, these results show the good reproducibility and reliability of the experimental procedures (from the deposits to the electrochemical measurements). The observations made on the different electrochemical measurements are compatible with a clear influence of the nature/composition (Pt *vs*. Pt_3Co nanoparticles, type of carbon support) and structure (size, extent of agglomeration of the Pt-based nanoparticles) of the materials studied. However, this electrochemical setup has drawbacks: since RDE employs a liquid electrolyte, the mass transport of the reactant (here

O_2 gas) is necessarily different compared to the PEMFC application. Hence, the very slow diffusivity and solubility of O_2 in liquid electrolyte leads to very large mass transfer limitation and the measured current densities are not (at all) representative of real PEMFC operation. As a matter of fact, the RDE setup cannot lead to any reliable measurement of the ORR activity at potential lower than 0.85 V *vs.* RHE for "good" ORR catalysts like Pt/C, while PEMFC cathodes operate nominally at potential around 0.60 – 0.75 V *vs.* RHE. This would require to extrapolate largely RDE data down to this potential interval, which of course is a source of uncertainty and is questionable. For this reason, it appears mandatory to compare these intrinsic properties of the four catalysts in real PEMFC environment, but in "model" conditions that also enable to access the materials intrinsic activity. To that goal, differential cell measurements were performed in a small PEMFC (1.8 cm²) fed with very large stoichiometries (see Chapter II for details). In addition, PEMFC usually operate at higher temperature than 25°C, which is why the RDE study was also conducted at 60°C, and the differential cell measurements have been reproduced at both temperatures also (the idea being to characterize the materials in operating conditions as close as possible between RDE and PEMFC differential cell). The differential cell tests are presented hereafter in sections III.2 to III.5.

III.2 FURTHER-FC MEA

The first MEA studied in this work is a MEA taken from European project FURTHER-FC, that deals with the understanding of operation and limitation processes of PEMFC. In this work, the FURTHER-FC MEA, denoted as FURTHER MEA thereafter for the sake of brevity, has been characterized in order to build a reliable dataset for modeling, based on a state-of-art MEA for automotive applications, which would be used to validate the model improvement/development, which will be presented in the Chapter IV. As a matter of fact, a complete electrochemical testing protocol was performed on this MEA to cover a wide range of operating conditions, including different temperatures, relative humidities and also two sets of oxygen partial pressure that could be used to help the model development and parametric identification. The molar fraction of oxygen was adapted by adjusting the nitrogen flow rate in order to keep the same partial pressure of oxygen for all the operating conditions. Table III-3 summarizes the different operating conditions at which the FURTHER MEA was characterized.

Table III-3 : Operations conditions of the electrochemical testing protocol in DC.

Temperature (°C)	**Total pressure an/cath (Bar abs.)**	***RH* (an/cath)**	**P_{H_2O} (Pa)**	**P_{O_2} (Pa)**	**$Q_{N_2+O_2}$ (NmL.min^{-1})** Q_{O_2} = 78 NmL.min^{-1}	**P_{O_2} (Pa)**	**$Q_{N_2+O_2}$ (NmL.min^{-1})** Q_{O_2} = 313 NmL.min^{-1}
30	1.5	100%	4219	5610	2038	23500	1946
60		50%	9958		1958		1869
60		80%	15934		1874		1790
60		100%	19917		1818		1736
80		50%	*23679*		1766		1686
80		80%	37887		1567		1496 (21% O_2)
80		100%	47359		1435		1370

III.2.1 Reproducibility study on FURTHER-FC MEA

Two FURTHER MEA were characterized to check the reproducibility of the measurements and to validate the experimental protocol. Figure III-9 (a) shows the third cycle of cyclic voltammetry performed on the two FURTHER MEA at 100 mV.s^{-1} under H_2 (627 NmL.min^{-1})/N_2 (1500 NmL.min^{-1}) at atmospheric pressure and 30°C, 100% RH (performed after break-in). The two cyclic voltammetries, corrected from H_2-crossover current, are almost superimposed. The brighter curve seems to show slightly lower coulometry in the H_{UPD} and Pt oxides regions, which is evidenced by the ECSA value measured and displayed on Figure III-9 (a). Figure III-9 (b) and (c) show the high frequency resistance, R_{HF}, and the protonic resistance inside the catalyst layer, $R_{H+,CL}$, determined from the PEIS measurement performed at 0.4 V (this voltage is held for two minutes before the measurement, allowing to get the H_2 crossover current) under H_2/N_2 configuration from 100 kHz to 0.1 Hz with 10 mV magnitude. From the values of resistances or of ECSA, one can conclude that there are only very few differences between the two FURTHER MEA, which evidences the reproducibility of the FURTHER MEA, as well as the validation of the protocol measurement under inert atmosphere.

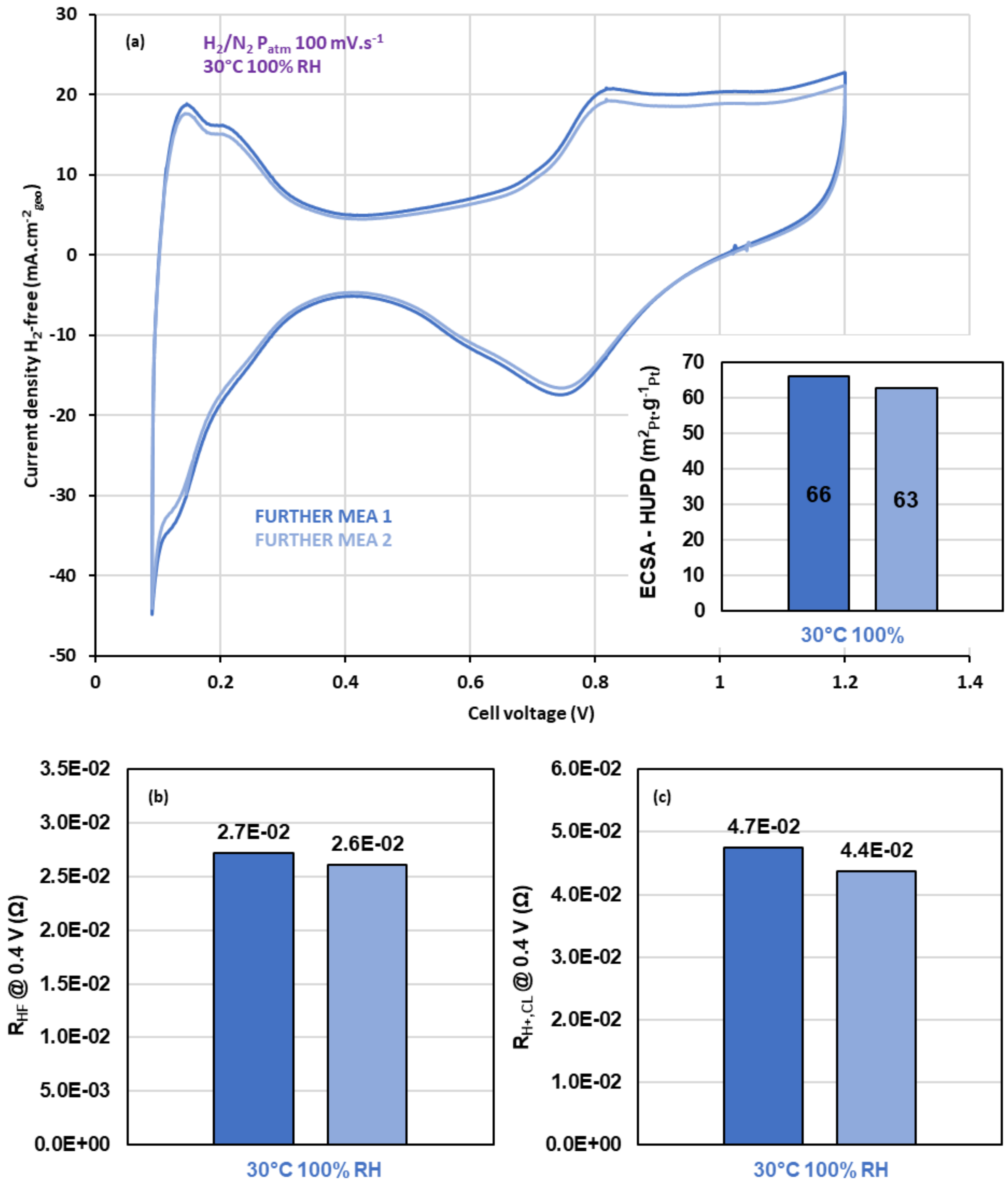

Figure III-9 : (a) Third cycle of cyclic voltammetries performed on two FURTHER MEA with the ECSA value measured (b) R_{HF} values obtained from PEIS performed on the two FURTHER MEA at 0.4 V from 100 kHz to 0.1 Hz with 10 mV magnitude (c) $R_{H+,CL}$ values obtained from PEIS performed on the two FURTHER MEA at 0.4 V from 100 kHz to 0.1 Hz with 10 mV magnitude.

Figure III-10 (a) shows the second cycle of polarization curves performed on two FURTHER MEA, with and without ohmic drop correction, at 10 mV.s^{-1} under H_2 (627 NmL.min^{-1})/O_2(21%)+N_2 (1496 NmL.min^{-1}) at 1.5 bar abs. and 80°C, 80% RH. The ohmic drop is corrected by considering the average R_{HF} value obtained from the PEIS done at the different cell voltages (which here will be assimilated as the cathode potential): 0.3, 0.5, 0.65 and 0.85 V (the potential is held two minutes before each measurement). These PEIS, performed from 100 kHz to 0.1 Hz with 10 mV magnitude under H_2/O_2+N_2 configuration and after the polarization curve measurement, are carried out in order to evaluate the hydration of the ionomer of the membrane and inside the catalyst layer at different working points during operation (e.g. along the polarization curve). The different resistance values are determined according to the method detailed in the Chapter II. In this case, the backward sweeps of both polarization curves are also almost superimposed. The hysteresis phenomenon is observed for both MEA (wider in the case of FURTHER MEA 2). In addition, no matter the working point, the different resistances values are almost the same between the two FURTHER MEA. The evolution of the resistances according to the working point will be discussed in the next sections; the results presented on Figure III-9 and Figure III-10 enable to attest the reproducibility between the two MEA in terms of performances, cathode ECSA and protonic resistances. It also supports and validates the experimental protocols used to gather electrochemical information under these operating conditions. In the next sections, the dispersion of the different quantitative electrochemical features measured is always checked.

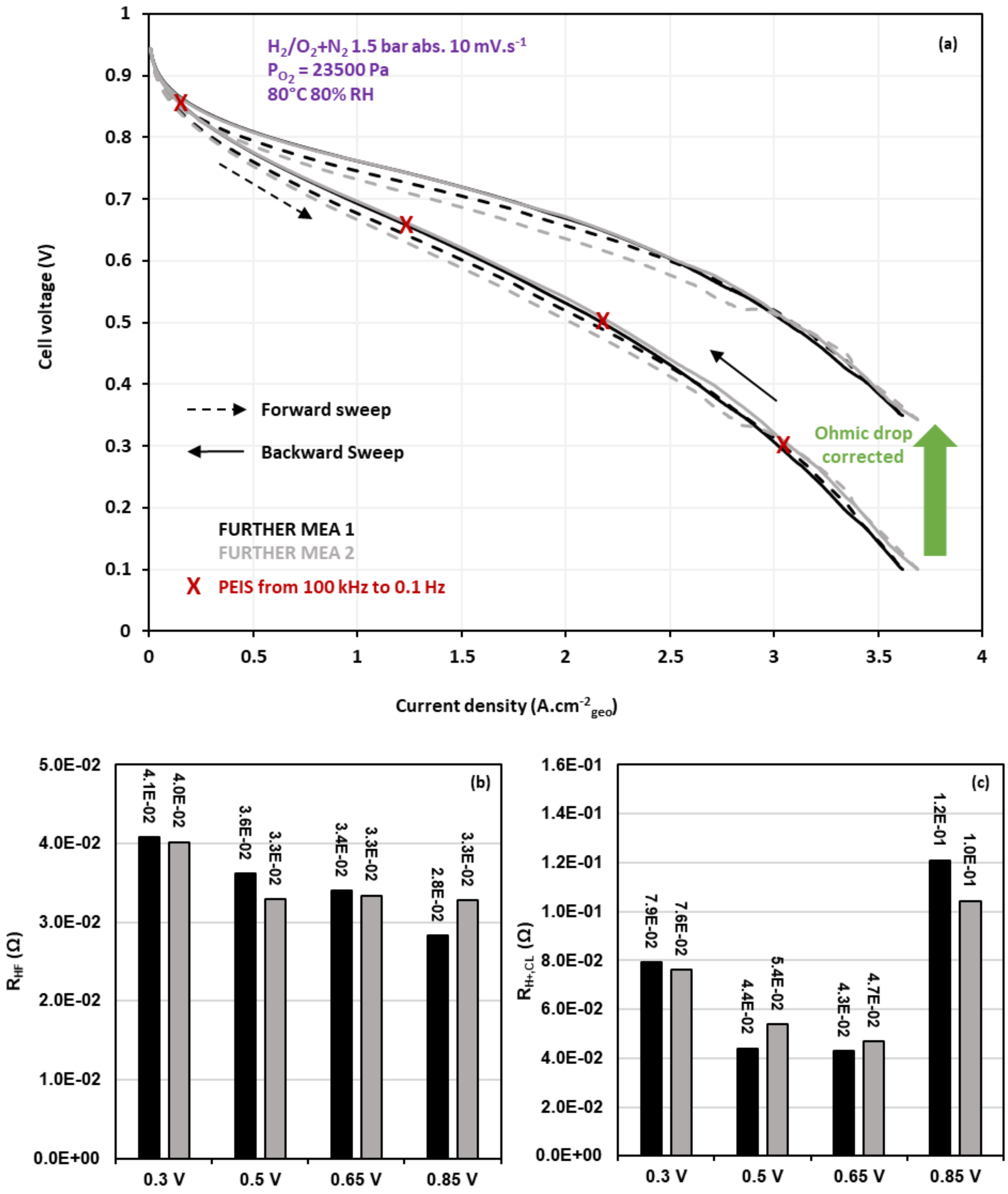

Figure III-10 : (a) Second cycle of polarization curves performed on two FURTHER MEA with and without ohmic drop correction (b) R_{HF} values obtained from PEIS performed on the two FURTHER MEA at different potential along the polarization curve (c) $R_{H+,CL}$ values obtained from PEIS performed on the two FURTHER MEA at different potential along the polarization curve.

III.2.2 Impact of the cell temperature

This section focuses on the impact of the cell temperature on the different electrochemical features and MEA behaviour under H_2/N_2 and H_2/O_2+N_2 configurations with fully hydrated gases. Figure III-11 (b) shows the ECSA value obtained at 30, 60 and 80 °C, 100% RH from the CV shown on Figure III-11 (a). The ECSA (measured from H_{upd} coulometry) decreases from 64 $m_{Pt}^2.g_{Pt}^{-1}$ to 43 $m_{Pt}^2.g_{Pt}^{-1}$ as the temperature increases from 30 to 80°C. This behaviour was also observed in RDE measurements in liquid electrolyte. In differential cell, the specific coulometry value considered for proton desorption is also taken equal to 210 $\mu C.cm^{-2}_{Pt}$ and it should probably be also lower at higher temperature than 30°C. It means that the adsorption/desorption of proton mechanism seems to be modified at 80°C, as witnessed by the absence of the characteristic peaks of these reactions at 80°C compared to 30°C on the CV. The decreasing trend is also observed for the evolution of R_{HF} and $R_{H+,CL}$ with temperature, as shown on Figure III-11 (c) and (d). The high frequency resistance, which accounts for the protonic mobility inside the membrane, is almost 3 times lower at 80°C compared to 30°C at 100% RH. The protonic resistance inside the catalyst layer, which accounts for the protonic mobility inside the catalyst layer, is lowered from 27 mΩ at 30°C to 16 mΩ at 80°C at 100% RH. In their review, Weber and Kusoglu highlight that the protonic mobility inside PFSA membrane follows an Arrhenius law, meaning that the protonic mobility is improved when the temperature increases [17]. Inside the catalyst layer, the ionomer used, that ensures the protonic mobility, is Nafion as the one used for the membrane. Thus, it is not surprising to promote the protonic mobility inside the catalyst layer with increased temperature at a constant relative humidity of 100%. These data will allow to update the parameters used in the models with state-of-art PEM components.

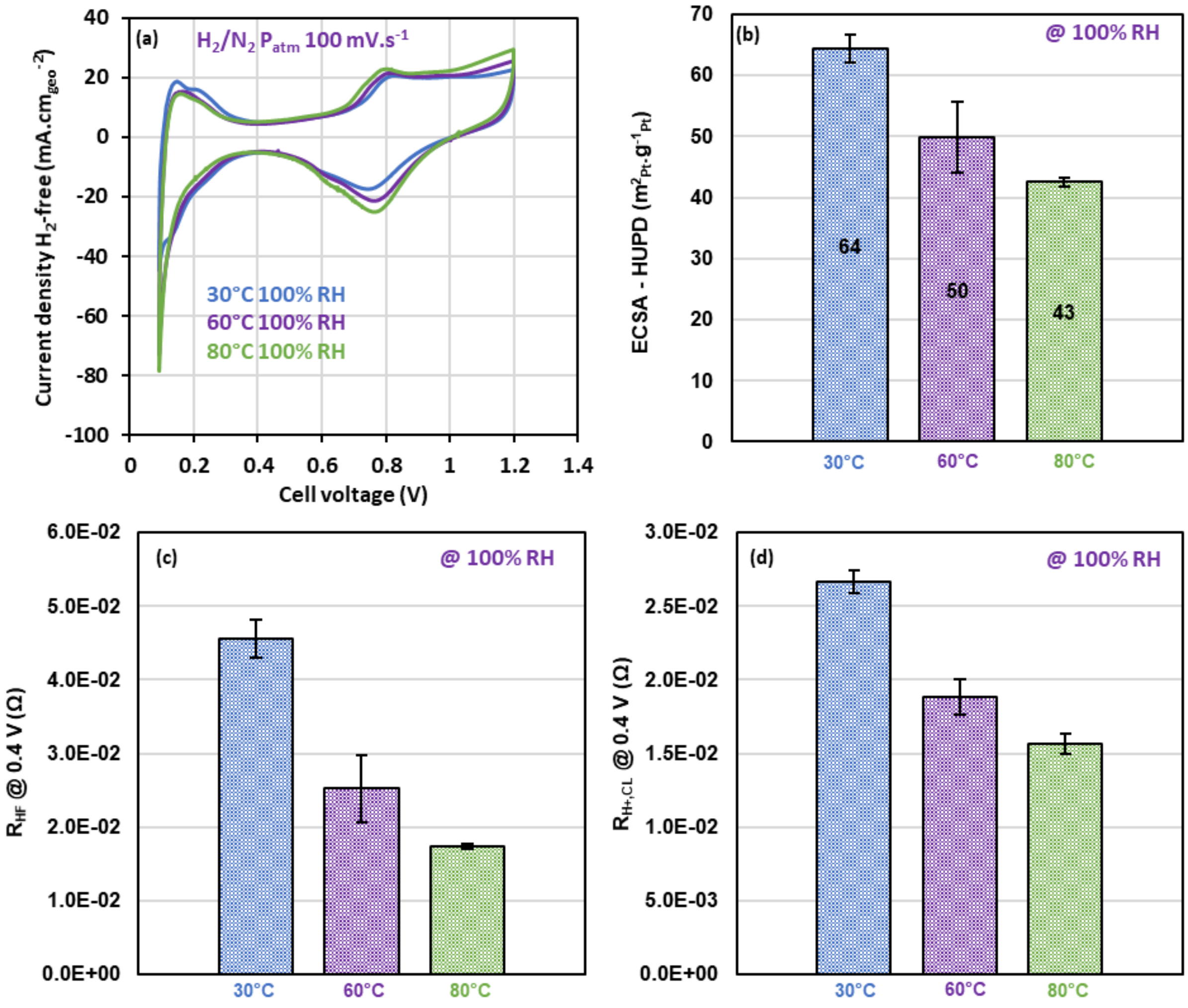

Figure III-11 : (a) Third cycle of cyclic voltammetries performed on FURTHER MEA at different temperatures with constant RH (b) ECSA values obtained at different temperatures at 100% RH under H_2/N_2 configuration (c) R_{HF} values obtained from PEIS performed at 0.4 V under H_2/N_2 configuration and (d) $R_{H+,CL}$ values obtained from PEIS performed at 0.4 V under H_2/N_2 configuration.

Figure III-12 (a) shows polarization curves performed at 30, 60 and 80°C with fully hydrated gases (e.g. 100% RH). Depending on the temperature, the gas flow rate of nitrogen was adjusted to keep a partial pressure of dioxygen equal to 23500 Pa. First, at 30°C, 100% RH, the hysteresis phenomenon observed on the polarization curve seems to be wider than at 80°C, 100% RH. On the CV shown on Figure III-11 (a), the Pt-oxidation peak potential is higher at 30°C, 100% RH than at 80°C, 100% RH and the Pt-reduction peak potential is lower at 30°C, 100% RH than at 80°C, 100% RH, which corresponds to faster Pt-oxide kinetics of formation/reduction at elevated temperature. Thus, the asymmetry of Pt oxides formation/reduction reactions is bigger at 30°C than at 80°C, which may account partly for the bigger hysteresis observed on the experimental polarization curve (this once again shows – as for the RDE characterizations – that the apparent ORR kinetics has a lot to do with the formation/reduction of Pt-oxides). Then, the temperature increase seems to improve the global performance of the FURTHER MEA (keeping 100% RH), which is mainly explained by the enhancement of ORR kinetics at higher temperature by reducing the activation losses [18]. The performance improvement with temperature may also be linked to the better protonic conductivity at 80°C than at 30°C, shown on Figure III-12 (b) and (c) under H_2/O_2+N_2 configuration. Regardless of the working point investigated during operation, a temperature increase leads to a non-negligible improvement of protonic mobility inside the membrane and inside the catalyst layer (up to 1.5 time higher for R_{HF} and 2 times higher for $R_{H+,CL}$). The different resistances are not only evolving with the temperature, but they are also evolving with the potential considered (e.g. the working point). At 30°C, 100% RH, there is almost no variation of R_{HF} and $R_{H+,CL}$, considering the dispersion, between the different potential investigated. At 60°C, the R_{HF} and $R_{H+,CL}$ seem to increase when the potential is decreasing. This trend is even sharper at 80°C. This increase of the resistances suggests that at low potential, the protonic mobility is hindered. This may be explained by the fact that besides water production, the ORR also generates heat, and the competition between local water production and local heat generation is changing with the working point considered and the operating temperature, which governs water vapour saturation (and the local RH level). At high potential (low current densities), the water and heat production is small, while at lower potential (high current densities), more water is produced as well as more heat: the heat generated may lead to less hydrated active layer, resulting in a decrease of the protonic conductivity. The heat locally produced may lead to a local cell temperature, in the active layers, increase up to 10°C more than the temperature set point [19].

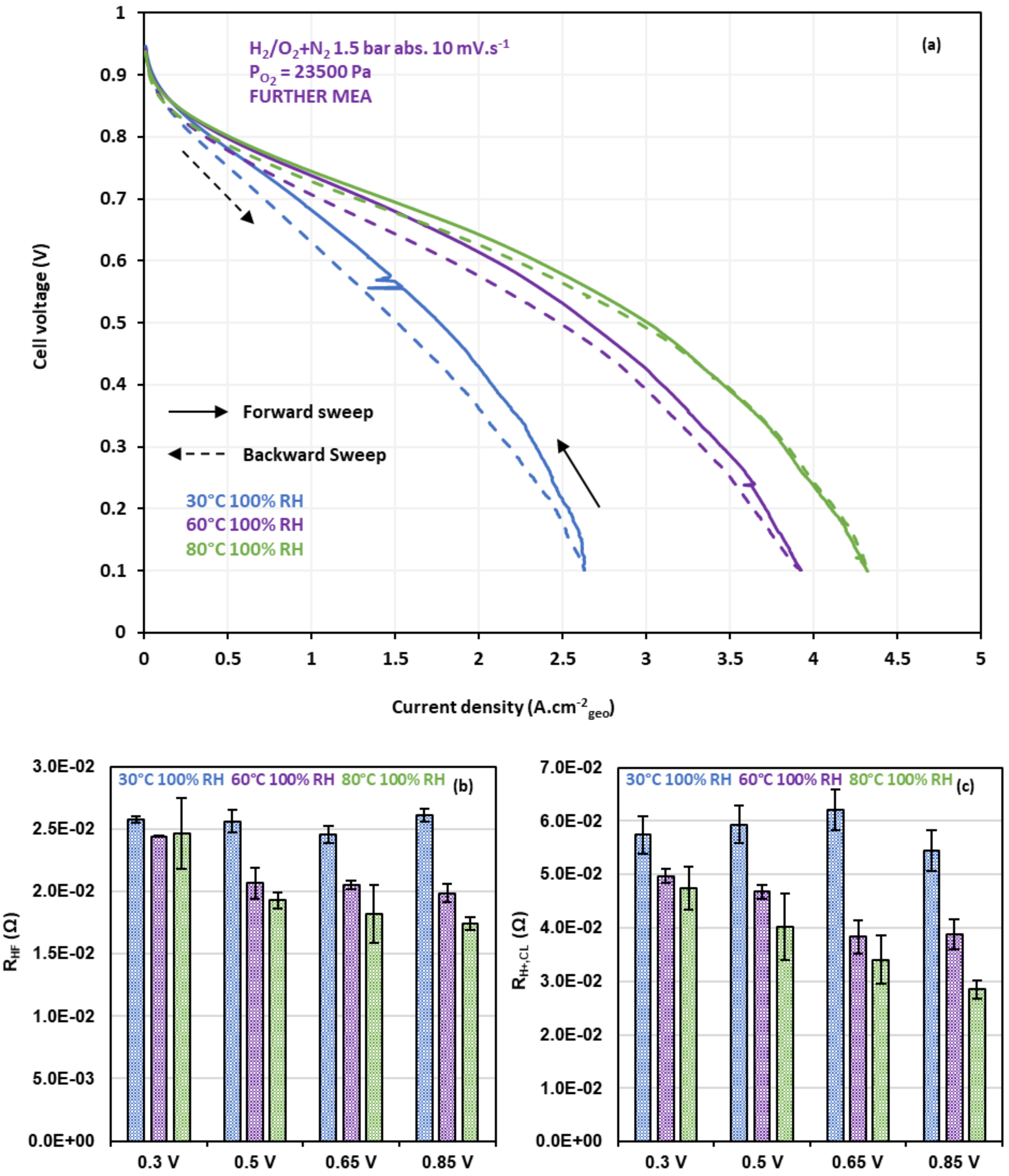

Figure III-12 : (a) Second cycle of polarization curves performed on FURTHER MEA without ohmic drop correction at different temperatures at 100% RH (b) R_{HF} values obtained from PEIS performed on the FURTHER MEA at different potentials (c) $R_{H+,CL}$ values obtained from PEIS performed on the FURTHER MEA at different potentials.

III.2.3 Impact of the relative humidity

In this section, the impact of the relative humidity on the different electrochemical features and MEA behaviour under H_2/N_2 and H_2/O_2+N_2 configuration at 80°C is investigated. Figure III-13 (b) shows the ECSA value obtained at 80°C with different levels of hydration of the inlet gases: 50, 80 and 100% RH from the CV shown on Figure III-13 (a). The ECSA values get lower as the relative humidity decreases (so does the extent of formation/reduction of Pt oxides). This makes sense, as a high hydration of the catalyst layer is helping the proton migration to the active site (and since water and protons are involved in the Pt/Pt oxides reactions). In particular, at 50% RH, which is a very dry condition, some pathway to active sites for protons may become unavailable, resulting in a lower ECSA than at higher relative humidity. In addition, the water activity may be significantly reduced, affecting all the electrochemical reactions in the different regions of the CV. At 80% RH and 100% RH, the ECSA values (and Pt oxide behavior) are almost the same, which means that a humidification at 80% RH is enough for proton (and water) to reach all active sites (at least under H_2/N_2 operation). Regarding R_{HF} and $R_{\mathrm{H+,CL}}$, they monotonously increase when the relative humidity decreases, as displayed on Figure III-13 (c) and (d). This is expected as these resistances account for the protonic mobility: a very dry condition results in very low hydrated catalyst layer and membrane, and then the protonic conductivity highly decreases (up to 10 times lower in the case of $R_{\mathrm{H+,CL}}$). However, even if at 80% RH and 100% RH, the ECSA values are the same, the R_{HF} and $R_{\mathrm{H+,CL}}$ are very different between both hygrometric conditions. However, these differences for proton resistances do seem to affect the proton transport to the Pt active sites (at the rates/currents necessary under H_2/N_2 operation).

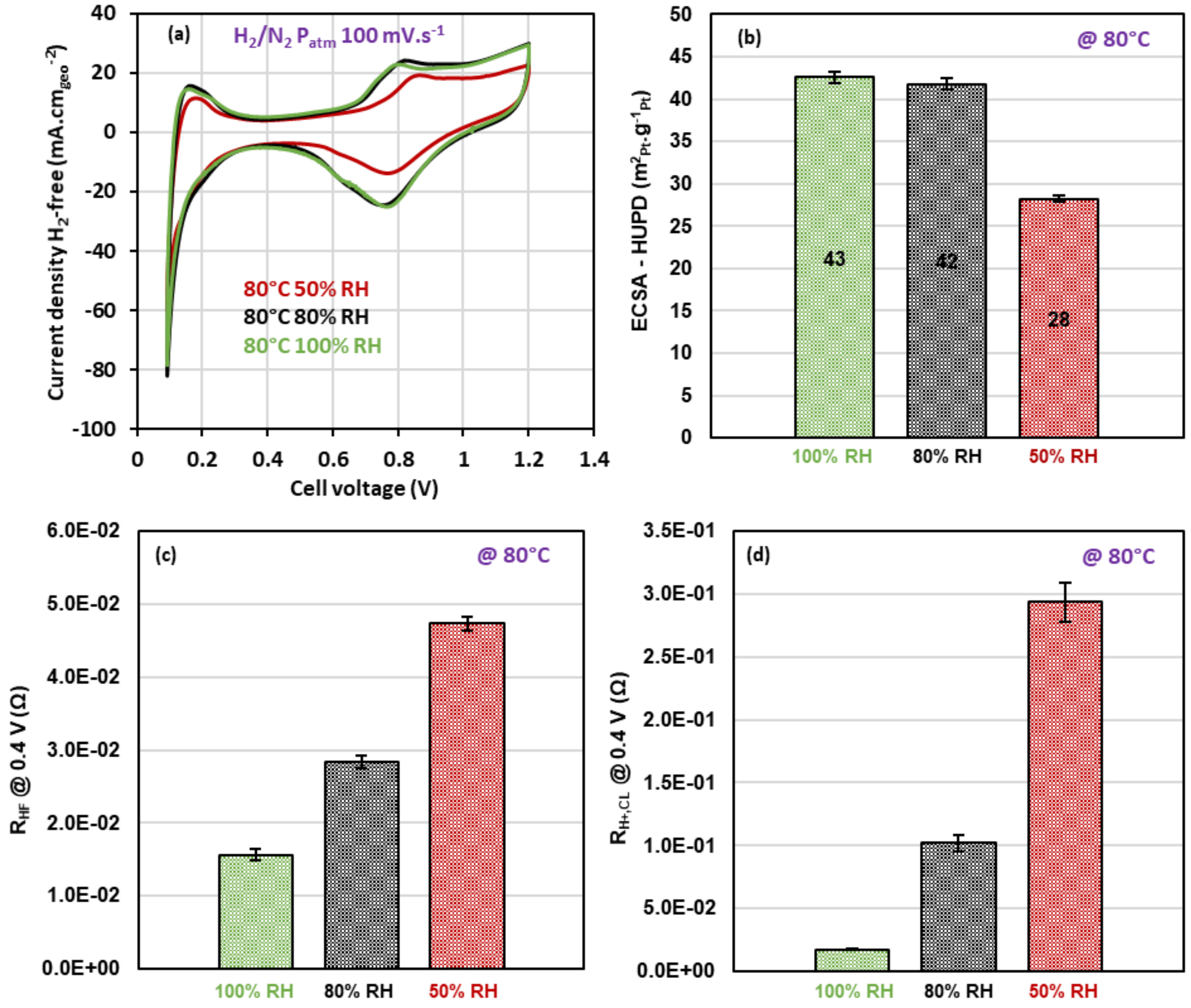

Figure III-13 : (a) Third cycle of cyclic voltammetries performed on FURTHER MEA at different relative humidities at 80°C under H_2/N_2 configuration (b) ECSA values obtained at different relative humidities (c) R_{HF} values obtained from PEIS performed at 0.4 V under H_2/N_2 configuration and (d) $R_{H+,CL}$ values obtained from PEIS performed at 0.4 V under H_2/N_2 configuration.

Figure III-14 (a) shows the second cycle of polarization curves performed on FURTHER MEA without ohmic drop correction at 80°C for different relative humidities. Depending on the relative humidity, the gas flow rate of nitrogen was adjusted to keep a partial pressure of dioxygen equal to 23500 Pa. First, the global performance are highly impacted by the hygrometry. The performance at 100% RH are much higher than at 50% RH. In fact, protons are required for the ORR to occur at the Pt|ionomer/water interface. As it was seen on the previous results on the ECSA, less hydrated catalyst layers exhibit limited Pt active sites that are available for electrochemical reaction involving proton such as the ORR. It is not so much the amount of protons available which decrease at low RH (it is fixed by the ion-exchange capacity of ionomer used – the same in all conditions), but more likely their lower mobility in dry conditions that render them unable to reach the aforementioned active sites "in due time" (in ORR conditions, the currents exchanged are much larger than in H_{upd} characterizations, hence the larger hindrances) [20]. As stated under H_2/N_2, Figure III-14 (b) and (c) shows that the R_{HF} and $R_{H+,CL}$ increase in very dry hygrometric condition under H_2/O_2+N_2 configuration. However, depending on the potential, the resistance values may highly be modified.

The R_{HF} is increasing with decreasing potential at 100% and 80% RH. This is due to more heat generation at lower potential that induces local drying within the membrane. However, at 50% RH, the R_{HF} value is decreasing at 0.65 V and 0.5 V, due to water production via the ORR, resulting in a better hydration state of the membrane before re-increasing at 0.3 V due to heat production. Similar trends can be observed with $R_{H+,CL}$ on Figure III-14 (c) At 100% RH, the protonic resistance inside the catalyst layer is increasing with decreasing potential, due to heat production. At 80% RH and 50% RH, more water is produced via the ORR at 0.5 and 0.65 V compared to 0.85 V, resulting in a better hydration state of the catalyst layer that promotes proton mobility. At 0.3 V, the heat production induces again local drying leading to a re-increase of $R_{H+,CL}$. At 50% RH, the hysteresis observed on the polarization curve seems to be wider than at 100% RH. This may be mainly explained by the different hydration states of the catalyst layer between the forward and backward sweeps, as there is a non-negligible evolution of $R_{H+,CL}$ under this operating condition coupled with the asymmetry of Pt oxides formation/reduction kinetic reactions, which is more pronounced at 80°C, 50% RH than at 80°C, 100% RH (Figure III-13 (a)).

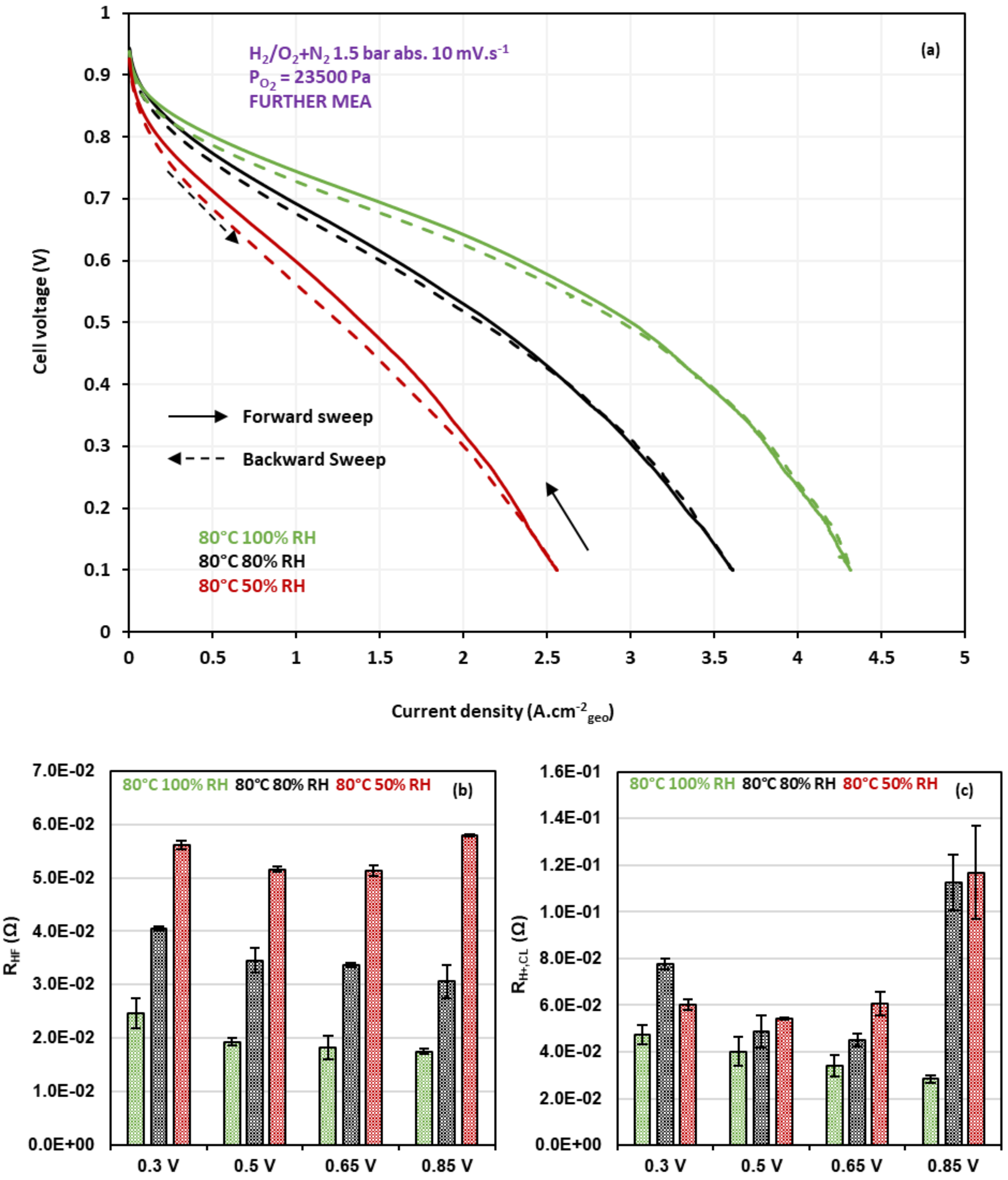

Figure III-14 : (a) Second cycle of polarization curves performed on FURTHER MEA without ohmic drop correction at 80°C for different relative humidities (b) R_{HF} values obtained from PEIS performed on the FURTHER MEA at different potentials (c) $R_{H+,CL}$ values obtained from PEIS performed on the FURTHER MEA at different potentials.

III.2.4 Impact of P_{O_2}

This section focuses on the impact of the partial pressure of dioxygen on the global performance, on the high frequency resistance and on the protonic resistance inside the catalyst layer. Figure III-15 (a) shows the second cycle of polarization curves performed on FURTHER MEA without ohmic drop correction at 80°C, 80% RH and a partial pressure of dioxygen P_{O_2} equal to 5610 Pa and 23500 Pa. First, the performance with P_{O_2} equal to 23500 Pa are much higher than with P_{O_2} equal to 5610 Pa, because the dioxygen concentration is 4 times higher, which increases (i) the reversible (thermodynamical) potential at the cathode, hence the cell voltage, but also (ii) the O_2 concentration near Pt actives sites, leading to larger dioxygen flux and larger current. One should note that increasing the dioxygen concentration by a factor 4 does not necessarily lead to 4 times more current produced, though, which is normal owing to the fact that the ORR kinetics order versus O_2 is not unity. In this case, at the lowest potential, the current ratio between the two partial pressure of dioxygen is only around 2.5. This ratio decreases with the potential increase. There is almost no variation of the R_{HF} between the two partial pressures of dioxygen investigated (Figure III-15 (b)). Only slight variations are observed according to the working point due to water/heat production competition, with a global increase of R_{HF} when the potential is decreasing. The evolution of $R_{\mathrm{H+,CL}}$ with potential has already been seen in the previous section, for $P_{\mathrm{O_2}}$ = 23500 Pa. However, if $P_{\mathrm{O_2}}$ = 5610 Pa, there are no variations, no matter the working point considered. The $R_{\mathrm{H+,CL}}$ value is equal to 120 mΩ and does not seem to evolve along the polarization curve. This may be due to the low current density produced, and then the small water production, that does not affect significantly the hydration state of the catalyst layer and of the membrane along the polarization curve compared to the case where $P_{\mathrm{O_2}}$ = 23500 Pa. Finally, the hysteresis observed on the polarization curve performed at the lowest $P_{\mathrm{O_2}}$ seems to be wider than on the one obtained with $P_{\mathrm{O_2}}$ = 23500 Pa. This may be explained by the fact that with the lowest $P_{\mathrm{O_2}}$, the current density produced is not sufficient to better hydrate the catalyst layer and the membrane (e.g. the local relative humidity remains probably constant equal to 80%). This is confirmed by the different impedance measurements and the almost unchanged/stable values of R_{HF} and $R_{\mathrm{H+,CL}}$ no matter the potential. The $R_{\mathrm{H+,CL}}$ values are higher in the case of $P_{\mathrm{O_2}}$ = 5610 Pa than $P_{\mathrm{O_2}}$ = 23500 Pa except at 0.85 V where in both cases, a small current density is produced. The impedance measurements are performed after 2 minutes of stabilization (stationary operation); thus, the hydration signature related to the hysteresis should not be captured by impedance measurement, which renders any conclusion about the impact of hydration on the hysteresis difficult. Moreover, the effect of oxygen on performances and Pt oxides formation/reduction is not fully understood yet. Thus, the partial pressure of oxygen has certainly an impact on these oxidation and reduction reactions, which is what has been considered for the modeling presented in Chapter IV.

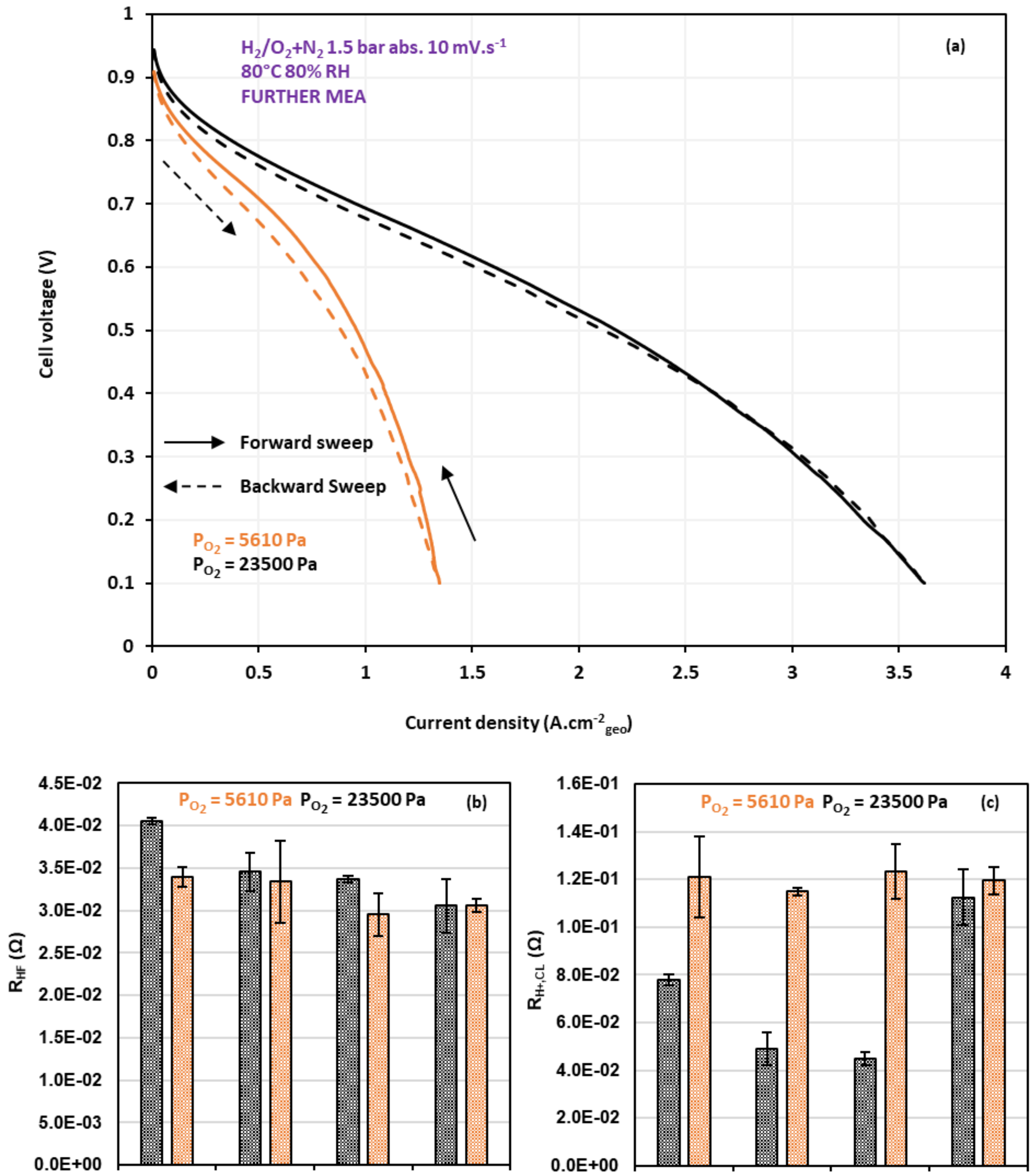

Figure III-15 : (a) Second cycle of polarization curves performed on FURTHER MEA without ohmic drop correction for different partial pressures of dioxygen (b) R_{HF} values obtained from PEIS performed on the FURTHER MEA at different potentials (c) $R_{H+,CL}$ values obtained from PEIS performed on the FURTHER MEA at different potentials.

The electrochemical characterizations performed on FURTHER MEA led to consistent and reliable dataset that can be used to validate modeling improvements. Global observations were made at several operating conditions with links made between the electrocatalytic features and the performance of the cell. However, due to specific needs and for the sake of modeling description improvements, electrochemical characterizations in differential cell shall also be performed on in-house MEA in order to control the composition of the CL, and other parameters such as the electrocatalyst nature, the membrane used and the catalyst layer loading. It allows also to work with very low loaded MEA (here 20 and 100 $\mu g_{Pt}.cm^{-2}$ was used at the cathode), and so very thin catalyst layers, which facilitates the analysis because some transport phenomena (in the catalyst layer) can be simplified or even neglected in a first step.

III.3 Very low loaded MEA (20 $\mu g_{Pt}.cm_{geo}^{-2}$)

This section focuses on electrochemical characterizations performed on catalyst layers loaded at 20 $\mu g_{Pt}.cm_{geo}^{-2}$ in differential cell with the same electrocatalysts studied in liquid electrolyte. In the frame of the paper dealing with the relevance of the electrochemical setup, the catalyst layers are characterized in DC with operating conditions and materials as close as possible as the one used in RDE. Because such very low loaded catalyst layer are very thin, below 1 µm, mass transport aspects through the thickness of the CL can be neglected, which enables to simplify the model by considering the catalyst layers as interfaces (0D active layers). This reduces the uncertainties due to transport, and leads to faster computation, hence allowing to increase the complexity of the ORR description (see Chapter IV). However, such measurements in differential cell are rarely referenced in literature. Thus, the first part will show some experimental results that led to specific operating conditions and choices of components, so to perform the most accurate and relevant electrochemical characterizations on such low loaded catalyst layers in DC. Then, ECSA values and specific/mass activities of the electrocatalysts obtained in differential cell at 30 and 60°C are compared to the ones obtained in RDE at 25 and 60°C. Finally, to help improving modeling, a focus on two electrocatalysts, Pt/VC and Pt/HSAC, is done with more advanced experimental results: qualitative coverage ratio of Pt oxides evolution with potential during cyclic voltammetry under inert atmosphere (H_2/N_2) and the evolution of the high frequency resistance (R_{HF}) along the polarization curve; these accessible data can be used to better describe the catalyst layer operation in numerical simulation.

III.3.1 Definition of components and operating conditions

This section aims at explaining the benefits and drawbacks as well as the different choices made to conduct the experiments in DC on the very low loaded catalyst layers used in this work. All the results are obtained here with catalyst layers made with Pt/VC electrocatalysts.

III.3.1.1 Thin membrane vs. thick membrane

At first, these experiments were conducted using a thin commercial membrane Gore MX 820.15, 15 µm thick; thin membrane are indeed usually now used in state-of-art MEA, which is the case, for instance, for the MEA taken from the FURTHER European Project. However, the use of a thin membrane leads to non-negligible oxidation signature of the H_2 crossover from the anode to the cathode at such low loading (Figure III-16). It shows the third cycle of cyclic voltammetry performed from 0.11 to 1.2 V on a MEA made of Pt/VC electrocatalyst with a Gore MX 820.15 membrane, in black, and Nafion® 115 membrane, in green, at 30°C, 100% RH under H_2 (627 NmL.min^{-1})/N_2 (1580 NmL.min^{-1}) at atmospheric pressure and 200 mV.s^{-1}. At 20 µg$_{Pt}$.cm$_{geo}^{-2}$, the capacitive current generated in the different areas of the CV (around 0.35 mA.cm$_{geo}^{-2}$) is so low that the faradaic H_2 crossover current has a significant impact on the measurement; indeed, the slower the sweeping rate, the more exacerbated that phenomenon, which is why cyclic voltammetry performed at a sweeping rate of 200 mV.s^{-1} is considered for 20 µg$_{Pt}$.cm^{-2} catalyst layer characterizations. The black curve (thin membrane) is shifted towards positive current densities and centered around 1.5 mA.cm$_{geo}^{-2}$ at 0.4 V in a region where no faradic reaction related to the Pt catalyst layer is supposed to occur and only capacitive current should be observed. This is in fact the fingerprint of the oxidation current generated by the H_2 crossover. The impact of permeation on the oxidation kinetics of hydrogen can also be observed in the oxide region. There is an increase of the current from 0.75 to 0.85 V due to Pt oxidation before a decrease of the current until 1.2 V. This behaviour in the Pt oxides region may be explained by the fact that there is a competition between hydrogen oxidation and Pt oxidation which means that the whole H_2 flow can no longer be oxidised above 1 V in the case of a thin membrane. It leads to a total oxidation current density (Pt oxides formation + H_2 oxidation) close to the case of the use of a thick membrane (in which lower faradaic current from H_2 crossover oxidation compared to the current from Pt oxidation). In fact, the use of a thick membrane greatly mitigates the H_2 crossover effect (green curve on Figure III-18). The CV is very slightly shifted towards positive current (0.04 mA.cm$^{-2}_{geo}$) but far less than the black curve (1.49 mA.cm$^{-2}_{geo}$). In addition, the impact of H_2 crossover in the oxides region is not observed for the thick Nafion® 115 membrane, leading to a “rather constant” oxidation plateau between 0.85 and 1.2 V, as the H_2 crossover oxidation current is greatly reduced.

III.3 Very low loaded MEA (20 µgPt.cmgeo-2)

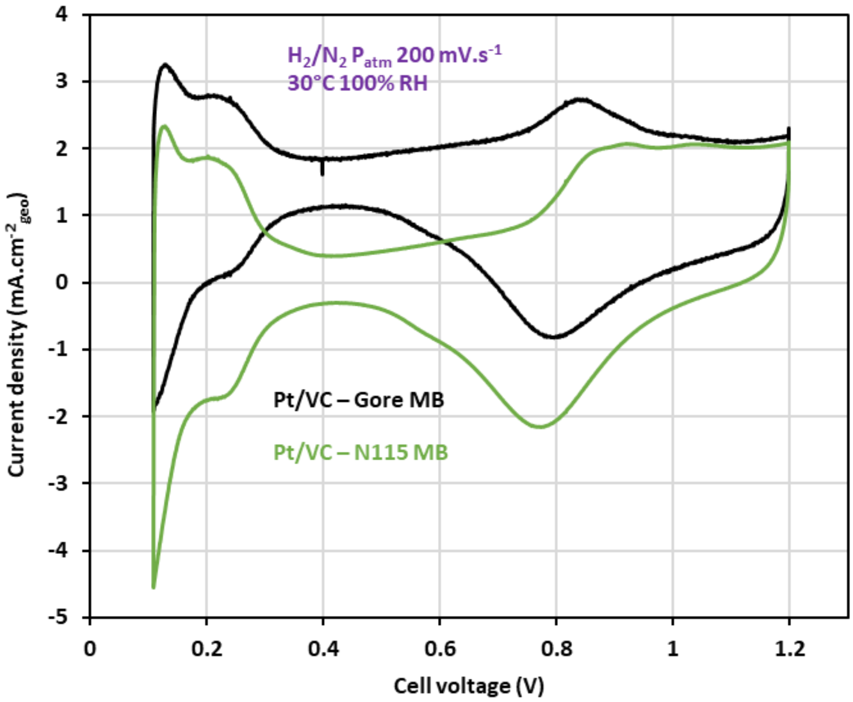

Figure III-16 : Third cycle of cyclic voltammetry performed at 200 mV.s^{-1} on MEA made of Pt/VC electrocatalyst (20 µg$_{Pt}$.cm$_{geo}$$^{-2}$).

The hydrogen oxidation at the cathode is investigated thanks to cyclic voltammetries performed at 1 mV.s^{-1} (Figure III-17). At such a low sweep rate, the transient current densities produced by Pt oxides formation/reduction reactions and proton adsorption/desorption reactions are greatly reduced, highlighting the current density coming from the H_2 crossover oxidation. On the black curve, from 0.8 to 1 V, the current density is dropping from around 1.6 mA.cm$_{geo}^{-2}$ to around 1 mA.cm$_{geo}^{-2}$, as less Pt sites are available, due to Pt oxides formation, hindering the complete oxidation of the H_2 flow. The same current density drop of 0.6 mA.cm$_{geo}^{-2}$ is observed on the CV, in black, shown on Figure III-16, which confirms that this current density drop, related to Pt oxidation, is a fingerprint of the H_2 crossover phenomenon that disturbs the classical Pt oxides region description. In addition, a hysteresis is observed between the oxidation and reduction sweeps, due to the asymmetry of Pt oxides formation/reduction kinetic reactions.

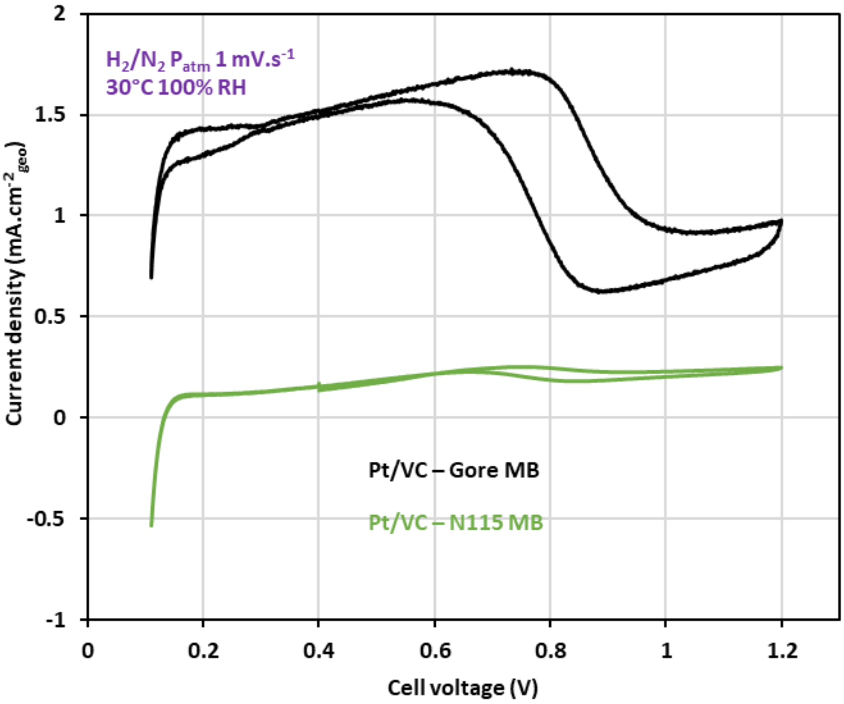

Figure III-17 : Third cycle of cyclic voltammetry performed at 1 mV.s^{-1} on MEA made of Pt/VC electrocatalyst.

A correction from H_2 crossover oxidation current may be done to get rid of its signature. The correction consists of subtracting the CV performed at 1 mV.s^{-1} to the one performed at 200 mV.s^{-1}. The CV corrected are shown on Figure III-18 ; such correction from the H_2 crossover current leads to a better definition of the Pt oxides region, by “erasing” the current density drop observed at 0.8 V on the raw CV with the use of a thin membrane. In addition, the CV are centred around the x-axis at 0.4 V: the contribution of capacitive current in that potential region largely dominates and enables a more relevant comparison between CV. The different coulometries in the H_{UPD} region and Pt oxides region originate from the different ECSA of the various cathode catalysts: 24 $m^2_{Pt}.g^{-1}_{Pt}$ for the black curve versus 29 $m^2_{Pt}.g^{-1}_{Pt}$ for the green curve. At higher loadings, the H_2 crossover current correction can be made considering a constant value of the H_2 crossover current (determined at 0.4 V) since the current generated by the Pt oxidation is around ten times higher or more than the current generated by the H_2 oxidation; overall, this procedure enables to limit the error made and the disruption on the CV description.

III.3 Very low loaded MEA (20 µgPt.cmgeo-2)

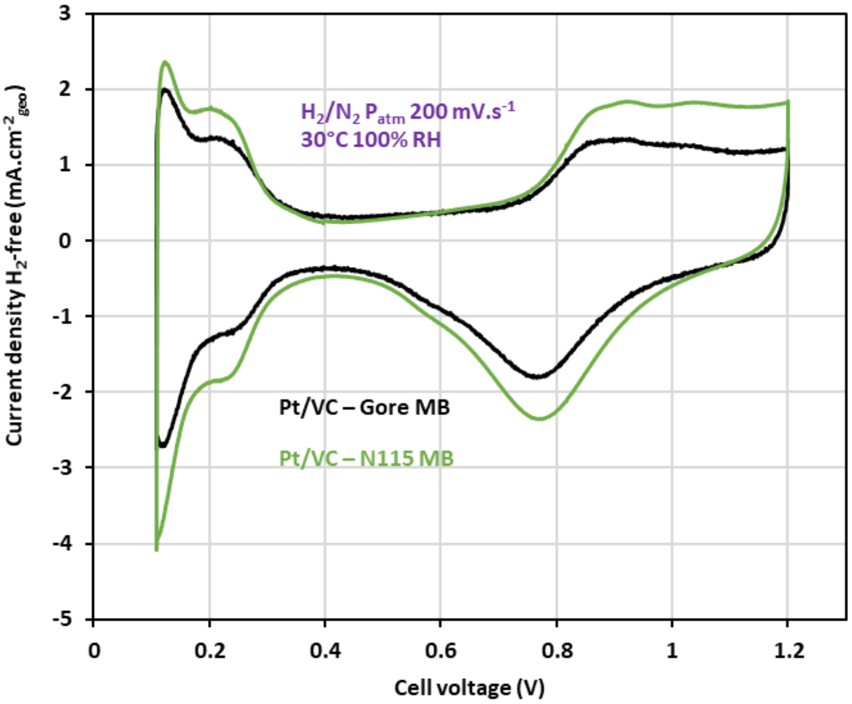

Figure III-18 : Cyclic voltammetries at 200 mV.s^{-1} corrected from the H_2 permeation current at 1 mV.s^{-1} based on the results from Figure III-16 and Figure III-17.

The following investigates the impact of H_2 crossover on performance measurements, under oxygenated atmosphere. Figure III-19 (a) shows the second cycle of polarization curves performed from OCV to 0.1 V on very low-loaded MEA made of Pt/VC electrocatalyst at the cathode, with a Gore MX 820.15 or a Nafion® 115 membrane at 80°C, 80% RH under H_2 (627 NmL.min^{-1})/ Air (1580 NmL.min^{-1}) at 1.34 bar abs. and 10 mV.s^{-1}. The curves are not corrected from ohmic drop. At low/medium current densities, the behaviour of the polarization curve is similar in both cases as most of Pt sites are probably already oxidized in air at these potentials. The use of a thick membrane (Nafion® 115) induces a larger high frequency resistance, resulting in a larger ohmic drop. This explains why the use of a thick membrane leads to worse performance at medium/low potentials. In fact, the real potential seen by the electrode is higher than the one showed on the polarization plot. The ohmic drop phenomenon with the use of thick membrane, and how to deal with it, will be discussed in section III.3.1.3. At voltage below 0.2 V, the current density starts to decrease in the case of a thin membrane. If there were only O_2 mass transport limitations, a constant limiting current would be observed, which should correspond to the current at 0.18 V (0.6 A.cm$^{-2}_{geo}$), potential at which the turning point is located on the black curve. Thus, this current density decrease means that an additional phenomenon is hindering the ORR in this potential region. In fact, the potential region below 0.4 V corresponds to the H_{UPD} region on the CV and the presence of H_2 in the cathode catalyst layer due to crossover phenomenon can generate proton species adsorbed on Pt sites at the cathode, coupled to the change of 4 to 2 electrons mechanism for ORR, may hinder the ORR; overall, both processes can explain the observed current drop. This phenomenon can also be observed in Rotating Disk Electrode measurements (see e.g. [13] for smooth (single-crystalline) Pt electrodes and [14] for Pt/C active layers).

Of course, the presence of H_2 at the cathode side decreases the OCV value, potential at which the polarization curve begins, as observed on the zoom at high potential/low current densities on Figure III-19 (a). The OCV value, defined by a mixed potential, is lower in the case of a thin membrane compared to a thick membrane, owing to the larger H_2 crossover in the former case, that tends to shift the OCV towards the H^+/H_2 equilibrium (roughly equal to 0 V *vs.* RHE in the PEMFC conditions). As a result, the OCV value under H_2/Air when using a thin membrane is equal to 0.79 V compared to 0.84 V in the case of a thick membrane Figure III-19 (b). This prevents the activities at 0.85, 0.9 and 0.95 V from being measured in the differential cell, which is a problem when a comparison with the activities obtained in RDE setup must be done.

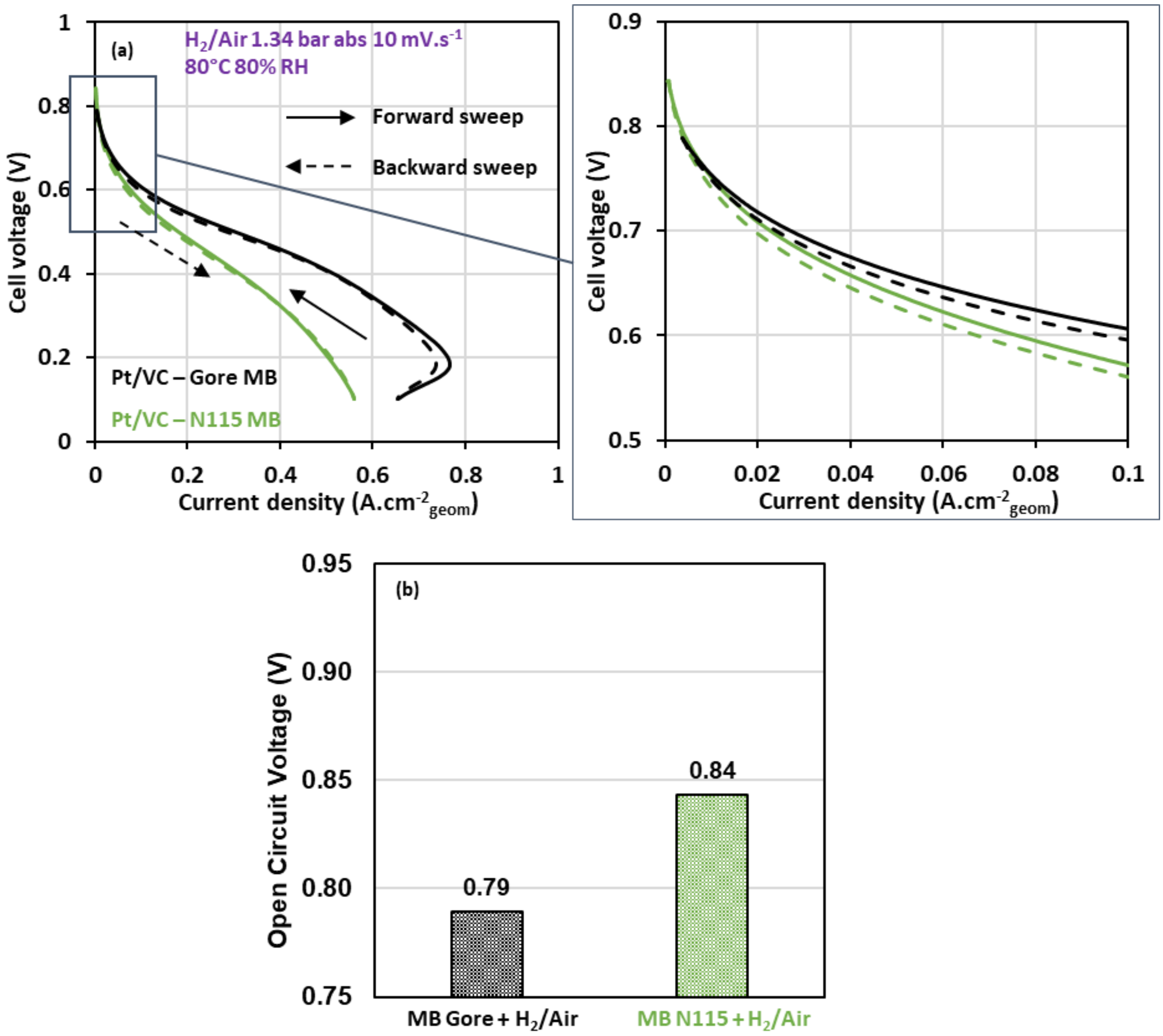

Figure III-19 : (a) Second cycle of polarization curves performed on MEA made of Pt/VC electrocatalyst with Gore MX 820.15 and Nafion® 115 membrane with a zoom at high potential/low current density (b) Open circuit values obtained in both cases.

Figure III-20 displays PEIS performed from 100 kHz to 0.1 Hz at 0.65 V on MEA made of Pt/VC electrocatalyst with a Gore MX 820.15 or a Nafion® 115 membrane at 80°C, 80% RH under H_2 (627 NmL.min^{-1})/Air (1580 NmL.min^{-1}) at 1.34 bar abs.; a zoom at high frequencies is also given. First, the use of a thick membrane leads to a higher high frequency resistance, around 140 mΩ for the green curve, than the use of a thin membrane, around 25 mΩ for the black curve, as shown on the zoom of the Figure III-20. As it was previously said, the use a thick membrane leads also to a bigger ohmic drop, resulting in a cathode potential which is higher in the case of a thick membrane than with a thin membrane at a given cell voltage, and thus a Pt more oxidized that may hinder the ORR. This may explain the differences between the R_{ct} values at low frequencies.

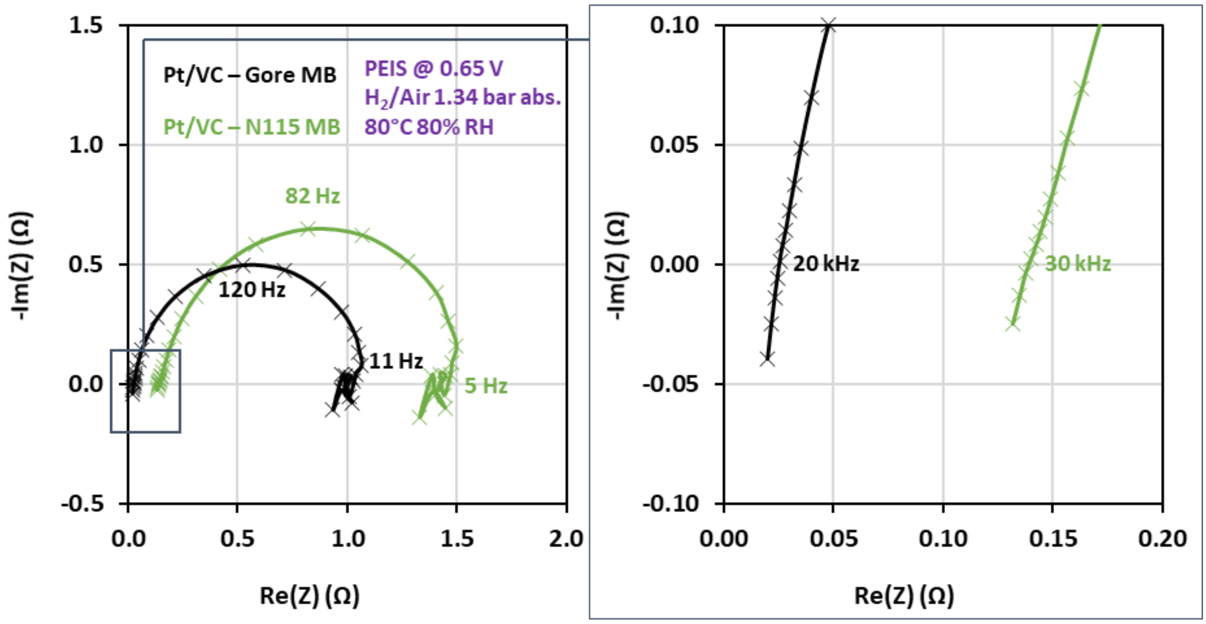

Figure III-20 : PEIS performed at 0.65 V on MEA made of Pt/VC electrocatalyst with Gore MX 820.15 and Nafion® 115 membrane with a zoom at high frequencies.

These results showed that the use of a thick membrane is relevant to perform electrochemical measurements on very low loaded catalyst layer in the DC setup, as it partially mitigates the H_2 crossover phenomenon that disturbs the measurements in a significant way. Moreover, mitigating the H_2 crossover allows elevating the OCV value, which is convenient for activity measurements at high potential. Thus, the results presented in the next sections related to very low-loaded MEA are obtained using a thick membrane.

III.3.1.2 H_2/Air vs. H_2/O_2 configuration

In fuel cell stacks, air is usually used as gas reactant at the cathode side to avoid an additional O_2 tank. In the case of small cell, both air and pure oxygen as gas reactant can be easily used. In this section, the impact of air *vs.* pure oxygen as oxidant is investigated when characterizing very low loaded catalyst layers. Figure III-21 (a) shows the second cycle of polarization curve performed on MEA made of Pt/VC electrocatalyst with Nafion® 115 membrane under H_2/Air and H_2/O_2 configurations and a zoom a high potential/low current density. Between the two configurations, there are near 5 times more dioxygen in the case of O_2 pure as oxidant. As it was already seen with the FURTHER MEA, multiplying the O_2 concentration by five does not lead to a five times higher current density production. At low potential, on the green curve, which was obtained under H_2/Air configuration, an inflexion point is observed near 0.3 V, which is not present on the blue curve. This may be explained by some mass transport limitation that happen earlier in the case of a gas reactant

5 times less concentrated in oxygen. Figure III-21 (b) displays the OCV value obtained in both configurations. In the case of pure O_2 as oxidant, the OCV value reaches potential above 0.9 V, allowing activity measurement at 0.9 V, which is not the case in H_2/air configuration. The use of pure oxygen increases the OCV value, as the activation losses are reduced and the mixed potential is shifted closer to the equilibrium potential of O_2/H_2O.

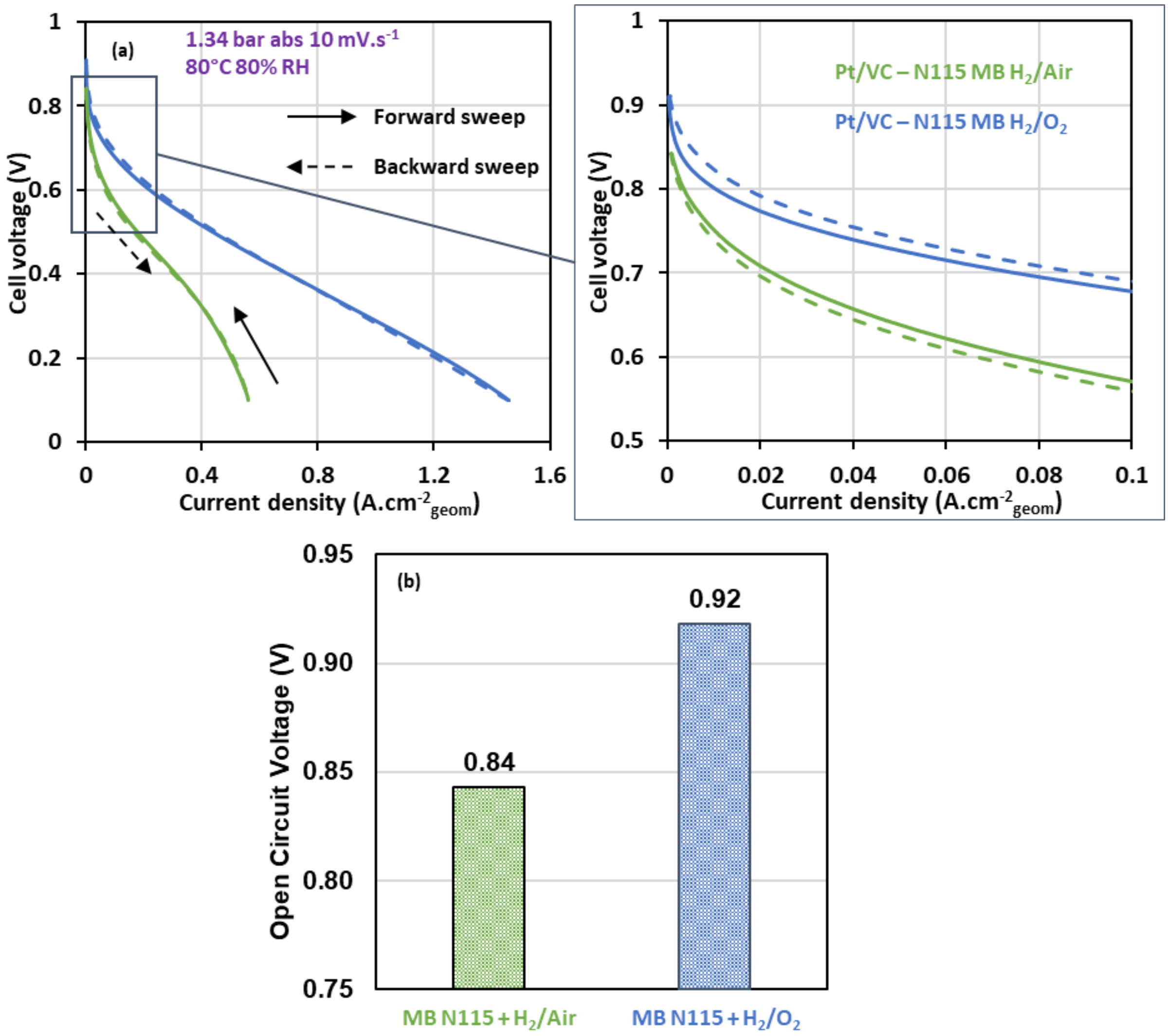

Figure III-21 : (a) Second cycle of polarization curves performed on MEA made of Pt/VC electrocatalyst with Nafion® 115 membrane in H_2/Air and H_2/O_2 configurations with a zoom at high potential/low current density (b) Open circuit values in both gas reactant configurations.

Figure III-22 shows the different impedance spectra plotted at 0.3, 0.5, 0.65 and 0.8 V in both gas reactant configurations. Depending on the potential, the difference between values can go up to 15% in the case of the PEIS performed at 0.3 V. This can be explained, though: in the case of pure O_2 gas reactant, more current thus more water is produced, which is favourable to the proton conduction of the membrane and leads to a lower R_{HF} value than in the case of air as gas reactant. Depending on the potential, more heat generation can locally occur, which leads to more important local drying in the catalyst layer and affects the (local) conductivity of the membrane. Regarding the semicircle related to the ORR, no matter the potential, in the case of pure O_2, the charge transfer resistance R_{ct} is lower than in the case of air, meaning that the kinetic and/or mass transport related to ORR is improved compared to the air supply.

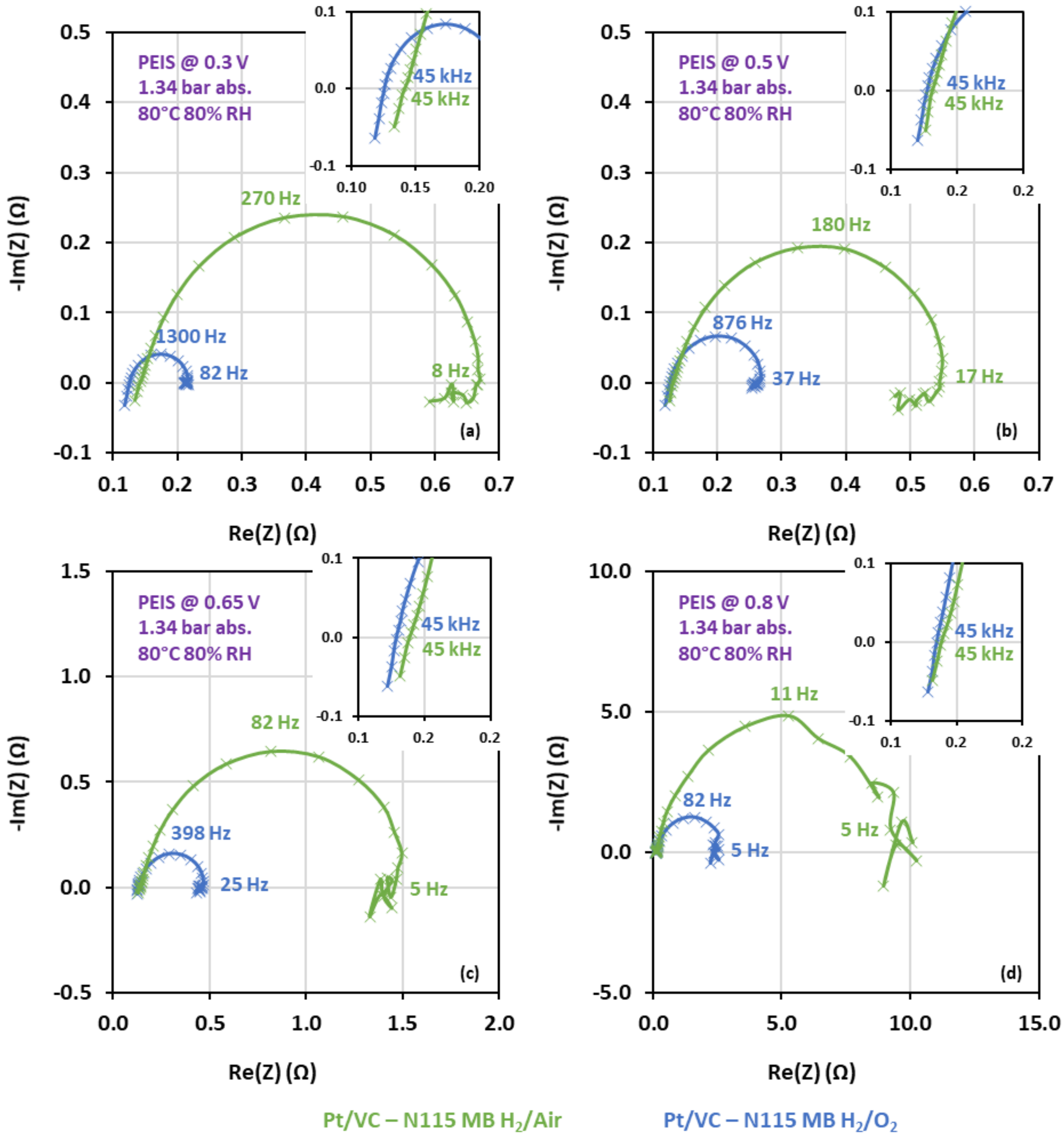

Figure III-22 : PEIS performed at (a) 0.3 V (b) 0.5 V (c) 0.65 V and (d) 0.85 V on MEA made of Pt/VC electrocatalyst with Nafion® 115 membrane with a zoom at high frequencies under H_2/Air and H_2/O_2 configurations.

These observations between H_2/air and H_2/O_2 configurations led to the choice of pure O_2 as gas reactant for very low loaded catalyst layer characterizations. Indeed, the use of pure O_2 allows intrinsic activity measurements at 0.9 V in differential cell (and also minimize the O_2 mass-transport issues), which is a point of interest in this work to be capable to compare the RDE and DC setups. In addition, even if the environment and the transport properties are different, pure O_2 is also used in RDE (dissolved in the electrolyte), which makes the operating conditions closer and the DC/RDE comparison more relevant. Finally, because the use of pure O_2 allows to get rid (to a certain extent) of the mass transport limitation, it also eases the modeling for the active layers. In the next sections, the H_2/O_2 configuration is retained.

III.3.1.3 Performance measurements and ohmic drop correction method

This section deals with the ohmic drop correction method and its impact on the performance measurements. At first, the ohmic drop correction was done by considering the average R_{HF} value obtained from PEIS performed at several potentials along the polarization curve (Figure III-23 (a) and (b)). There is an evolution of the R_{HF} along the polarization curve, according to the applied/measured cell voltage. Indeed, depending on the cell voltage, more or less current density is produced, resulting in more or less water production and heat generation. These different quantities of water and heat produced affect the hydration state of the membrane and ionomer, leading to (slight) changes for R_{HF} values (Figure III-23 (b)): R_{HF} varies from around 136 mΩ at 0.85 V to 126 mΩ at 0.3 V. At very low loadings, the R_{HF} variation is slightly less than 10%; however, at higher loadings, and depending on the operating conditions, the R_{HF} variation may reach up to 50%, as seen in the case of FURTHER MEA at 80°C, 50% RH for instance (see Figure III-13 (c)). This could result in inaccurate ohmic drop correction at high or low current densities if an averaged R_{HF} value was considered for the correction, this averaged value not being representative of the real hydration state in all current density regions. In the end, considering the averaged R_{HF} value at different potentials along the polarization curve may not be suitable for ohmic drop correction and relevant performance measurements.

III.3 Very low loaded MEA (20 µgPt.cmgeo-2)

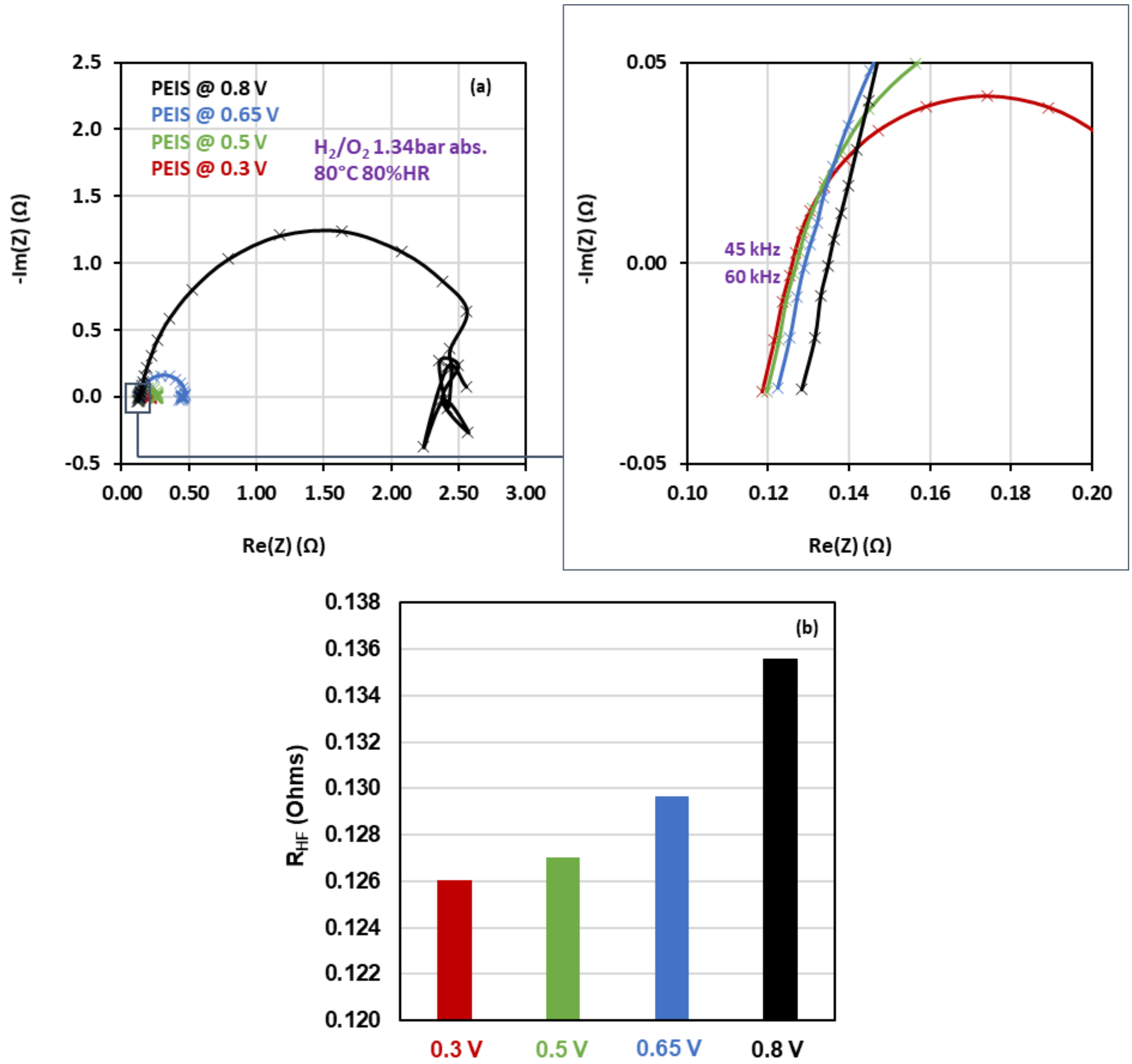

Figure III-23 : (a) PEIS performed at 0.3 V, 0.5 V, 0.65 V and 0.85 V on MEA made of Pt/VC electrocatalyst with Nafion® 115 membrane with a zoom at high frequencies under H_2/O_2 configuration and (b) the corresponding R_{HF} values.

In addition to the fact that the hydration state of the membrane/catalyst layer vary along the polarization curve, the hysteresis phenomenon observed on experimental polarization curves can be partly explained by different hydration states of the ionomer in the membrane and in the catalyst layer between the forward and backward sweeps. Consequently, these impedance spectra obtained after a potentiostatic conditioning step for 2 min before the measurements do not necessarily give information on the dynamic evolution of the hydration state and resistance values between the two sweeps.

In that context, it was decided to perform polarization curve by 'fast' potential impedance steps, every 50 mV. In addition to the performance measurement, it gives insights into the evolution of the high frequency resistance at each potential step along the forward sweep, but also along the backward sweep of the polarization curve. Considering a polarization curve from OCV (around 0.9 V) to 0.1 V, 16 PEIS are performed, every 50 mV, on the forward sweep and another 16 PEIS on the backward sweep. The potential is set for 3 seconds to avoid the influence of capacitive current due to the step transitions and then the PEIS is done from 50 kHz to 1 kHz with 10 mV amplitude. The other acquisition parameters are adjusted in order to make each PEIS step lasts 6-7 seconds, maximum. This methodology enables to perform a polarization curve by fast PEIS steps at a rather "equivalent rate" than a dynamic polarization curve (e.g. similar sweeping rate and overall duration of the characterization). Thus, an ohmic drop correction point by point is possible and leads to a more accurate ohmic drop corrected performance measurement keeping the same duration. Figure III-24 shows a comparison between both methods to perform a polarization curve: we obtain the exact same i-V characteristics, as well as the small hysteresis between the forward and the backward sweeps, which validates the experimental protocol of the method by PEIS steps. In addition, for each step, a R_{HF} value can be estimated and used for "local" ohmic drop correction (the respective one at each potential step). For all the PEIS steps, the R_{HF} value is taken at a frequency of 26 kHz, which is the frequency leading to a value of impedance that is the closest to the x-axis (in the high frequency domain).

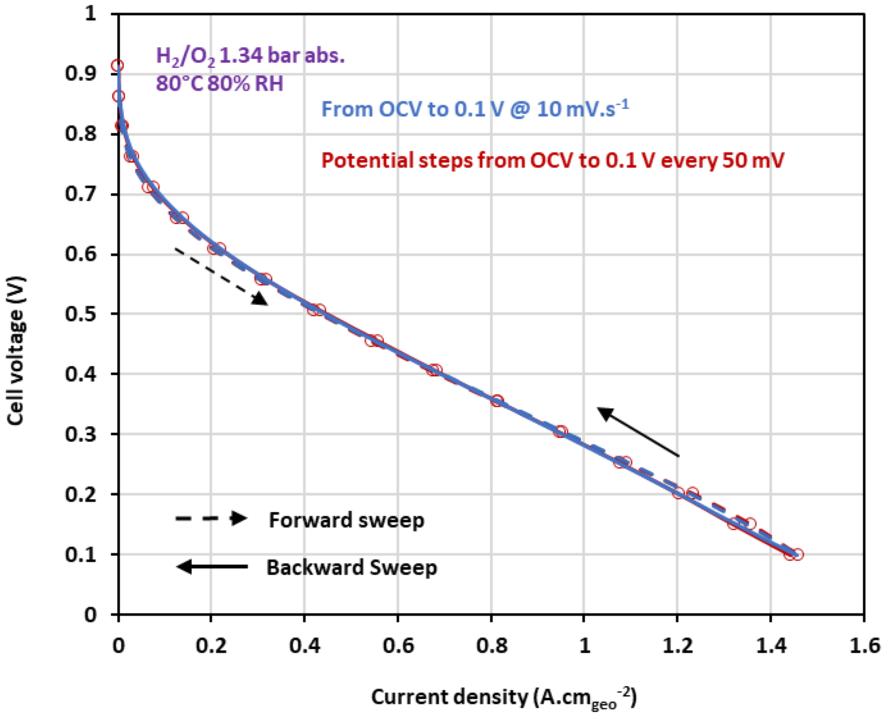

Figure III-24 : Comparison of the second cycle of polarization curves performed on MEA made of Pt/VC electrocatalyst with Nafion® 115 membrane with the dynamic method (lines) and by PEIS steps (symbols).

Figure III-25 shows a comparison between the averaged R_{HF} values obtained from the PEIS performed at 0.3, 0.5, 0.65 and 0.8 V along the polarization curve and the R_{HF} evolution at each PEIS. There is an effective change of the high frequency resistance along the polarization curve but also a hysteresis between the two sweeps.

III.3 Very low loaded MEA (20 µgPt.cmgeo-2)

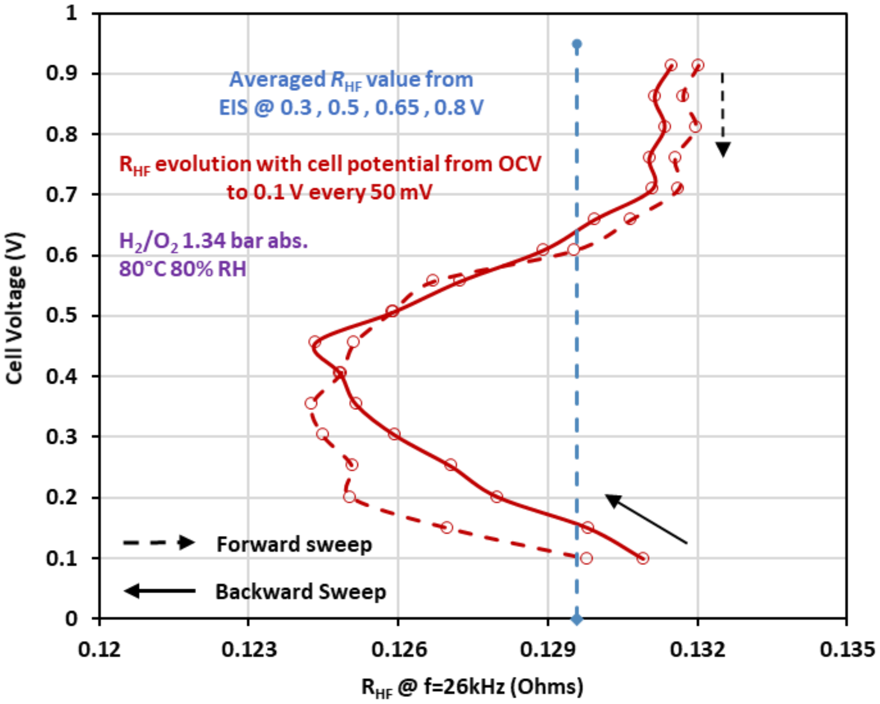

Figure III-25 : Comparison of the averaged R_{HF} value obtained from the PEIS along the polarization curve and the RHF evolution with potential obtained from the PEIS steps.

Figure III-26 shows a comparison between the dynamic polarization curve, ohmic drop corrected from the averaged R_{HF} value obtained from the PEIS performed at 0.3, 0.5, 0.65 and 0.8 V, and the polarization curve made by PEIS steps with correction from the R_{HF} value at each step of the polarization curve. In this case of very low loaded catalyst layers and R_{HF} variation less than 10%, both correction methods lead to similar ohmic drop corrected polarization curves. Nevertheless, the correction point by point is still more accurate, as it is representative of the real hydration state of the membrane at each point of the polarization curve. One should note that the ohmic drop is quite important in these tests: the real potential seen by the cathode catalyst layer does hardly go below 0.45 V, due to the use of a thick membrane, that increases the high frequency resistance, while the use of pure O_2 increases the current density produced. Thus, the almost complete reduction of Pt oxides is hardly reached in that case.

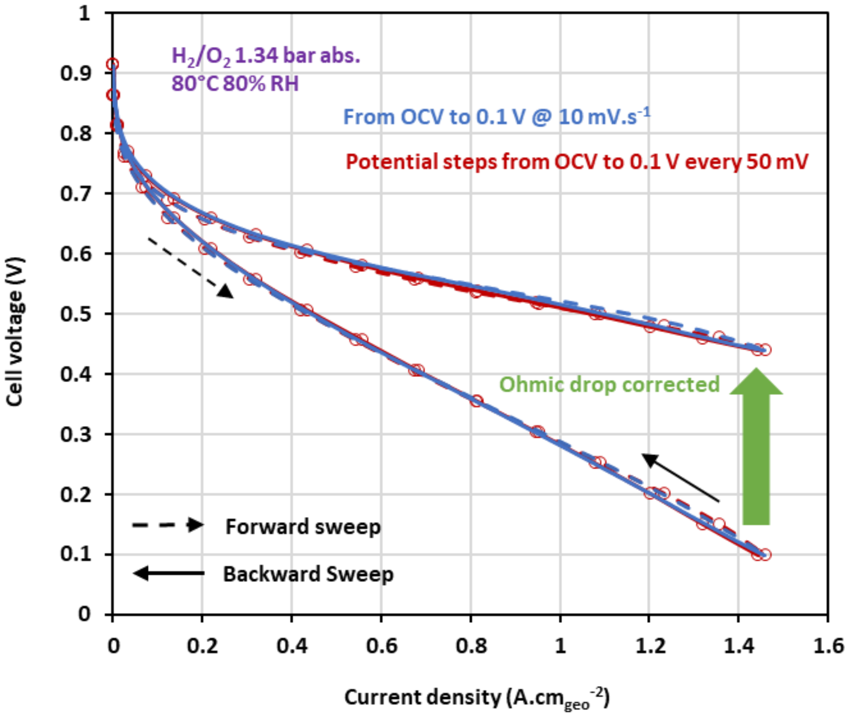

Figure III-26 : Comparison of the second cycle of polarization curves performed on MEA made of Pt/VC electrocatalyst with Nafion® 115 membrane with the dynamic method and by PEIS steps including the ohmic drop corrected curve.

In the next sections, the performance characterizations are done by PEIS steps in order to make the most accurate and relevant dynamic measurements and ohmic drop correction on forward and backward sweeps. Moreover, these data are computed with the models, and thus, will be used to validate the improvements of model description.

III.3.2 Electrocatalytic features comparison at 25 and 60°C between the electrochemical setups

The previous section highlighted the different issues encountered with electrochemical characterizations on very low loaded MEA. It also helped to define the operating conditions and components to perform the most accurate and reliable electrochemical measurements on very low loaded catalyst layer in differential cell setup in order to: i) make a relevant comparison between the RDE setup and the DC setup regarding the electrocatalytic features of the materials studied in this work and ii) help validating the modeling description improvements that will be presented in the Chapter IV. In this section, the ECSA and the different activity of Pt/VC, Pt_3Co/VC, Pt/GC and Pt/HSAC electrocatalysts obtained from characterizations of very low loaded catalyst layers in differential cell at 30°C, 100% RH and 60°C, 100% RH are shown. The comparison with the results obtained in RDE setup is also discussed.

III.3.2.1 ECSA comparison

All the results presented in this section are obtained at 30 and 60°C with fully hydrated gas reactants, to have operating conditions and experimental environment as close as possible as in the RDE setup. Figure III-27 shows the ECSA values obtained via proton desorption in H_{UPD} region of cyclic voltammetry performed between 0.11 and 1.2 V at 200 mV.s^{-1} under H_2/N_2 configuration for all the electrocatalysts at 30°C, 100% RH and at 60°C, 100% RH in differential cell. The temperature increase seems to lead to lower ECSA values for all the electrocatalyst, as it was observed in RDE setup. Here again, this may be explained by the use of the specific coulometry value for bulk Pt (25°C/liquid electrolyte) for proton desorption that may not be strictly equal to 210 $\mu C.cm_{Pt}^{-2}$ at 60°C. Regarding the dispersion for the Pt/HSAC electrocatalyst, only two MEA were characterized in this work (instead of three MEA for the others when writing these lines.

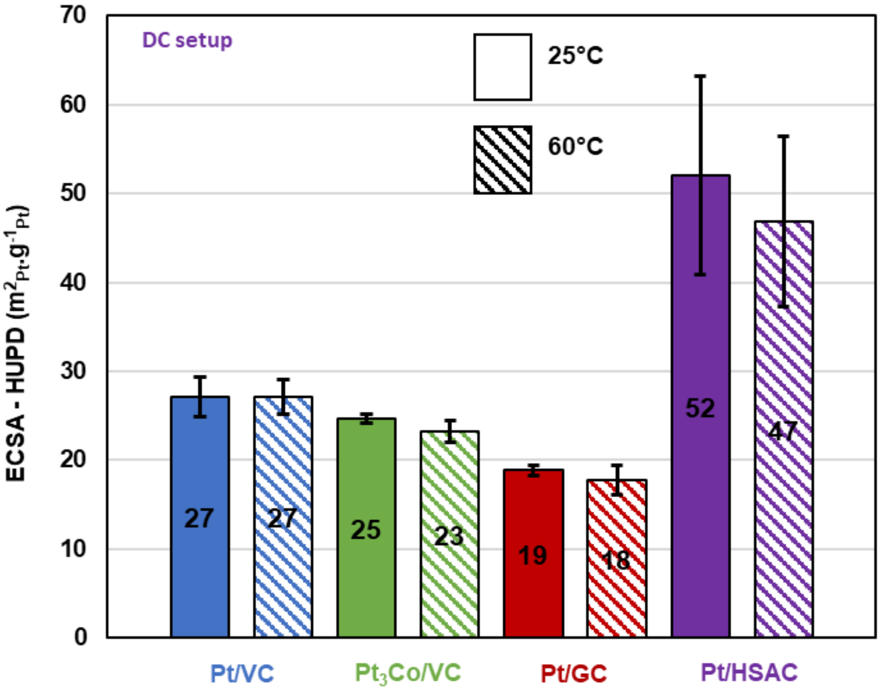

Figure III-27 : ECSA values of all the electrocatalysts obtained in differential cell setup at 30°C, 100% RH and 60°C, 100% RH.

Figure III-28 (a) and (b) displays a comparison of the ECSA values obtained in RDE and in DC setups at 25°C(RDE)/30°C(DC) and at 60°C, respectively, via proton desorption for both setups. In differential cell, the ECSA value was assessed at 30°C instead of 25°C due to bubbler temperature controlling limitations. At 25°C/30°C, the ECSA is higher in RDE for all the electrocatalysts than in DC, except for the Pt/GC electrocatalyst, for which wettability issues were observed in RDE, resulting in a very low ECSA value. In fact, in differential cell, it is not possible to go as low as 0.05 V during the potential cycling (as in RDE), especially at high sweeping rate, because of the H_2 production on the cathodic sweep and the H_2 oxidation on the anodic sweep; the related HER and HOR currents at these low potential values would severely affect the determination of the ECSA value. This may explain why lower ECSA values are measured in DC at 30°C compared to those obtained in RDE at 25°C, especially for the Pt/VC and Pt/HSAC catalysts. In addition, the difference between RDE and DC for Pt/VC electrocatalyst is quite surprising at low temperature (factor 2), which is not observed for the other electrocatalysts (Figure III-28 (a)). This might be related to the catalyst layer formulation or structure. At 60°C, the differences of the ECSA values between the two setups seem to be partially mitigated. However, in both electrochemical setups, the proton adsorption/desorption coulometry is decreasing with temperature due to modified proton adsorption/desorption properties. To have a better comparison of ECSA values between the two setups, it would have been more interesting to compare the values obtained from CO-stripping measurements, but it could not have been done in DC setup due to safety issue and availability of the test bench allowing such measurements.

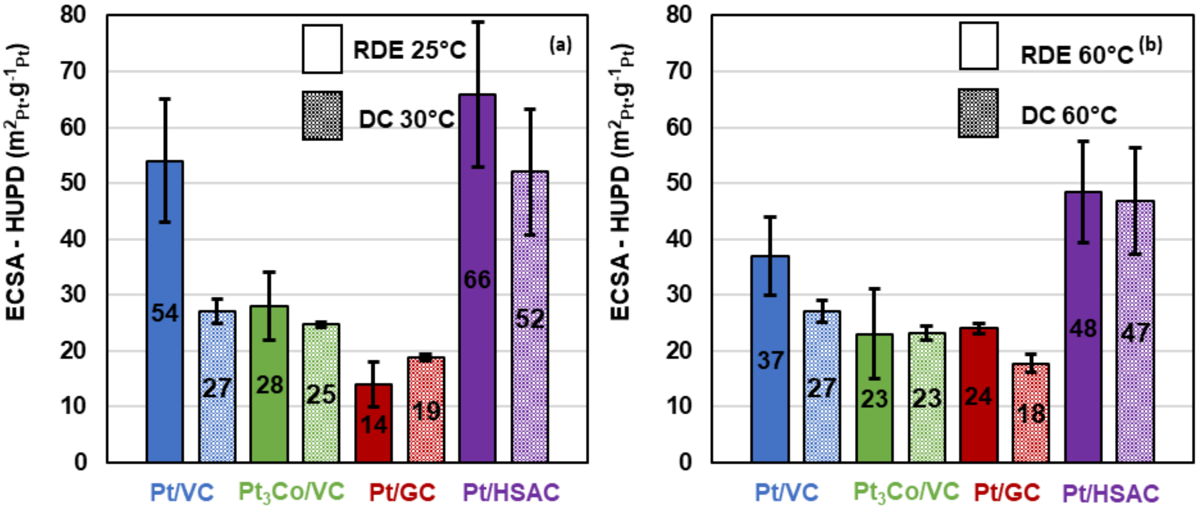

Figure III-28 : (a) Comparison of ECSA values of all the electrocatalysts obtained in differential cell setup at 30°C, 100% RH and in RDE setup at 25°C and (b) (a) comparison of ECSA values of all the electrocatalysts obtained in DC setup at 60°C, 100% RH and in RDE setup at 60°C.

III.3.2.2 Activity comparison

Activity measurements at high potential are done in differential cell by using thick membrane and under O_2 supply at the cathode, which elevate the OCV value. Even though the real PEMFC operation usually occurs around 0.6-0.7 V, this ORR activity measurement in DC at high cell voltage (high cathode potential) is important to compare the two electrochemical setups. Thus, in addition to the activities measured at 0.9 and 0.85 V (as in RDE), activities at 0.8, 0.7 and 0.6 V are also shown for the electrocatalysts characterized in DC (these lower potential values not being accessible in RDE). All the activities in DC are assessed after ohmic drop correction. Figure III-29 shows the specific activity assessed at different cathode potentials in differential cell at 30°C, 100% RH and 60°C, 100% RH for all the electrocatalysts. For the sake of clarity, in the Tafel representation of the impact of temperature between 25 and 60°C, the specific activity values at 60°C are slightly shifted towards positive potential. As in RDE, be it at 30 or 60°C, the Pt_3Co/VC outperforms the other electrocatalysts, except at 0.6 V, potential at which it is caught up by the Pt/GC and, in a lesser extent, the Pt/VC. Again, as in RDE, the Pt/HSAC seems to show the worst performance, due to its high ECSA value (small Pt particles size), no matter the potential and considering the dispersion at 30 and 60°C. Pt/GC and Pt/VC seem to have similar trend regarding the specific activity, at 30 and 60°C. For all the electrocatalysts, the temperature increase leads to better specific activity, which is mainly explained by the enhancement of the ORR kinetics at higher temperature that reduces the activation losses, as it was seen on the FURTHER MEA. Finally, at 0.7 V, an inflexion point seems to be observed, which marks the transition between the activation region at potential above 0.8 V, where the proton and oxygen mass transport limitations are negligible (in DC) and the region at potential below 0.7 V where these mass transport limitations may no longer be negligible.

III.3 Very low loaded MEA (20 µgPt.cmgeo-2)

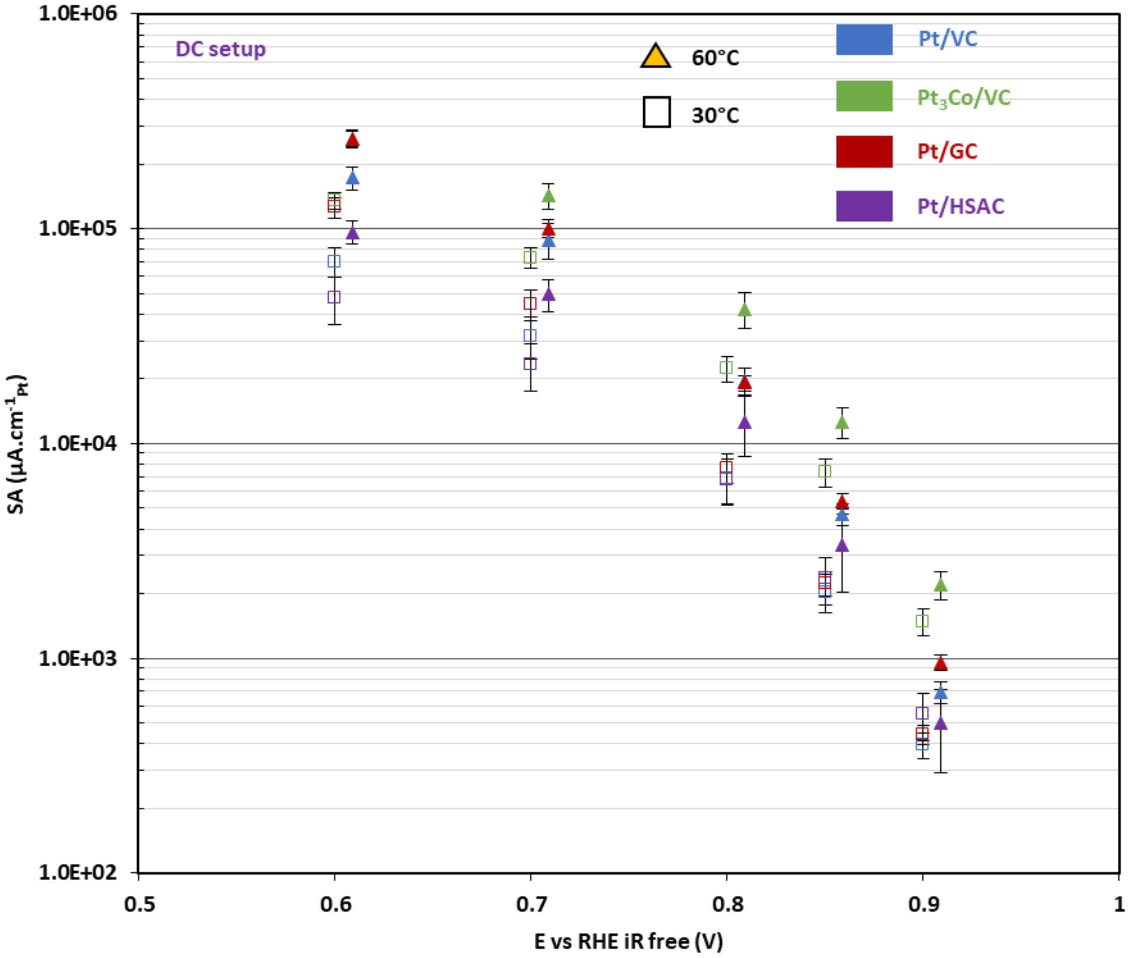

Figure III-29 : Tafel representation of specific activity values at 0.9, 0.85, 0.8, 0.7, and 0.6 V obtained in differential cell setup at 30°C, 100% RH and 60°C, 100% RH for all the electrocatalysts. For better visualization between 25 and 60°C, the activity values at 60°C are slightly shifted towards positive potential.

Figure III-30 shows a comparison between the specific activity obtained in RDE and DC setups for all the electrocatalysts. For each electrocatalyst, and each potential, the specific activity obtained in differential cell is higher than in RDE. In fact, the global ECSA obtained in DC are lower than the ECSA obtained in RDE, which would (at least partially) explain the aforementioned observation. In addition, the differences may also be explained by the faster O_2 mass transport in differential cell: mass transport in differential cell occurs mostly in gaseous phase, followed by diffusion through the ionomer/water film recovering the Pt actives sites, instead of dissolved gas reactant in liquid electrolyte, with a limited O_2 concentration and smaller diffusion coefficient. One should note that at 0.85 V, the Pt/VC and Pt/GC electrocatalysts have similar activities in both RDE and DC setups at low temperature. This is not the case for Pt/HSAC, which shows higher specific activity in DC than in RDE at 0.85 V. Thus, the specific activity measured in RDE might not be representative of the one in catalyst layer configuration for all the electrocatalysts.

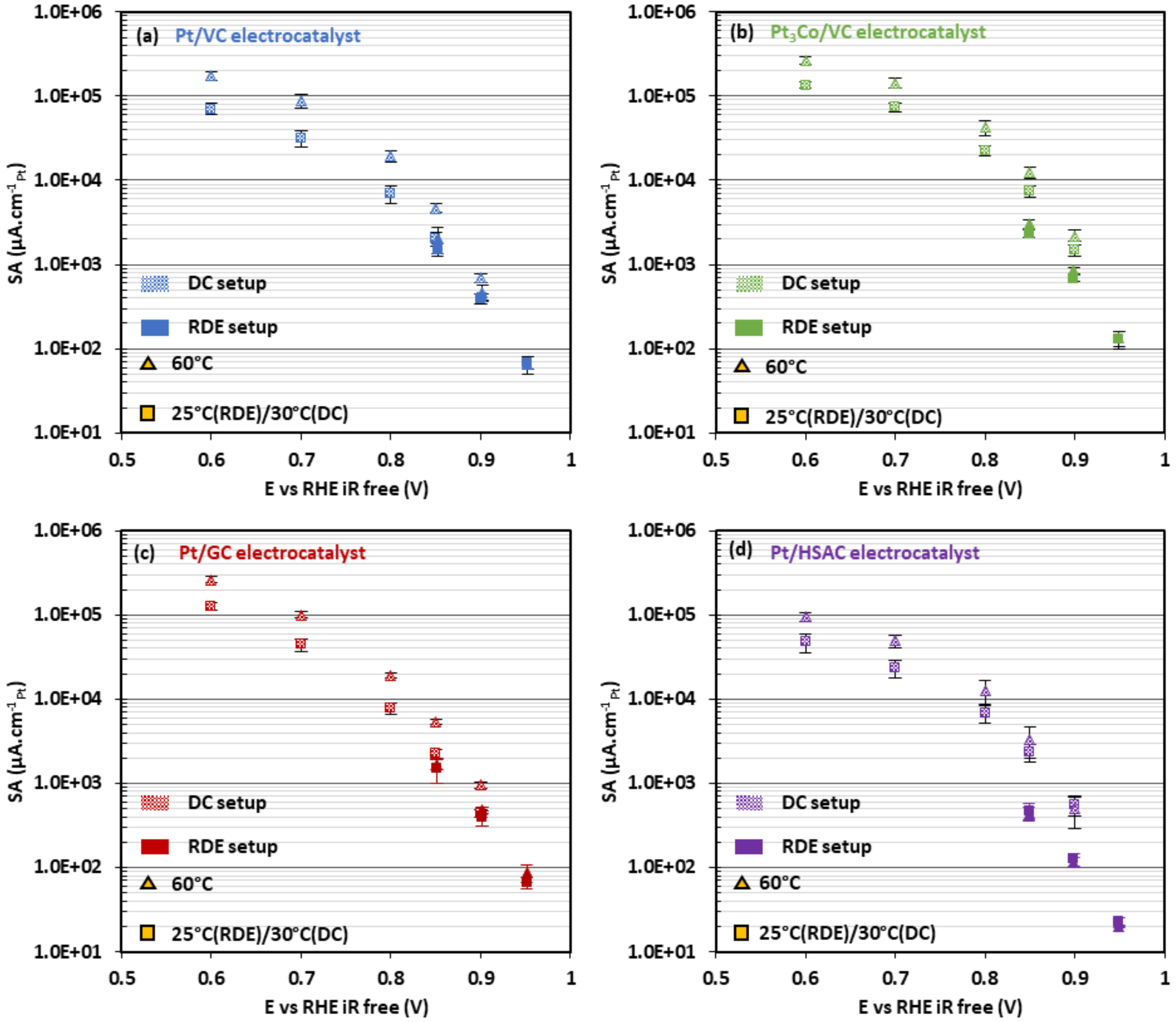

Figure III-30 : Tafel representation of specific activity values at 0.9, 0.85, 0.8, 0.7, and 0.6 V obtained in differential cell setup at 30°C, 100% RH and 60°C, 100% RH and specific activity values at 0.95, 0.9 and 0.85 V obtained in RDE setup at 25 and 60°C for (a) Pt/VC (b) Pt3Co/VC (c) Pt/GC and (d) Pt/HSAC.

III.3 Very low loaded MEA (20 µgPt.cmgeo-2)

Figure III-31 shows the mass activity assessed at different potentials in differential cell at 30°C, 100% RH and 60°C, 100% RH for all the electrocatalysts. As previously, for better visualization in Tafel representation of the impact of temperature between 25 and 60°C on the mass activity, the values at 60°C are graphically shifted towards positive potential. Be it at 30 or 60°C, over the whole potential range, the Pt_3Co/VC electrocatalyst outperforms the others in terms of mass activity. Pt/HSAC shows higher mass activity than Pt/VC and Pt/GC electrocatalysts, owing to its smaller Pt particles size (better Pt dispersion), which positively counters the well-known particle size effect mentioned in the RDE section. As for the specific activity, for all the electrocatalysts, the temperature increase leads to higher mass activity values: the ORR kinetic is enhanced by the temperature with a smaller gap at 0.6 V than at the other potential. Finally, the same inflexion point is present at 0.7 V as witnessed for the specific activity data.

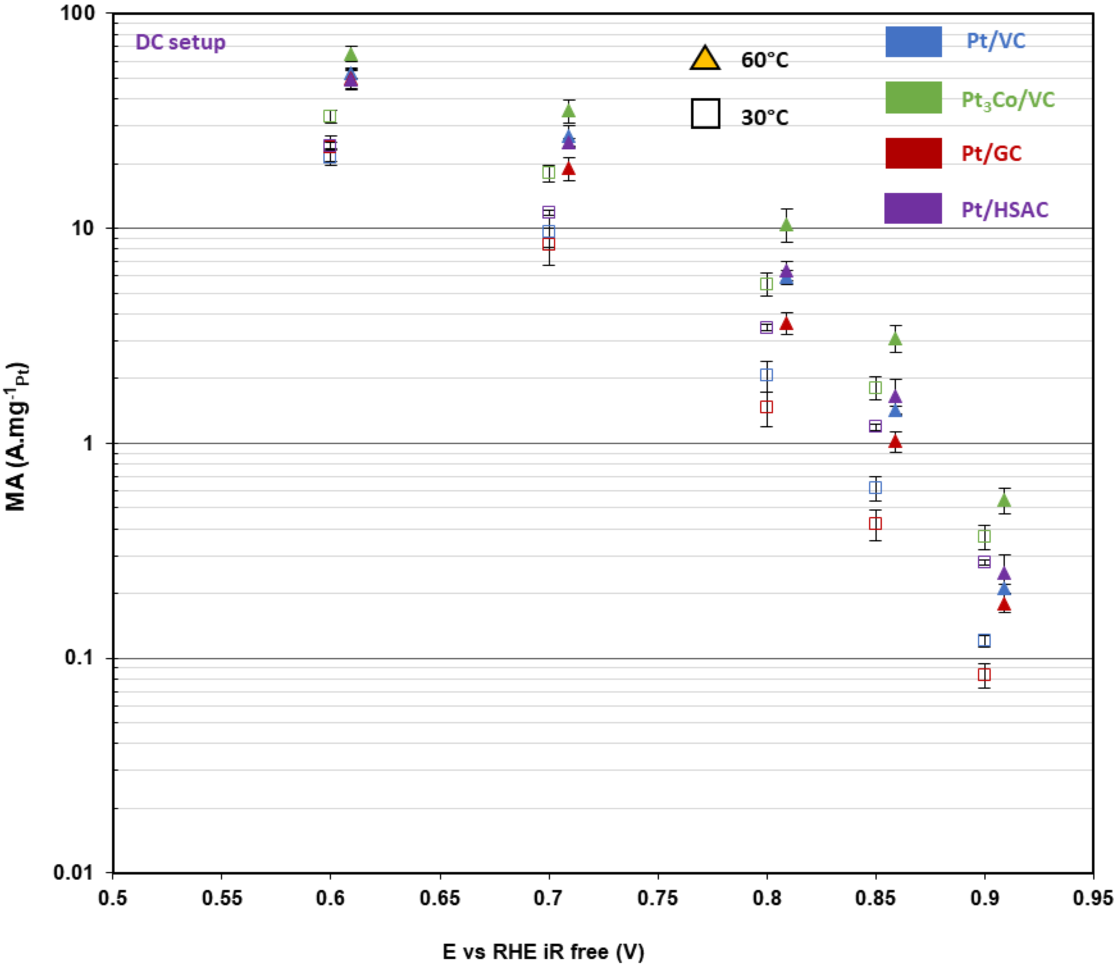

Figure III-31 : Tafel representation of mass activity values at 0.9, 0.85, 0.8, 0.7, and 0.6 V obtained in differential cell setup at 30°C, 100% RH and 60°C, 100% RH for all the electrocatalysts. For better visualization between 25 and 60°C, the activity values at 60°C are slightly shifted towards positive potential.

Figure III-32 shows a comparison between mass activity obtained in RDE and DC setups for all the electrocatalysts. For Pt_3Co/VC and Pt/HSAC, the mass activity obtained in differential cell seem to be higher than in RDE at 0.9 and 0.85 V (Figure III-32 (b) and (d), respectively). On the contrary, Figure III-32 (a) and (c) shows that Pt/VC and Pt/GC have worse mass activities in differential cell than in RDE setup at high potential. In addition, the different materials do not behave in the same way between the two setups. At 0.9 and 0.85 V, the differences observed regarding the mass activities are less significant between the two setups for Pt/VC and Pt/GC (factor 2-3), while the gap is much larger for Pt_3Co/VC and Pt/HSAC (factor 7-8).

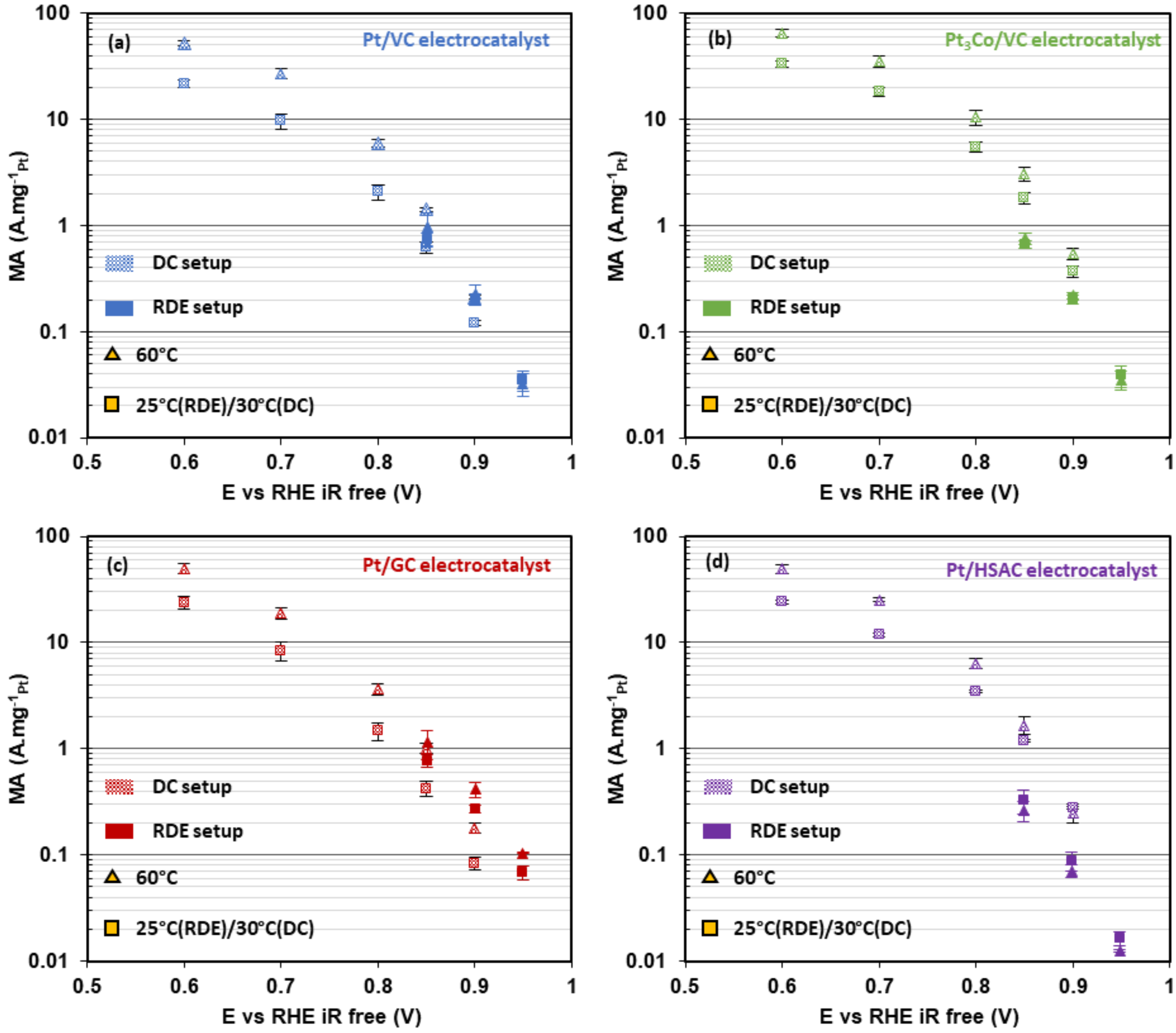

Figure III-32 : Tafel representation of mass activity values at 0.9, 0.85, 0.8, 0.7, and 0.6 V obtained in differential cell setup at 30°C 100% RH and 60°C 100% RH and specific activity values at 0.95, 0.9 and 0.85 V obtained in RDE setup at 25°C and 60°C for (a) Pt/VC (b) Pt_3Co/VC (c) Pt/GC and (d) Pt/HSAC.

Overall, this set of data shows that the DC setup is capable to access the intrinsic ORR activities as the RDE does, with the advantage of enabling measurements in the same cell voltage (0.6 < cathode potential < 0.9 V *vs*. RHE) interval as for real PEMFC operation (which the RDE cannot, owing to the detrimental mass transport limitation experienced below 0.85 V *vs*. RHE). For this reason, the DC results will be used for the modeling of Chapter IV. However, RDE and DC setups may lead to significant different specific or mass activity values depending on the electrocatalyst (Pt/HSAC at 0.85 V *vs*. RHE for instance). It seems that the RDE might minimize the real "gains" in fuel cell and catalyst layer configuration at low current density/high potential. In addition, the mass activity measured at 0.6 V is close for all the electrocatalysts. This might be related to the formulation or structure effect of catalyst layer (catalyst layers manufactured by spray coating for all the electrocatalyst).

III.4 Focus on Pt/VC and Pt/HSAC electrocatalysts – Very low loaded catalyst layers

The next results focus on the Pt/VC and Pt/HSAC electrocatalysts. The same electrochemical characterizations as shown previously are performed under more various operating conditions, in order to better understand how the very low loaded catalyst layers behave/operate, so as to feed the models of Chapter IV. In that frame, the impact of the temperature and relative humidity on the qualitative coverage ratio of Pt surface oxides obtained via cyclic voltammetry under H_2/N_2 configuration will be investigated for both electrocatalysts. In addition, the ECSA value, the performance as well as the R_{HF} evolution along the polarization curve under these various operating conditions will be also shown and discussed. The electrochemical characterizations and results that will be presented is this section are used to refine and validate the model description of the Chapter IV.

III.4.1 Under inert atmsophere

III.4.1.1 Impact of operating conditions on the ECSA value

This section deals with the impact of the operating conditions on the ECSA value for both Pt/VC and Pt/HSAC very low loaded catalyst layers. Figure III-33 shows the ECSA values obtained under the different operating conditions calculated via the proton desorption coulometry. First, for both Pt/VC and Pt/HSAC, at constant relative humidity, the ECSA values decrease with temperature and at constant temperature, the ECSA values increase with the relative humidity. These trends were already observed and explained in the case of the FURTHER MEA. The loading does not seem to affect the behaviour described above. Then, the Pt/HSAC shows a higher ECSA than the Pt/VC, which was already the case in RDE but to a lesser extent. It was already explained why the ECSA value obtained in DC is lower than in RDE. However, it seems that the Pt/HSAC is not as affected as Pt/VC by the electrochemical setup and the electrochemical protocol used to assess the ECSA. A hypothesis to account for this is that the HSAC carbon support is more microporous, hence more compatible with capillary water retention (even in polymer electrolyte environment), rendering the Pt nanoparticles of Pt/HSAC more accessible to proton adsorption/desorption DC setup than for the Pt/VC electrocatalyst, which is more hydrophobic [20], [21]. Of course, in fully flooded active layers in

RDE, such differences of water retention are not present, at least between the HSAC and the VC supports, which are not very hydrophobic, and for which the active layers are well (fully) wetted by the liquid electrolyte. Finally, it must also be recalled that the ECSA dispersion for the Pt/HSAC is quite large, because only two MEA were characterized at that stage.

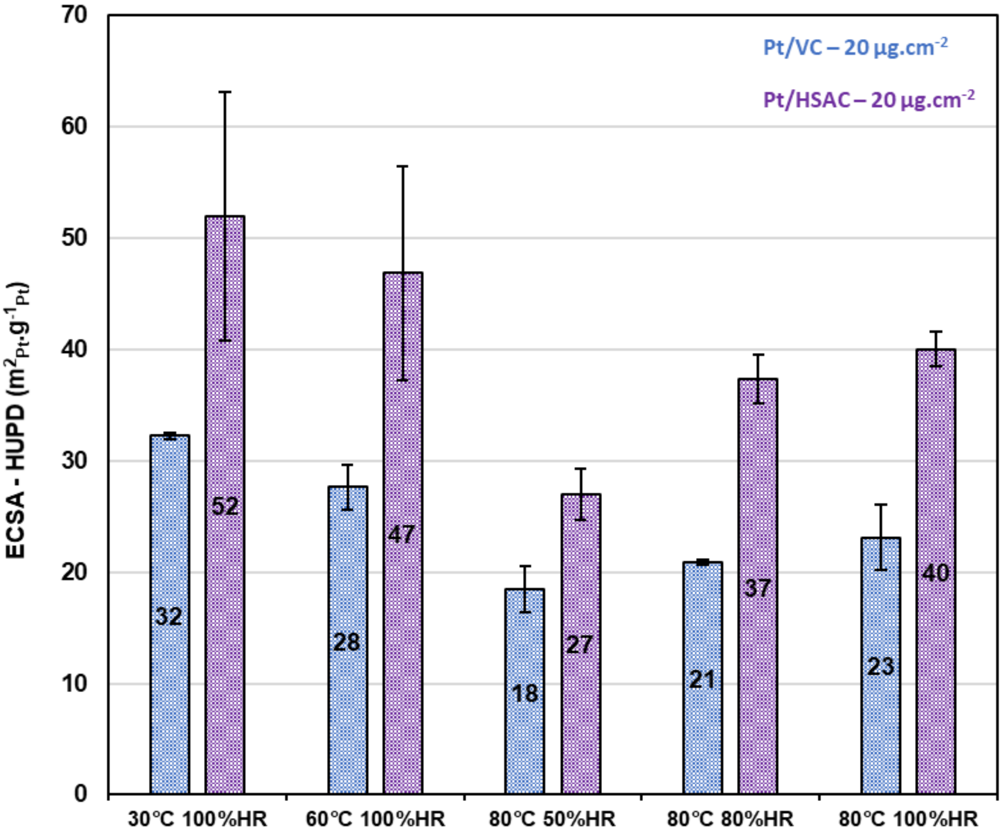

Figure III-33 : ECSA value evolution with T and RH obtained in differential cell setup for both Pt/VC and Pt/HSAC electrocatalysts.

III.4.1.2 Qualitative coverage ratio of Pt surface oxides evolution during CV under H_2/N_2 configuration

As detailed in the Chapter II, cyclic voltammetry gives information on the Pt oxides formation (Pt oxidation) and reduction reactions. Figure III-34 (a) shows the third cycle of H_2-crossover current-corrected cyclic voltammetries from the current constant baseline taken at 0.4 V, performed on both Pt/VC and Pt/HSAC electrocatalysts. As expected, the double layer capacity current is higher in the case of Pt/HSAC (the HSAC carbon has a higher developed surface area than the Vulcan carbon, *ca*. 800 *vs*. 240 $m^2.g^{-1}$). The coulometries in the H_{UPD} and in the Pt oxides regions are also higher in the case of Pt/HSAC, which agrees with the Pt morphology in both cases and with the materials' ECSA values from RDE measurements (see Table III-2 and Figure III-4). Figure III-34 (b) shows the qualitative coverage ratio evolution of Pt surface oxides for both Pt/VC and Pt/HSAC electrocatalysts. It is noticeable that the hysteresis linked to Pt oxides formation/reduction is bigger in the case of Pt/HSAC: the CV from Figure III-34 (a) show that the Pt oxides reduction peak is shifted towards the negative potential for Pt/HSAC, indicating that the Pt oxides reduction is more sluggish; this is naturally ascribed to the presence of very small Pt nanoparticles, Pt oxides on the latter being harder to reduce than on larger Pt nanoparticles/agglomerates. On the oxidation sweep, it is difficult to conclude though, as the only differences are in the potential range of 0.5-0.7 V. Although the oxidation signature in this potential region is usually ascribed to quinone/hydroquinone (H/QH) oxidation, it may also be due to early Pt oxides formation on very small Pt particles (that are more oxophilic than larger ones), but less likely in the case of Pt/HSAC as the pre-peak of CO_{ad} oxidation appears around 0.7 V on RDE measurements (see Figure III-2 (d)).

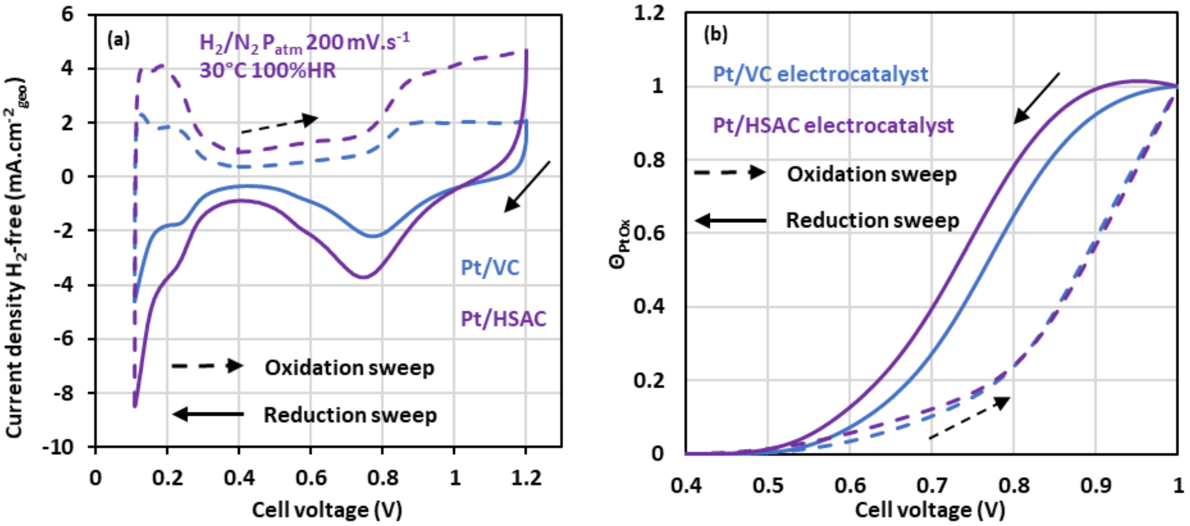

Figure III-34 : (a) Third cycle of cyclic voltammetries performed on both Pt/VC and Pt/HSAC electrocatalysts and (b) Qualitative coverage ratio evolution of Pt surface oxides obtained from the CV for both Pt/VC and Pt/HSAC (see Chapter II).

III.4.1.3 Impact of temperature and relative humidity on coverage ratio Pt surface oxides evolution

In this section, the impact of both temperature and relative humidity on the qualitative coverage ratio of Pt surface oxides is investigated by cyclic voltammetry keeping H_2O vapour partial pressure constant, as the total pressure is adjusted according to the operating conditions (Figure III-35 (a) et (b) for Pt/VC). Figure III-35 (c) shows the impact of temperature at constant relative humidity on the qualitative evolution of the coverage ratio of Pt surface oxides of the Pt/VC electrocatalyst. The hysteresis observed is wider at 30°C than at 60 and 80°C, meaning that the Pt oxidation and the Pt oxides reduction kinetics are enhanced by temperature. At a fixed potential of 0.75 V, the Pt is more covered by surface oxides at 80°C than at 60 or 30°C at 100% RH: the temperature increase promotes the Pt oxides formation and reduction, resulting in a reduced asymmetry between the kinetics of the two reactions. Regarding the impact of the relative humidity at constant temperature, on Figure III-35 (d), the increase of *RH* seems to also promote the Pt oxides formation and reduction reactions; this makes sense, because water is consumed during Pt oxides formation. As such, the hysteresis is wider at 50% RH than at 100% RH, with more Pt oxides formed at 0.75 V in the case of fully hydrated gases than at 50% RH at 80°C. The trends at 80% RH and 100% RH are interesting because it seems that the use of fully hydrated gases slightly hinders the Pt oxides formation and reduction reactions as more Pt oxides are formed at 80% RH than at 100% RH in the potential region 0.5 - 0.7 V. One should know that the value of the Pt oxides surface coverage ratio is probably overestimated in the region 0.5 - 0.65 V. In that potential region, the carbon surface oxidation occurs and it is difficult to correct its signature. In addition, the CVs are H_2 crossover corrected from a constant current baseline taken at 0.4 V, which is not strictly accurate and may overestimate θ_{PtOx}. Finally, the increase of temperature at constant relative humidity and the increase of relative humidity at constant temperature seem to promote the formation of H/QH groups, as the corresponding electrochemical signature is more pronounced at high temperature/relative humidity.

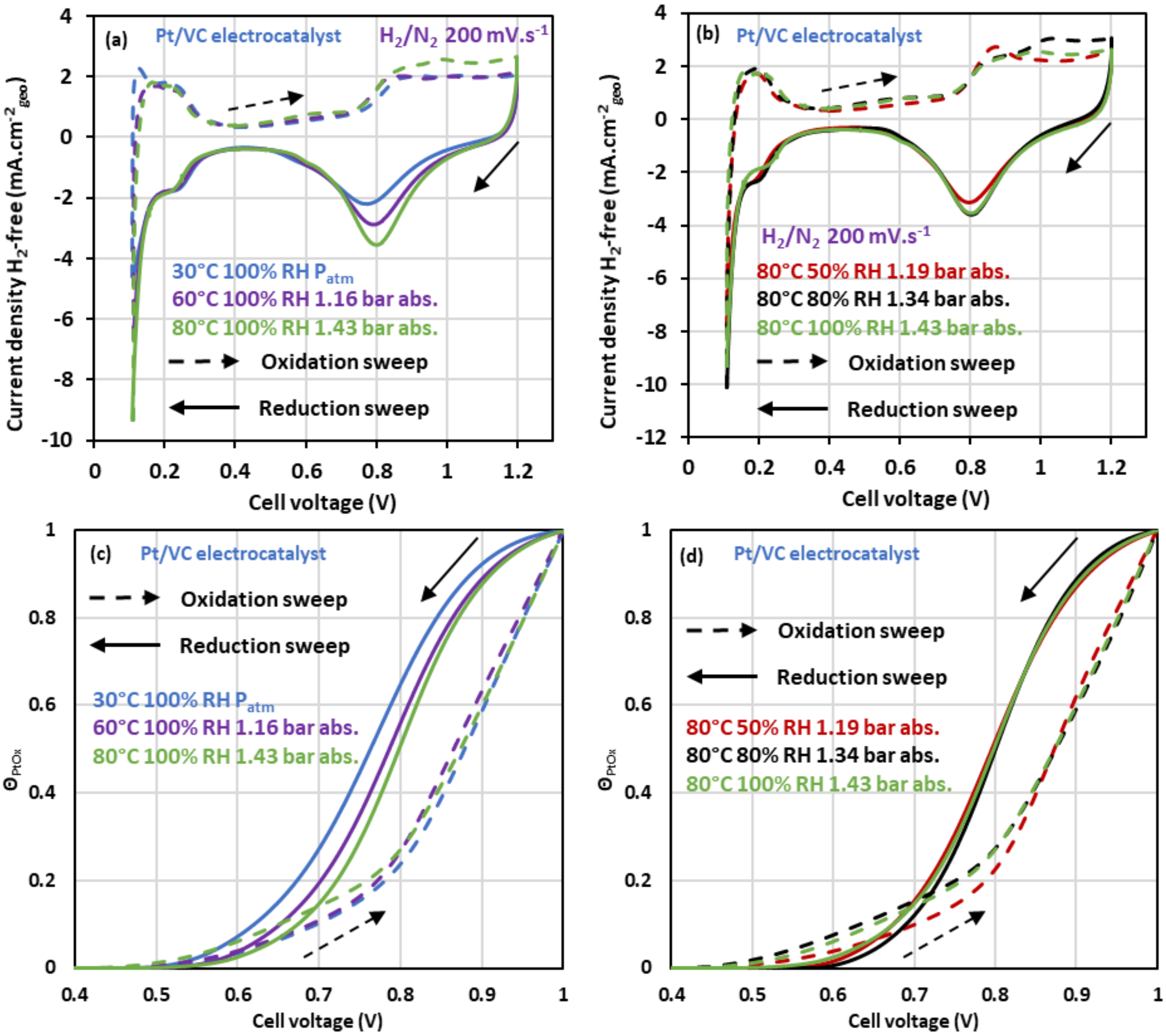

Figure III-35 : Third cycle of cyclic voltammetries performed on MEA made of Pt/VC electrocatalyst at (a) different temperatures at constant RH and (b) different RH at constant temperature (c) Impact of temperature on the qualitative coverage ratio evolution of Pt surface oxides Pt/VC at constant relative humidity and (d) Impact of relative humidity on the qualitative coverage ratio evolution of Pt surface oxides Pt/VC at constant temperature.

Figure III-36 shows the impact of temperature at constant relative humidity on the cyclic voltammetry and qualitative coverage ratio evolution of Pt surface oxides for Pt/HSAC electrocatalyst. The Pt oxidation and the Pt oxides reduction reactions are enhanced with temperature and relative humidity increase. For Pt/HSAC, the trends observed on the hysteresis of coverage ratio evolution of Pt surface oxides according to temperature and relative humidity (see (Figure III-36 (c) and (d)) are similar to the ones for Pt/VC electrocatalyst. This makes sense as the Pt oxidation evolution with these operating conditions is independent on the carbon substrate.

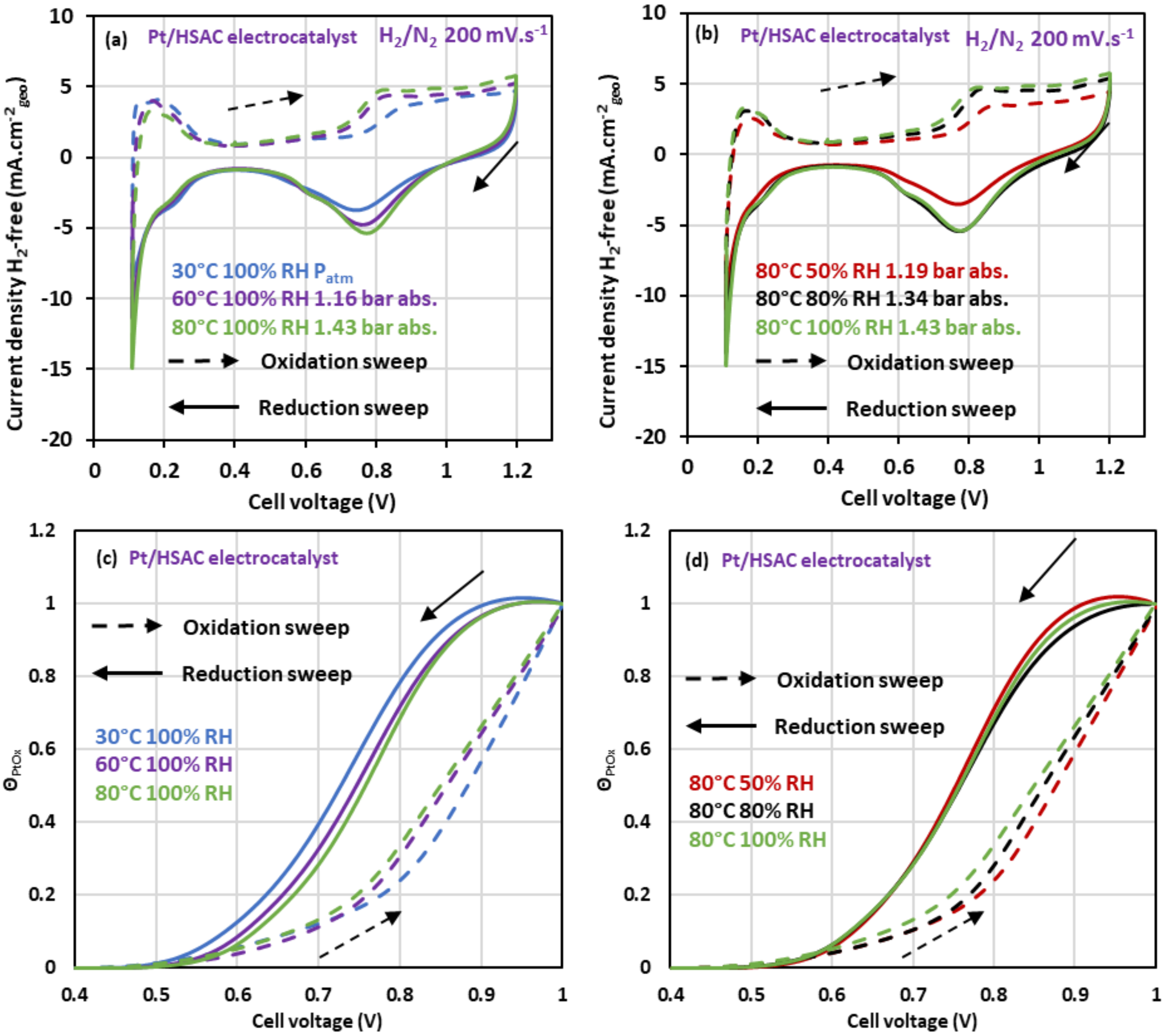

Figure III-36 : Third cycle of cyclic voltammetries performed on CL made of Pt/HSAC electrocatalyst at (a) different temperatures at constant RH and (b) different RH at constant temperature (c) Impact of temperature on the qualitative coverage ratio evolution of Pt surface oxides Pt/HSAC at constant relative humidity and (d) Impact of relative humidity on the qualitative coverage ratio evolution of Pt surface oxides Pt/HSAC at constant temperature.

III.4.1.4 Impact of sweeping rate on coverage ratio Pt surface oxides evolution

Another parameter may affect the Pt oxides formation/reduction: the sweeping rate. Figure III-37 (a) shows the third cycle of cyclic voltammetries performed on Pt/VC electrocatalyst at two different sweeping rates, 50 and 200 mV.s^{-1}. The transient current density is higher at 200 mV.s^{-1} than at 50 mV.s^{-1}, which is expected for capacitive currents like those monitored in these CVs. Figure III-37 (b) shows the impact of the sweeping rate on the coverage ratio of Pt surface oxides versus potential. At the lowest sweeping rate (50 mV.s^{-1}), more Pt oxides seem to be formed than at 200 mV.s^{-1}. This likely originates from the intrinsic slowness of Pt oxides formation, which requires sufficient time to reach the equilibrium state of the oxide coverage at a given potential. This behaviour was also observed using *in situ* X-Ray diffraction measurements in the work of Martens et *al.* [22]. However, at low sweeping rates, the electrochemical signals become small and increasingly difficult to separate from the H_2 permeation current at 20 µg$_{Pt}$.cm$_{geo}^{-2}$.

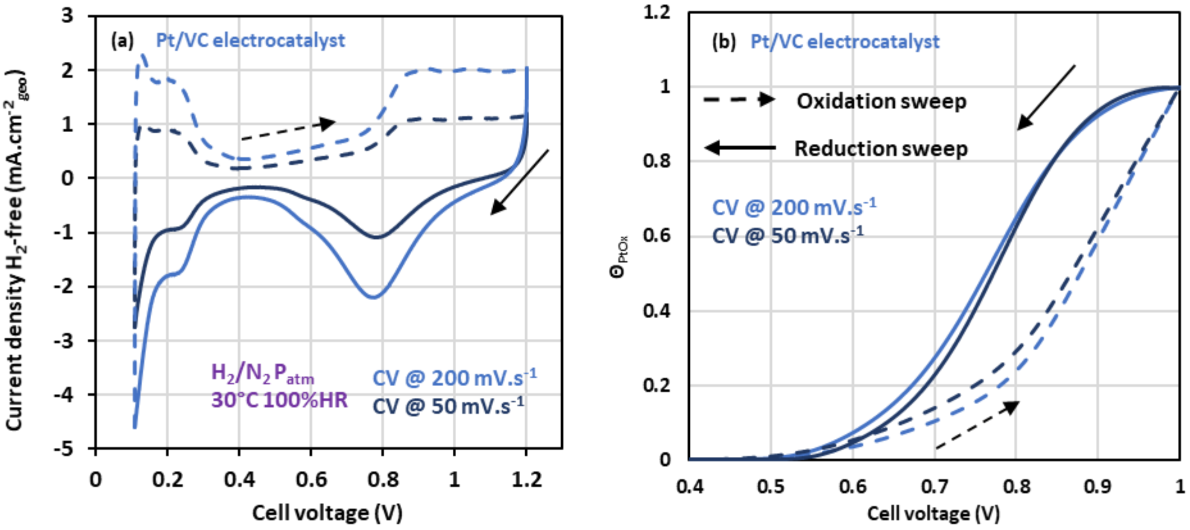

Figure III-37 : (a) Third cycle of cyclic voltammetries performed on MEA with Pt/VC electrocatalyst at 50 mV.s^{-1} and 200 mV.s^{-1} (b) Qualitative coverage ratio evolution of Pt surface oxides obtained from the CV for Pt/VC at both sweeping rate.

III.4.2 Under oxygen atmosphere

In the following sections, the impacts of temperature and relative humidity on global performance for both electrocatalysts are investigated. In addition, a comparison of the performance between Pt/VC and Pt/HSAC will be discussed.

III.4.2.1 Performance measurements at 80°C, 80% RH

Figure III-38 (a) shows a comparison of the global performance of MEA using Pt/VC and Pt/HSAC electrocatalysts at the cathode (20 $\mu g_{Pt}.cm_{geo}^{-2}$). No matter the potential, the Pt/HSAC catalyst layer seems more active regarding the ORR: more current density is produced than in the case of Pt/VC catalyst layer along the whole polarization curve. At high potential, Pt/VC was more active than the Pt/HSAC. Thus, this inverted behaviour in differential cell is probably not related to the intrinsic activity of the catalyst. The higher current density produced in the case of Pt/HSAC, yielding to more water produced, results in a lower R_{HF} and a better hydration state of the membrane, until 0.3 V, than for Pt/VC electrocatalyst (Figure III-38 (b)). In addition, the water production may result in more water retention in the micro-pores of the electrocatalyst, improving the hydration. Below 0.3 V, for both Pt/VC and Pt/HSAC, R_{HF} reaches the same value, which may be due to the higher local heat production in the case of Pt/HSAC than for Pt/VC, related to the higher current density produced, which counter-balances the beneficial effect of larger water production. Also, for Pt/HSAC, the hysteresis observed on the R_{HF} evolution seems to be wider than Pt/VC, which partly explains the wider hysteresis observed on the experimental polarization curve. However, as the hysteresis is observed on the polarization curve, even after the ohmic drop correction, other phenomena are accounting for the hysteresis, such as Pt oxides formation/reduction.

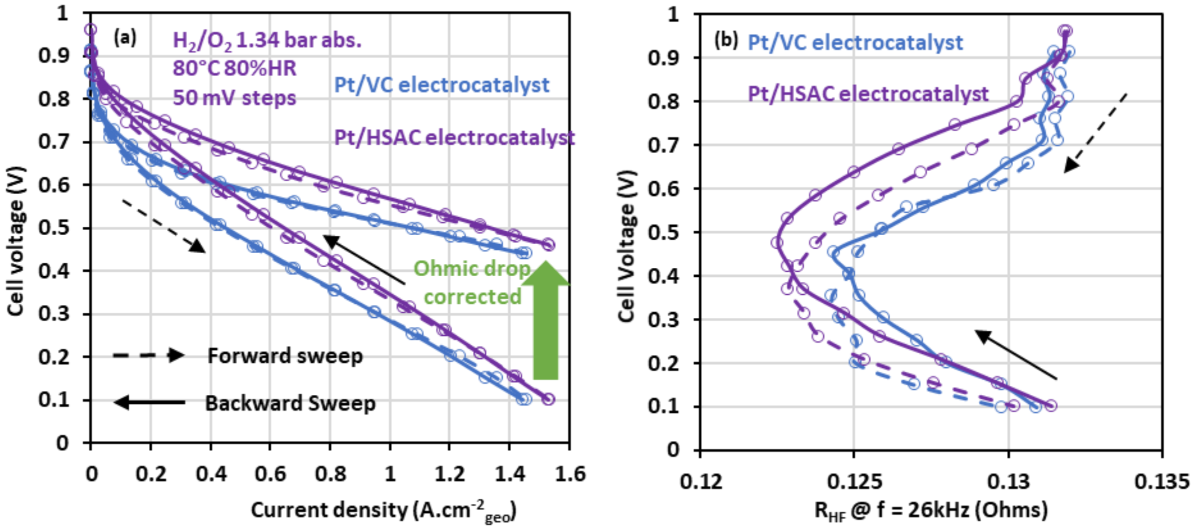

Figure III-38 : (a) Second cycle of polarization curve performed on MEA with Pt/VC and Pt/HSAC electrocatalysts by 50 mV potential steps (see section III.3.1.3), with and without ohmic drop correction, and (b) R_{HF} evolution along the polarization curve for both Pt/VC and Pt/HSAC.

III.4.2.2 Performance evolution with temperature and relative humidity

In this section, the impact of temperature and relative humidity on the global performance and the evolution of R_{HF} with the cell voltage (cathode potential) is investigated for both the Pt/VC and Pt/HSAC electrocatalysts. The performance at 60°C are better than at 30°C (Figure III-39 (a)), which is likely due to the enhancement of ORR kinetics at higher temperature (reduced activation losses, as already seen for the MEA FURTHER). The behaviour of the polarization curve at 80°C is surprising and unexpected, with a very pronounced hysteresis between the forward and backward sweeps (at the large benefit of the backward sweep). This behaviour is actually reproducible; a hypothesis to account for it is that on the forward sweep, the heat production in the active layer overwhelms the water production (water can still be expelled “easily” from the active layer, because there is yet no “saturation” of the active layer by liquid water), resulting in depreciated proton conductivity in the ionomer. On the contrary, on the backward sweep, the performance gain may originate from non-negligible water accumulation in the ionomer, thereby decreasing the proton resistance and increasing the apparent performance of the cathode. The R_{HF} evolution with potential for the three operating conditions, displayed on Figure III-39 (c), is for its part expected: an increase of temperature leads to improved ionic conductivity and proton mobility, which explains the lower R_{HF} values at 80°C than at 30°C. At 100% RH, it is interesting to note that the R_{HF} values are increasing with potential decrease/current density increase. This is due to local heat production, inducing a more severe local drying of the catalyst layer that counter-balances the water production. In addition, the R_{HF} variations at 30°C, 100% RH are much higher than at 80°C, 100% RH: up to 40% variation compared to 20% respectively. A possible explanation may be that, if the membrane conductivity follows an Arrhenius law, and considering that the hysteresis is driven by the pre-exponential term, which depends on the water content, the temperature evolution should affect the hysteresis amplitude.

The impact of the relative humidity at 80°C on the global performance and on the evolution of R_{HF} with the potential is shown on Figure III-39 (b) and (d): larger hydration of the gas reactants leads to better global performance. This behaviour was also observed with the FURTHER MEA. At 100% RH, the proton conductivity is improved, which leads to better performance. This assumption is clearly shown on Figure III-39 (b): at 100% RH, the R_{HF} values vary from 60 mΩ to around 80 mΩ, compared to 300 mΩ to around 280 mΩ at 50% RH, which is around 4 times higher. The R_{HF} values are almost only decreasing with increasing current at 80°C, 50% RH, which is a very dry operating condition, because the water production is only favourable to the hydration of the catalyst layer/membrane. The interesting point is that the forward sweep of the polarization curve obtained at 80°C, 50% RH shows better performance for potentials varying from 0.6 to 0.4 V, than in the backward sweep. This is explained by the better hydration of the active layer due to water production on the forward sweep, while on the backward sweep, the benefits from the water production and better hydration seem to be significantly counterbalanced by the local heat production.

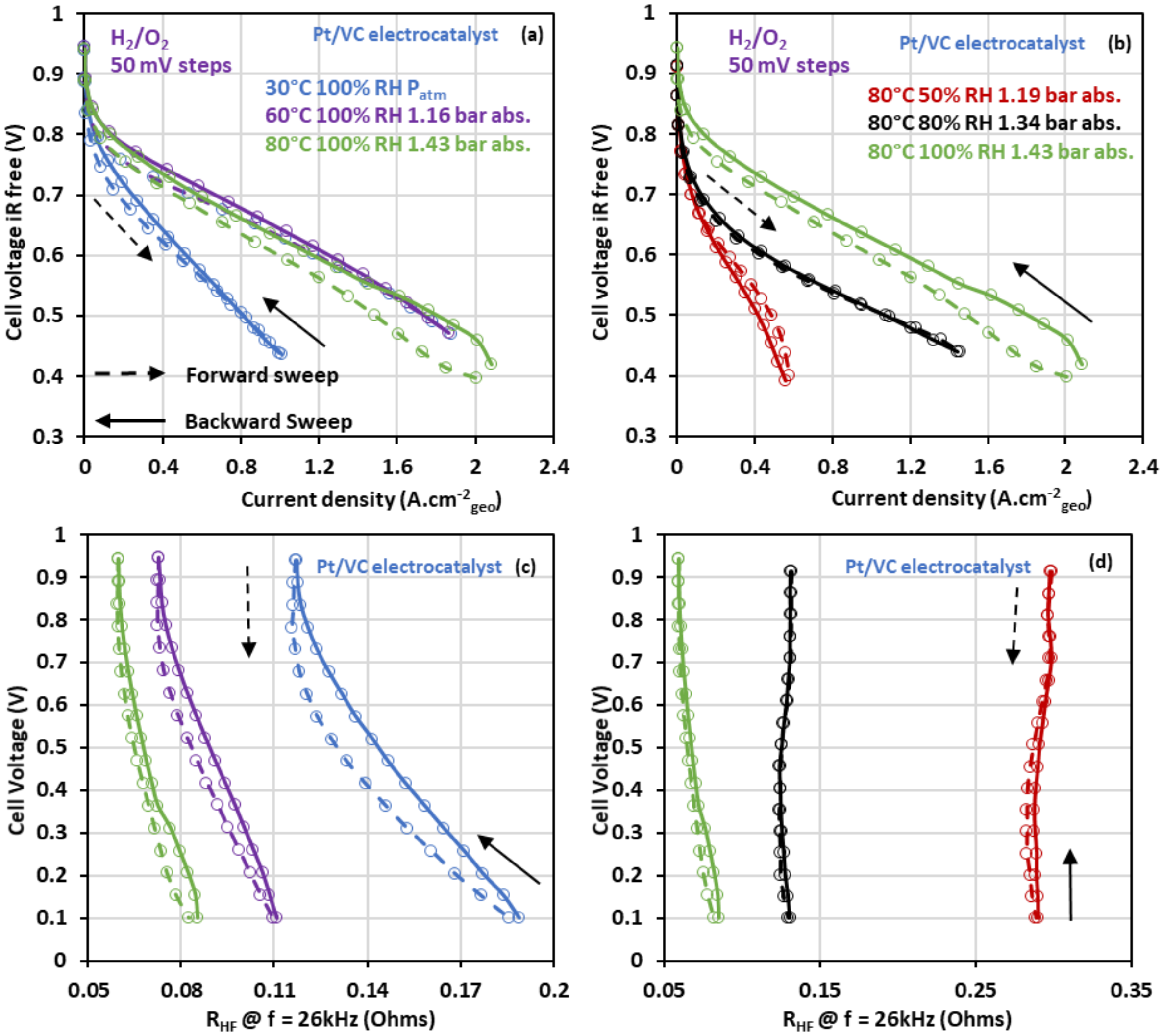

Figure III-39 : Second cycle of polarization curve ohmic drop corrected performed on MEA with Pt/VC at (a) different temperatures with constant relative humidity (b) at different relative humidities with constant temperature and R_{HF} evolution along the polarization curve for Pt/VC at (c) different temperatures with constant relative humidity and (d) different relative humidities with constant temperature.

The same study has been done with the Pt/HSAC electrocatalyst. Figure III-40 (a) and (c) show the impact of relative humidity at constant temperature on the global performance and *R*$_{HF}$ evolution. Figure III-40 (b) and (d) shows the impact of relative humidity at constant temperature on the global performance and *R*$_{HF}$ evolution. The global performance for Pt/HSAC is enhanced by temperature and gases humidification as it was the case for Pt/VC. Finally, the *R*$_{HF}$ evolution with the potential, the temperature and the relative humidity for Pt/HSAC (Figure III-40 (c) and (d), respectively) is similar to those observed with Pt/VC.

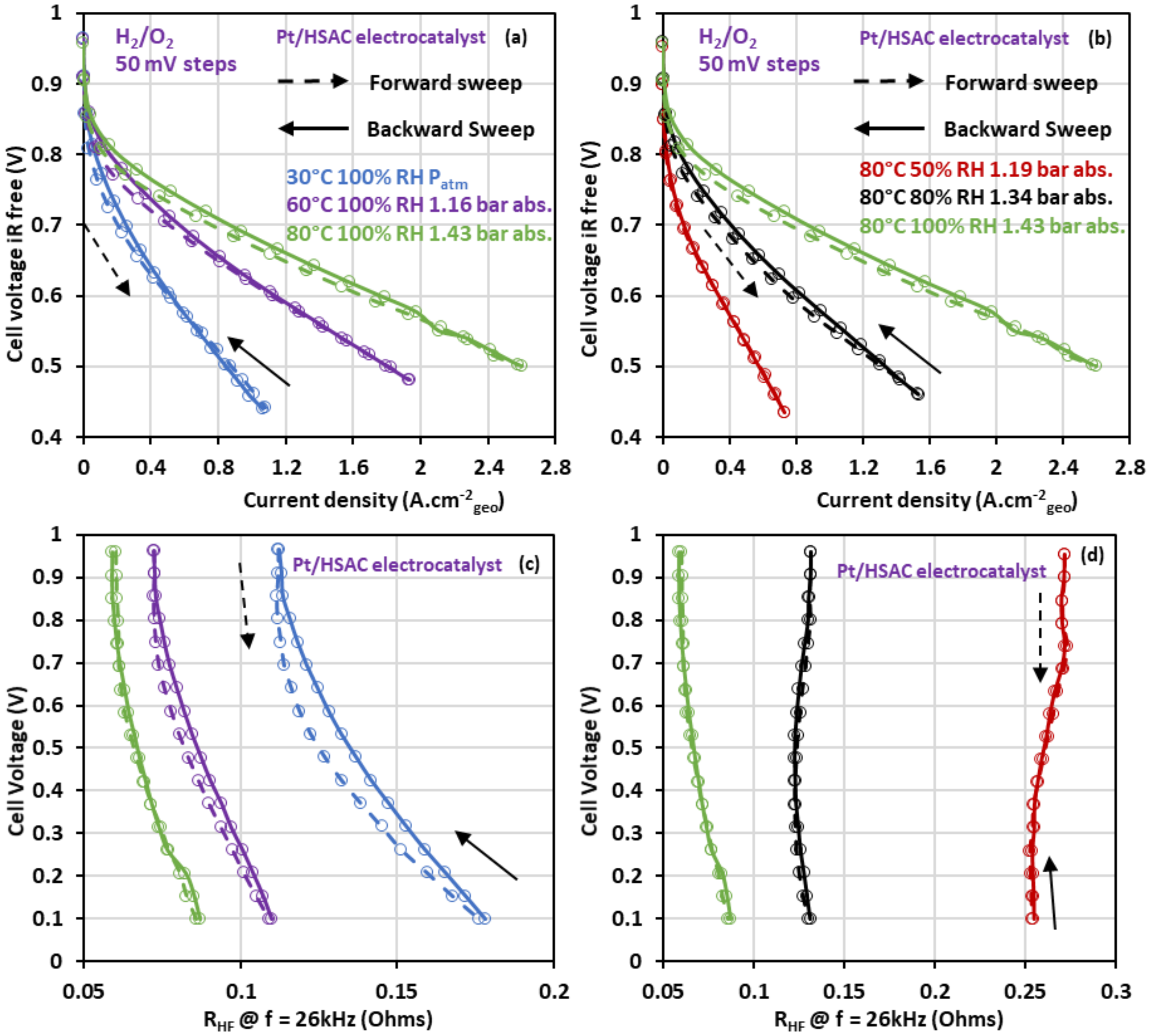

Figure III-40 : Second cycle of polarization curve ohmic drop corrected performed on MEA with Pt/HSAC at (a) different temperatures with constant relative humidity (b) at different relative humidities with constant temperature and R$_{HF}$ evolution along the polarization curve for Pt/HSAC at (c) different temperatures with constant relative humidity and (d) different relative humidities with constant temperature.

All these observations and results lead to an overview of the Pt/VC and Pt/HSAC very low loaded catalyst layer operation according to different temperatures and relative humidities, providing a solid dataset that will be used to improve the modeling. However, catalyst layer loaded at 20 µg$_{Pt}$.cm$_{geo}^{-2}$ are not representative of real catalyst layers (with much higher loadings), such as the ones that compose the FURTHER MEA, because the transport properties in thin catalyst layer strongly differ from those in thicker ones. Thus, the same study was performed on MEAs with cathode catalyst layers loaded at 100 $\mu g_{Pt}.cm_{geo}^{-2}$; comparing these two cathode loadings should further enable to evaluate and better understand the impact of the thickness and the mass transport properties on the catalyst layer operation under the same range of operating conditions. In addition, it is mandatory to include the mass transport properties description of the catalyst layer in the model description to have a numerical simulation as accurate as possible.

III.5 Impact of catalyst layer loading

The same study as in the previous section was done considering the same cathode catalyst layers made of Pt/VC and Pt/HSAC, but this time loaded at 100 $\mu g_{Pt}.cm_{geo}^{-2}$. The idea is to see to what extent the catalyst layer thickness (2-3 µm for 100 $\mu g_{Pt}.cm_{geo}^{-2}$ CL) and loading have an impact on the different behaviour observed in the previous section. The characterizations are performed on MEA including the membrane Nafion® 115 as for 20 $\mu g_{Pt}.cm_{geo}^{-2}$ catalyst layers. The different experimental results obtained on catalyst layers loaded at 100 $\mu g_{Pt}.cm_{geo}^{-2}$ under the various operating conditions (the same as for 20 $\mu g_{Pt}.cm_{geo}^{-2}$ catalyst layer) for both Pt/VC and Pt/HSAC are not shown as the trends observed according temperature and relative humidity on the different behaviour are similar to the ones observed on 20 $\mu g_{Pt}.cm_{geo}^{-2}$ catalyst layers. The global performance, as well as the Pt oxides formation/reduction are enhanced with temperature and relative humidity increase. The next sections deal with the impact of loading increase on cyclic voltammetry measurements, Pt surface oxides coverage ratio evolution under inert atmosphere, the global performance and the R_{HF} evolution during polarization curve measurements.

III.5.1 Impact of loading increase on ECSA and coverage ratio of Pt surface oxides evolution

Figure III-41 (a) and (b) show a comparison of the ECSA values, obtained under various operating conditions, between catalyst layers loaded at 20 $\mu g_{Pt}.cm_{geo}^{-2}$ and 100 $\mu g_{Pt}.cm_{geo}^{-2}$ for Pt/VC and Pt/HSAC, respectively. For both electrocatalysts, there is almost no difference regarding the ECSA values (normalized by the loadings, expressed in $m_{Pt}^{2}.g_{Pt}^{-1}$) between the two loadings, whatever the operating conditions: this means that (within the error bar) multiplying the loading by five, leads effectively to a 5 times higher surface of Pt available for proton adsorption/desorption in this loading range. In the following, only the results obtained at 30°C, 100% RH under H_2/N_2 and 80°C, 80% RH under H_2/O_2 configuration are considered, since the model description improvements were prioritized at these aforementioned operating conditions.

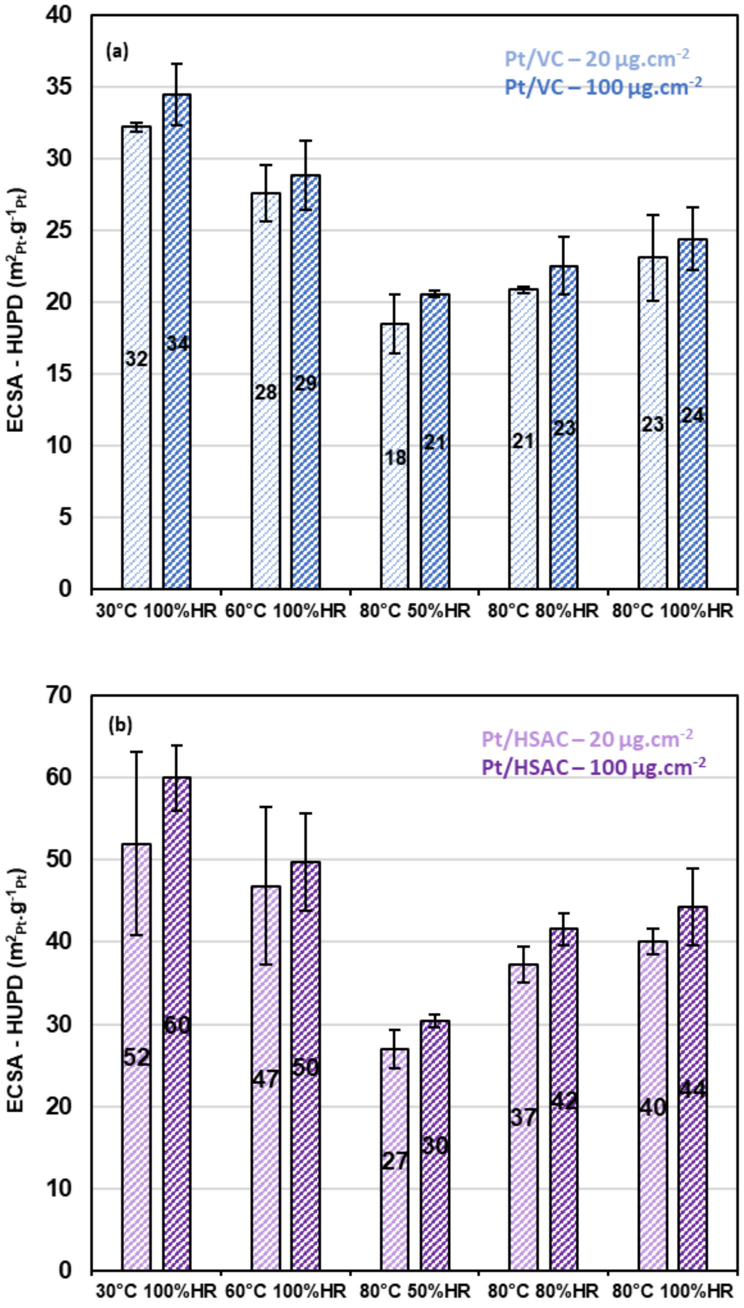

Figure III-41 : Comparison of ECSA values obtained at different catalyst layer loadings in differential cell setup for (a) Pt/VC and (b) Pt/HSAC electrocatalyst under various operating conditions.

Figure III-42 (a) and (b) show a comparison of the CV obtained at 30°C, 100% RH normalized by the Pt active surface for proton desorption between catalyst layers loaded at 20 $\mu g_{Pt}.cm_{geo}^{-2}$ and 100 $\mu g_{Pt}.cm_{geo}^{-2}$ for Pt/VC and Pt/HSAC, respectively. The normalization has been done to have a relevant comparison between CV obtained at different loadings. The CVs are corrected from H_2 crossover current. In the H_{UPD} region, there are almost no differences between the two loadings. In the Pt oxides region, it seems that the coulometry of Pt oxides formation is bigger at 100 $\mu g_{Pt}.cm_{geo}^{-2}$ than at 20 $\mu g_{Pt}.cm_{geo}^{-2}$, meaning that more oxides are formed, which seems to be confirmed by the oxidation sweeps of the coverage ratio Pt surface oxides evolution with potential shown on Figure III-42 (c) and (d) for both electrocatalysts. From around 0.75 to 1 V, the Pt surface state seems to be more oxidized in the case of thick catalyst layers. Regarding the reduction sweep, it seems that in the case of catalyst layers loaded at 100 $\mu g_{Pt}.cm_{geo}^{-2}$, the characteristic peak of Pt oxides reduction is slightly shifted towards negative potential. It may be explained by the fact that in case of thick catalyst layers, the response may not be the same at the membrane side or at the GDL side. In addition, thick catalyst layer enables the presence of water in larger quantity, which would promote the Pt oxides formation. Thus, more oxides need to be reduced during the reduction sweep, which would explain the negative potential shift of the oxides reduction peak. This is highlighted by the bigger hysteresis observed on the coverage ratio of Pt surface oxides evolutions for both electrocatalyst, particularly at a fixed potential on the reduction sweep, the Pt is more covered by oxides in the case of high loadings.

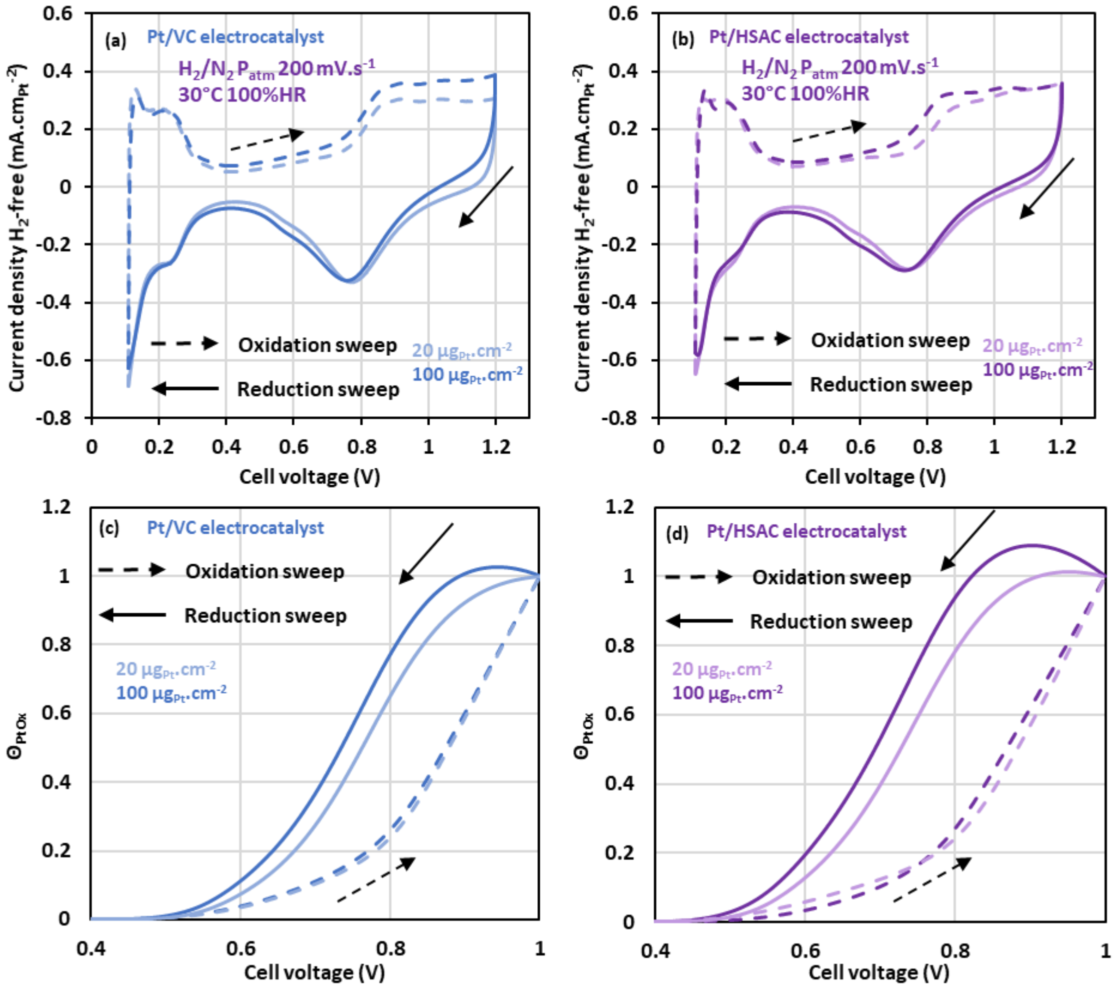

Figure III-42 : Comparison of the third cycle of cyclic voltammetries normalized by the Pt active surface for proton desoprtion obtained at different catalyst layer loadings in differential cell setup for (a) Pt/VC and (b) Pt/HSAC electrocatalyst at 30°C 100% RH and comparison of coverage ratio of Pt surface oxides evolution with potential obtained at different catalyst layer loadings in differential cell setup for (c) Pt/VC and (d) Pt/HSAC electrocatalyst at 30°C 100% RH.

III.5.2 Impact of loading on global performance and R_{HF} evolution

In this section, the impact of loading on global performance and R_{HF} evolution obtained at 80°C, 80% RH is investigated for both electrocatalysts. The local concentration of O_2 near Pt sites is different due to the bigger gradient concentration of O_2 in the case of a thicker catalyst layer. Thus, the correction from Pt active surface is not relevant to compare polarization curves performed at different loadings. No matter the potential and the electrocatalyst, the global performance is not multiplied by a factor 5, as the loading is (Figure III-43 (a) and (b)). For both electrocatalysts, at 100 $\mu g_{\mathrm{Pt}}.cm_{\mathrm{geo}}^{-2}$, larger current density is produced, which leads to a bigger ohmic drop than at 20 $\mu g_{\mathrm{Pt}}.cm_{\mathrm{geo}}^{-2}$. More water is also produced, which leads to a better hydration state of the ionomer in the active layer and in the membrane, as shown on the R_{HF} evolution (Figure III-43 (c) and (d)). Regardless of the potential, the R_{HF} values are lower in the case of catalyst layers loaded at 100 $\mu g_{\mathrm{Pt}}.cm_{\mathrm{geo}}^{-2}$ than for catalyst layers loaded at 20 $\mu g_{\mathrm{Pt}}.cm_{\mathrm{geo}}^{-2}$, which is explained by the fact that thin catalyst layers do not retain water as well as thicker ones and due to the use of thick membrane, the water exchange capacity between anode and cathode is enhanced. Be it on the R_{HF} evolution or polarization curves, the hysteresis between the forward and backward sweep seems to be wider in the case of 100 $\mu g_{\mathrm{Pt}}.cm_{\mathrm{geo}}^{-2}$ than for catalyst layers loaded at 20 $\mu g_{\mathrm{Pt}}.cm_{\mathrm{geo}}^{-2}$. This may be mainly explained by the different response through thickness of the catalyst layer (PEM side *vs.* GDL side) and thus the wider hysteresis for R_{HF}. Regarding the polarization curve, the wider hysteresis may be explained by the asymmetry of the Pt oxides formation/reduction kinetic in the case of 100 $\mu g_{\mathrm{Pt}}.cm_{\mathrm{geo}}^{-2}$ catalyst layers mentioned above. In addition, the increase of the catalyst layer loading leads also to an increase of the catalyst layer thickness. This probably results in different mass transport properties of proton, and maybe also of O_2, due to different hydration state of the catalyst layer between the forward sweep and backward sweep (presence of water in the porosity). Indeed, it was seen with FURTHER MEA that $R_{\mathrm{H+,CL}}$ was evolving with the working point, thus, it should also evolving along the polarization curve and between the forwards and backward sweeps, as the R_{HF} does.

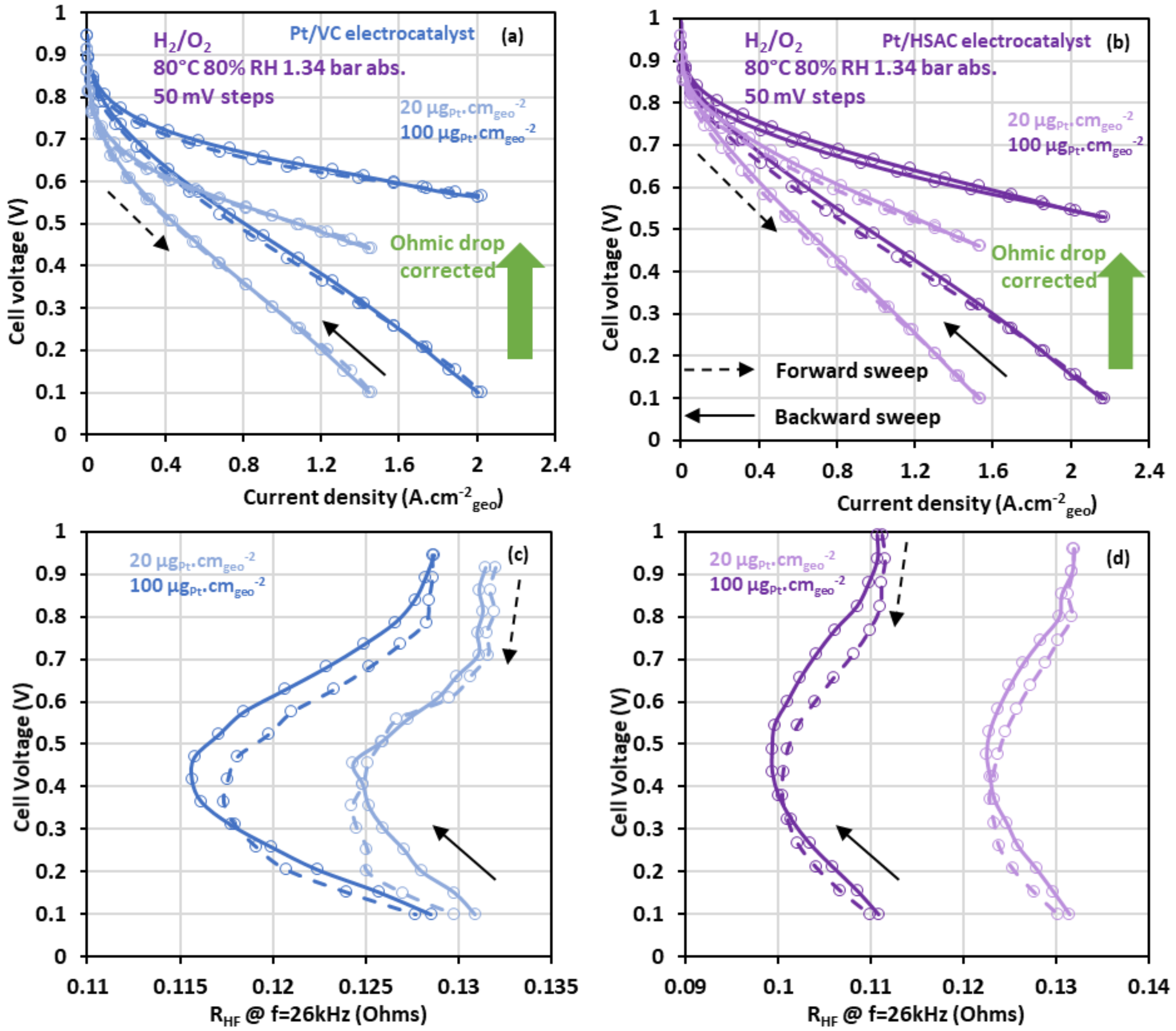

Figure III-43 : Second cycle of polarization curve with and without ohmic drop correction performed at different loadings for (a) Pt/VC and (b) Pt/HSAC electrocatalysts and R_{HF} evolution along the polarization curve at different loadings for (c) Pt/VC and (d) Pt/HSAC.

III.6 Conclusions

This chapter is the experimental core of the PhD. All the experimental characterizations in this work were carried out in order to unravel the relevance of the electrochemical setup used to assess the electrocatalytic features of electrocatalyst (ECSA, intrinsic activity), including the choice of operating conditions and protocols, the electrochemical techniques and the materials used for the electrochemical characterizations. The RDE setup has been, for a long time, used to assess the intrinsic activity of electrocatalysts, as it has shown its non-negligible benefits compared to fuel cell configuration: low catalyst amount, small experiment duration, ultra-clean environment. However, the main drawbacks of this electrochemical setup is the mass transport regime and the liquid electrolyte used, which lead to very limited mass transport and an operation that is not representative of a real PEMFC [23]. It has been shown that due to limited mass transport, activity measurements are only possible at potential in the range of 0.85 – 0.95 V *vs.* RHE, which does not correspond to the potential range of real PEMFC operation (*i.e.* 0.6 - 0.75 V). Mostly, RDE measurements are done at room temperature, as the electrolyte stability and the O_2 solubility and diffusivity may be questioned at higher temperature. On the contrary, the differential cell usually operates at medium/high temperature (40 – 80°C). The electrochemical characterizations were also done is order to better understand the electrocatalyst operation from raw materials to its utilization in catalyst layer under various operating conditions, considering several loadings. No matter the loadings, or the electrocatalysts, it has been seen that the temperature increase as well as the relative humidity increase often lead to higher performance, due to (i) the promotion of the ORR due to the reduction of the activation losses and (ii) the improved water management in the ionomer phases, resulting in an improved protonic conductivity to the actives sites. However, behind these expected behaviours, the catalyst layer operation is much more complex, as a lot of physico-chemical and electrochemical phenomena, including their interplay, make the understanding of catalyst layer operation difficult with such experimental characterizations. Thus, to go further and to evaluate some hypothesis, it is useful to analyse the raw experimental data with as comprehensive as possible physical models, which often implies numerical simulation. In that context, these electrochemical characterizations were also performed to build a reliable dataset using well-defined and well-known compositions in order to give some clues to improve the modeling description. These experimental data can also be used to validate the models and the assumptions and to tune the parameter values used for the numerical simulations.

References of Chapter III

[1] M. Inaba, A. W. Jensen, G. W. Sievers, M. Escudero-Escribano, A. Zana and M. Arenz, “Benchmarking high surface area electrocatalysts in a gas diffusion electrode: measurement of oxygen reduction activities under realistic conditions,” *Energy Environ. Sci.*, vol. 11, no. 4, pp. 988–994, 2018, doi: 10.1039/C8EE00019K.

[2] F. Maillard, M. Eikerling, O. V. Cherstiouk, S. Schreier, E. Savinova and U. Stimming, “Size effects on reactivity of Pt nanoparticles in CO monolayer oxidation: The role of surface mobility,” *Faraday Disc.*, vol. 125, p. 357, 2004, doi: 10.1039/b303911k.

[3] B. Andreaus, F. Maillard, J. Kocylo, E. R. Savinova and M. Eikerling, “Kinetic Modeling of CO_{ad} Monolayer Oxidation on Carbon-Supported Platinum Nanoparticles,” *J. Phys. Chem. B*, vol. 110, no. 42, pp. 21028–21040, Oct. 2006, doi: 10.1021/jp063856k.

[4] F. Maillard, S. Schreier, M. Hanzlik, E. R. Savinova, S. Weinkauf and U. Stimming, “Influence of particle agglomeration on the catalytic activity of carbon-supported Pt nanoparticles in CO monolayer oxidation,” *Phys. Chem. Chem. Phys.*, vol. 7, no. 2, pp. 385–393, 2005, doi: 10.1039/B411377B.

[5] L. Dubau, F. Maillard, M. Chatenet, J. André and E. Rossinot, “Nanoscale compositional changes and modification of the surface reactivity of Pt3Co/C nanoparticles during proton-exchange membrane fuel cell operation,” *Electrochimica Acta*, vol. 56, no. 2, pp. 776–783, Dec. 2010, doi: 10.1016/j.electacta.2010.09.038.

[6] H. A. Gasteiger, S. S. Kocha, B. Sompalli and F. T. Wagner, “Activity benchmarks and requirements for Pt, Pt-alloy, and non-Pt oxygen reduction catalysts for PEMFCs,” *Applied Catalysis B: Environmental*, vol. 56, no. 1, pp. 9–35, Mar. 2005, doi: 10.1016/j.apcatb.2004.06.021.

[7] I. Takahashia and S. S. Kocha, “Examination of the activity and durability of PEMFC catalysts in liquid electrolytes,” *Journal of Power Sources*, vol. 195, no. 19, pp. 6312–6322, Oct. 2010, doi: 10.1016/j.jpowsour.2010.04.052.

[8] Y. Garsany, O. A. Baturina, K. E. Swider-Lyons and S. S. Kocha, “Experimental Methods for Quantifying the Activity of Platinum Electrocatalysts for the Oxygen Reduction Reaction,” *Anal. Chem.*, vol. 82, no. 15, pp. 6321–6328, Aug. 2010, doi: 10.1021/ac100306c.

[9] L. Castanheira, L. Dubau, M. Mermoux, G. Berthomé, N. Caqué, E. Rossinot, M. Chatenet and F. Maillard, “Carbon Corrosion in Proton-Exchange Membrane Fuel Cells: From Model Experiments to Real-Life Operation in Membrane Electrode Assemblies,” *ACS Catal.*, vol. 4, no. 7, pp. 2258–2267, Jul. 2014, doi: 10.1021/cs500449q.

[10] L. Castanheira, W. O. Silva, F. H.B. Lima, A. Crisci, L. Dubau and F. Maillard, “Carbon Corrosion in Proton-Exchange Membrane Fuel Cells: Effect of the Carbon Structure, the Degradation Protocol,

and the Gas Atmosphere," *ACS Catal.*, vol. 5, no. 4, pp. 2184–2194, Apr. 2015, doi: 10.1021/cs501973j.

[11] L. M. Roen, C. H. Paik and T. D. Jarvic, "Electrocatalytic Corrosion of Carbon Support in PEMFC Cathodes," *Electrochem. Solid-State Lett.*, vol. 7, no. 1, p. A19, 2004, doi: 10.1149/1.1630412.

[12] F. Maillard, A. Bonnefont and F. Micoud, "An EC-FTIR study on the catalytic role of Pt in carbon corrosion," *Electrochemistry Communications*, vol. 13, no. 10, pp. 1109–1111, Oct. 2011, doi: 10.1016/j.elecom.2011.07.011.

[13] N. M. Marković and P. N. Ross Jr., "Surface science studies of model fuel cell electrocatalysts," *Surface Science Reports*, vol. 45, no. 4, pp. 117–229, Apr. 2002, doi: 10.1016/S0167-5729(01)00022-X.

[14] Y. Garsany, I. L. Singer and K. E. Swider-Lyons, "Impact of film drying procedures on RDE characterization of Pt/VC electrocatalysts," *Journal of Electroanalytical Chemistry*, vol. 662, no. 2, pp. 396–406, Nov. 2011, doi: 10.1016/j.jelechem.2011.09.016.

[15] Y. Takasu, N. Ohashi, X.-G. Zhang, Y. Murakami, H. Minagawa, S. Sato and K. Yahikozawa, "Size effects of platinum particles on the electroreduction of oxygen," *Electrochimica Acta*, vol. 41, no. 16, pp. 2595–2600, Jan. 1996, doi: 10.1016/0013-4686(96)00081-3.

[16] O. Antoine, Y. Bultel, R. Durand and P. Ozil, "Electrocatalysis, diffusion and ohmic drop in PEMFC: Particle size and spatial discrete distribution effects," *Electrochimica Acta*, vol. 43, no. 24, pp. 3681–3691, Aug. 1998, doi: 10.1016/S0013-4686(98)00126-1.

[17] A. Kusoglu and A. Z. Weber, "New Insights into Perfluorinated Sulfonic-Acid Ionomers," *Chem. Rev.*, vol. 117, no. 3, pp. 987–1104, Feb. 2017, doi: 10.1021/acs.chemrev.6b00159.

[18] M. A.R. S. Al-Baghdadi and H. A.K. S. Al-Janabi, "Effect of operating parameters on the hygro–thermal stresses in proton exchange membranes of fuel cells," *International Journal of Hydrogen Energy*, vol. 32, no. 17, pp. 4510–4522, Dec. 2007, doi: 10.1016/j.ijhydene.2007.05.007.

[19] F. Nandjou, J.-P. Poirot-Crouvezier, M. Chandesris, S. Rosini, D.S. Hussey, D.L. Jacobson, J.M. LaManna, A. Morin and Y. Bultel, "A pseudo-3D model to investigate heat and water transport in large area PEM fuel cells – Part 2: Application on an automotive driving cycle," *International Journal of Hydrogen Energy*, vol. 41, no. 34, pp. 15573–15584, Sep. 2016, doi: 10.1016/j.ijhydene.2016.06.007.

[20] T. Gaumont, G. Maranzana, O. Lottin, J. Dillet, L. Guétaz and J. Pauchet, "In Operando and Local Estimation of the Effective Humidity of PEMFC Electrodes and Membranes," *J. Electrochem. Soc.*, vol. 164, no. 14, pp. F1535–F1542, 2017, doi: 10.1149/2.0161714jes.

[21] K. Malek, T. Mashio and M. Eikerling, "Microstructure of Catalyst Layers in PEM Fuel Cells Redefined: A Computational Approach," *Electrocatal*, vol. 2, no. 2, p. 141, May 2011, doi: 10.1007/s12678-011-0047-0.

[22] N. Nonoyama, S. Okazaki, A. Z. Weber, Y. Ikogi and T. Yoshida, “Analysis of Oxygen-Transport Diffusion Resistance in Proton-Exchange-Membrane Fuel Cells,” *J. Electrochem. Soc.*, vol. 158, no. 4, p. B416, 2011, doi: 10.1149/1.3546038.

[23] I. Martens, R. Chattot, M. Rasola, M. Valeria Blanco, V. Honkimäki, D. Bizzotto, D. P. Wilkinson and J. Drnec, “Probing the Dynamics of Platinum Surface Oxides in Fuel Cell Catalyst Layers Using in Situ X-ray Diffraction,” *ACS Appl. Energy Mater.*, vol. 2, no. 11, pp. 7772–7780, Nov. 2019, doi: 10.1021/acsaem.9b00982.

[24] T. Lazaridis, B. M. Stühmeier, H. A. Gasteiger and H. A. El-Sayed, “Capabilities and limitations of rotating disk electrodes versus membrane electrode assemblies in the investigation of electrocatalysts,” *Nat Catal*, vol. 5, no. 5, pp. 363–373, May 2022, doi: 10.1038/s41929-022-00776-5.

Chapter IV PEMFC modeling and improvements of electrochemical and physico-chemical processes description at the cathode catalyst layer

This chapter introduces the modeling platform used at CEA LITEN and the global description of the model used in this work, which includes the geometry and the domains simulated and the different physics modelled within the domains. In this thesis, based on the experimental work, improvements regarding the electrochemical processes occurring in the catalyst layer are done in order to better describe and understand Pt catalyst characteristics under nitrogen atmosphere and the catalyst layer operation, especially platinum oxide formation, under oxygen atmosphere. As many experiments have been achieved in differential cell, the model has to also address the whole cell and associated transport phenomena.

IV.1 Modeling in the literature

Several models have been developed in the literature, which cover all relevant scales to describe as much as possible the PEMFCs physical processes. Jahnke *et al*. reviewed many models that aim at identifying limiting behaviours or simulating the performance and degradation of cell components from atomic scale up to system level [1]. One of the strengths of mathematical models is to quantify the contribution of each mechanism by choosing relevant operating conditions and scales, which is rarely possible experimentally. For instance, it is the case when one wants to unveil the concomitant degradation mechanisms and wants to develop and optimize mitigation strategies. However, the most challenging step is to be able to appropriately couple the different physical descriptions and to capture correctly the complex interactions of the different mechanisms involved in PEMFC operation at all relevant scales [2]. Regarding performance modeling and the understanding of the ORR mechanism for instance, some studies investigate the water formation through associative or dissociative mechanism thanks to electronic energy profile [3], [4]. Other studies focus more on the modeling of the catalyst layer operation to simulate the performance [2], [5]. Mathematical PEMFC models can be really powerful to support relevant choices for the technology, by saving a lot of time and reducing the development costs. In fact, one of the purposes of modeling is to develop a predictive and accurate numerical tool to assess the PEMFC performance and lifetime.

Specific and accurate physical description modeling often leads to simulation with restricted domain model, which motivates the development of numerous macro-models at the cell level, including all the components and the relevant processes in each domain for PEMFC single cell performance simulation [5]–[9]. For the different cell components, several models can be found in the literature.

For membranes, most of the models focus on perfluorinated polymers materials, as it is the material of interest for now. The models usually deal with sorption properties (e.g. the water concentration inside the membrane) and transport of water and proton properties. The challenge here relies in the good description of the coupling between both aspects of membrane, as their interplay is significant [10], [11].

For GDL/MPL, three approaches can be found in the literature: Continuous media, Lattice Boltzmann description and Pore Network models. Continuum media considers averaged physical properties of GDL and MPL, which may lead to some inaccuracy [12]. Porous structure were recently described by Lattice Boltzmann models taking into account the complex porous structure/geometry of GDL and MPL to simulate flow in these media, by considering the real morphology of the materials [12]–[14]. Finally, Pore Network models use the structural/physico-chemical properties such as porosity or the pore size distribution to describe the transport properties [15], [16].

For catalyst layers, which are the major point of interest in this work, two phenomena have to be described: the mass transport properties and the electrochemistry. Regarding mass transport description, some models tend to discretize the catalyst layer structure and the Pt particles supported on carbon [17]–[20]. On the other hand, some models consider an agglomerate scale approach with catalyst layer made of spherical or cylindrical Pt/C embedded in an ionomer film [21]–[23]. Regarding the electrochemistry, Nernst and Butler-Volmer approaches in one single-step reaction often describe the HOR and ORR. This simple description allows the calculation of reverse potential according to the activities of the oxidizer and reductant thanks to Nernst equation and the faradic current generated according to the overpotential, which is the difference between the electrode potential and the reverse potential, thanks to Butler-Volmer law. However, the ORR is a much more complex mechanism involving the participation of several intermediates species and a lot of work is carried out to unveil its operation [4], [24]–[27]. Moreover, using Nernst and Butler-Volmer equations does not take into account surface state, coverage effects and dynamic evolution. Thus, a more mechanistic approach with multiple steps is required to get further information on surface coverage of Pt by oxygen or hydroxyl species, which seems to be closely linked to its activity. Taking into account such surface coverage effects allows describing in details the adsorption/desorption of intermediate species, in addition to the intermediate reaction steps occurring at the electrocatalytic sites. This description is also attractive when catalyst contamination, impurities and even degradation mechanisms relative to electrocatalyst are considered [28], [29].

IV.2 Simulation framework and general description of the model

The Multi-Scale Simulation of Electrochemical Systems (MUSES) is a multi-physics and multi-scale modeling framework developed at CEA for PEMFC, PEM Water Electrolyser and Li-ion batteries. The Figure IV-1 illustrates the different platforms from the active material (EDMOND) up to the whole system (MePHYSTO). All the models developed in MUSES share their languages and databases to easily enable the integration of new data or the update of models. The EuROPIUM sub-platform, used in this work, dedicated to active layer and local operation in PEMFC will be described in details in the following section.

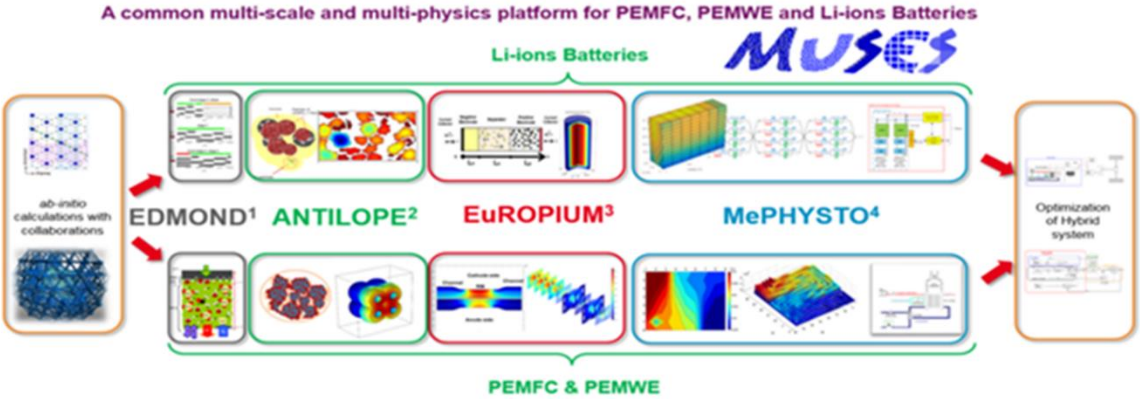

Figure IV-1 : The MUSES Platform.

IV.2.1 EUROPIUM platform

The model used in this thesis has been developed within EuROPIUM, which stands for ElectRochemistry OPtImization Understanding Modeling. This numerical platform is used to simulate fuel cell performances at the local cell level using both COMSOL® Multiphysics software for commercial code and Matlab software to build the models. EuROPIUM includes three different codes that calculate the physics and electrochemistry at three scales of the PEMFC:

- A 2D cell model taking into account gas flows from inlet to outlet and discretized also for each layer (GDL, MPL, CL and membrane) through the thickness of the MEA (2D channel code) [30], [31];
- A 2D rib-channel model that simulates the transport phenomena and electrochemistry of a 2D MEA in plane and through plane, between two consecutive channels where boundary conditions, from the 2D cell model, are imposed [30], [31];
- A pseudo-3D description of the whole cell by superimposing 2D layers for each component through cell (ps3D cell) [32].

The 2D rib-channel code will be quickly presented, as a 1D through thickness version of this code (1D rib-channel) is used in this thesis. The Figure IV-2 illustrates the domains where the internal gas fluxes and electrochemistry are simulated, which is between two consecutives channels and through the cell (from anode to cathode). The Table IV-1 summarizes the different processes that are relevant for fuel cell performances simulation using the 2D rib-channel code and the domains where they are considered. Please note that the channel domain is not simulated here (which is justified by the use of DC and high stoichiometry), thus boundary conditions for the GDL are used and values at channel|GDL interface come from the 2D cell model that simulates the flow in the channel domain. On the contrary, the ribs are simulated to get the current density profile at the rib|channel interface, reflecting more the reality. In addition, the water transport is only simulated through the ionomer phase at the moment. In fact, in the porosity, the liquid water management is quite hard to model, especially its impact on mass transport properties: if 50% of the porosity is filled with water, what are the consequences on the mass transport and the active surface available ? This is a strong hypothesis made here but in the case of differential cell measurements, apart from extreme operating condition close to 100% RH, this hypothesis is not that wrong. Thus, at the ionomer phase|porosity interface, an equilibrium between liquid water (ionomer phase) and vapour water (pores) is considered. In the following, the different description will only focus on the 1D rib-channel model.

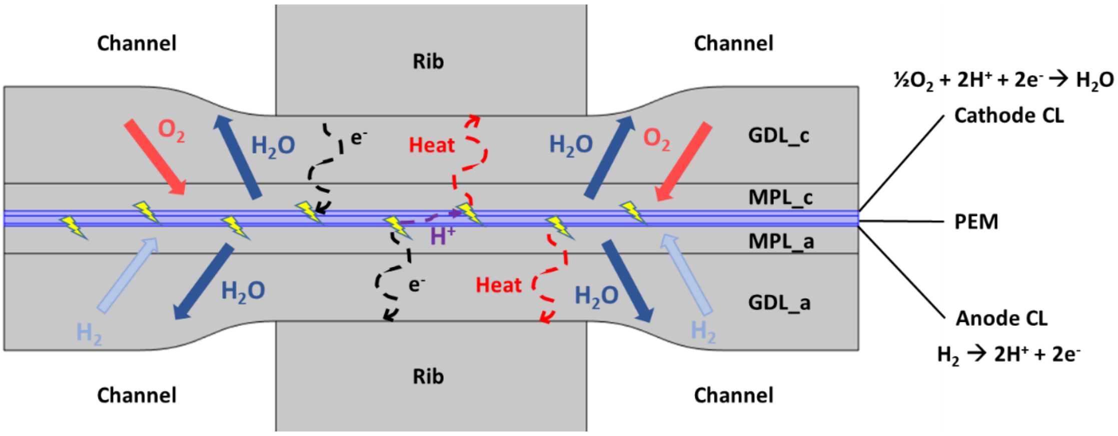

Figure IV-2 : 2D rib-channel modelled domains with the different fluxes and electrochemical reactions.

Table IV-1 : Domains of the fuel cell and the different physico-chemical processes included within the 2D rib-channel code.

	BP	GDL (including MPL)	CL	PEM
Proton transport			X	X
Liquid Water transport			X	X
Gas transport		X	X	X
Electrochemical reactions			X	
Electron transport	X	X	X	
Thermal		X	X	X

IV.2.2 Geometry and domains

The 1D MEA code used in this work is a simplified version of the 2D rib/channel model that makes it possible to perform many simulations in a reasonable amount of time. It is used for instance, to fit the model parameters on experimental data, when many simulations are needed during the process. Such a model can be used in the case of low rib/channel effect or the use of thin flow field rib/channel design, which is the case for the differential cell used in this work. The Figure IV-3 shows the simulated domains obtained via the 1D rib-channel code. At the extremities, gas concentrations and current are imposed as boundary conditions. In addition, all the other physics are the same when the different areas of the cell are shared for both the 2D and 1D version of the rib-channel code.

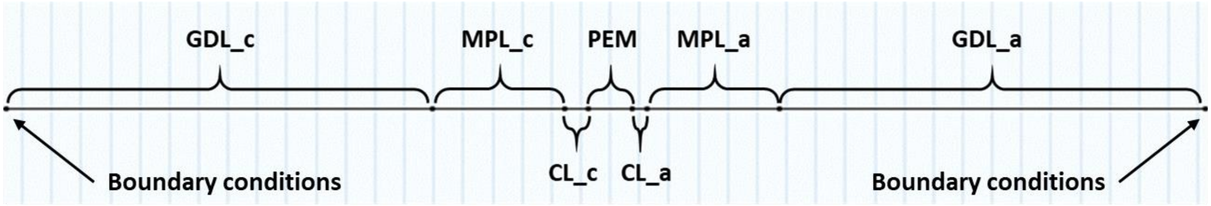

Figure IV-3 : Simulated domains using the 1D-rib-channel code

IV.2.3 Physics taken into account

This section presents the equations used to model the transport properties in the different domains of the PEMFC, as well as the electrochemistry and heat transfer descriptions that are used in the 1D rib-channel model. All the equations have already been described in the work of Randrianarizafy [30], but it is important to remind how the equations of the different physics are linked. Moreover, it will help to make the link between the initial description and the modification provided in this work, to improve the description of the cathode catalyst layer used in the 1D rib-channel model.

IV.2.3.1 Transport modeling for gases in porous media

The diffusion in porous media such as in the GDL, MPL and CL, has been modelled using the approach of Young and Todd [33]. The following equations are used to compute the motion of gases that results from both diffusion and convection. First, as said previously, according to Equation IV-1 gas concentrations are imposed as boundary conditions considering the continuity of concentrations and flows at the Channel|GDL interface:

Equation IV-1 : $$c_{\mathrm{i}}^{\mathrm{CH}} = c_{\mathrm{i}}^{\mathrm{GDL}} \quad \text{at channel|GDL interface}$$

With $c_{\mathrm{i}}^{\mathrm{CH}}$ the concentration of the specie *i* in the channel and $c_{\mathrm{i}}^{\mathrm{GDL}}$ the concentration of the specie *i* in the GDL. The mass balance in all the layers is computed via Equation IV-2:

Equation IV-2 : $$\varepsilon \frac{\partial c_{\mathrm{i}}}{\partial t} = \nabla \cdot \overrightarrow{N_{\mathrm{i}}} + S_{\mathrm{i}}$$

Where ε is the porosity, $\overrightarrow{N_{\mathrm{i}}}$ is the total molar flux of the specie *i* and S_{i} the source term of the specie *i*. In the case of vapour, the source term S_{i} is expressed by Equation IV-3:

Equation IV-3 : $$S_{\mathrm{i}} = S_{\mathrm{vap}}^{\mathrm{d}} + S_{\mathrm{cond}}$$

With $S_{\mathrm{vap}}^{\mathrm{d}}$ is the source term corresponding to the water adsorption by the ionomer in the CL and S_{cond} is the vapour condensation source term. In the case of the other gases, the source term is simplified accord to Equation IV-4:

Equation IV-4 : $$S_{\mathrm{i}} = S_{\mathrm{i}}^{\mathrm{a}}$$

Where $S_{\mathrm{i}}^{\mathrm{a}}$ stands for the diffusion flux through the ionomer film in the CL. The flux $\overrightarrow{N_{\mathrm{i}}}$ is the solution obtained from diffusion and convection in the pores described respectively by Equation IV-5 and Equation IV-6:

Equation IV-5 :

$$\frac{c_{\mathrm{g}}\cdot\varepsilon}{\tau^2}\cdot\overrightarrow{\nabla X_{\mathrm{i}}} = \sum_{\mathrm{j}}\left[\frac{X_{\mathrm{i}}\cdot\overrightarrow{N_{\mathrm{j}}}}{(D_{\mathrm{A}})_{\mathrm{ji}}} - \frac{X_{\mathrm{j}}\cdot\overrightarrow{N_{\mathrm{i}}}}{(D_{\mathrm{A}})_{\mathrm{ij}}}\right]$$

Equation IV-6 :

$$\frac{\varepsilon}{\tau^2}\cdot\vec{\nabla}P_{\mathrm{g}} = -A_{\mathrm{A}}\sum_{\mathrm{i}}\sqrt{M_{\mathrm{i}}}\cdot\overrightarrow{N_{\mathrm{i}}}$$

With τ the tortuosity, c_g and P_{g} the total concentration and pressure of gases respectively, X_{i} is the molar fraction of specie *I*, M_{i} the molar mass of the specie *i* and $(D_{\mathrm{A}})_{\mathrm{ij}}$ a mean coefficient diffusion calculated thanks to Equation IV-7:

Equation IV-7 :

$$\frac{1}{(D_{\mathrm{A}})_{\mathrm{ij}}} = \frac{1}{D_{\mathrm{ij}}} + \frac{1}{D_{\mathrm{i}}^{\mathrm{k}}}$$

Where D_{ij} corresponds to the binary diffusion coefficient and $D_{\mathrm{i}}^{\mathrm{k}}$ corresponds to the Knudsen diffusion coefficient expressed in Equation IV-8 as:

Equation IV-8 :

$$D_{\mathrm{i}}^{\mathrm{k}} = \left(\frac{2}{3}\cdot R_{\mathrm{p}}\cdot\sqrt{\left(\frac{8\cdot R\cdot T}{\pi\cdot M_{\mathrm{i}}}\right)}\right)$$

With R the universal gas constant, T the temperature and R_{p} the pore radius. The average convection coefficient A_{A} is calculated thanks to Equation IV-9:

Equation IV-9 :

$$\frac{1}{A_{\mathrm{A}}} = \frac{1}{A_{\mathrm{C}}} + \frac{1}{A_{\mathrm{K}}}$$

With the convection coefficient A_{C} being expressed according to the permeability k, which is an input of the model instead of the pore radius, as it the case for Young and Todd [33], and the coefficient A_{K} being the convection coefficient related to Knudsen diffusion, respectively described by Equation IV-10 and Equation IV-11:

Equation IV-10 :

$$A_{\mathrm{C}} = \frac{\mu}{c_{\mathrm{g}}\cdot k\cdot\sum_{\mathrm{i}}X_{\mathrm{i}}\sqrt{M_{\mathrm{i}}}}$$

Equation IV-11 :

$$A_{\mathrm{K}} = \frac{3}{4\cdot R_{\mathrm{p}}}\cdot\sqrt{\left(\frac{\pi\cdot R\cdot T}{2}\right)}$$

Where μ the dynamic viscosity.

IV.2.3.2 Transport modeling for gases in electrolyte phase

The diffusion of the dissolved gases occurs in the ionomer of the membrane and in the ionomer covering the Pt in the catalyst layer. The species balance is computed thanks to Equation IV-12:

Equation IV-12 :
$$(1-\varepsilon)\varepsilon_{\mathrm{ionomer}}\frac{\partial C_{\mathrm{i}}}{\partial t} = -\nabla\cdot\left(\vec{N}_{\mathrm{i}}^{\mathrm{a}}\right)+S_{\mathrm{i}}^{\mathrm{a}}+S_{\mathrm{i}}$$

Where ε is the porosity, $\varepsilon_{\mathrm{ionomer}}$ the ionomer proportion in the membrane and catalyst layers (equal 1 in the membrane) and $\vec{N}_{\mathrm{i}}^{\mathrm{a}}$**,** the flux of dissolved gases calculated according to a Fick's law (Equation IV-13):

Equation IV-13 :
$$\vec{N}_{\mathrm{i}}^{\mathrm{a}} = -D_{\mathrm{i}}^{\mathrm{a}}\vec{\nabla}(C_{\mathrm{i}})$$

With $D_{\mathrm{i}}^{\mathrm{a}}$ the diffusion coefficient in electrolyte phase of specie *i*. The source term $S_{\mathrm{i}}^{\mathrm{a}}$ corresponds to the diffusion flux of the specie *i* through ionomer film, which is calculated in the catalyst layers according to Equation IV-14:

Equation IV-14 :
$$S_{\mathrm{i}}^{\mathrm{a}} = \frac{D_{\mathrm{i}}^{\mathrm{a}}\cdot\Gamma_{\mathrm{Pt}}}{e_{\mathrm{ionomer}}}\left(C_{\mathrm{i}}^{\mathrm{eq}}-C_{\mathrm{i}}\right)$$

And in the membrane via Equation IV-15:

Equation IV-15
$$S_{\mathrm{i}}^{\mathrm{a}} = 0$$

Where Γ_{Pt} is the specific surface area of Pt, C_{i} the concentration of the dissolved specie *i*, e_{ionomer} the ionomer film thickness at the catalyst surface (Equation IV-16) and $C_{\mathrm{i}}^{\mathrm{eq}}$ the concentration of the specie *i* at equilibrium at the interface electrolyte|porous media (gas in the porous phase and dissolved in the electrolyte) calculated thanks to Equation IV-17:

Equation IV-16 :
$$e_{\mathrm{ionomer}} = \frac{(1-\varepsilon)\varepsilon_{\mathrm{ionomer}}}{\Gamma_{\mathrm{Pt}}}$$

Equation IV-17 :
$$C_{\mathrm{i}}^{\mathrm{eq}} = P_{\mathrm{i}}H_{\mathrm{i}}$$

With P_{i} the partial pressure of the specie *i* in the pores and H_{i} the Henry 'constant' (depending on temperature). Finally, the source term S_{i} is calculated for hydrogen and oxygen thanks to Equation IV-18 and Equation IV-19 respectively:

Equation IV-18 :
$$S_{\mathrm{H_2}} = -\frac{J_{\mathrm{r}}}{2F}$$

Equation IV-19 :
$$S_{\mathrm{O_2}} = -\frac{J_{\mathrm{r}}+J_{\mathrm{p}}}{4F}$$

With J_{r} and J_{p} the current generated by the electrochemical reactions and permeation reactions respectively. At the anode side, J_{p} is equal to 0 as the model does not take into account the O_2 permeation from the cathode to the anode, whereas at the cathode side, the hydrogen crossover leads to a permeation current, evenly distributed over the thickness of the CL, calculated from the H_2 flux that reach the cathode side as described by Equation IV-20:

Equation IV-20 :
$$J_{\mathrm{p}}=\frac{\vec{N}_{\mathrm{H_2}}^{\mathrm{a}}\cdot 2\cdot F}{e_{\mathrm{CL_c}}}$$

IV.2.3.3 Water motion in the electrolyte phase

This section focuses on the description of water motion inside the ionomer phase due to diffusion and electro-osmosis. The domains concerned are the membrane and the catalyst layers. The molar species balance is described by Equation IV-21:

Equation IV-21 :

$$(1-\varepsilon)\varepsilon_{\mathrm{ionomer}}\frac{\partial C_{\mathrm{H_2O}}}{\partial t} = -\nabla\cdot\left(\vec{N}_{\mathrm{H_2O}}\right)+S_{\mathrm{H_2O}}^{\mathrm{d}}+S_{\mathrm{H_2O}}$$

With $C_{\mathrm{H_2O}}$ the water concentration in the ionomer. The molar flux of water $\vec{N}_{\mathrm{H_2O}}$ described by an electro-osmosis term and a diffusion term (Equation IV-22):

Equation IV-22 :

$$\vec{N}_{\mathrm{H_2O}} = n_{\mathrm{d}}\frac{\vec{\mathrm{i}}_{\mathrm{i}}}{F} - D_{\mathrm{H_2O}}\vec{\nabla}\left(C_{\mathrm{H_2O}}\right)$$

With the water diffusion coefficient $D_{\mathrm{H_2O}}$ calculated via Equation IV-23, according to [34], [35]:

Equation IV-23 :

$$D_{\mathrm{H_2O}} = (6.707\cdot 10^{-8}\lambda+6.387\cdot 10^{-7})\cdot \mathrm{e}^{\left(-\frac{2416}{T}\right)}$$

And the electro-osmosis coefficient n_{d} calculated thanks to Equation IV-24, according to [36]:

Equation IV-24 :

$$n_{\mathrm{d}} = 1.0+0.0028\lambda+0.0026\lambda^2$$

Where λ represents the relative water content in the ionomer as a function of both the concentration of water $C_{\mathrm{H_2O}}$ and the concentration of SO_3^- sites in the ionomer $C_{\mathrm{SO_3^-}}$ the Equation IV-25:

Equation IV-25 :

$$C_{\mathrm{H_2O}} = \lambda C_{\mathrm{SO_3^-}}$$

The model also takes into account the equilibrium concentration at the interface ionomer|pore and it is estimated according to [35] in Equation IV-26:

Equation IV-26 :

$$\lambda_{\mathrm{eq}}\left(a_{\mathrm{H_2O}}\right) = 0.043+17.81a_{\mathrm{H_2O}} - 39.85a_{\mathrm{H_2O}}^2+36a_{\mathrm{H_2O}}^3$$

With the water activity $a_{\mathrm{H_2O}}$ calculated via Equation IV-27:

Equation IV-27 :

$$a_{\mathrm{H_2O}} = \frac{P_{\mathrm{vap}}}{P_{\mathrm{sat}}(\mathrm{T})} = \frac{c_{\mathrm{vap}}RT}{P_{\mathrm{sat}}(\mathrm{T})}$$

The source term $S_{\mathrm{H_2O}}^{\mathrm{d}}$ is determined thanks to Equation IV-28:

Equation IV-28 :

$$S_{\mathrm{H_2O}}^{\mathrm{d}} = h_{\mathrm{des}}\cdot\Gamma_{\mathrm{Pt}}\left(C_{\mathrm{H_2O}}^{\mathrm{eq}} - C_{\mathrm{H_2O}}\right)$$

With h_{des} a diffusion resistance term calculated via Equation IV-29:

Equation IV-29 :

$$h_{\mathrm{des}} = \frac{1}{k_{\mathrm{film}}}+\frac{1}{k_{\mathrm{int}}}$$

With k_{film} the diffusion resistance term through the ionomer film and k_{int} which describes the adsorption/desorption kinetic of water from the pore to the ionomer film. These terms are expressed respectively according to Equation IV-30 and Equation IV-31, respectively:

Equation IV-30 :
$$k_{\text{film}} = \frac{D_w}{e_{ionomer}}$$

Equation IV-31 :
$$k_{\text{int}} = b_0 \cdot \mathrm{e}^{\frac{-a}{RT}}$$

With b_0 a diffusion resistance coefficient and a a molar energy coefficient. The source term $S_{\mathrm{H_2O}}$ is equal to 0 in the anode catalyst layer since there is no production/consumption of water, and in the cathode catalyst layer the source term is calculated with Equation IV-32:

Equation IV-32 :
$$S_{\mathrm{H_2O}} = -\frac{J_{\mathrm{r}}}{2F}$$

Figure IV-4 shows a simplified representation of the flux and source terms of the different species, modelled by the 1D rib/channel code.

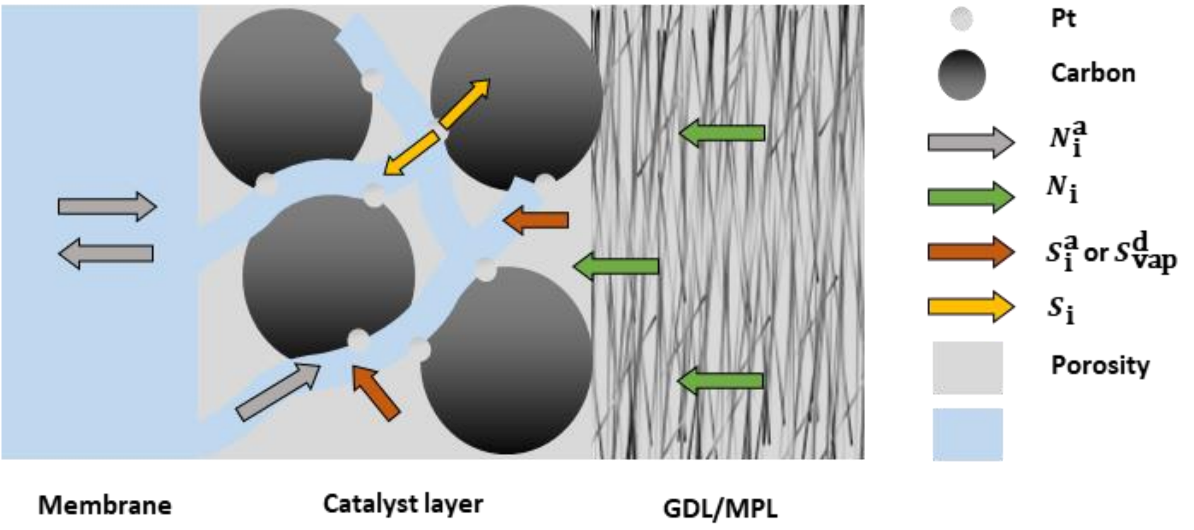

Figure IV-4 : Schematic representation of the different flux and source terms; the exponent "a" is related to the ionomer phase

IV.2.3.4 Electronic transport

The electronic transport is related to the electronic potential distribution by writing the charge conservation coupled with the Ohm's law in all the solid materials except the membrane, which act as electronic insulator (Equation IV-33):

Equation IV-33 :
$$\nabla \cdot \vec{\mathrm{i}_{\mathrm{e}}} = -\nabla \cdot \left(\sigma_{\mathrm{e}} \cdot \vec{\nabla} \Psi\right) = S_{\mathrm{e}}$$

With i_{e} the electronic current, σ_{e} the effective electronic conductivity, S_{e} a source term and Ψ the electronic potential. In the BP, GDL and MPL, there is no production/consumption of electronic current (Equation IV-34):

Equation IV-34 :

$$S_{\mathrm{e}} = 0$$

The only domain where electronic current is produced or consumed is in the catalyst layers from the electrochemical (J_{r}) and permeation (J_{p}) reactions (Equation IV-35):

Equation IV-35 :

$$S_{\mathrm{e}} = J_{\mathrm{r}} - J_{\mathrm{p}}$$

IV.2.3.5 Ionic transport

The ionic transport deals with the protonic conduction through the ionomer phase inside the membrane and the catalyst layers. The following equations present the computation of the ionic potential distribution ϕ:

Equation IV-36 :

$$\nabla\cdot\vec{\mathrm{i}}_{\mathrm{i}} = -\nabla\cdot\left(\sigma_{\mathrm{i}}\cdot\vec{\nabla}\phi\right) = S_{\mathrm{i}}$$

With i_{i} the ionic current, σ_{i} the effective ionic conductivity and S_{i} a source term which is equal to 0 in the membrane (see Equation IV-37), as there is no production/consumption of protons that would generate an ionic current:

Equation IV-37 :

$$S_{\mathrm{i}} = 0$$

Whereas the source term is equal to $-S_{\mathrm{e}}$ in the CL (Equation IV-38):

Equation IV-38 :

$$S_{\mathrm{i}} = -J_{\mathrm{r}} + J_{\mathrm{p}}$$

The ionic conductivity depends on the hydration of the ionomer, which is related to its water content [37], [38] and the effective ionic conductivity, and it can be written as a function of porosity and tortuosity as described by Equation IV-39:

Equation IV-39 :

$$\sigma_{\mathrm{i}} = \frac{(1-\varepsilon)\varepsilon_{\mathrm{ionomer}}}{\tau_{\mathrm{ionomer}}^{2}}\sigma_{\mathrm{i,m}}$$

With $\sigma_{\mathrm{i,m}}$ the ionic conductivity of the ionomer, defined by Equation IV-40 [37]:

Equation IV-40 :

$$\sigma_{\mathrm{i,m}} = \mathrm{e}^{1268\left(\frac{1}{303}-\frac{1}{T}\right)}\left(-0.326+0.5139\lambda\right)$$

IV.2.3.6 Thermal modeling

Regarding heat transfer, the equations are based on the Fourier's law. The model takes into account the conduction, the heat convection by gases and the balance in solid media, which leads to the Equation IV-41:

Equation IV-41 :

$$\varepsilon(\rho c_{\mathrm{p}} + c_{\mathrm{g}}C_{\mathrm{pg}}(T))\frac{\partial T}{\partial t} + \nabla\cdot\left(-\kappa\vec{\nabla}T\right) = \sum Q - \nabla H_{\mathrm{g}}(T)\cdot N_{\mathrm{g}}$$

With ε the porosity, ρ the material density, c_{p} the mass heat capacity at constant pressure, c_{g} the molar concentration of the gas, C_{pg} the molar heat capacity of the gas, κ the effective thermal conductivity of the media, Q the term source, H_{g} the enthalpy formation of the gas and N_{g} the molar flux density of the gas. In the catalyst layers, the heat and the electrical energy are generated by the electrochemical reactions according to Equation IV-42:

Equation IV-42 :
$$\frac{\Delta H^{\circ}_{\mathrm{a/c}}}{nF} J_{\mathrm{r}} = W_{\mathrm{e^-}} + Q_{\mathrm{reac}}$$

Where $\Delta H^{\circ}_{\mathrm{a/c}}$ is the enthalpy of the HOR at the anode and the ORR at the cathode side, $W_{\mathrm{e^-}}$ the electrical energy and Q_{reac} the heat produced by the reactions. The electrical energy can be expressed according to Equation IV-43:

Equation IV-43 :
$$W_{\mathrm{e^-}} = (\Psi - \phi)\cdot J_{\mathrm{r}}$$

Which leads to the heat generated by the electrochemical reactions in Equation IV-44:

Equation IV-44 :
$$Q_{\mathrm{reac}} = \left((\Psi - \phi) + \frac{\Delta H^{\circ}_{\mathrm{a/c}}}{nF}\right)\cdot J_{\mathrm{r}}$$

As permeation, at the cathode side, is taken into account in the model, the reaction linked to gas permeation also leads to heat production following Equation IV-45:

Equation IV-45 :
$$Q_{\mathrm{perm}} = -\frac{\Delta H^{\circ}_{\mathrm{c}}}{nF}\cdot J_{\mathrm{p}}$$

The last heat source term is related to Joule heating effect, everywhere in the domain considered, described by Equation IV-46:

Equation IV-46 :
$$Q_{\mathrm{j}} = \frac{i^2}{\sigma_{\mathrm{j}}}$$

As boundary condition at the BP|GDL interface, the temperature is fixed and equal to the electrode rib/channel temperature T_0, defined as operating condition (Equation IV-47):

Equation IV-47 :
$$T = T_0$$

Finally, there is no other thermal flux in the cell since the latter is considered as thermally insulated (Equation IV-48):

Equation IV-48 :
$$-\kappa\vec{\nabla}T = \vec{0}$$

IV.2.3.7 Electrochemistry

This section presents the equation used to calculate the potential and the current density inside the CL, where the electrochemical reactions take place [31]. The Faradic current density J_{r} as a function of overpotential η, is given by the Butler-Volmer law at the anode catalyst layer (Equation IV-49):

Equation IV-49 :
$$J_{\mathrm{r,a}} = J_{0,\mathrm{a}}\left[\mathrm{e}^{\frac{\alpha_{\mathrm{a}} nF}{RT}\eta_{\mathrm{a}}} - \mathrm{e}^{\frac{-(1-\alpha_{\mathrm{a}})nF}{RT}\eta_{\mathrm{a}}}\right]$$

At the cathode catalyst layer (Equation IV-50):

Equation IV-50 :

$$J_{\mathrm{r,c}}=J_{0,\mathrm{c}}\left[\mathrm{e}^{\frac{\alpha_{\mathrm{c}}nF}{RT}\eta_{\mathrm{c}}}-\mathrm{e}^{\frac{-(1-\alpha_{\mathrm{c}})nF}{RT}\eta_{\mathrm{c}}}\right]$$

With n the number of electron exchanged for the reaction considered, α_{a} the symmetry factor of the HOR, α_{c} the symmetry factor of the ORR, $1-\alpha_{\mathrm{a}}$ the symmetry factor of the hydrogen evolution reaction (HER), $1-\alpha_{\mathrm{c}}$ the symmetry factor of the oxygen evolution reaction (OER), and $J_{0,\mathrm{a/c}}$ the exchange current density expressed as a function of the different activities and kinetic rate of the reaction according to Equation IV-51:

Equation IV-51 :

$$J_{0,\mathrm{a/c}}=nF(k^{\circ}_{\mathrm{ox,a/c}})^{1-\alpha_{\mathrm{a/c}}}(k^{\circ}_{\mathrm{red,a/c}})^{\alpha_{\mathrm{a/c}}}\left(\prod\nolimits_{\nu_{\mathrm{j}}>0}(a_{\mathrm{j}}^{\nu_{\mathrm{j}}})\right)^{1-\alpha_{\mathrm{a/c}}}\left(\prod\nolimits_{\nu_{\mathrm{j}}<0}(a_{j}^{-\nu_{\mathrm{j}}})\right)^{\alpha_{\mathrm{a/c}}}$$

Where a_{j} and ν_{j} stand for the activity and the stoichiometry coefficient respectively of the specie j and $k^{0}_{\mathrm{ox,a/c}}$ and $k^{0}_{\mathrm{red,a/c}}$ are the kinetic rate coefficient of the oxidation and reduction reaction, respectively, at the anode/cathode catalyst layer; they can be expressed according to Equation IV-52 and Equation IV-53:

Equation IV-52 :

$$k^{\circ}_{\mathrm{ox,a/c}}=k^{\circ}\mathrm{e}^{-\frac{\Delta G^{\ddagger}_{\mathrm{ox,a/c}}}{RT}}$$

Equation IV-53 :

$$k^{\circ}_{\mathrm{red,a/c}}=k^{\circ}\mathrm{e}^{-\frac{\Delta G^{\ddagger}_{\mathrm{red,a/c}}}{RT}}$$

With $\Delta G^{\ddagger}_{\mathrm{ox,a/c}}$ and $\Delta G^{\ddagger}_{\mathrm{red,a/c}}$ the activation free enthalpy of the oxidation and reduction reaction, respectively, at the anode/cathode catalyst layer that characterizes the difference in energy between oxidiser/reductant and the transition state (energy barrier to overcome for a reaction to proceed) and k° expressed as in Equation IV-54:

Equation IV-54 :

$$k^{\circ}=\frac{k_{\mathrm{b}}T}{s_{0}N_{\mathrm{A}}h}$$

With k_{b} the Boltzmann constant, h the Planck constant, s_{0} the average Pt surface per active site and N_{A} the Avogadro constant. Regarding the activation free enthalpy of the oxidation reaction, the Equation IV-55 shows its expression as function of the activation enthalpy and the activation entropy:

Equation IV-55 :

$$\Delta G^{\ddagger}_{\mathrm{ox}}=\Delta H^{\ddagger}_{\mathrm{ox}}-T\cdot\Delta S^{\ddagger}_{\mathrm{ox}}$$

The activation free enthalpy of the reduction reaction can be written as a function of the free enthalpy of the oxidation reaction and the reaction free enthalpy ΔG° as in Equation IV-56:

Equation IV-56 :

$$\Delta G^{\ddagger}_{\mathrm{red}}=\Delta G^{\ddagger}_{\mathrm{ox}}+\Delta G^{\circ}$$

The reaction free enthalpy ΔG° is characterized by the change in energy between the reactants and products and can be expressed as in Equation IV-57:

Equation IV-57 :
$$\Delta G^{\circ} = \Delta H^{\circ} - T{\cdot}\Delta S^{\circ}$$

The reaction free enthalpy ΔG° is a thermodynamic quantity that can be determined from tables. It leads to the calculation of the standard potential of the electrochemical reaction considered, which is defined by Equation IV-58:

Equation IV-58 :
$$E^{\circ} = -\frac{\Delta G^{\circ}}{nF}$$

The overpotential η is the difference between the electrode and the ionic potential $(\Psi - \phi)$ and the equilibrium potential E_{eq} (Equation IV-59):

Equation IV-59 :
$$\eta = (\Psi - \phi) - E_{\mathrm{eq}}$$

The equilibrium potential is expressed as a function of the standard potential and the activity of the species (Nernst law) thanks to Equation IV-60:

Equation IV-60 :
$$E_{\mathrm{eq}} = -\frac{\Delta G^{\circ}}{nF} + \frac{RT}{nF}\ln\left(\prod\nolimits_{\nu_{\mathrm{j}}} a_{\mathrm{j}}^{\nu_{\mathrm{j}}}\right)$$

The activities of dissolved species are calculated according to Equation IV-61:

Equation IV-61 :
$$a_{\mathrm{j}} = \frac{C_{\mathrm{j}}}{H_{\mathrm{j}}P^{\circ}}$$

Where P° is the standard pressure for which the reaction enthalpy (Equation IV-57) is given.

In the initial version of the 1D rib/channel code, the ORR at the cathode catalyst layer, and the HOR at the anode catalyst layer are described by a single one-step reaction. This model allows to simulate quite accurately the performance of a PEMFC, as it is shown in the work of Randrianarizafy [30]. However, the use of Nernst and Butler-Volmer equations to describe, on the one hand the HOR at the anode, and on the other hand the ORR at the cathode, is not sufficient to understand in detail how the ORR mechanism occurs and the possible limitating phenomena related. For instance, with a description in single one-step, it is not possible to have information on the place-exchange phenomenon, which was identified for being partly responsible of the catalyst degradation. Moreover, the behaviour of Pt under nitrogen atmosphere during potential cycling is not accessible via the single one-step reaction, as it involves the adsorption/desorption of several species at the catalyst surface. The following focuses on a more detailed description of the ORR mechanism at the cathode catalyst layer, and the adsorption/desorption reaction that take place during potential cycling under nitrogen atmosphere.

IV.3 Improvement of the electrocatalyst description by the implementation of Pt surface states

The previous section dealt with the general description of the model used. The numerical implementation of the equations previously described and their numerical resolution are not shown here as the model is based on the previous work of Randrianarizafy [30]. The aim of the present work is to improve the description of physico-chemical and electrochemical processes that occur at the cathode with a more mechanistic approach via the implementation of a multi-step ORR mechanism replacing the one-step global approximation. In the Chapter I, it has been seen that the ORR mechanism is much more complex than a single step reaction. It notably includes the participation of several intermediate species, which have an impact on the kinetics of the reaction and may lead to the degradation of the catalyst through the Pt oxides formation/reduction. Thus, to have more insights into the ORR mechanism, and better describe the physico-chemical and electrochemical phenomena involved in the cathode catalyst layer, a more detailed description of the surface state of Pt active sites by considering the formation of different Pt oxides is developed as reaction intermediates thanks to several reaction steps. The place exchange phenomenon will also be described as it plays a crucial role on the performance of the PEMFC and in degradation processes. This improvement introduces new parameters that will help describing the Pt surface state and its coverage ratio as a function of the potential. Fuel cell operation in presence of oxygen and electrochemical characterization under nitrogen atmosphere will be considered and studied in this work. The electrochemistry at the anode catalyst layer remains unchanged and is still described by Nernst and Butler-Volmer equations in a one-step reaction.

IV.3.1 Multi-step mechanism implemented at the cathode

IV.3.1.1 Pt oxides formation/reduction mechanism

The behaviour of the Pt catalysts has been studied in order to introduce new electrocatalytic features in the EuROPIUM model and especially the Pt surface oxides formation and reduction, which define platinum surface state. To that goal, a multi-step ORR mechanism has been developed, based on the work of Jahnke *et al.* and Maranzana *et al.* [28], [29]. It better describes the physical and electrochemical phenomena involved in the catalyst layers during fuel cell operation and potential cycling under inert atmosphere, which would explain (at least in part) dynamic response and/or the reversible degradation during fuel cell operation. The multi-steps ORR mechanism is described by the Equation IV-62 to Equation IV-65 and the Figure IV-5 illustrates the different types of oxides that can be formed.

Equation IV-62 : $$Pt_s + H_2O \leftrightarrow PtOH_s + H^+ + e^- \qquad r_1$$

Equation IV-63 : $$PtOH_s \leftrightarrow PtO_s + H^+ + e^- \qquad r_2$$

Equation IV-64 : $$PtO_s + Pt_b \leftrightarrow PtO_b + Pt_s \qquad r_3$$

Equation IV-65 : $$2Pt_s + O_2 \rightarrow 2PtO_s \qquad r_4$$

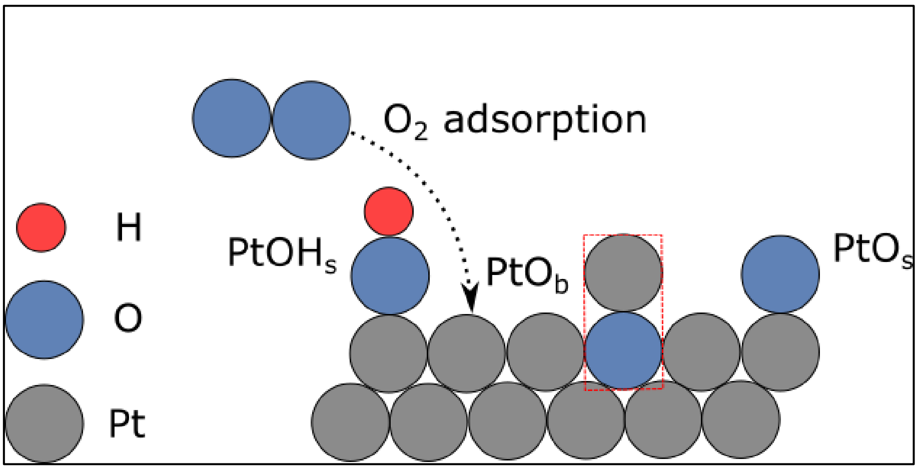

Figure IV-5 : Illustration of the different Pt oxides formed via the multi-step mechanism and the chemical O_2 adsorption on Pt.

This multi-step ORR mechanism consists of two electrochemical reversible steps (Equation IV-62 and Equation IV-63), a chemical place exchange reaction (Equation IV-64) and the adsorption of oxygen on surface Pt (Equation IV-65). The “s” and “b” subscripts are referring to platinum oxides species on the surface of Pt and in the bulk (under the Pt surface), respectively. The three first equations allow to simulate cyclic voltammetry and to reproduce the behaviour observed and attributed to platinum oxides in the potential range of 0.45 - 1.2 V during CV experiments under inert atmosphere. To reproduce an ORR mechanism in presence of gaseous oxygen and simulate the performance of the PEMFC, the chemical O_2 adsorption on Pt must be taken into account. The choice of the mechanism has been done in order to start with a ‘simple’ description (choice of the dissociative pathway to limit the number of parameters introduced) but enough complex to simulate and capture the main electrochemical phenomenon observed under both inert and oxygenated atmosphere (Pt oxides formation, hysteresis phenomenon, etc). In addition, there was a will to describe what is at stake under both atmospheres thanks to one single mechanism and a unique set of kinetic parameters. To these different reactions are associated direct kinetics, r_1-r_4 described by the Equation IV-66 to Equation IV-72. These direct kinetic expressions introduce new electrocatalytic features, related to the different surface and bulk species, such as: the coverage ratio θ_i of the specie i, the interaction parameter between the different adsorbed species ω_j, with ‘*j*’ subscript referring to the reaction *j*, and the kinetic rate constant of each reaction k_j. The interaction parameter ω has been introduced considering isotherm adsorption and based on the Frumkin interaction between surface adsorbed species (attractive if $\omega < 0$ and repulsive if $\omega > 0$). This parameter was also introduced in the work of Jahnke *et al.* and Maranzana *et al.* [28], [29]. Thanks to this multi-step ORR mechanism description, it is possible to have more insights into the platinum surface state via the coverage ratio of surface Pt: θ_{Pt_s}. It also enables the capture of the different Pt oxides coverage ratio θ_{PtOH_s}, θ_{PtO_s} and θ_{PtO_b} evolution with potential during cyclic voltammetry and polarization curve simulation.

Equation IV-66 : $$r_{1_{ox}} = k_{1_{ox}} \theta_{Pt_s} a_{H_2O} e^{\frac{-\omega_1 \theta_{PtOH_s}}{RT}} e^{\frac{\alpha_{1_{ox}} F}{RT} \Delta\phi}$$

Equation IV-67 :
$$r_{1_{\mathrm{red}}} = k_{1_{\mathrm{red}}}\theta_{\mathrm{PtOH_s}}a_{\mathrm{H+}}\mathrm{e}^{\frac{\omega_1\theta_{\mathrm{PtOH_s}}}{RT}}\mathrm{e}^{\frac{-\alpha_{1_{\mathrm{red}}}F}{RT}\Delta\phi}$$

Equation IV-68 :
$$r_{2_{\mathrm{ox}}} = k_{2_{\mathrm{ox}}}\theta_{\mathrm{PtOH_s}}\mathrm{e}^{\frac{-\omega_2\theta_{\mathrm{PtO_s}}}{RT}}\mathrm{e}^{\frac{\alpha_{2_{\mathrm{ox}}}F}{RT}\Delta\phi}$$

Equation IV-69 :
$$r_{2_{\mathrm{red}}} = k_{2_{\mathrm{red}}}\theta_{\mathrm{PtO_s}}a_{\mathrm{H+}}\mathrm{e}^{\frac{\omega_2\theta_{\mathrm{PtO_s}}}{RT}}\mathrm{e}^{\frac{-\alpha_{2_{\mathrm{red}}}F}{RT}\Delta\phi}$$

With “ox” subscript standing for an oxidation reaction and “red” subscript for a reduction reaction.

Equation IV-70 :
$$r_{3_{\mathrm{s\_b}}} = k_{3_{\mathrm{s\_b}}}\theta_{\mathrm{PtO_s}}\theta_{\mathrm{Pt_b}}$$

Equation IV-71 :
$$r_{3_{\mathrm{b\_s}}} = k_{3_{\mathrm{b\_s}}}\theta_{\mathrm{Pt_s}}\theta_{\mathrm{PtO_b}}$$

With “s_b” subscript standing for the transition from surface oxide $\mathrm{PtO_s}$ to bulk site $\mathrm{PtO_b}$ and “b_s” the recovery of Pt surface oxide site $\mathrm{PtO_s}$ from $\mathrm{PtO_b}$.

Equation IV-72 :
$$r_{4_{\mathrm{PtO_s}}} = k_{4_{\mathrm{PtO_s}}}a_{\mathrm{O_2}}\theta_{\mathrm{Pt_s}}^{2}$$

With “$\mathrm{PtO_s}$” subscript standing for the O_2 adsorption reaction. The chemical desorption on oxygen was not considered here to force the adsorbed oxygen to react through the mechanism.

The currents resulting from the reactions r_1 and r_2 are calculated according to Equation IV-73 toEquation IV-76:

Equation IV-73 :
$$i_{1_{\mathrm{ox}}} = \Gamma_{\mathrm{Pt}}F\frac{r_{1_{\mathrm{ox}}}}{s_{0\_\mathrm{c}}N_{\mathrm{A}}}$$

Equation IV-74 :
$$i_{1_{\mathrm{red}}} = \Gamma_{\mathrm{Pt}}F\frac{-r_{1_{\mathrm{red}}}}{s_{0\_\mathrm{c}}N_{\mathrm{A}}}$$

Equation IV-75 :
$$i_{2_{\mathrm{ox}}} = \Gamma_{\mathrm{Pt}}F\frac{r_{2_{\mathrm{ox}}}}{s_{0\_\mathrm{c}}N_{\mathrm{A}}}$$

Equation IV-76 :
$$i_{2_{\mathrm{red}}} = \Gamma_{\mathrm{Pt}}F\frac{-r_{2_{\mathrm{red}}}}{s_{0\_\mathrm{c}}N_{\mathrm{A}}}$$

With Γ_{Pt} the specific surface of Pt in the CL, r_{j} the rate of the reaction *j* and s_{0_c} the average Pt surface per active site at the cathode side. The total current generated by the oxides formation/reduction reactions is calculated as the sum of the currents of each electrochemical reaction (Equation IV-77):

Equation IV-77 :
$$i_{\mathrm{oxides}} = i_{1_{\mathrm{ox}}}+i_{1_{\mathrm{red}}}+i_{2_{\mathrm{ox}}}+i_{2_{\mathrm{red}}} \qquad \text{under nitrogen atmosphere}$$

In the presence of O_2, the current related to the ORR is equal to i_{oxides} (Equation IV-78):

Equation IV-78 :
$$i_{\mathrm{ORR}} = i_{\mathrm{oxides}}$$

The different coverage temporal variations are calculated by the balance Equation IV-79 to Equation IV-81:

Equation IV-79 :
$$\frac{\mathrm{d}\theta_{\mathrm{PtOH_s}}}{\mathrm{d}t} = r_{1_{\mathrm{ox}}} - r_{1_{\mathrm{red}}} + r_{2_{\mathrm{red}}} - r_{2_{\mathrm{ox}}}$$

Equation IV-80 :
$$\frac{\mathrm{d}\theta_{\mathrm{PtO_s}}}{\mathrm{d}t} = r_{2_{\mathrm{ox}}} - r_{2_{\mathrm{red}}} - r_{3_{\mathrm{s\_b}}} + r_{3_{\mathrm{b\_s}}} + 2r_{4_{\mathrm{PtO_s}}}$$

Equation IV-81 :
$$\frac{\mathrm{d}\theta_{\mathrm{PtO_b}}}{\mathrm{d}t} = r_{3_{\mathrm{s\_b}}} - r_{3_{\mathrm{b\_s}}}$$

To sum up, this multi-step mechanism enables to go beyond the previous model of Randrianarizafy and will help to describe the physico-chemical and electrochemical processes at the electrode, during ORR and under inert atmosphere when performing CV; it will also give access to the potential and temporal evolution of oxide coverages.

IV.3.1.2 Proton adsorption/desorption on Pt

The proton adsorption/desorption reactions that proceed on platinum under 0.4 V *vs.* RHE have also been introduced at the cathode side. The steps are based on a Volmer-Heyrovsky mechanism and are built in a similar way as the Pt oxides formation/reduction reactions. The reversible mechanism is described by Equation IV-82 and Equation IV-83:

Equation IV-82 :
$$Pt_s + H^+ + e^- \leftrightarrow PtH_s \qquad r_{1\_H}$$

Equation IV-83 :
$$PtH_s + H^+ + e^- \leftrightarrow Pt_s + H_2 \qquad r_{2\_H}$$

The kinetics associated to these reactions are presented by the Equation IV-84 to Equation IV-87:

Equation IV-84 :
$$r_{1_{\mathrm{ox\_H}}} = k_{1_{\mathrm{ox\_H}}}\theta_{\mathrm{PtH_s}}\mathrm{e}^{\frac{\omega_{1\_\mathrm{H}}\theta_{\mathrm{PtH_s}}}{RT}}\mathrm{e}^{\frac{\alpha_{1_{\mathrm{ox\_H}}}F}{RT}\Delta\phi}$$

Equation IV-85 :
$$r_{1_{\mathrm{red\_H}}} = k_{1_{\mathrm{red\_H}}}\theta_{\mathrm{Pt_s}}a_{\mathrm{H^+}}\mathrm{e}^{\frac{-\omega_{1\_\mathrm{H}}\theta_{\mathrm{PtH_s}}}{RT}}\mathrm{e}^{\frac{-\alpha_{1_{\mathrm{red\_H}}}F}{RT}\Delta\phi}$$

Equation IV-86 :
$$r_{2_{\mathrm{ox\_H}}} = k_{2_{\mathrm{ox\_H}}}\theta_{\mathrm{Pt_s}}a_{\mathrm{H_2}}\mathrm{e}^{\frac{\alpha_{2_{\mathrm{ox\_H}}}F}{RT}\Delta\phi}$$

Equation IV-87 :
$$r_{2_{\mathrm{red\_H}}} = k_{2_{\mathrm{red\_H}}}\theta_{\mathrm{PtH_s}}a_{\mathrm{H^+}}\mathrm{e}^{\frac{-\alpha_{2_{\mathrm{red\_H}}}F}{RT}\Delta\phi}$$

The currents resulting from the reactions r_{1_H} and r_{2_H} are calculated according to Equation IV-88 to Equation IV-91:

Equation IV-88 :
$$i_{1_{\mathrm{ox\_H}}} = \Gamma_{\mathrm{Pt}}F\frac{r_{1_{\mathrm{ox}}}}{s_{0\_c}N_{\mathrm{A}}}$$

Equation IV-89 :
$$i_{1_{\mathrm{red\_H}}} = \Gamma_{\mathrm{Pt}}F\frac{-r_{1_{\mathrm{red\_H}}}}{s_{0\_c}N_{\mathrm{A}}}$$

Equation IV-90 :
$$i_{2_{\mathrm{ox\_H}}} = \Gamma_{\mathrm{Pt}}F\frac{r_{2_{\mathrm{ox\_H}}}}{s_{0\_c}N_{\mathrm{A}}}$$

Equation IV-91 :
$$i_{2_{\mathrm{red\_H}}}=\Gamma_{\mathrm{Pt}}F\,\frac{-r_{2_{\mathrm{red\_H}}}}{s_{0\_\mathrm{c}}N_{\mathrm{A}}}$$

The total current $\mathrm{i_H}$ generated by the proton adsorption/desorption on Pt mechanism is calculated as the sum of the currents of each electrochemical reaction (Equation IV-92):

Equation IV-92 :
$$i_{\mathrm{H}}=i_{1_{\mathrm{ox\_H}}}+i_{1_{\mathrm{red\_H}}}+i_{2_{\mathrm{ox\_H}}}+i_{2_{\mathrm{red\_H}}}$$

The coverage temporal variations of $\theta_{\mathrm{PtH_s}}$ is calculated as follows in Equation IV-93:

Equation IV-93 :
$$\frac{\mathrm{d}\theta_{\mathrm{PtH_s}}}{\mathrm{d}t}=r_{1_{\mathrm{ox\_H}}}-r_{1_{\mathrm{red\_H}}}+r_{2_{\mathrm{ox\_H}}}-r_{2_{\mathrm{red\_H}}}$$

The HOR/HER mechanism introduces the same kind of parameters as the ones applied to Pt oxides formation/reduction. The global current measured at the electrode is known by summing the current generated by the Pt oxides formation/reduction and the current generated by the proton adsorption/desorption on Pt (Equation IV-94):

Equation IV-94 :
$$i_{\mathrm{total}}=i_{\mathrm{oxides}}+i_{\mathrm{H}}$$

Finally, the free platinum surface and free platinum bulk coverage are calculated thanks to Equation IV-95 and Equation IV-96 respectively:

Equation IV-95 :
$$\theta_{\mathrm{Pt_s}}=1-\theta_{\mathrm{PtOH_s}}-\theta_{\mathrm{PtO_s}}-\theta_{\mathrm{PtH_s}}$$

Equation IV-96 :
$$\theta_{\mathrm{Pt_b}}=1-\theta_{\mathrm{PtO_b}}$$

The different kinetic parameters introduced with the multi-step mechanisms are unknown. Thus, they must be estimated empirically using the experimental data through a fitting procedure that is detailed in the following section.

IV.3.1.3 Parameter fitting process

Using realistic parameters is a mandatory step before starting any numerical study, that requires experimental data (see Chapter II). If the parameters are not directly available, they may be estimated by fitting the model on experimental results. Usually, the main data used for the fitting process are experimental polarization curves performed at various operating conditions (temperature, relative humidity, etc.). In this thesis, values for kinetic parameters were initially taken from the work of Jahnke *et al.* and Maranzana *et al.* [28], [29] or set equal to 1 for kinetic parameters that were not described in their work. Then, the kinetic parameters were roughly fitted through parametric studies at one specific operating condition, in order to get the correct order of magnitude for each parameter, according to experimental data. Finally, an automatic iterative fitting procedure was performed to further tune these values and get the best description for voltammogram under $\mathrm{N_2}$ or for performance response obtained by polarization curves. This iterative procedure consists of:

1. A first estimation of the parameters is given to the code (comes from the rough estimation from the parametric study);

2. Then, the polarization curve is simulated thanks to Matlab scripts that launch the COMSOL simulation. In this case, the potential is imposed and the current is simulated;
3. The polarization curve simulated is compared to the experimental one at the defined operating condition. The deviations obtained leads to a new set of parameters values using a minimization algorithm provided by Mathworks;
4. Using the new parameters' estimation, another polarization curve is simulated and then compared to the experiment (step 2). The procedure ends when a defined maximum number of iterations or minimum of deviations is reached.

Let us stress that this procedure does not necessarily give a unique solution, meaning that another set of parameters values may give the same or really close results. Moreover, the solution obtained with this procedure may only be valid within the range of the operating conditions considered, depending on the parameters chosen for the fitting procedure. The extrapolation outside this range may be questionable or may lead to inaccurate results. Thus, this fitting procedure also acts as a validation tool at the operating condition considered, which justifies the use of the kinetic parameters values obtained. In the following, all the numerical polarization curves and cyclic voltammetries were obtained using the last kinetic parameters values coming from the fitting procedure.

IV.3.2 Very low loaded MEA simulation

IV.3.2.1 Overall presentation of modeling results

In order to facilitate the implementation of the new electrochemical description, it was decided to consider at first the catalyst layers as interfaces (which corresponds to infinitely thin active layer) to rule out catalyst layers transport properties and to focus only on electrochemical aspects. This choice was made to decrease significantly the simulation time and facilitate the debugging of the implementation. Considering catalyst layers as 0D-layers implies to use specific very low loaded MEA: 20 $\mu g_{Pt}.cm_{geo}^{2}$ cathode catalyst layer was chosen as its thickness is very small (around 0.7 µm). To be able to compare rigorously modeling and experiments, all the material features and operating conditions considered for simulation are similar to the ones used during experiments. The Figure IV-6 illustrates the simulated domains obtained with the 1D rib-channel code considering the two catalyst layers as interfaces. All the transport phenomena through the thickness of the CL are neglected, but electrochemical kinetics are unchanged compared to 1D.

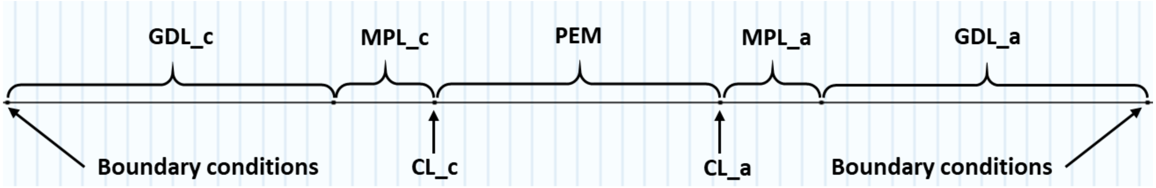

Figure IV-6 : Simulated domains using the 1D-rib-channel code with a 0D of CL.

IV.3 Improvement of the electrocatalyst description by the implementation of Pt surface states

Both the H_2/O_2 configuration and H_2/N_2 configuration operating conditions used to perform the simulations that are compared to experiments are presented in the Table IV-2. The different geometric parameters used for very low loaded simulations are given in the Table IV-3.

Table IV-2 : Operating conditions used for very low loaded MEA performance simulation.

	Under H_2/O_2 configuration	**Under H_2/N_2 configuration**
Anode channel pressure	134000 Pa	100000 Pa
Cathode channel pressure	134000 Pa	100000 Pa
Anode rib/channel temperature	353 K	303 K
Cathode rib/channel temperature	353 K	303 K
Anode channel relative humidity	80 %	100 %
Cathode channel relative humidity	80 %	100 %
Anode hydrogen molar fraction (in dry gas)	1	1
Cathode oxygen molar fraction (in dry gas)	1	0
Sweeping rate	10 $mV.s^{-1}$	200 $mV.s^{-1}$

Table IV-3 : General parameters used for very low loaded MEA simulations.

	Value	**Estimation**
GDL Thickness	145 µm	Manufacturer data
MPL thickness	45 µm	Manufacturer data
Membrane thickness	127 µm	Manufacturer data
Anode thickness	2 µm	Cross section SEM
Anode loading	100 $\mu g_{Pt}.cm_{geo}^{-2}$	Assumed
Cathode thickness	0.7 µm	Cross section SEM
Cathode loading	23 $\mu g_{Pt}.cm_{geo}^{-2}$	XRF measurement
Γ_{Pt} (Cathode)	$1.07.10^{7}$ m^{-1}	ECSA measured experimentally

The Table IV-4 and Table IV-5 sum up the different kinetic parameters' values used to perform the simulations. Some of the values are obtained either from the fitting procedure or assumed/taken from literature. Regarding the fitted parameters, they were adjusted manually, after the fitting procedure aforementioned, in order to describe as accurately as possible both polarization curve under H_2/O_2 configuration and cyclic voltammetry under nitrogen atmosphere. The fitted kinetic parameters for Pt oxides formation/reduction reactions are obtained at 80°C, 80% RH and 1.34 bar abs. Regarding proton adsorption/desorption, the kinetic parameters were only fitted manually, thanks to parametric studies at 30°C, 100% RH and P_{atm}, in order to have a global description of the H_{UPD} region, during CV under nitrogen atmosphere. Less time was dedicated to the description of the H_{UPD} region as the Pt oxides formation/reduction reactions are the point of interest here. Regarding the time stepping, an initial study led to the use of a Backward Differentiation Formula with a tolerance criteria of 0.01 and a maximum time step (adaptative) of 0.05 s and a Newton including PARDISO solver in COMSOL. Figure IV-7 shows a comparison between experimental data, obtained on Pt/VC based very low loaded catalyst layer, and numerical simulation of the Pt/VC very low loaded catalyst layer of polarization curves (Figure IV-7 (a)) and cyclic voltammetries (Figure IV-7 (b)) at the operation conditions H_2/O_2 and H_2/N_2, respectively, from Table IV-2.

Table IV-4 : Kinetic parameters values for Pt oxides formation/reduction reactions.

Kinetic parameters for Pt oxides formation/reduction	Value	Estimation
$k_{1_{ox}}$	$9.05.10^{-7}$ s^{-1}	Fitted (in this work)
$k_{1_{red}}$	$1.27.10^{4}$ s^{-1}	Fitted (in this work)
ω_1	$5.90.10^{3}$ $J.mol^{-1}$	Fitted (in this work)
$\alpha_{1_{ox}}$	0.45	Maranzana & al. [29]
$\alpha_{1_{red}}$	0.3	Maranzana & al. [29]
$k_{2_{ox}}$	$7.51.10^{-10}$ s^{-1}	Fitted (in this work)
$k_{2_{red}}$	$1.70.10^{6}$ s^{-1}	Fitted (in this work)
ω_2	$1.53.10^{4}$ $J.mol^{-1}$	Fitted (in this work)
$\alpha_{2_{ox}}$	0.5	Assumed
$\alpha_{2_{red}}$	0.5	Assumed
$k_{3_{s\_b}}$	$4.00.10^{-2}$ s^{-1}	Fitted (in this work)
$k_{3_{b\_s}}$	2.02 s^{-1}	Fitted (in this work)
$k_{4_{PtO_s}}$	$3.19.10^{3}$ s^{-1}	Fitted (in this work)

Table IV-5 : Kinetic parameters values for proton adsorption/desorption on Pt.

Kinetic parameters for proton adsorption/desorption on Pt	Value	Estimation
$k_{1_{\mathrm{ox\_H}}}$	1.10^{-1} s^{-1}	Fitted manually
$k_{1_{\mathrm{red\_H}}}$	3.10^{2} s^{-1}	Fitted manually
ω_{1_H}	$5.0.10^{3}$ $J.mol^{-1}$	Fitted manually
$\alpha_{1_{\mathrm{ox\_H}}}$	0.5	Assumed
$\alpha_{1_{\mathrm{red\_H}}}$	0.5	Assumed
$k_{2_{\mathrm{ox\_H}}}$	5.10^{3} s^{-1}	Fitted manually
$k_{2_{\mathrm{red\_H}}}$	8.10^{1} s^{-1}	Fitted manually
$\alpha_{2_{\mathrm{ox\_H}}}$	0.5	Assumed
$\alpha_{2_{\mathrm{red\_H}}}$	0.5	Assumed

Both simulated polarization curve and cyclic voltammetry from Figure IV-7 are obtained using a unique set of kinetic parameters values between the two atmosphere configurations. The polarization curves presented are not corrected from ohmic drop. The ohmic drop correction will be done later in this chapter as it is used partly as a probe to validate the new description. First, the simulated polarization curve seems to match quite well the experimental one. On the one hand, the medium current densities are quite well captured by the new electrochemical description. However, at low/high current densities there is still a mismatch between experiment and modeling. At high current densities, it is probably due to transport properties of the CL that are not taken into account with the catalyst layer considered as interfaces. Regarding the very low current densities, the differences between experiment and modeling will be discussed later in the chapter, when the evolution of the different coverage ratio for the Pt oxides will be introduced. On the other hand, the new electrochemical description has been implemented in order to capture the surface phenomena during the ORR, especially the hysteresis phenomenon observed on experimental polarization curve. However, with the current description/set of kinetic parameters, the hysteresis phenomenon is not captured.

There is a good match between the simulated cyclic voltammetry and the experimental one as displayed on Figure IV-7 (b). The different peak potential specific to the Pt oxides formation/reduction and proton adsorption/desorption are qualitatively well located and captured compared to the experiment. In the H_{UPD} region, only the peak characteristic to the oxidation of H_2 is missing. In the oxides region, the peak relative to the oxides reduction is slightly shifted towards lower potential, meaning that the Pt oxides reduction kinetic is probably a little underestimated and the coulommetry of oxides reduction seems to be higher numerically than experimentally. This was also monitored in the work of Maranzana *et al.*, but no explanation was given regarding this observation [29]. Regarding the differences on the oxidation sweep, between 1 V and 1.2 V, they may come from the fact that the description of the formation of another oxide specie is missing. Indeed, according to their XPS measurements, Saveleva *et al.* found that the PtO_2 oxide specie can be formed at high anodic polarization. They also proposed a three-dimensional oxide growth mechanism, after the first nucleation of PtO/PtO_2 oxides [39]. This 3D oxide growth is not described here because, taking into account all the complex phenomena and their interplay would lead to a huge increase of the number of unknown parameters, making difficult their accurate estimation and the model validation. Thus, this work uses a 'simple' description in order to unravel and give more insights into the complex surface interactions between Pt and its oxides forms and the ORR mechanism.

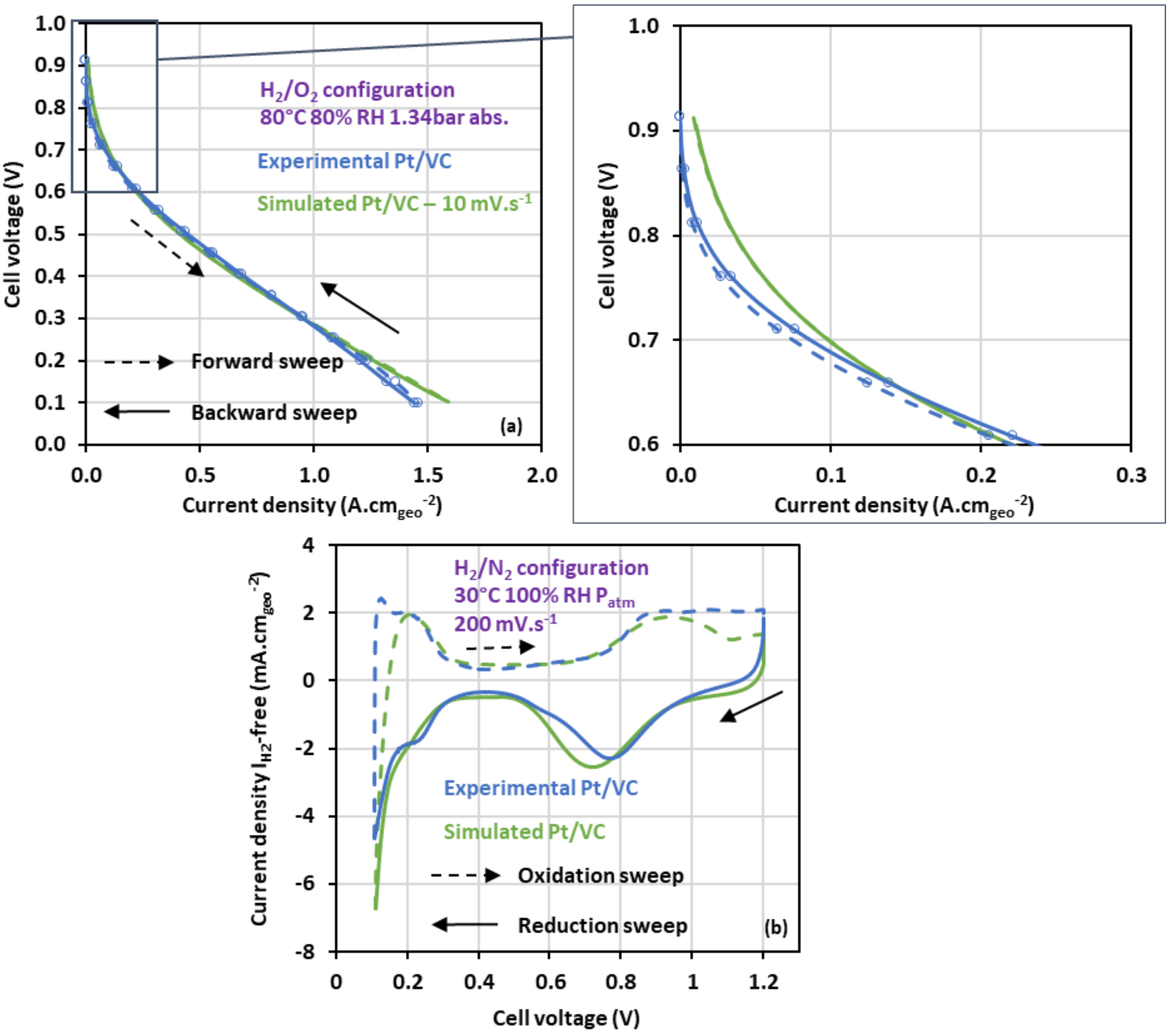

Figure IV-7 : Comparison of experimental and simulated (a) polarization curves measured on very low loaded Pt/VC MEA under H_2/O_2 configuration, with a zoom at low current densities and (b) cyclic voltammetries measured on very low loaded Pt/VC MEA under H_2/N_2 configuration.

From these first observations, it is reasonable to say that, in a first approach, the implementation of the multi steps ORR mechanisms allows to catch quite well the electrochemical response under nitrogen atmosphere, as well as the global performance of the MEA under oxygen atmosphere. However, regarding the global performance, the hysteresis phenomenon is not captured. In fact, with the current description of the ORR mechanism and the calculation of the coverage ratio of surface Pt (θ_{Pt_s}) from Equation IV-95, the Pt 'bulk' oxides formed through place exchange do not affect the Pt surface oxidation, as it was suggested in the work of Martens *et al.* [40]. In that extent, the following section will present another way to calculate the coverage ratio of surface Pt (θ_{Pt_s}) and a comparison between the two calculations will be done and discussed.

IV.3.2.2 Calculation of Pt coverage ratio: investigated scenario under H_2/O_2 configuration

A more advanced approach can be then figured out from the previous observations, by considering that the presence of 'bulk' oxides can have an impact on the surface oxides coverage of Pt. In this section, two extreme opposite cases will be investigated regarding the calculation of the Pt surface coverage ratio. Figure IV-8 shows an illustration of the two cases investigated and the way Pt sites can be covered by the different types of oxides via the multi-step mechanism. On the first hand, on Figure IV-8 (a), free Pt active sites only depend of the other surface adsorbates (PtH_s, $PtOH_s$ and PtO_s). This calculation of the free Pt surface coverage ratio θ_{Pt_s} means that the presence of a 'bulk' oxide PtO_b underneath one Pt site does not affect the surface oxidation on this active site. In other words, the Pt surface oxidation into $PtOH_s/PtO_s$ remains possible and the surface activity of this Pt site is unchanged when a 'bulk' oxide is present below the surface. On the second hand, on Figure IV-8 (b), free Pt active sites are impacted by the presence of a bulk oxide. The Pt 'bulk' oxide coverage ratio is now taken into account in the calculation of the Pt surface coverage ratio. This corresponds to the extreme opposite of the first case investigated. This second approach to calculate the Pt surface coverage ratio means that the presence of a 'bulk' oxide on a Pt site completely inhibits the surface oxidation and ORR activity on this site. This site will be reactivated once the oxygen below the Pt goes back to the surface.

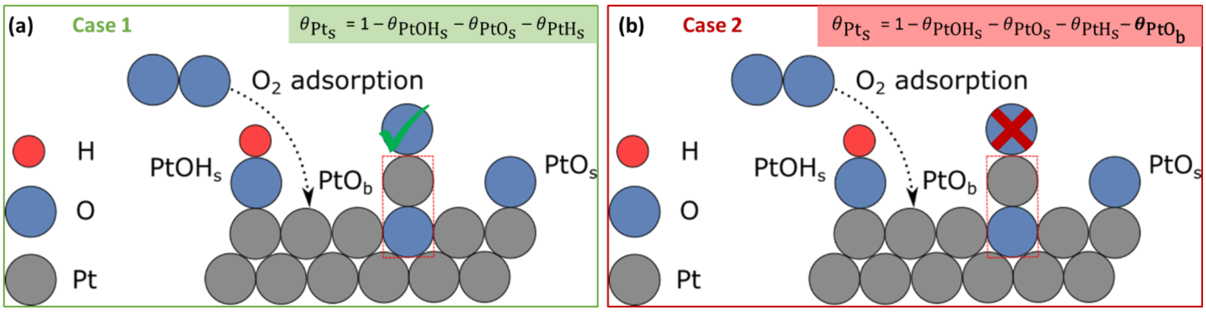

Figure IV-8 : Illustration of (a) the Pt surface oxidation in the presence of a bulk oxide on the same Pt site that still enables formation of surface oxides at this site (b) the Pt surface oxidation in the second case with a bulk oxide impacting surface properties and preventing further surface oxide formation at this site.

Figure IV-9 presents the comparison of the simulated polarization curves obtained via the two different calculations of the Pt surface coverage ratio investigated and the experimental polarization curve on MEA with cathode catalyst layer loaded at 20 $\mu g_{Pt}.cm^{-2}$ under H_2/O_2 operating conditions (see Table IV-2) from OCV to 0.1 V, with a focus at low current densities. The polarization curves presented are corrected from the current density generated by the H_2 crossover, but they are not corrected from ohmic drop. The global description at medium/high current densities between the two cases studied seems to be identical. Now, at low current densities, a better match between modeling and experiments is obtained in the case 2, as the simulated curve is slightly shifted towards the experimental data. In addition, the hysteresis phenomenon between the forward and backward sweeps is now captured on the simulated polarization curve with Pt 'bulk' oxide coverage ratio taken into account in the calculation of the Pt surface coverage ratio. The next results will supplement the case studies, with comparison with experiment when it is possible.

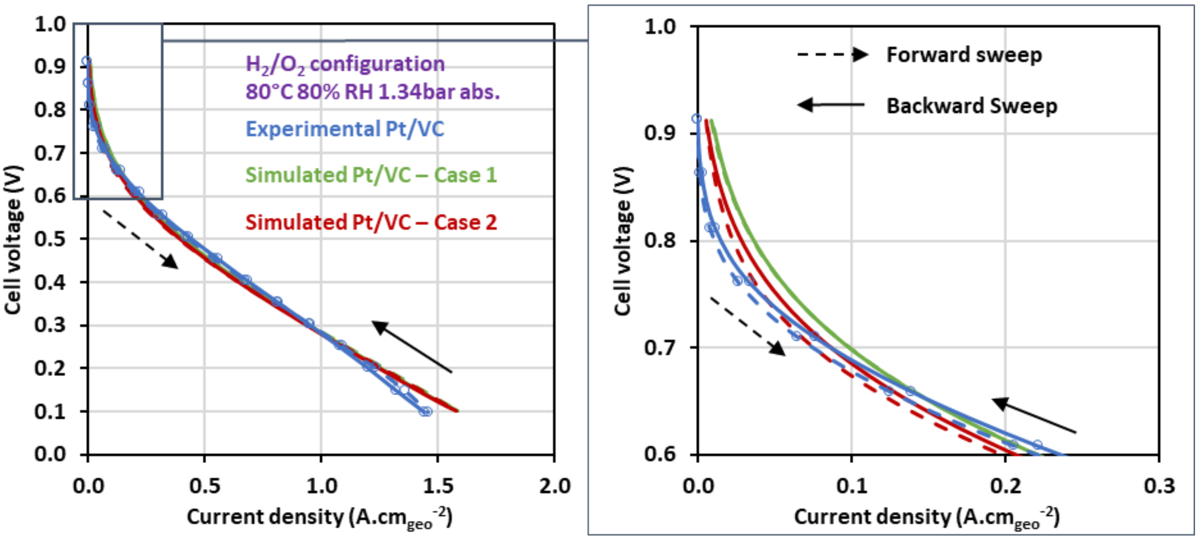

Figure IV-9 : Comparison between the two calculation of Pt surface coverage ratio investigated and the experimental polarization curve.

Figure IV-10 shows the evolution of different parameters simulated during polarization curve with the two different free-Pt surface coverage ratio θ_{Pt_s} calculation methods. Figure IV-10 (a) displays the evolution of the high frequency resistance obtained experimentally with the Pt/VC catalyst layer and a comparison with the simulated ionic resistance of the membrane along the polarization curve and between the forward and backward sweeps for the two cases investigated. First, there is quite a good match between the experimental and simulated evolution. The simulated resistance values are in the same order of magnitude than experimental resistances value. In addition, both experimental and simulated resistances are decreasing from OCV to 0.4 - 0.5 V, due to increasing current generation, thus increasing water production and better hydration of the membrane. This is confirmed by the Figure IV-10 (b), which shows the simulated relative humidity evolution in the catalyst layer along the polarization curve and between the two sweeps. The relative humidity goes from 80% to 81% from OCV to 0.4-0.5 V, which accounts for the better hydration of the catalyst layer due to water production. From 0.4 - 0.5 V to 0.1 V, the electrolyte resistance is increasing, both experimentally and numerically, which may be explained by the larger heat production at high current density. This is confirmed by the temperature evolution of the catalyst layer along the polarization curve and between the two sweeps, as shown on Figure IV-10 (c). The temperature of the catalyst layer increases from OCV to 0.1 V and goes from 353 K to 359 K. As experimentally, the hysteresis observed on the high frequency resistance between the two sweeps of the polarization curve is also captured and observed on the electrolyte resistance evolution simulated by the model. This shows the consistency of the physico-chemical description of the model regarding the water management in the electrolyte phase. Finally, Figure IV-10 (d) shows the ohmic drop corrected polarization curves from Figure IV-9. The ohmic drop correction was done point by point as experimentally, considering the electrolyte resistances from Figure IV-10 (a). There is still a good match between experiments and the simulation of the corrected polarization curve. In addition, the ohmic drop corrected polarization curves still exhibit a hysteresis phenomenon, which somewhat confirms that a part of the hysteresis phenomenon is ascribed to Pt surface state, and linked to Pt oxides formation/reduction.

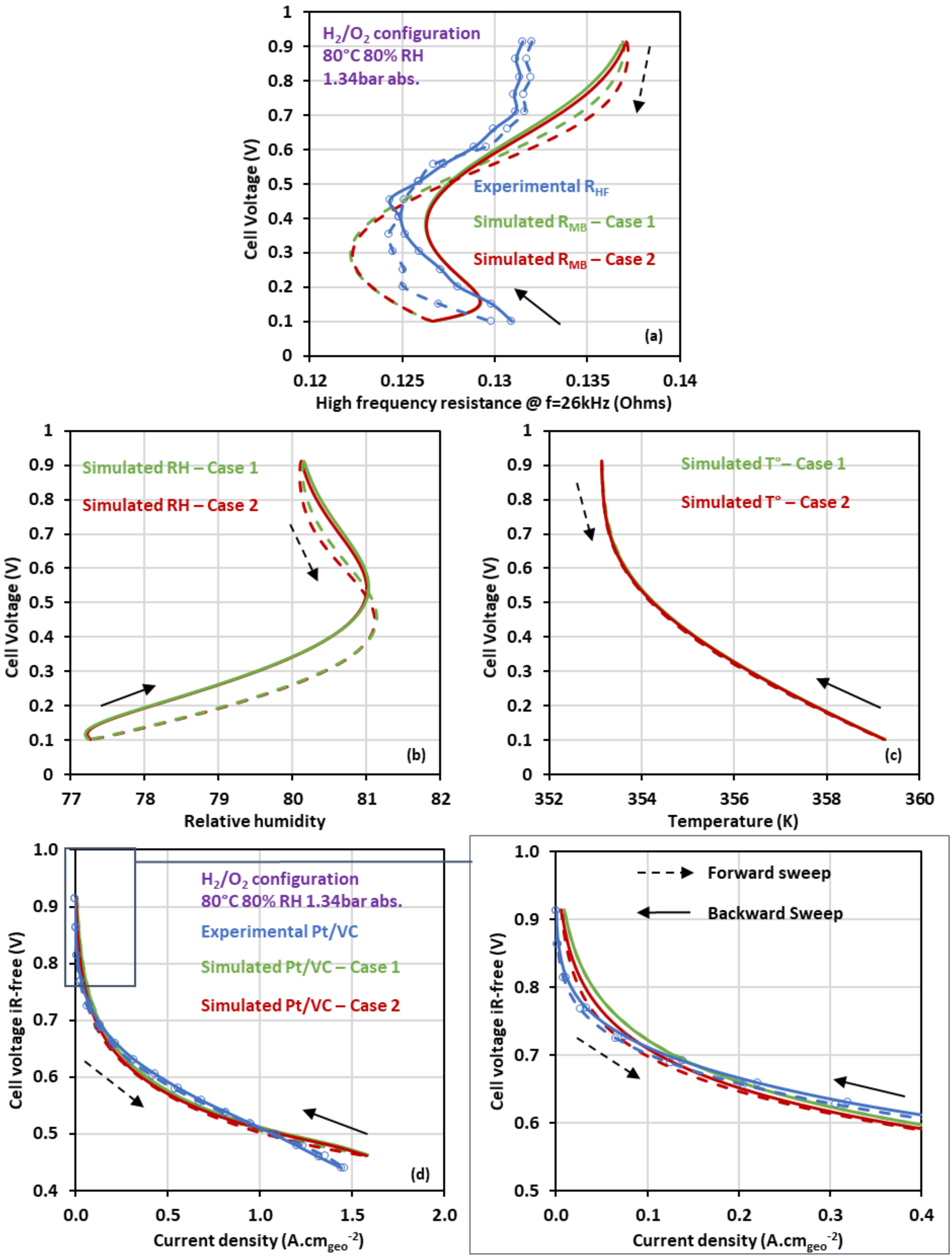

Figure IV-10 : (a) Evolution of the high frequency resistance obtained experimentally on MEA with Pt/VC catalyst layer and a comparison with the simulated electrolyte resistance of the membrane along the polarization curve (b) evolution of the relative humidity in the CL between both cases (c) evolution of the CL temperature between both cases (d) experimental and simulated ohmic drop corrected polarization curves with a zoom at low current density.

Figure IV-11 displays the evolution of the different Pt oxides coverage ratio (Figure IV-11 (a) to (c)) and the evolution of the Pt surface coverage ratio evolution (Figure IV-11 (d)) with potential along the polarization curve for the two cases considered. On Figure IV-11 (a) and (b) for the case 1, no difference can be observed regarding the Pt surface oxides coverage ratio; this explains why no hysteresis is captured by the current description of the model. It is also the case for the Pt surface coverage ratio: there is no difference between the forward and the backward sweeps, as observed on Figure IV-11 (d). Consequently, the surface oxides participate identically to the ORR during the polarization curve, whether PtO_b specie is present or not on the active site. The hysteresis for PtO_b coverage, visible on Figure IV-11 (c) and coming from different kinetics between the insertion and deinsertion of oxygen specie inside the Pt layer, has no impact on the catalyst operation. Interestingly, the amount of Pt surface covered by oxides along the polarization curve under H_2/O_2 configuration is available in the model: at 0.9 V, 97% of Pt surface is covered by oxides and still 65% at 0.1 V. This may be explained by the fact that the real potential seen by the catalyst layer does not go below 0.4 V because of the ohmic drop, meaning that the complete reduction of the oxides cannot be achieved. In addition, the presence of oxygen may promote the Pt oxides formation. With the new calculation of the Pt surface coverage ratio (case 2), the hysteresis phenomenon is now observed on the evolution of the surface oxides coverage ratio (Figure IV-11 (a) and (b)) and on the evolution of the Pt surface coverage ratio (Figure IV-11 (d)), with potential along the polarization curve. Thus, by modifying the Pt site surface activity when a 'bulk' oxide is present underneath this Pt site, a modification of the Pt surface state between the forward and backward sweeps happens and the hysteresis on performance is captured on the simulated polarization curve.

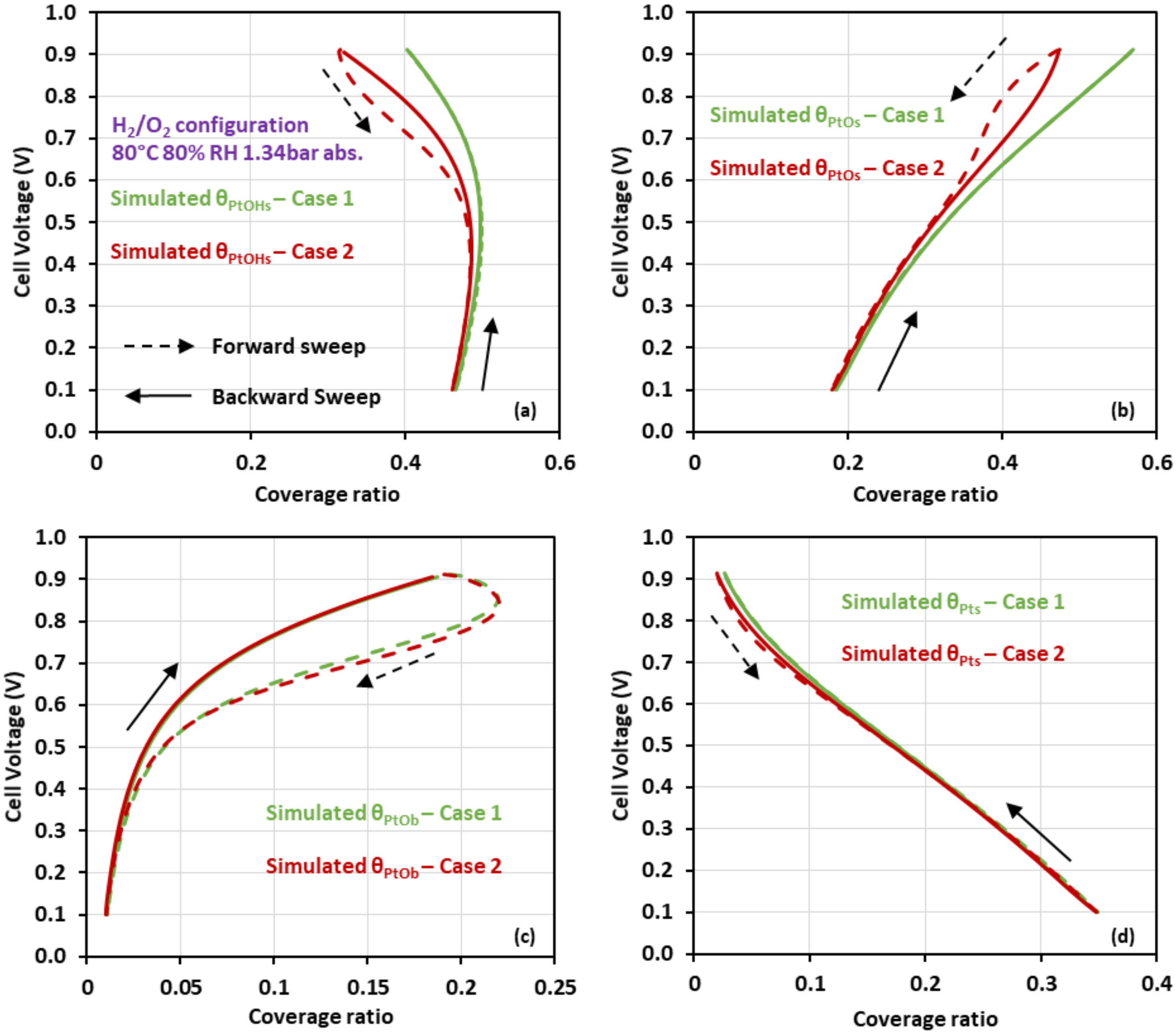

Figure IV-11 : Comparison between the two calculations of (a) Simulated PtOH$_s$ coverage ratio evolution with potential (b) Simulated PtO$_s$ coverage ratio evolution with potential (c) Simulated PtO$_b$ coverage ratio evolution with potential (d) Simulated Pt$_s$ coverage ratio evolution with potential along the simulated polarization curve in Figure IV-9.

It was said previously that at very low current densities, there is a mismatch between experiment and modeling. Figure IV-12 (a) shows the experimental and simulated polarization curves obtained for both cases studied with a zoom at low current density. At very low current density, the OCV is not reached with the model (e.g. the current density never strictly reaches 0 A.cm$_{geo}^{-2}$). This may be explained by the fact that there are still free Pt sites, not covered by oxides formed, as shown on Figure IV-12 (b). In fact, if the Pt sites were entirely covered by oxides, no current density could be produced which could lead to model converging issues. Thus, it is assumed that the differences at very low current density are not a major issue since PEMFC rarely operates near OCV. The description in this region can be improved, with a better kinetic parameters fit for instance, but it will not be further optimized in this work.

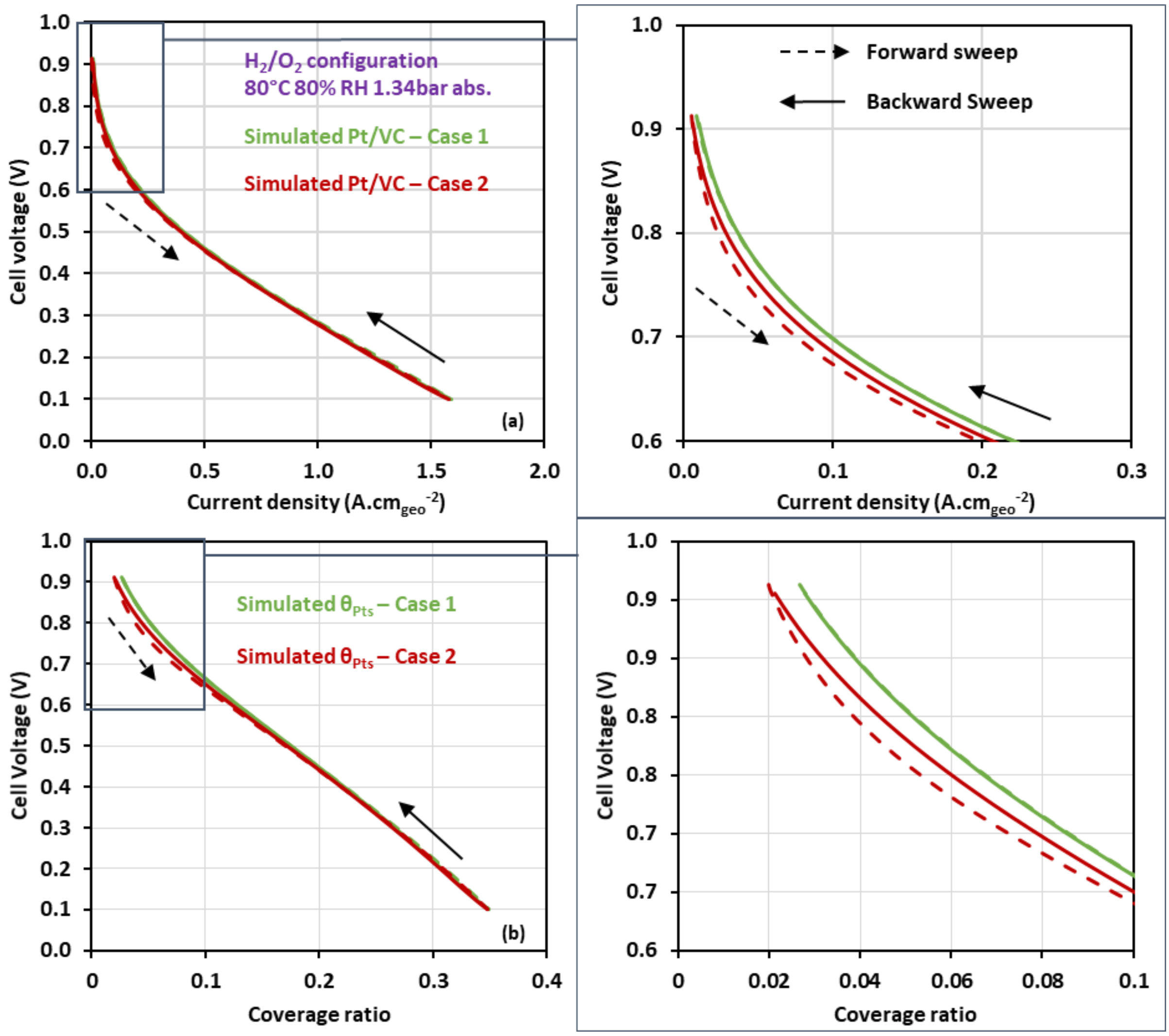

Figure IV-12 : (a) Experimental and simulated polarization curves for both cases studied with a zoom a low current density and (b) Simulated Pt$_S$ coverage ratio evolution with potential along the simulated polarization curve with a zoom at high potential.

IV.3.2.3 Calculation of Pt coverage ratio: investigated scenario under H$_2$/N$_2$ configuration

These two extreme cases as well as the new electrochemical description presented in the section IV.3.1 were also investigated under H$_2$/N$_2$ configuration, by simulating the cyclic voltammetry data classically used to determine Pt ECSA. All the numerical simulation under H$_2$/N$_2$ configuration were obtained using the exact same set of kinetic parameters used for numerical simulation under H$_2$/O$_2$ configuration, the pure oxygen atmosphere is “simply” replaced by nitrogen. Figure IV-13 compares simulated voltammograms considering respectively the two “bulk oxide” cases investigated and the experimental data obtained under H$_2$/N$_2$ configuration (see Table IV-2) on the very low loaded MEA at 20 $\mu g_{Pt}.cm_{geo}^{-2}$ from 0.11 V to 1.2 V. Please note that for simulated voltammograms, the double layer capacitance value is determined and fixed manually to match the experimental data in the “double layer region” between 0.4 and 0.45 V. First, the two calculation methods of free Pt surface coverage ratio lead to the same simulated cyclic voltammetry. The good match and the differences remaining between experimental and simulated cyclic voltammetries were already discussed in the previous section.

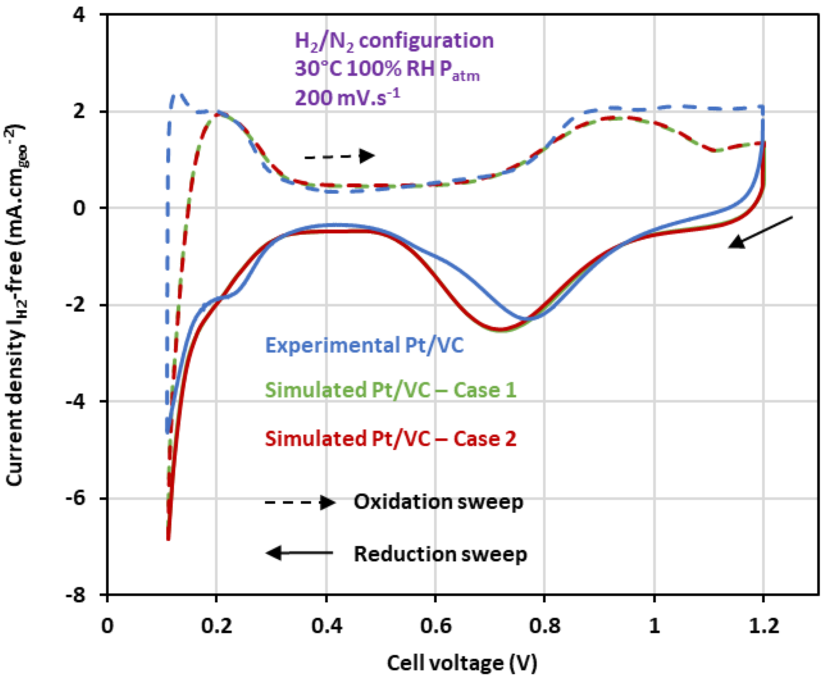

Figure IV-13 : Comparison of very low loaded MEA cyclic voltametries between experiment and according to the two extreme cases investigated in modeling.

Figure IV-14 (a) to (c) shows the different oxides coverage ratio evolution with potential under H_2/N_2 configuration for both cases and Figure IV-14 (d) displays the free Pt surface coverage ratio evolution. Previously, under H_2/O_2 configuration, taking into account the Pt 'bulk' oxide coverage ratio in the calculation of the Pt surface coverage ratio had a significant impact on the surface Pt oxides coverage ratio and made the hysteresis phenomenon possible. However, the amount of PtO_b produced under H_2/O_2 was not negligible (up to 20% of the Pt sites), which is not the case under H_2/N_2 with almost 5 to 10 times less PtO_b produced as shown on Figure IV-14 (c). This low amount of PtO_b produced leads to very slight modification of surface PtOH coverage ratio during the reduction sweep displayed on the Figure IV-14 (a) between both cases. Consequently, it is understandable that under H_2/N_2 configuration, almost no differences can be generated in the model in terms of Pt oxide evolution. The qualitative shape of the simulated free Pt surface and Pt surfaces oxides coverage ratio evolution is in agreement with the ones presented in the work of Maranzana *et al.* [29]. However, the differences remain in the values of the different Pt surface and bulk oxides coverage ratio. This may be explained by the fact that the operating conditions are different. The CV was obtained at 80°C and 50 $mV.s^{-1}$ sweeping rate in the work of Maranzana *et al.* [29], while in this work, the polarization curve was simulated at 80°C, 80% RH, 1.34 bar abs. and 10 $mV.s^{-1}$ and the CV was simulated at 30°C, 100%RH, P_{atm} and 200 $mV.s^{-1}$, operating conditions at which the fitted kinetic parameters were obtained.

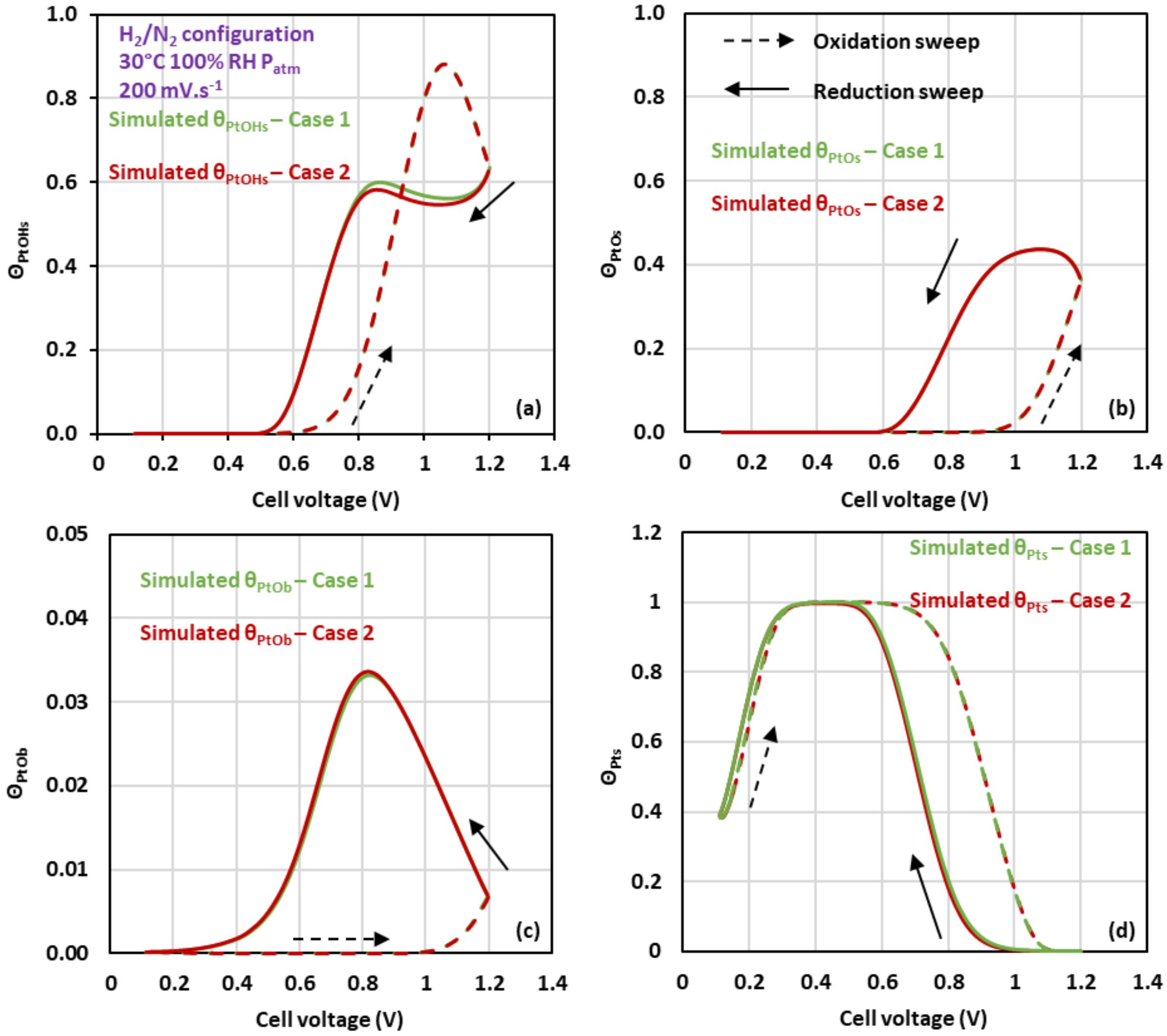

Figure IV-14 : Comparison between the two calculation of Pt surface coverage ratio investigated for (a) Simulated PtOH$_s$ coverage ratio evolution (b) Simulated PtO$_s$ coverage ratio evolution (c) Simulated PtO$_b$ coverage ratio evolution (d) Simulated Pt$_s$ coverage ratio evolution.

Figure IV-15 (a) shows a comparison between experimental and simulated cyclic voltammetries, considering the Case 2, and Figure IV-15 (b) a comparison between experimental and simulated Pt surface oxides coverage ratio evolution with potential. On Figure IV-15 (b), the differences observed on the reduction sweep may be explained by the overestimation of the Pt oxides reduction coulommetry of the numerical simulations. Regarding the differences on the oxidation sweep, they may be explained by the fact that, experimentally the capacitive current may be taken into account when estimating the Pt surface oxides coverage ratio evolution, resulting in an overestimation of θ_{PtOx}. In fact, it is difficult to correct properly the experimental CV from that current contribution. In addition, the capacitive current is not well described by the model as only a fixed value is computed.

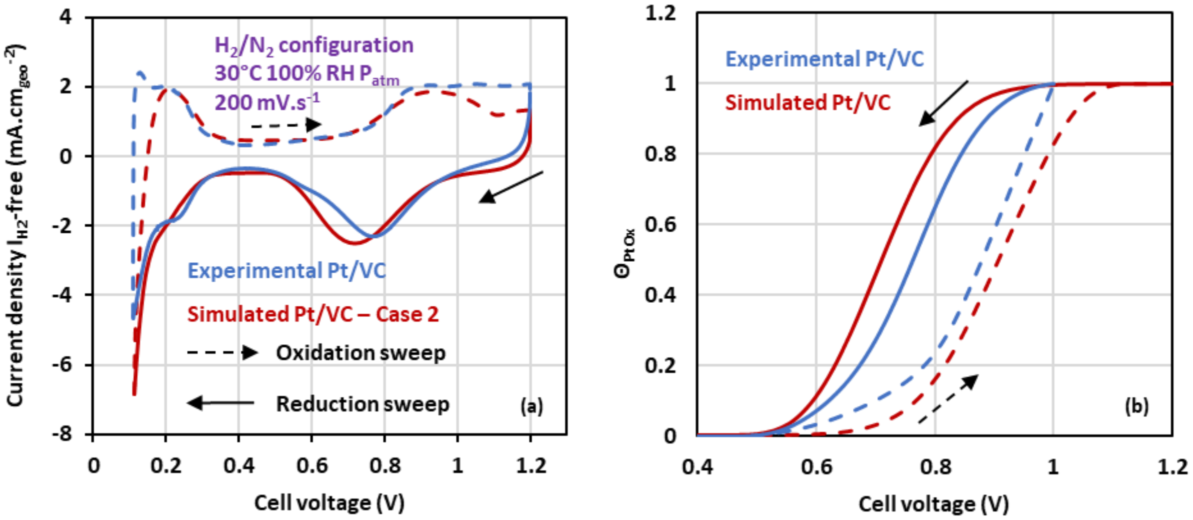

Figure IV-15 : Comparison between experiment and the case 2 investigated in modeling of (a) very low loaded MEA cyclic voltammetries and (b) the Pt surface oxides coverage ratio evolution with potential.

Finally, a parametric study under various operating conditions must be done in order to see in which operating conditions range the set of kinetic parameters values is valid. An interesting point is that between H_2/N_2 and H_2/O_2 configurations, the quantity and the shape of the different coverage ratio presented are drastically different, meaning that the presence oxygen has a non-negligible impact on the Pt oxides formation/reduction reactions. This is in line with some observations made by Saveleva *et al.* [39], who found that the presence of gaseous oxygen enhances the surface Pt oxidation and increases the contribution and the growth of PtO_2 oxide. One should know that the different results shown here do not exclude the fact that the truth is probably between the two cases investigated. It means that 'bulk' oxides may be responsible for a modification in the Pt surface activity regarding the surface oxides formation/reduction, which still remains possible, and thus accounts partly for the hysteresis observed experimentally on polarization curve. All the next modeling results that will be presented were obtained considering the Pt 'bulk' oxide coverage ratio in the calculation of the Pt surface coverage ratio (see Figure IV-8 (b) Case 2), as it led to the best match between experiments and simulation with the current electrochemical description of the ORR mechanism and set of kinetic parameters values.

IV.4 Parametric studies

The previous section showed that there is a good match between modeling and experiments regarding the global performance (at 80°C, 80% RH and 1.34 bar abs.) and cyclic voltammetry (at 30°C, 100% RH and P_{atm}). In order to further validate the model and the new electrochemical description of the ORR, parametric studies under various operating conditions have been done. The following sections deal with the investigation and the impact of various operating conditions on the model response with the 0D version of the model (catalyst layers considered as interface). The idea is to check to what extent the different trends observed experimentally, are captured by the model. Comparison with results and studies from literature will not be shown here as the operating conditions considered for simulations are the same as our experiments. Thus comparison with experiments are shown to support the different observations.

IV.4 Parametric studies

IV.4.1 Impact of sweeping rate

This section investigates the impact of sweeping rate on the cyclic voltammetry simulation and the coverage ratio of the different species under H_2/N_2 configuration. Figure IV-16 (a) shows the comparison between experiment and modeling of cyclic voltammetries performed at 50 mV.s^{-1}. There are significant differences regarding the current density obtained with the simulation compared to the experiment. This may be mainly explained by the fact that capacitive contributions are not well described in the model. The double layer capacity value is fixed to match the experimental one, but its evolution with the sweeping rate or other parameters is not taken into account. What is interesting is that the characteristic peak related to Pt oxides reduction is located at the same potential. By decreasing the sweeping rate, this peak has been shifted positively in simulation, which was also observed experimentally (see Figure III-37 (a)). However, the shift seems to be more important in modeling than experimentally. Regarding the Pt surface coverage ratio evolution (Figure IV-16 (b)), there is a global match between experiment and modeling. The differences observed between 0.5 and 0.8 V may also be explained by undescribed capacitive contributions, but also by the fact that the carbon oxidation reaction is not modelled. The differences observed between 0.95 and 1 V may come from an underestimation of the kinetic parameters of the oxidation of $PtOH_s$ into PtO_s.

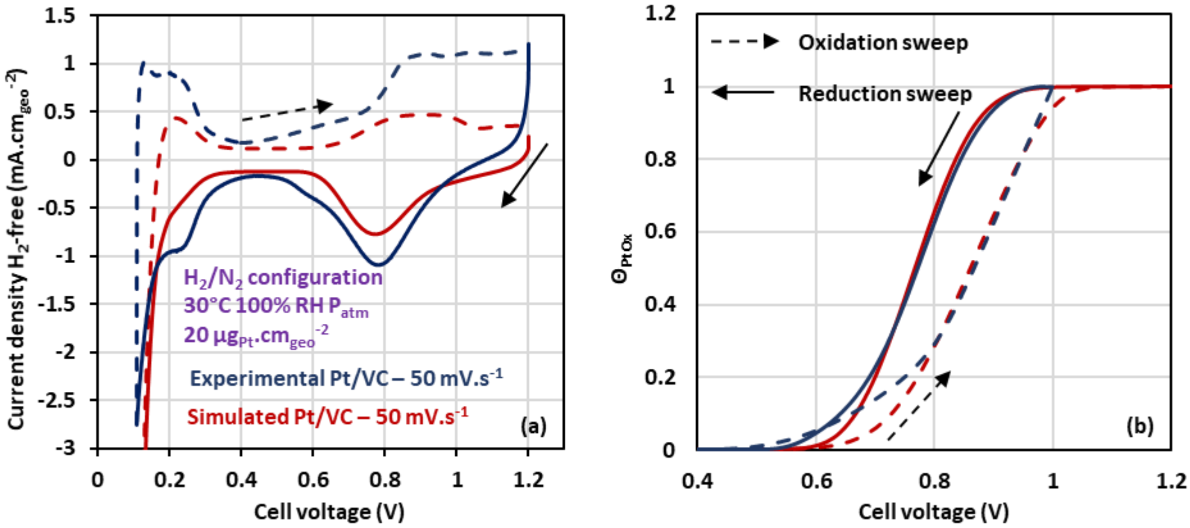

Figure IV-16 : Comparison between experiment and modeling of (a) cyclic voltammetries performed at 50 mV.s^{-1} and (b) the Pt surface oxides coverage ratio evolution with potential.

Figure IV-17 shows the impact of the sweeping rate on cyclic voltammetry simulation and the coverage ratio of the different species under H_2/N_2 configuration. Two sweeping rates are considered, 50 and 200 mV.s^{-1}. In both cases, the double layer capacity value is adjusted to match the experimental value at the sweeping rate considered. In the oxides region of the simulated CV (Figure IV-17 (a)), the characteristic peak related to Pt oxides reduction is effectively shifted towards positive potential in the case of 50 mV.s^{-1}, as mentioned previously. It seems that the characteristic peak related to Pt oxides formation is slightly shifted towards negative potential at the lowest sweeping rate. Both observations were also captured experimentally and can be explained by the fact that at the lowest sweeping rate, the surface of the catalyst is more in equilibrium with the potential applied than in the case of 200 mV.s^{-1}. This statement is confirmed by the coverage ratio evolution of the different oxides (Figure IV-17 (b) to (d)). From 0.6 to 1 V, for the same potential, more $PtOH_s$ oxides are formed at 50 mV.s^{-1} than at 200 mV.s^{-1}, and from 1 to 1.2 V, more $PtOH_s$ species are further oxidized into PtO_s oxides Figure IV-17 (b), which explains that, more PtO_s oxides are formed, and thus PtO_b at the lowest sweeping rate (Figure IV-17 (c) and (d)). On the reduction sweep, the oxides formed are reduced faster at 50 mV.s^{-1} than at 200 mV.s^{-1}. The PtO_b coverage ratio goes from 0.14 to 0 in 200 mV at 50 mV.s^{-1}, while it goes from around 0.035 to 0 in 500 mV at 200 mV.s^{-1} (Figure IV-17 (d)). The same applies for PtO_s and $PtOH_s$ oxides, more of these oxides are formed but at the end, they are reduced faster at 50 mV.s^{-1} than at 200 mV.s^{-1} (Figure IV-17 (b) and (c)). The 'better' equilibrium between surface and potential applied to the electrode induces a thinner hysteresis on the free Pt surface coverage ratio evolution, as it was already observed experimentally (Figure III-37 (b)), and now captured by the model (Figure IV-17 (e)).

IV.4 Parametric studies

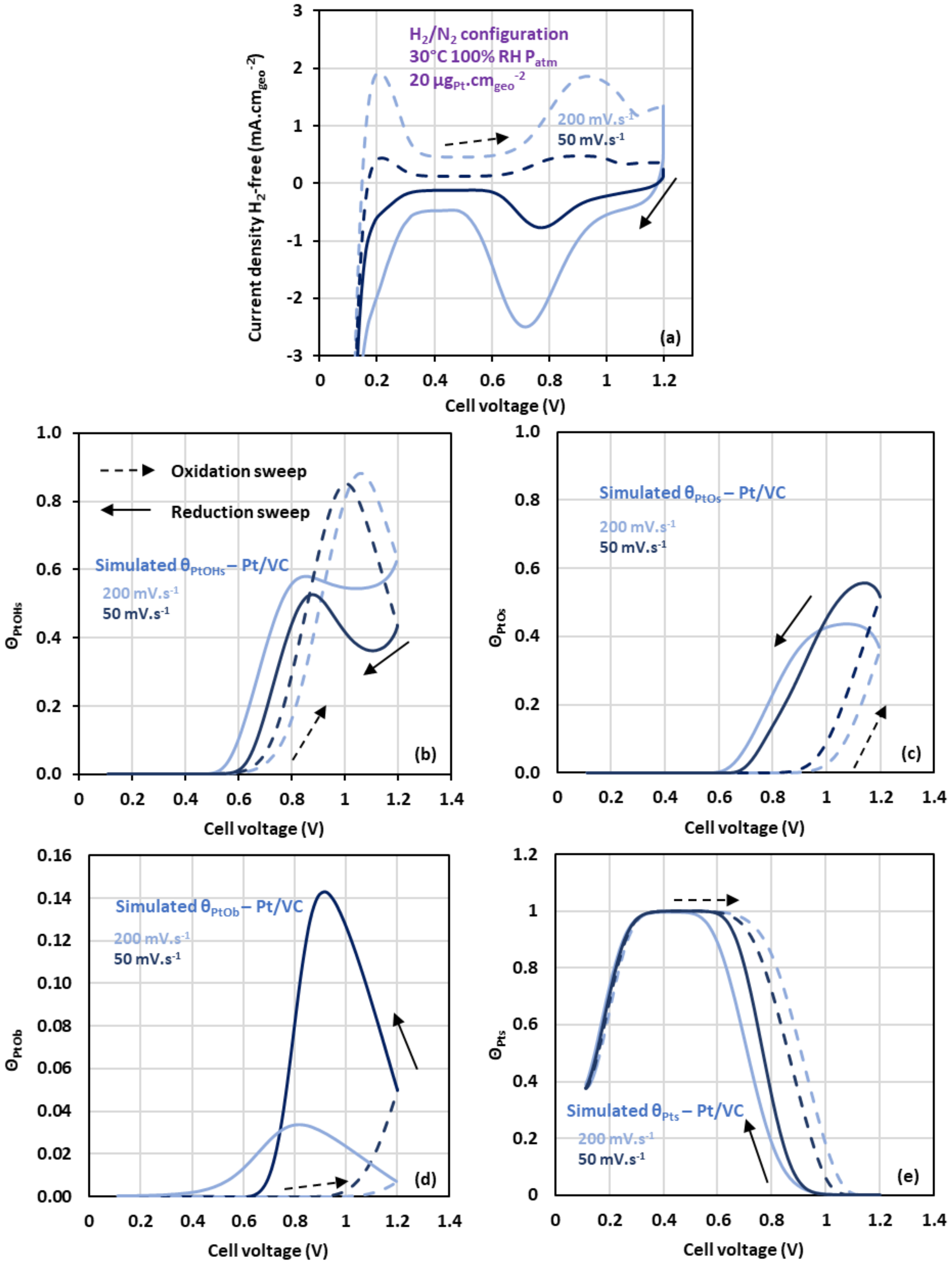

Figure IV-17 : Impact of sweeping rate on (a) Simulated cyclic voltammetries (b) Simulated $PtOH_s$ coverage ratio evolution (c) Simulated PtO_s coverage ratio evolution (d) Simulated PtO_b coverage ratio evolution (e) Simulated Pt_s coverage ratio evolution.

IV.4.2 Impact of temperature

This section investigates the model response according to temperature variation at constant relative humidity (100% RH), under both H_2/O_2 and H_2/N_2 configurations. As for experiments, the total pressure is adjusted according to temperature and relative humidity operating conditions to keep the same partial pressure of oxygen and have a more relevant comparison.

IV.4.2.1 Under H_2/O_2 configuration

At both temperatures investigated with fully hydrated gases (30 and 80°C, 100% RH), the polarization curves, with and without ohmic drop correction from the resistances evolution from Figure IV-18 (c) and (d), do not match the experimental data (Figure IV-18 (a) and (b)), in terms of current density and amplitude of the hysteresis. Looking at the resistances evolution along the polarization curves (Figure IV-18 (c) and (d)), there is quite a good match between experiment and modeling at the operating condition 80°C, 100% RH, which results in similar ohmic drop correction for the experimental and simulated polarization curve (Figure IV-18 (b)). At 30°C, 100% RH, the resistances value are quite similar from OCV to 0.55 V, even if the trend does not match at lower potential, which leads to a bad description of the simulated R_{MB} below 0.55 V.

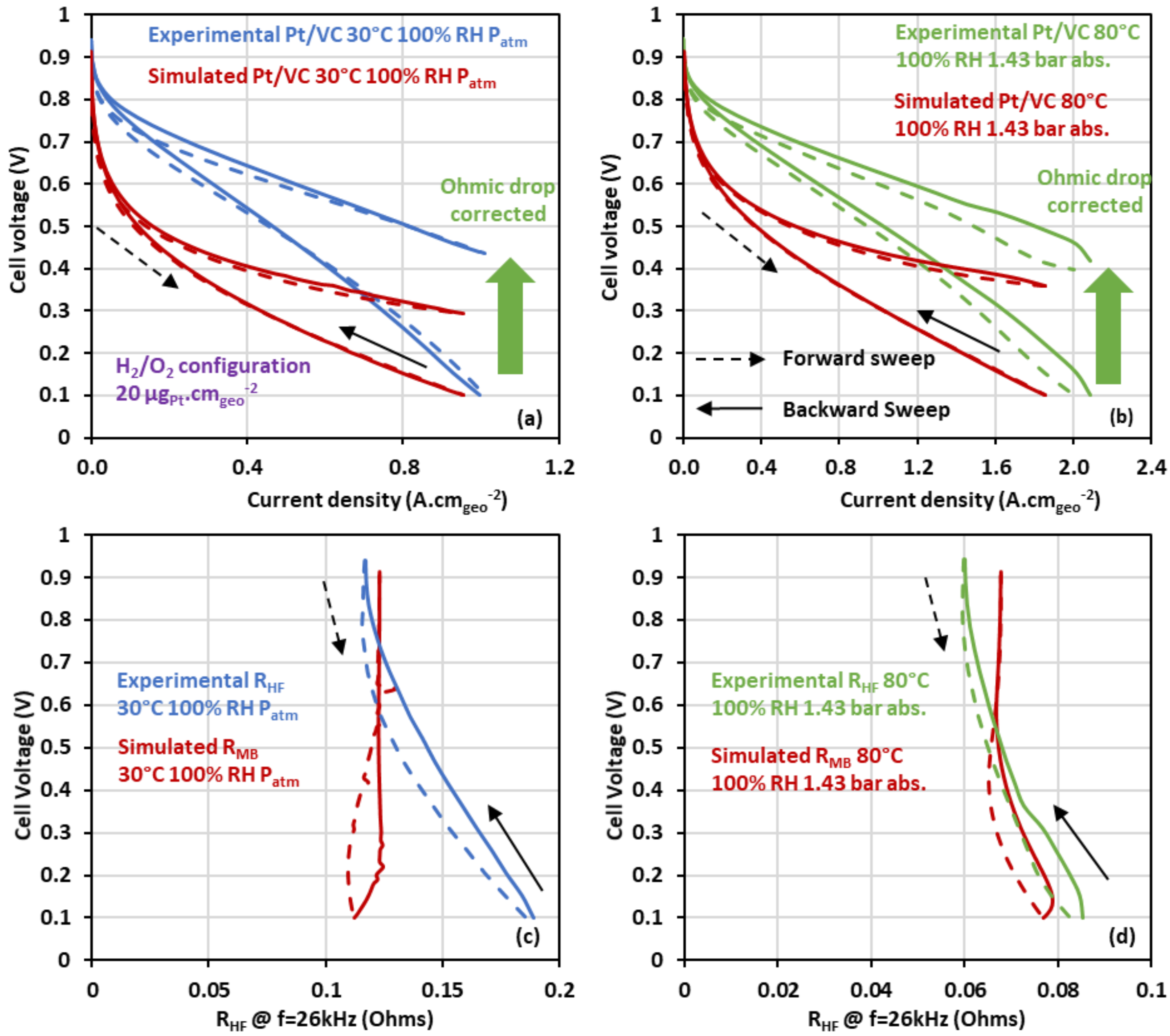

Figure IV-18 : Experimental and simulated polarization curves, with and without ohmic drop, obtained at (a) 30°C 100% RH P_{atm} (b) 80°C 100% RH 1.43 bar abs. and comparison between experiment R_{HF} and simulated R_{MB} obtained at (c) 30°C 100% RH P_{atm} (d) 80°C 100% RH 1.43 bar abs.

Figure IV-19 shows the comparison between the two operating conditions investigated, for simulated polarization curve, with and without ohmic drop, membrane resistances along the polarization curve, relative humidity and temperature. Even if the simulated polarization curves do not match the experimental one, an increase of temperature leads to better performance as captured by the model (Figure IV-19 (a)). A temperature increase also leads to lower membrane resistances value, as it improves the conductivity of the membrane, which was also seen experimentally. The increase of the membrane resistance from 0.5 to 0.1 V, at 80°C, 100% RH, is explained by the decrease of the relative humidity at the cathode and the temperature increase (Figure IV-19 (c) and (d)). The heat production at the cathode induces drying of the catalyst layer and of the membrane. At 30°C, 100% RH, the relative humidity evolution is quite surprising (Figure IV-19 (c)), and is probably related to either numerical issues due to a high condensation rate for the vapour. Further time step studies should solve this numerical issue but could not be done. In both cases, the catalyst layer operation leads to an increase of the catalyst layer temperature (from 303 to 307 K at 30°C, 100% RH and from 353 to 360 K at 80°C, 100% RH).

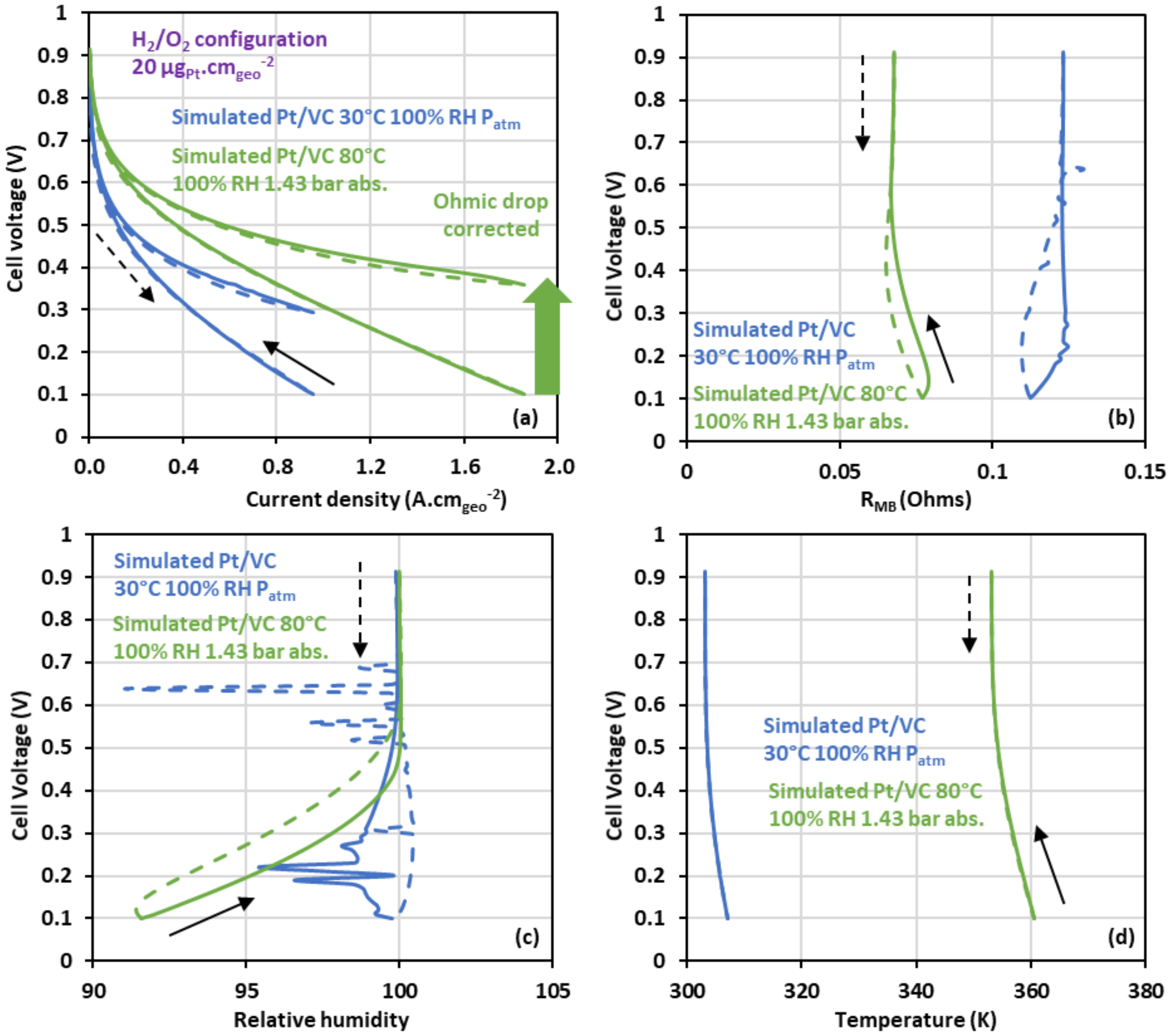

Figure IV-19 : Comparison between 30°C, 100% RH and 80°C, 100% RH operating conditions of (a) simulated polarization curve with and without ohmic drop correction (b) simulated resistances of the PEM (c) simulated CL relative humidity and (d) simulated CL temperature along the polarization curve.

Figure IV-20 shows the evolution of the coverage ratio of the different oxide species and the free Pt surface along the polarization curve. First, it seems that the hysteresis amplitude of the coverage ratio of the different oxides species is bigger at 30°C, 100% RH than 80°C, 100% RH (Figure IV-20 (a) to (c)). This may be explained by the fact that both Pt oxidation and Pt oxides reduction reactions are promoted by the temperature increase. One should note that the Pt is less covered by the oxides at higher temperature (Figure IV-20 (d)). Thus, the Pt oxides reduction reaction seems to be more enhanced by the temperature increase than the Pt oxidation reaction. This may explain the better performance at 80°C, 100% RH, than at 30°C, 100% RH. This makes sense as the performance are described by Pt oxides formation/reduction reactions. Finally, at low current density, the hysteresis seems to be bigger on the free Pt surface coverage at low temperature, which is probably related to the larger hysteresis amplitude observed on the coverage ratio of Pt 'bulk' oxides.

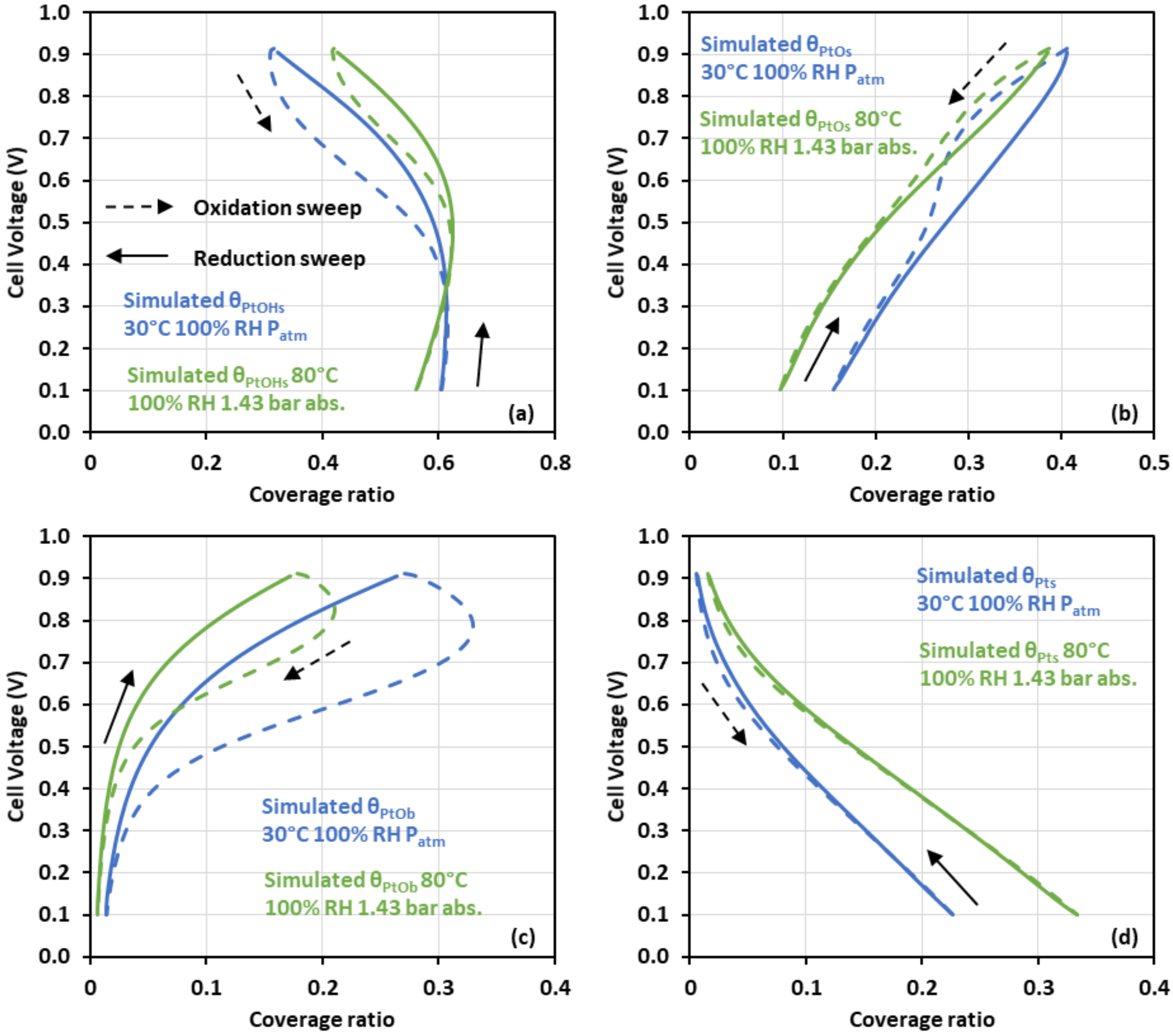

Figure IV-20 : Comparison between 30°C, 100% RH and 80°C, 100% RH operating conditions of (a) θ_{PtOHs} (b) θ_{PtOs} (c) θ_{PtOb} and (d) θ_{Pts} along the polarization curve.

As a result, the simulations at different temperatures reveal that the model does not capture well the experimental performance. So as they are directly related to Pt oxides formation/reduction, a description improvement of the different kinetic parameters according to the temperature should lead to more accurate simulations. For instance, the kinetic constants of the electrochemical reactions of the multi-steps ORR mechanism follow usually an Arrhenius law (Equation IV-52 and Equation IV-53), but this effect has not been yet included in the new version model. However, even if the performance is not well described by the model at other operation conditions, the global trends according to temperature evolution seem to be captured and are in agreement with experiments.

IV.4.2.2 Under H_2/N_2 configuration

The impact of temperature on the model response is also investigated under nitrogen atmosphere during cyclic voltammetries simulations. The comparison between experiment and modeling at 30°C, 100% RH (Figure IV-21 (a) and (c)) has already been discussed in section IV.3.2.3. Figure IV-21 (b) and (d) show a comparison between experimental and simulated cyclic voltammetries obtained at 80°C, 100% RH, and the coverage ratio evolution of Pt oxides during the cyclic voltammetry. It seems that all the simulated electrochemical responses (characteristic peaks of proton adsorption/desorption and Pt oxides formation/reduction) under inert atmosphere are shifted towards positive potential when the temperature increases. It is expected to have a positive potential shift of the characteristic peak related to Pt oxides reduction reaction as it is also observed experimentally. However, the positive potential shift of the peak related to Pt oxidation is surprising because it does not agree with experimental observations (see Figure III-35 (a)). These shifts result is less surface oxide formation as observed on the Figure IV-21 (d), with Pt never being entirely covered by oxides during the simulated CV. In addition, because of the positive potential shifts of the different electrochemical responses, the Pt oxides coverage ratio evolution does not match the experimental one. Finally, the hysteresis observed on the simulated Pt oxides coverage ratio evolution seems to be thinner at 80°C, 100% RH (Figure IV-21 (d)), compared to the one observed at 30°C, 100% RH (Figure IV-21 (c)). This has also been observed experimentally (see Figure III-35 (c)) and is probably due to the promotion of Pt oxides formation/reduction reaction with temperature, which mitigates the kinetic asymmetry between the two reactions.

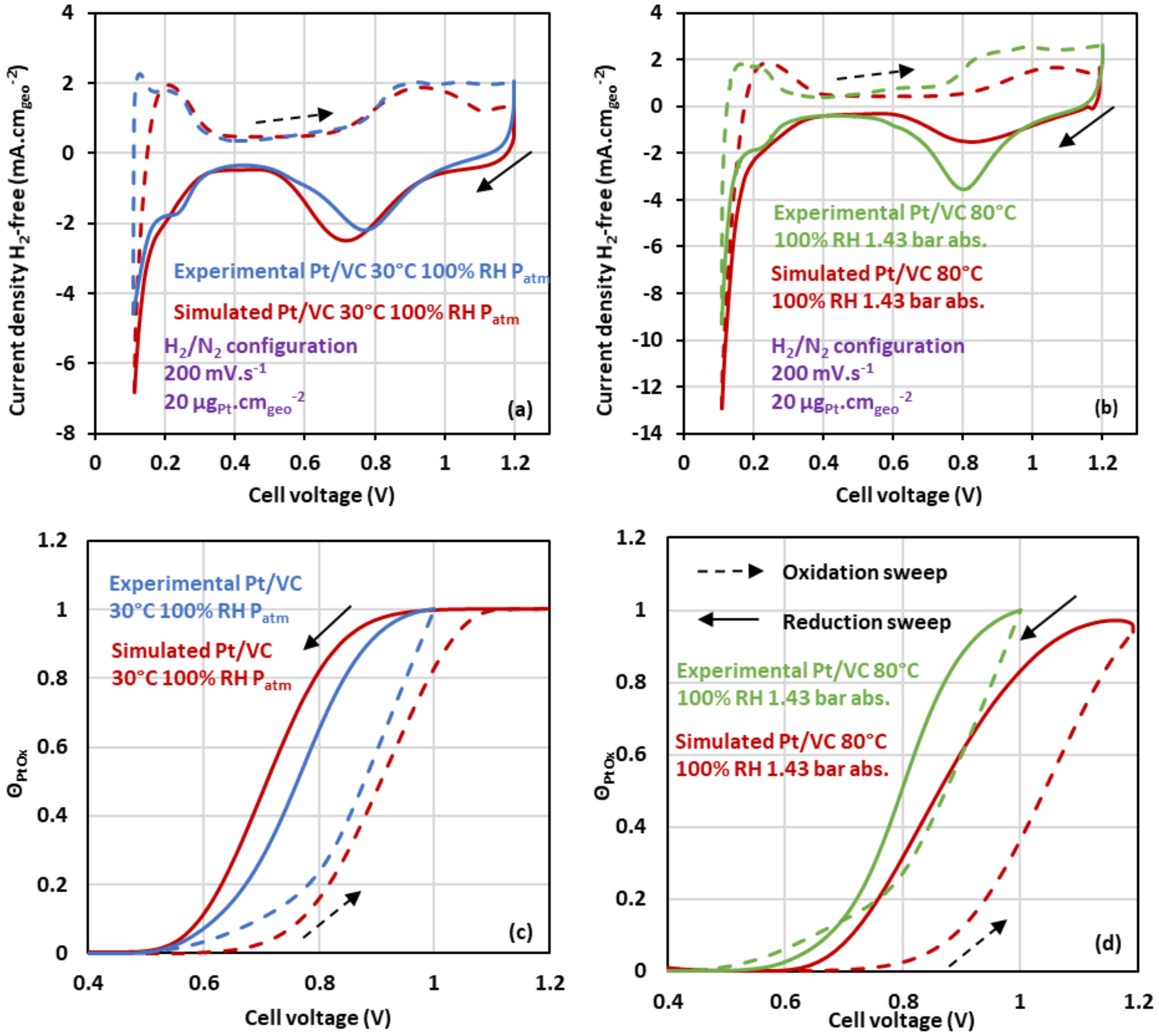

Figure IV-21 : Experimental and simulated cyclic voltammetries, corrected from constant H_2 crossover current, obtained at (a) 30°C, 100% RH, P_{atm} (b) 80°C, 100% RH, 1.43 bar abs. and comparison between experiment qualitative coverage ratio of Pt surface oxides and simulated coverage ratio of Pt oxides obtained at (c) 30°C, 100% RH, P_{atm} (d) 80°C, 100% RH, 1.43 bar abs.

Figure IV-22 shows a comparison between simulated cyclic voltammetries, $PtOH_s$, PtO_s, PtO_b and Pt_s coverage ratio evolutions for both operating conditions considered. Figure IV-22 (a) highlights the positive potential shifts of the different electrochemical responses previously mentioned when the temperature increases. Figure IV-22 (c) and (d) show that at higher temperature, less PtO_s and PtO_b oxides are formed and it occurs at higher potential than at 30°C, 100% RH. This is due to almost the same the same quantity of $PtOH_s$ oxides formation between the two operating conditions, but at higher temperature the maximum is reached at 1.2 V compared to 1.05 V at 30°C 100% RH. Thus, if less oxides are formed, less Pt oxides are then reduced and the electrochemical signature of Pt oxides reduction is observed at more positive potential. Figure IV-22 (e) shows the free Pt surface coverage ratio evolution and it reveals the thinner hysteresis between the oxidation and reduction sweeps in the oxides region, with Pt sites that are never entirely covered by oxides. In addition, as the global electrochemical responses are shifted towards positive potential, the adsorption of proton begins at more positive potential at 80°C, 100% RH compared to 30°C, 100% RH, which results in Pt more covered by protons in the H_{UPD} region.

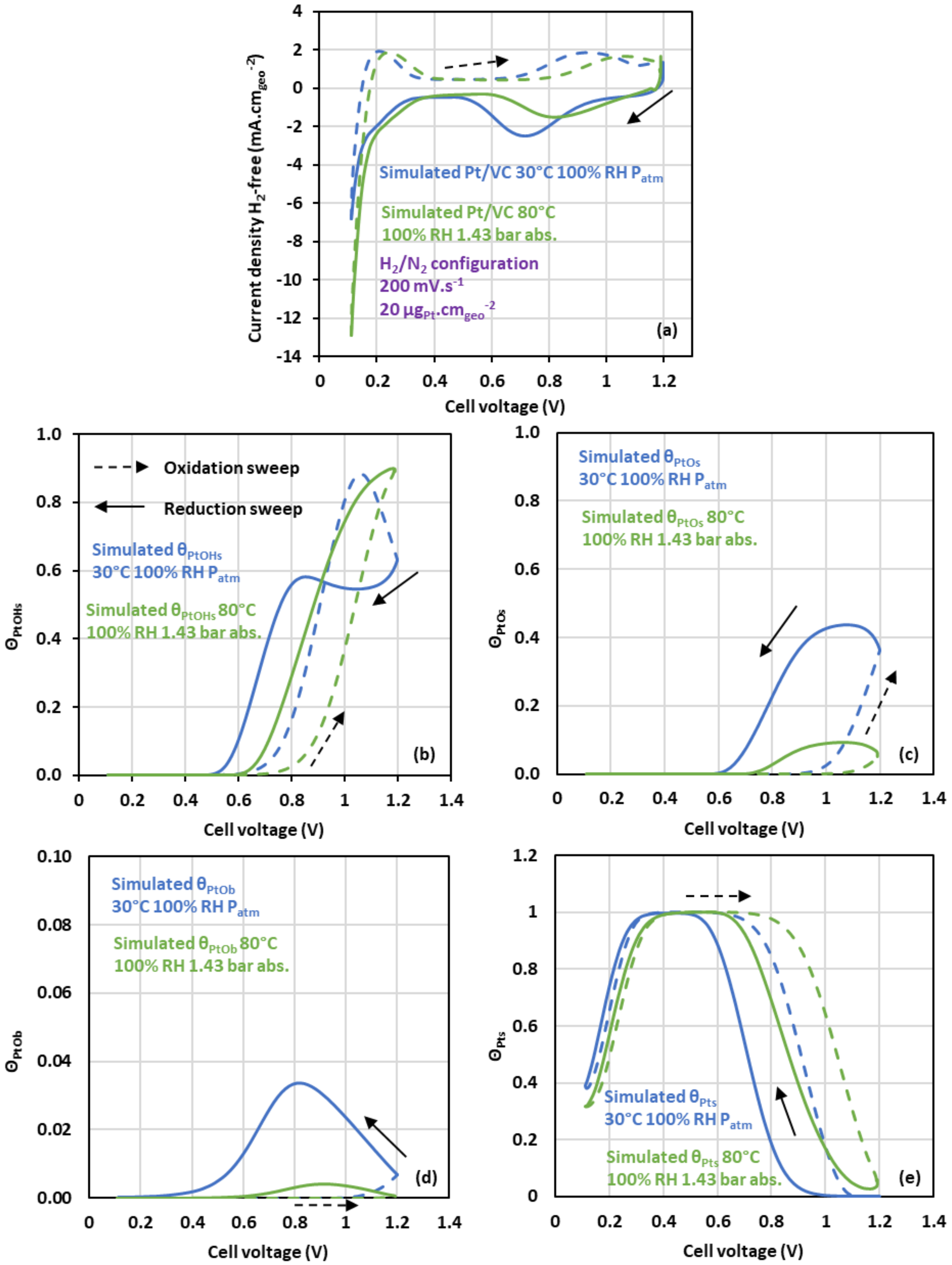

Figure IV-22 : Impact of temperature on (a) simulated cyclic voltammetries (b) Simulated PtOH$_s$ coverage ratio evolution (c) Simulated PtO$_s$ coverage ratio evolution (d) Simulated PtO$_b$ coverage ratio evolution (e) Simulated Pt$_s$ coverage ratio evolution.

To summarise, be it under nitrogen atmosphere or under H_2/O_2 configuration, the model does not capture quite well the temperature dependency of the different electrochemical phenomena. In fact, global trends between 30 and 80°C match the experimental trends, but the simulated data do not match the experimental results. Thus, the model still needs to be improved in order to be able to accurately simulate the different phenomena observed experimentally. First, mismatch between experiment and modeling at different temperatures may come from the electrochemical description, which does not take into account all the reactions/contributions that take place at the cathode catalyst layer (contribution of carbon or other Pt oxides formation reaction). In addition (and this may be the dominant factor), the kinetic constants should be described by an Arrhenius law and depend on the temperature to improve the electrochemical description. The implementation in the model would be straight forward, but then it leads to additional parameters that are mostly unknown and need further fitting. Transport properties, especially the water transport in the ionomer phase can also be improved, as the parameters come from the literature and have not yet been fitted on our experimental results. In a first approach, one may use the experimental electrochemical impedance spectroscopy measurements to update the parameter values. This may also be done thanks to advanced experimental characterization of neutron imaging, which gives information on ionomer distribution and behaviour when hydrated in the catalyst layer in order to feed the model with more realistic description/parameter values. Finally, some work in better determining parameters such as the porosity of the catalyst layer, the tortuosity of ionomer in the catalyst layer could also further improve the simulations. Thus, more work on the characterization of these parameters shall lead to description improvements.

IV.4.3 Impact of relative humidity

This section investigates the model response according to relative humidity at constant temperature (80°C), under both H_2/O_2 and H_2/N_2 configurations.

IV.4.3.1 Under H_2/O_2 configuration

Figure IV-23 (a) and (b) show a comparison between experimental and simulated polarization curves, with and without ohmic drop correction from the experimental R_{HF} evolution and simulated R_{MB} evolution along the polarization curve, at 80°C, 50% RH and 80°C, 100% RH. The case at 80°C, 100% RH (Figure IV-23 (b) and (d)) has already been discussed in the previous section. At 80°C, 50% RH, the simulated performance, with and without ohmic drop correction, are globally overestimated compared to the experimental performances. The global R_{MB} evolution along the polarization curve (Figure IV-23 (c)) is quite in agreement with experiments: the membrane is hydrated due to current density production, thus water production, which leads to a decrease of the R_{MB} values from OCV to 0.1 V. However, the hydration is larger with simulation, as more current density is produced compared to the experiment (Figure IV-23 (a)). Finally, the hysteresis reproduced by the simulation is inverted compared to the experimental one. On the simulated backward sweep, the membrane is more hydrated than on the forward sweep, which results in higher R_{MB} value on the forward sweep. This makes sense as more current density has been produced when the backward sweep begins. It is not the case experimentally: it was supposed that the benefits from the water production and better hydration seem to be significantly counterbalanced by the local heat production.

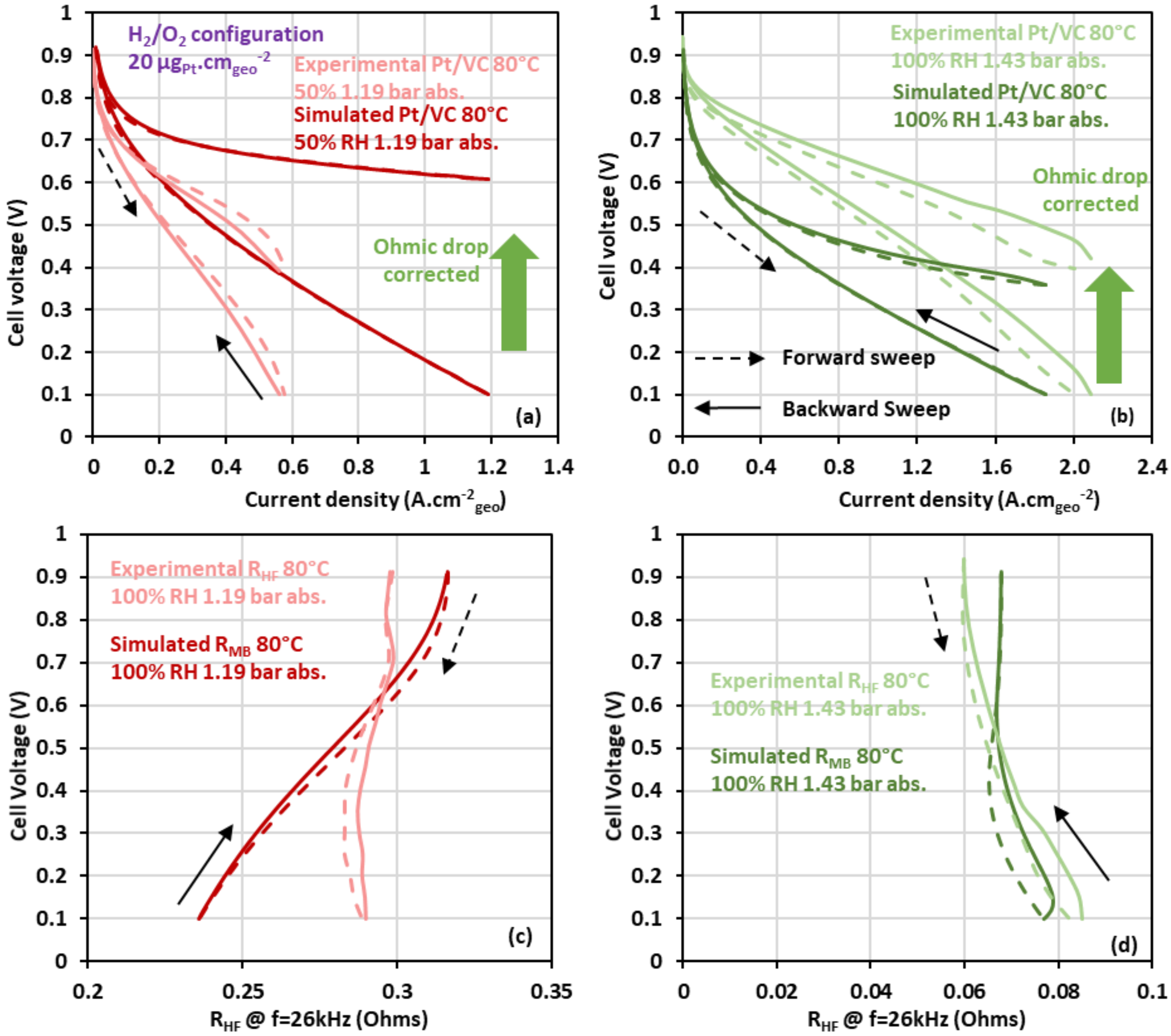

Figure IV-23 : Experimental and simulated polarization curves, with and without ohmic drop, obtained at (a) 80°C, 50% RH, 1.19 bar abs. (b) 80°C, 100% RH, 1.43 bar abs. and comparison between experimental R_{HF} and simulated R_{MB} obtained at (c) 80°C, 50% RH, 1.19 bar abs. (d) 80°C, 100% RH, 1.43 bar abs.

Figure IV-24 shows the impact of relative humidity at 80°C on simulated global performance, with and without ohmic drop correction from the membrane resistances evolution (Figure IV-24 (b)). At low current density, the simulated performance is better at 50% RH than at 100% RH. The differences in performance cannot be explained by the hydration state, as the catalyst layer and the membrane are less hydrated at 50% RH than at 100% RH, according to the relative humidities of the catalyst layer and the membrane resistances evolutions along the polarization curve (Figure IV-24 (c) and (b), respectively). At medium/low current density, this trend is inverted. One should note that the performance at 80°C, 50% RH after ohmic drop correction, are significantly better compared to the performance at 80°C 100% RH, which is mainly explained by the surprisingly high current density produced (twice higher with simulation compared to experiment at 0.1 V), resulting in a significant ohmic drop. Figure IV-24 (d) shows the simulated temperature evolution of the catalyst layer along the polarization curve. At 50% RH, the temperature increase from 353 to 357 K from OCV to 0.1 V, while at 100 % RH it goes from 353 to 360 K. Thus, the simulations show that the temperature increase is not that important at 50% RH, and thus the heat production may not account for the inverted hysteresis behaviour observed experimentally (Figure IV-23 (a)).

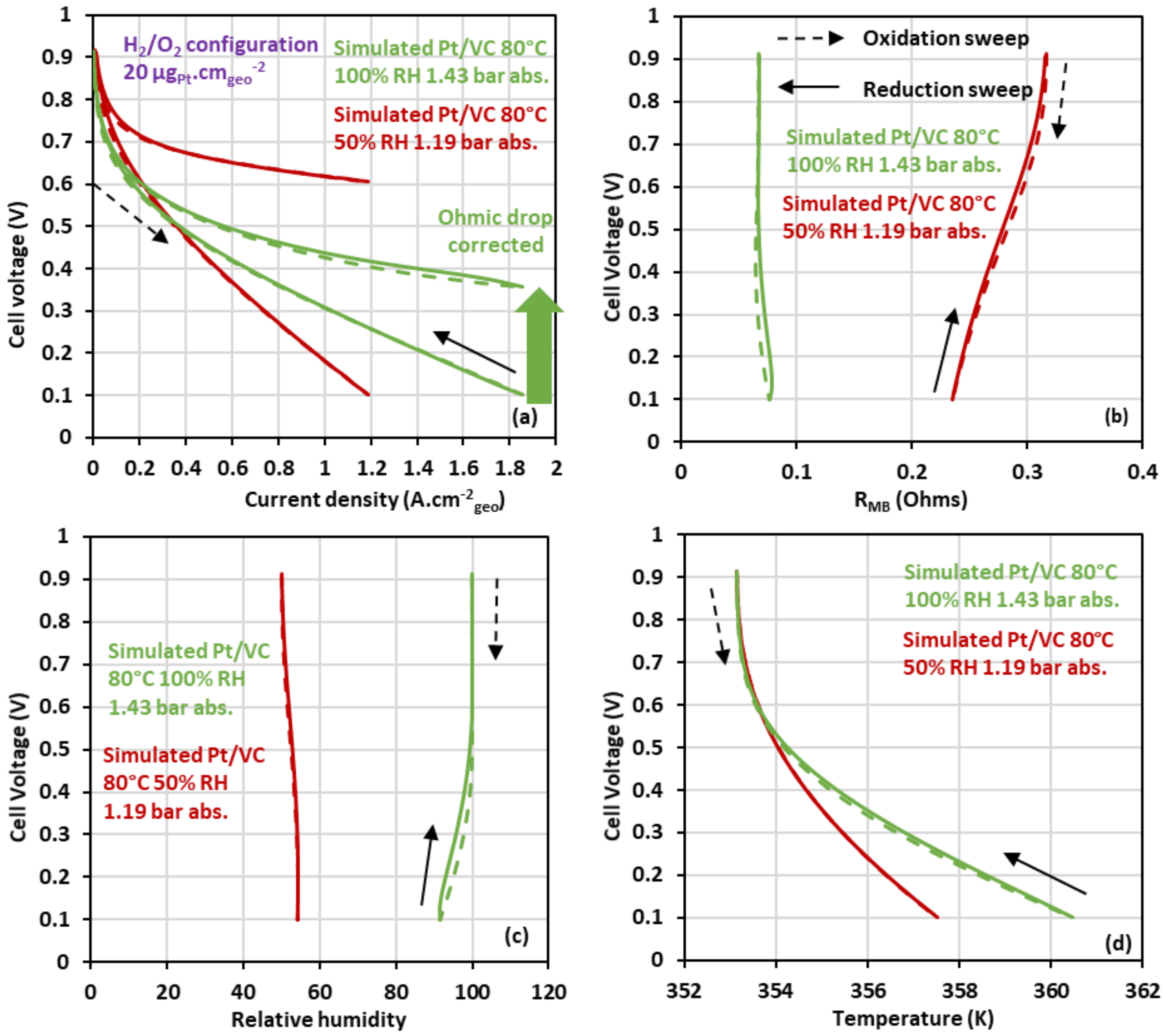

Figure IV-24 : Comparison between 80°C, 50% RH and 80°C, 100% RH operating conditions of (a) Simulated polarization curve with and without ohmic drop correction (b) Simulated resistances of the PEM (c) simulated CL relative humidity and (d) Simulated CL temperature along the polarization curve.

Figure IV-25 gives insights into the simulated coverage ratio evolution of the different Pt oxides species and free Pt surface along the polarization curve. First, one should note that at low current density, the Pt is less covered by oxides at 50% RH than at 100 % RH (Figure IV-25 (d)). This behaviour likely explains the better performance at 50% RH than at 100% RH in the same current density region (see Figure IV-24 (a)), which could not be explained by the hydration. At 50% RH, from 0.5 to 0.1 V, the Pt is more covered by oxides, which results in worse performance than at 100 % RH. This is confirmed by the coverage ratio of the different Pt oxides species in that potential region (Figure IV-25 (a) to (c)). Finally, as more PtO_b oxides are formed at 100% RH at high potential, the hysteresis observed on the coverage ratio of Pt 'bulk' oxide is larger, and thus the hysteresis related to Pt surface oxides and free Pt surface is also larger.

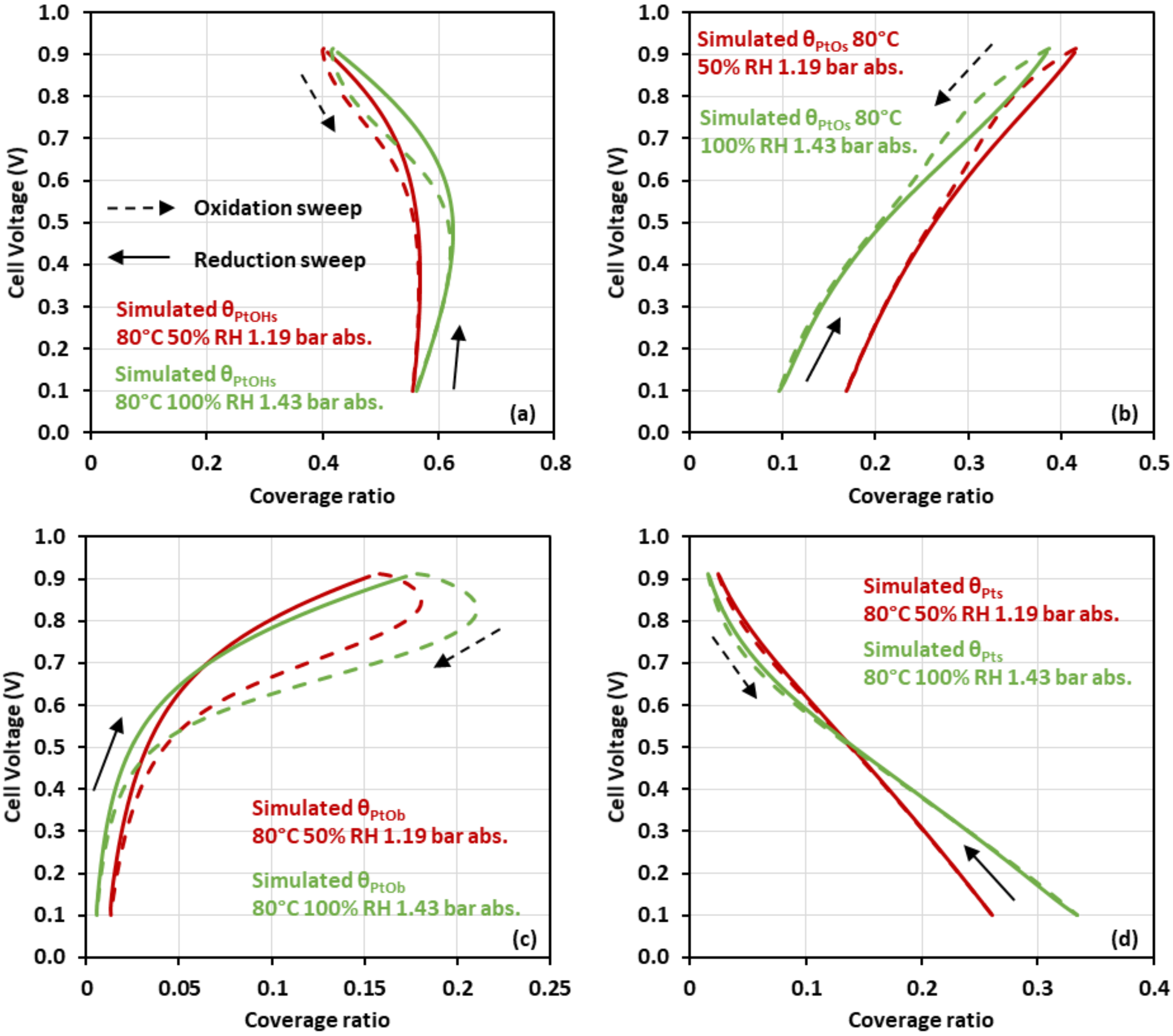

Figure IV-25 : Comparison between 80°C, 50% RH and 80°C, 100% RH operating conditions of (a) θ_{PtOHs} (b) θ_{PtOs} (c) θ_{PtOb} and (d) θ_{Pts} along the polarization curve.

As a result, under H_2/O_2 configuration, the simulated data at different relative humidities do not match well the experimental data. Some global trends are in agreement with experiments and some simulated parameter/behaviour gave information that allow denying or confirming some of the assumptions made regarding experimental trends observed. However, it seems that hydration plays a limited role on the global performance, the latter being maybe too much driven by the Pt oxidation and Pt oxides reduction reaction. Thus, kinetic parameters value are probably not correct, as phenomena related to the multi-steps ORR mechanism seem to dominate the performance, limiting the impact of hydration (thus, water and proton activities), which is probably not accurately described and taken into account, on the polarization curve.

IV.4.3.2 Under H_2/N_2 configuration

The impact of relative humidity on the model responses has also been investigated under nitrogen atmosphere during cycling voltammetries simulations. The comparison between experiment and modeling at 80°C, 100% RH (Figure IV-26 (b) and (d)) has already been discussed in section IV.4.2.2 during investigation of the temperature impact on the model responses. Figure IV-26 (a) shows the comparison between experiment and modeling of cyclic voltammetries obtained at 80°C, 50% RH. As it is the case at 100% RH, the different electrochemical responses under nitrogen atmosphere are significantly shifted towards positive potential compared to experiment. This results in a shifted simulated hysteresis observed on the coverage ratio of Pt oxides evolution during cyclic voltammetries (Figure IV-26 (c)). As less oxides are formed, the simulated coverage ratio of Pt oxides is never entirely covered. The amplitude of the hysteresis between the two relative humidities seems to be the same. Finally, the impact of relative humidity, at 80°C, is not significant on the simulated cyclic voltammetries and coverage ratio evolution of Pt oxides, which seems to be in agreement with experiments.

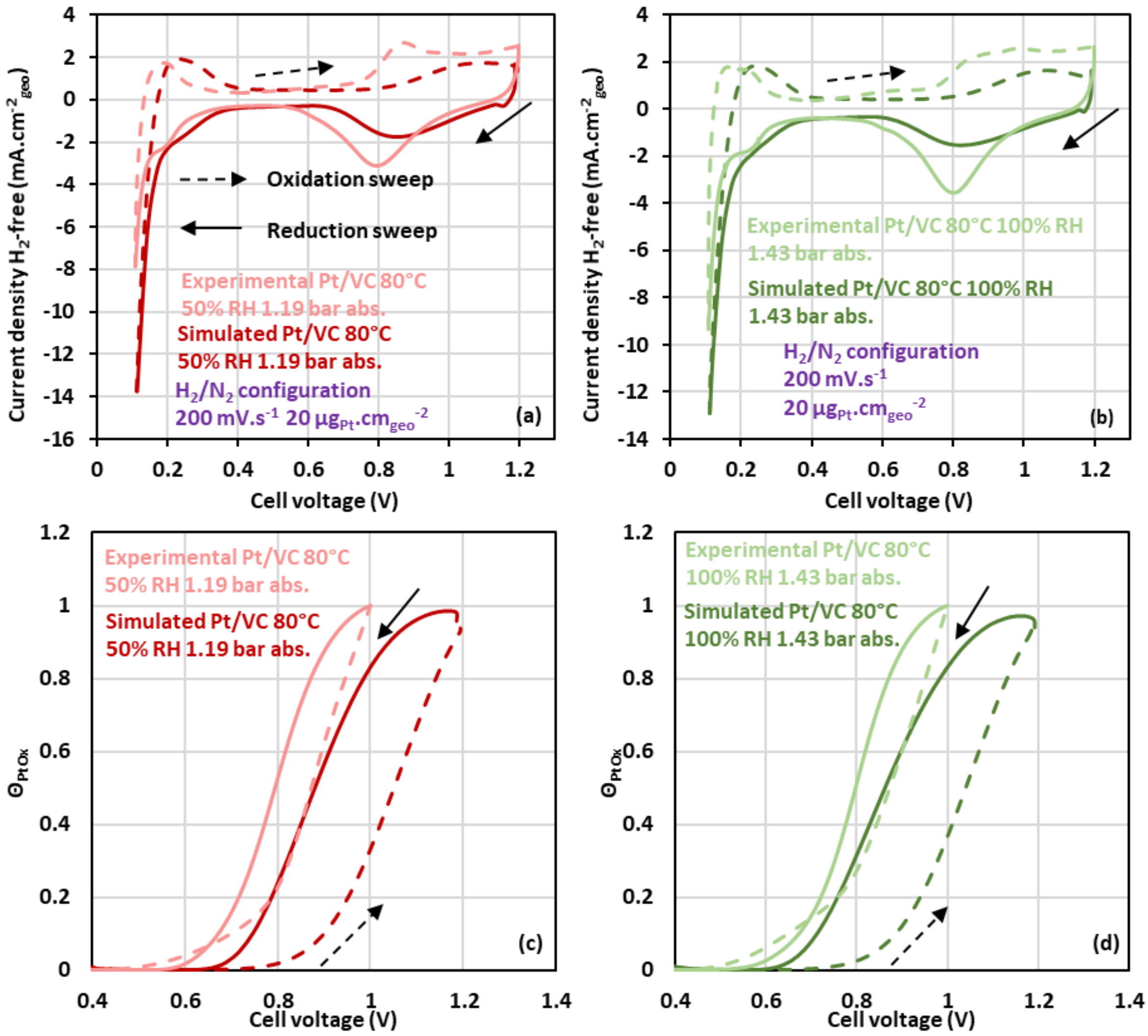

Figure IV-26 : Experimental and simulated cyclic voltammetries, corrected from constant H_2 crossover current, obtained at (a) 80°C, 50% RH (b) 80°C, 100% RH and comparison between experiment qualitative coverage ratio of Pt surface oxides and simulated coverage ratio of Pt oxides obtained at (c) 80°C, 50% RH (d) 80°C, 100% RH.

Figure IV-27 shows a comparison between simulated cyclic voltammetries, $PtOH_s$, PtO_s, PtO_b and Pt_s coverage ratio evolutions for both relative humdities considered at 80°C. As previously stated, the relative humidity plays a minor impact on the shape of the simulated CV (Figure IV-27 (a)). The only differences are observed in the oxides region. At 50% RH, the characteristic peak of the Pt oxides reduction is slightly shifted towards positive potential compared to one at 100 % RH. On the oxidation sweep, it seems that at 50% RH, a little more oxides are formed. This is confirmed by the free Pt surface coverage ratio evolutions (displayed on Figure IV-27 (e)). At 50% RH, on the beginning of the reduction sweep (from 1.2 V), the θ_{Pts} value is slightly lower than at 100% RH, meaning that the Pt has been more covered by oxides during the oxidation sweep. It also seems that the Pt oxides reduction occurs faster at 50% RH than at 100% RH. This may be explained by the fact that due to the presence of water at 100% RH, the $PtOH_s$ formation is promoted, thus more of this oxide are formed and more must be reduced on the reduction sweep, which explains the larger hysteresis observed at 100% RH than at 50% RH on Figure IV-27 (b). Finally, more PtO_s and PtO_b oxides are formed at 50% RH than at 100% RH (Figure IV-27 (c) and (d)). This may be explained by the fact that at 100% RH, more $PtOH_s$ are more willing to be formed (the formation of $PtOH_s$ depends on the water activity).

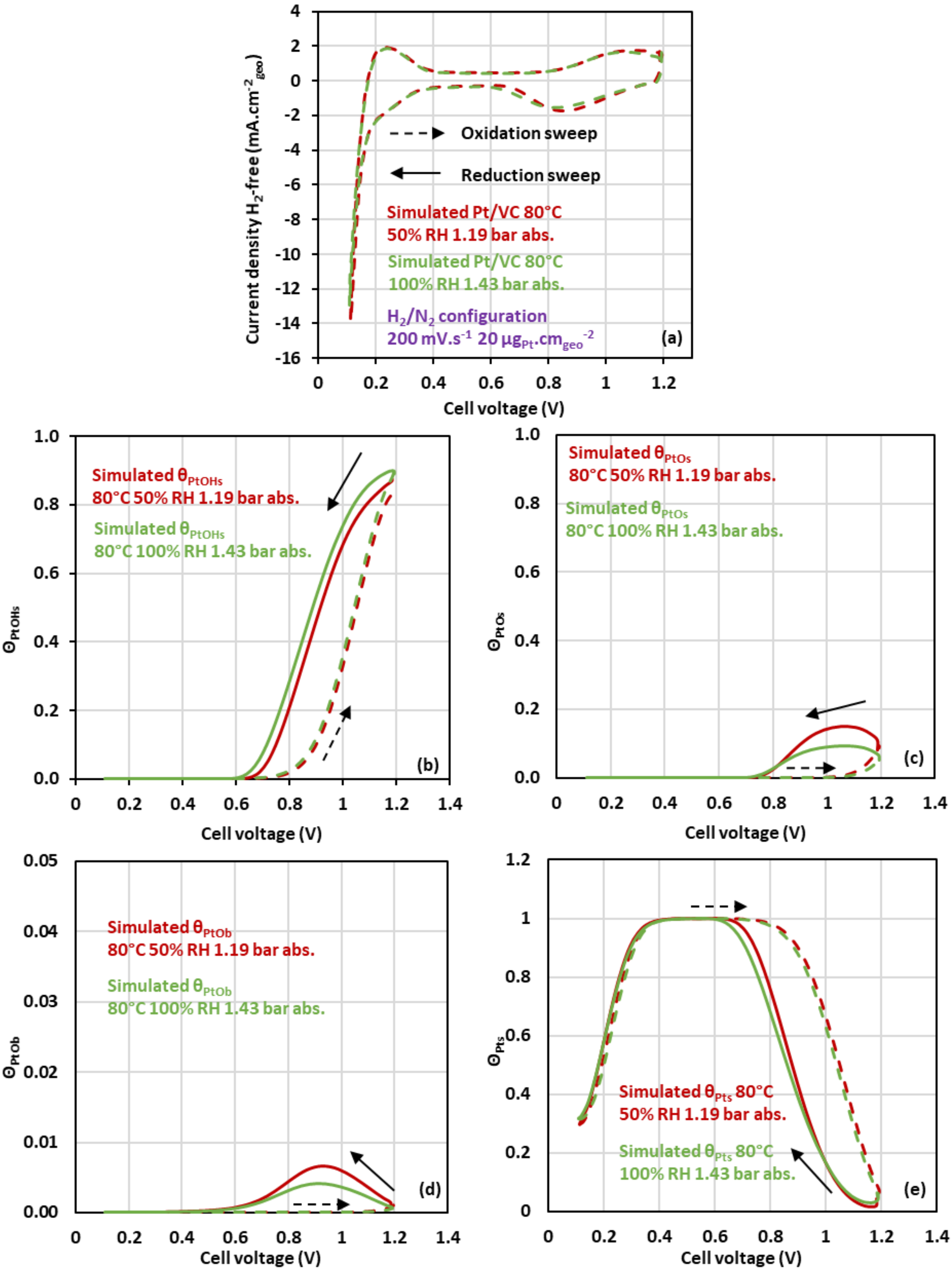

Figure IV-27 : Impact of relative humidity on simulated (a) cyclic voltammetries (b) PtOH$_s$ coverage ratio evolution (c) PtO$_s$ coverage ratio evolution (d) PtO$_b$ coverage ratio evolution (e) Pt$_s$ coverage ratio evolution.

To summarise, be it under nitrogen atmosphere or under H_2/O_2 configuration, the simulated data do not match the experimental one, but some of the global trends observed experimentally are still captured. Under H_2/O_2 configuration, it seems that the relative humidity does not have a significant impact on the performance simulated. They seem to be mainly driven by the kinetics of the different reactions of the multi-steps ORR mechanism. Even if the activity of water and proton are involved in the kinetics of the reactions, the simulations revealed that the trends according to relative humidity evolution are not necessarily in agreement with experiment. Thus, improvements need to be done on the water transport description, but also on the different kinetics values of the Pt oxides formation and reduction reactions. Under H_2/N_2 configuration, there are not many differences with experiments between the two relative humidities, which is also the case with simulations. However, the simulated CV do not exactly match the experimental one.

IV.4.4 Potentiostatic study under H_2/N_2 configuration

In this section, potentiostatic study is performed to see if the kinetic of Pt surface oxides growth is following a logarithmic law with time as it was stated in the work of Conway *et al.* [41], [42] Figure IV-28 (a) shows the different potential profile applied to perform the potentiostatic simulations under H_2/N_2 configuration at 30°C, 100% RH and P_{atm}. Initially, the potential is set equal to 0.4 V, potential at which the Pt is entirely free. Then a potential jump is applied to the desired potential (0.7 to 0.9 V), which is held for 100 seconds. Figure IV-28 (b) displays the Pt oxides coverage ratio evolution with time at different potential held, from 0.7 to 0.9 V every 50 mV. Surprisingly, at all the potential considered, almost all the oxides (mainly $PtOH_s$) are formed within the first second, which is extremely fast. At 0.9 V, after the first second, the Pt oxidation still occur until 20 seconds. This phenomenon is also observed at 0.85 V but in a less significant way and is not observed for the other potential considered. This further oxidation is probably due to the $PtOH_s$ oxidation into PtO_s, as the onset potential of this oxidation reaction is near to 0.9 V as witnessed by the simulated PtO_s coverage ratio evolution (see Figure IV-14 (b)).

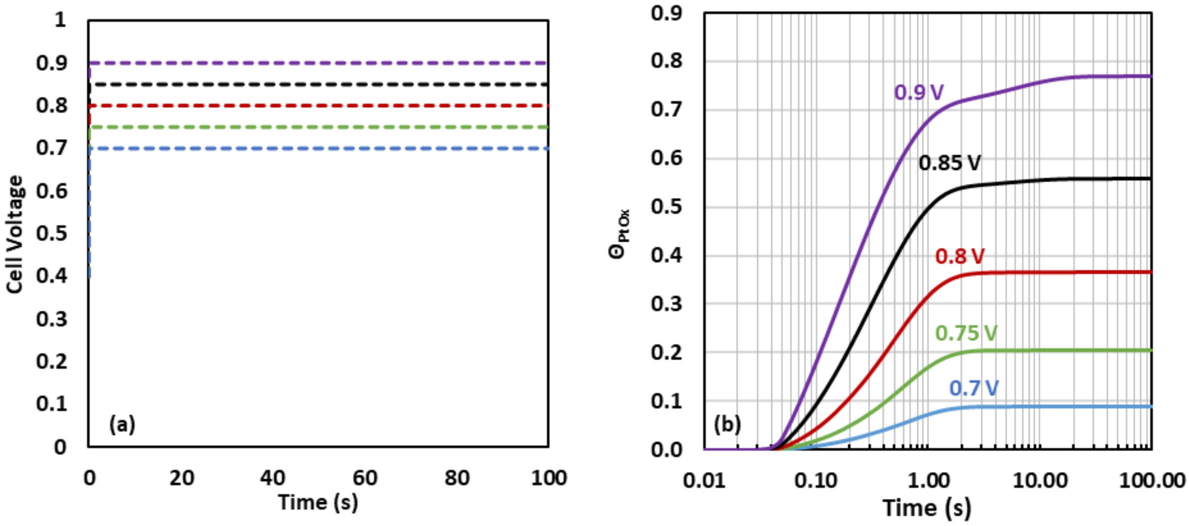

Figure IV-28 : (a) Potential profiles applied for potentiostatic simulations under H_2/N_2 configuration and (b) Pt oxides coverage ratio evolution with time during potentiostatic simulations.

Thus, in 20 seconds, the equilibrium between the Pt surface coverage and the potential applied is reached. This is not what Jahnke *et al*. observed in their work at 80°C, 100% RH [28]. The oxidation still occurs even after more than 2 hours. However, the final value of the Pt oxides coverage ratio at the different potential are quite in agreement with the values found by Jahnke *et al.* after more than 2 hours (see Table IV-6). The comparison was not made at the same operating conditions as the best description of the CV and the evolution of the different Pt oxides coverage ratio are obtained at 30°C, 100% RH.

Table IV-6 : Pt oxides coverage ratio comparison with values from [28].

Voltage applied	**Θ_{PtOx} in this work after 100 s**	**Θ_{PtOx} in [28] after 10000 s (estimated)**
0.7 V	0.09	0.08
0.75 V	0.2	0.23
0.8 V	0.38	0.38
0.85 V	0.56	0.51

From the potentiostatic simulation, one can conclude that the oxide growth does follow a logarithmic law even if the equilibrium is fastly reached. The fact that the equilibrium between the potential applied and the Pt oxides surface coverage is quickly reached may be due to inaccurate estimation of the different kinetic parameters for potentiostatic measurements. However, they describe quite well the dynamic behaviour during CV simulation at 30°C, 100% RH. In addition, almost no PtO_s oxides is formed from 0.7 to 0.85 V, meaning that the potentiostatic measurements only describe the $PtOH_s$ oxides growth. At 0.9 V, the contribution of PtO_s growth starts to be captured by simulation. Finally, to have more insights and improve the description of the Pt oxides formation/reduction, more potentiostatic study must be done and further explored under nitrogen as well as oxygen atmospheres, which could not be achieved in this work when writing these lines.

IV.5 Simulations of thicker catalyst layer

This section investigates the transition to the 1D catalyst layer description. Indeed, as global performance (at 80°C, 80% RH and 1.34b) and cyclic voltammetry (at 30°C, 100% RH and P_{atm}) simulations with 0D catalyst layers description match quite well the experiments for 20 $\mu g_{Pt}.cm_{geo}^{-2}$ Pt/VC catalyst layer, the following section investigates the transition to the 1D catalyst layers (simulations of 100 $\mu g_{Pt}.cm_{geo}^{-2}$ catalyst layer) under the same operating conditions. In the following, the model takes into account the thickness of the catalyst layers. The thickness of the cathode is set to 2 µm (vs. 0.7 µm for 20 $\mu g_{Pt}.cm_{geo}^{-2}$ catalyst layer), the loading is increased to 90 $\mu g_{Pt}.cm_{geo}^{-2}$ and the ECSA is set to 31.6 $cm_{Pt}^{2}.cm_{geo}^{-2}$ (*i.e.* Γ_{Pt} = 1.58.10^{7} m^{-1}) to perform the simulations. In the next results, 20 $\mu g_{Pt}.cm_{geo}^{-2}$ refers to very low loaded catalyst layer and 100 $\mu g_{Pt}.cm_{geo}^{-2}$ refers to the thicker catalyst layer.

IV.5 Simulations of thicker catalyst layer

IV.5.1.1 Under H_2/O_2 configuration

Figure IV-29 (a) shows the comparison of experiment and simulated polarization curves with 100 $\mu g_{Pt}.cm_{geo}^{-2}$ catalyst layer, with and without ohmic drop correction from the resistances evolution shown on Figure IV-29 (b). It seems that at low current density, the simulations match the experiments. However, at medium/high current densities, the model does not catch well the i-V characteristic. Regarding the resistances evolution, the global shape of the simulated PEM resistance seems to be in agreement with experimental R_{HF} evolution. However, the values of R_{MB} are higher than the R_{HF} in all the potential range considered, which may be explained by the fact that less current density is produced with the simulation, thus the membrane is less hydrated. One should note that the inversion point between forward and backward sweeps occurs around 0.55 V with the simulation, compared to 0.3 V for the experiment. In addition, the hysteresis observed seems to be bigger with the simulation than with the experiment. As a result, on one hand, the bad performance description of simulated polarization curve may explain the differences observed on the PEM resistance evolution along the polarization curve, and on the other hand, the water motion in the membrane and in the ionomer in the catalyst layer may suffer from lack of accurate description. A study of the impact of the different diffusion resistance coefficients (see Equation IV-29 to Equation IV-31) on the membrane resistance evolution must be done in order to improve the water motion inside the ionomer phase.

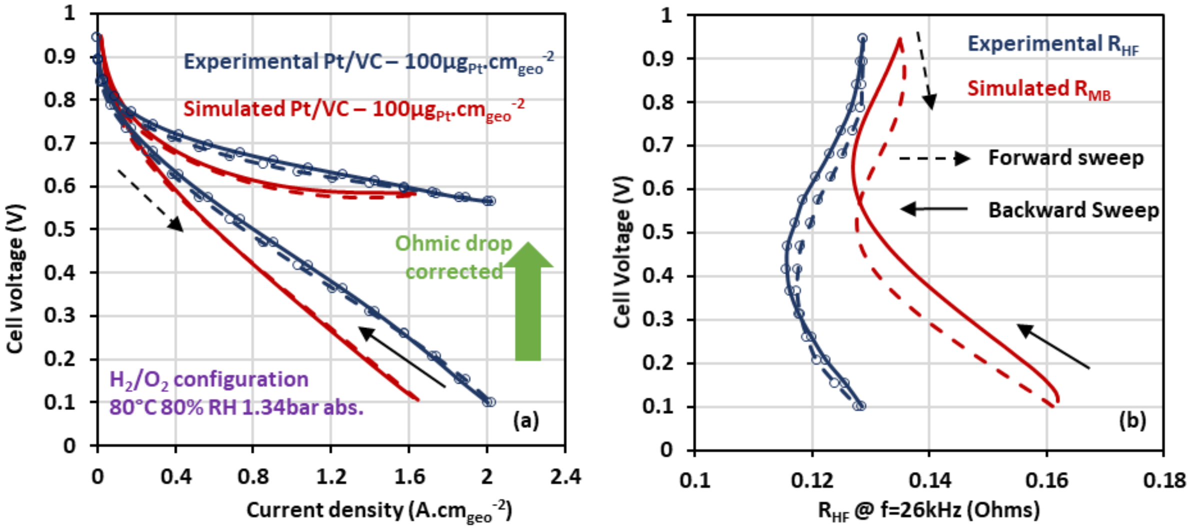

Figure IV-29 : Comparison between (a) Experimental and simulated polarization curve with and without ohmic drop correction of 100 $\mu g_{Pt}.cm_{geo}^{-2}$ catalyst layers and (b) Experimental high frequency resistance and simulated PEM resistance evolution along the polarization curve.

Figure IV-30 (a) shows the simulated polarization curves of 20 $\mu g_{Pt}.cm_{geo}^{-2}$ and 100 $\mu g_{Pt}.cm_{geo}^{-2}$ catalyst layer loadings with and without ohmic drop. As observed experimentally, the loading increase leads to more current density production in all the potential range considered and to a bigger hysteresis between the forward and the backward sweeps. On the raw simulated polarization curves (e.g. without ohmic drop correction), the gap in performance is decreasing with potential, while on the ohmic drop corrected polarization curves, the gap in performance between the two loadings is held in all the potential range considered. This is explained by the resistances evolution

(Figure IV-30 (b)) along the polarization curve. The significant increase of the R_{MB} from 0.5 to 0.1 V in the case of 100 $\mu g_{Pt}.cm_{geo}^{-2}$ compared to 20 $\mu g_{Pt}.cm_{geo}^{-2}$ leads to a bigger adjustment of the polarization curve. Figure IV-30 (c) and (d) shows the average evolution, through thickness of the CL, of relative humidity and temperature in the catalyst layer along the polarization curve. One should note that increasing the loading, and thus the current density production, does not necessarily lead to an averaged temperature increase. However, especially near the GDL, the catalyst layer produces more current than on the membrane side, which may result in more hydration/heat and the apparition of local operating conditions. This assumption is not investigated here. The relative humidity evolution for the 100 $\mu g_{Pt}.cm_{geo}^{-2}$ case is surprising: on the contrary to 20 $\mu g_{Pt}.cm_{geo}^{-2}$, the average relative humidity is only increasing from around 80% to almost 100%, along the polarization curve in the catalyst layer. In fact, it has been observed in the model (not shown here) that the average relative humidity of the anode is decreasing from around 80% to almost 60%. In a first approach, one may consider that the electro-osmosis phenomenon from the anode to the cathode is dominating the water motion in the PEM, compared to the water diffusion from the cathode to the anode, resulting in a significant drying of the anode. The hysteresis observed on the relative humidity evolution is bigger in the case of 100 $\mu g_{Pt}.cm_{geo}^{-2}$, which may partly account for the larger hysteresis observed on the ohmic drop corrected polarization curve.

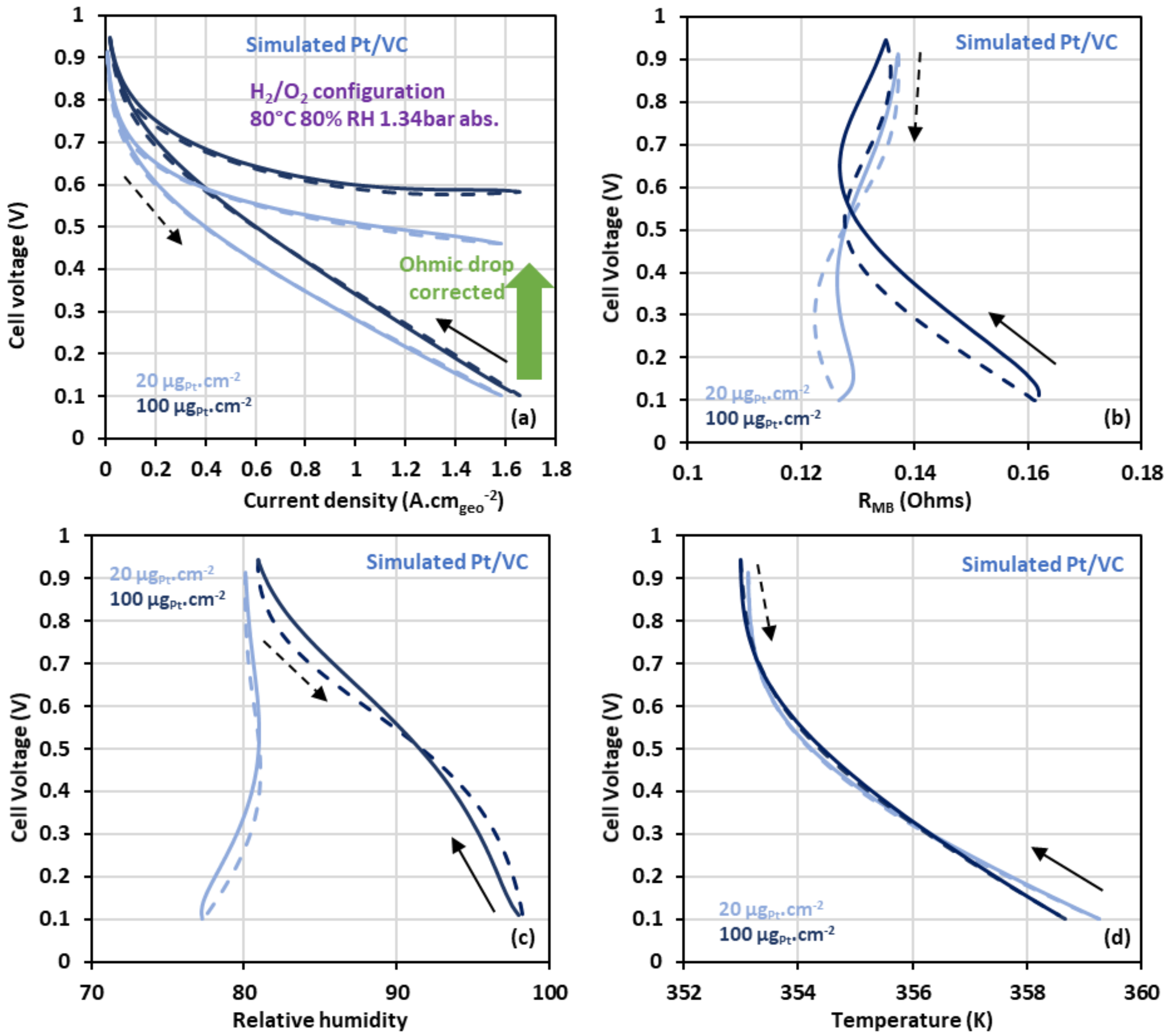

Figure IV-30 : Comparison between 20 µg$_{Pt}$.cm$_{geo}^{-2}$ and 100 µg$_{Pt}$.cm$_{geo}^{-2}$ catalyst layer of (a) Simulated polarization curve with and without ohmic drop correction (b) Simulated resistances of the PEM (c) Simulated relative humidity and (d) Simulated temperature along the polarization curve.

The different coverage ratio evolution of oxides species and free Pt along the polarization curve are shown on Figure IV-31. The free Pt surface coverage ratio evolution (Figure IV-31 (d)) indicates that with more loaded catalyst layer, more oxides are formed in all the potential range considered, except at 0.9 V, potential at which in both cases, all the Pt sites are almost covered by oxides. This might be explained by the fact that thick catalyst layers better trap water, which is necessary for oxides formation. The fact that more oxides are formed is also witnessed by the Pt 'bulk' and PtO surface oxides coverage ratio evolution (Figure IV-31 (b) and (c)). In addition, it seems that the hysteresis observed on the different Pt oxides coverage ratio evolution (Figure IV-31 (a) to (c)) is larger with more loaded catalyst layer. This makes sense as more oxides are formed, 'bulk' oxides included, it exacerbates the hysteresis phenomenon and this may account partly for the wider hysteresis observed on the simulated polarization curves from Figure IV-30 (a).

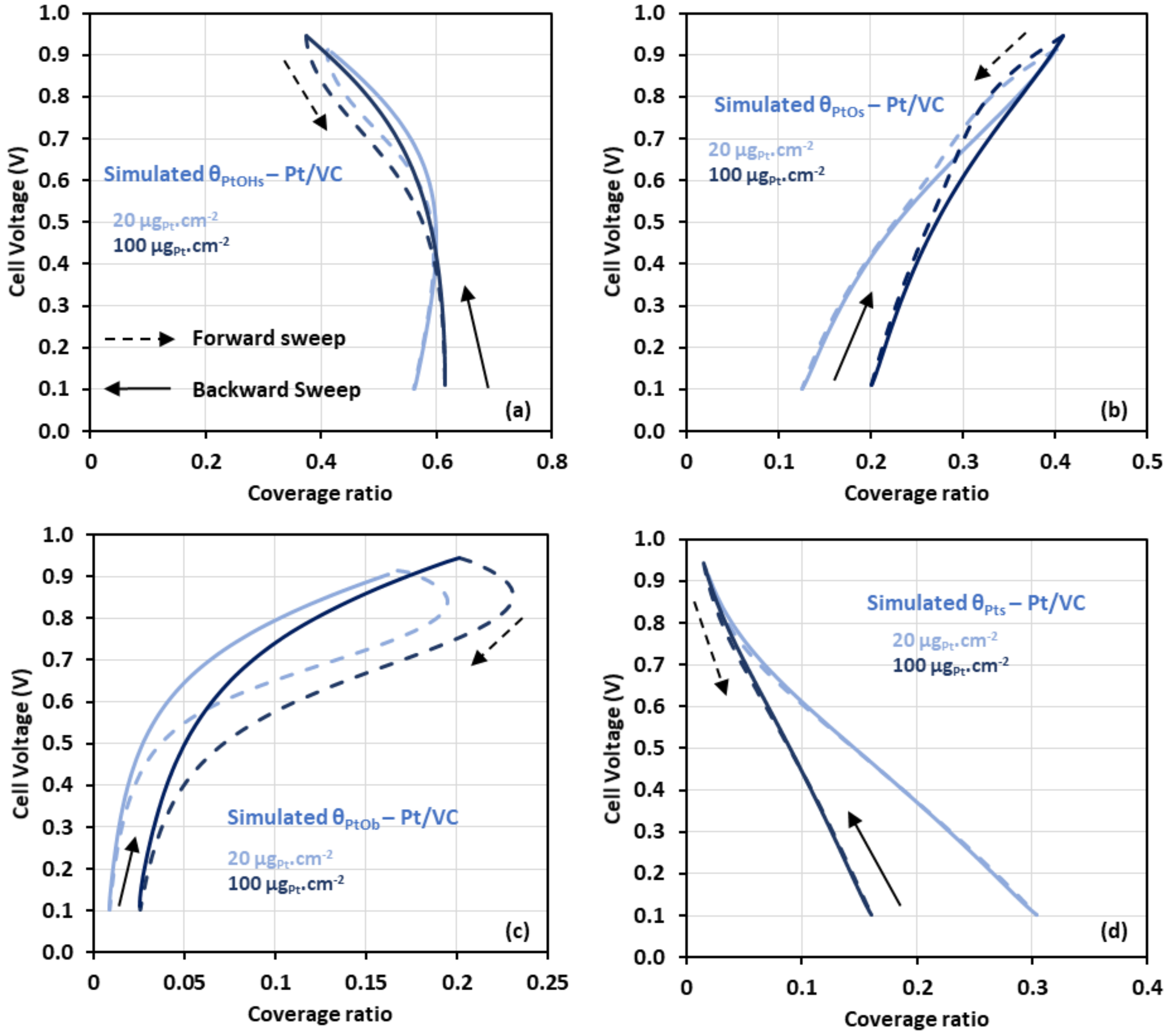

Figure IV-31 : Comparison between 20 µg$_{Pt}$.cm$_{geo}^{-2}$ and 100 µg$_{Pt}$.cm$_{geo}^{-2}$ catalyst layer of (a) θ_{PtOHs} (b) θ_{PtOs} (c) θ_{PtOb} and (d) θ_{Pts} along the polarization curve.

IV.5.1.2 Under H_2/N_2 configuration

In this section, the different results regarding the 100 µg$_{Pt}$.cm$_{geo}^{-2}$ simulations were obtained with the 0D version of the model (catalyst layers considered as interface), as the transport properties should not have a significant impact on cyclic voltammetries. However, the catalyst layer loading and the ECSA values were modified to match the experimental value obtained on the 100 µg$_{Pt}$.cm$_{geo}^{-2}$ catalyst layers. This being set, Figure IV-32 (a) shows a comparison between experimental and simulated cyclic voltammetries corrected from H_2 crossover current. In the H$_{UPD}$ region, there is still a quite good match of the global shape of the CV between experiment and modeling. However there are differences regarding the coulometry, especially on the reduction sweep. In the oxide region, the Pt oxides formation is badly described as the coulommetry between experiment and modeling do not match at all. However, there is no evolution of the differences between experiment and modeling regarding the Pt oxides coverage ratio evolution when comparing the 100 µg$_{Pt}$.cm$_{geo}^{-2}$ case (Figure IV-32 (b)) and the 20 µg$_{Pt}$.cm$_{geo}^{-2}$ case (see Figure IV-15 (b)). In fact, there were also almost no differences regarding the experiments between the two loadings (see Figure III-40). Regarding the reduction sweep in the oxide region, the description of the CV seems to better match the experiment in the case of 100 $\mu g_{Pt}.cm_{geo}^{-2}$ than in the case of 20 $\mu g_{Pt}.cm_{geo}^{-2}$, which is actually confirmed by the Pt oxides coverage ratio evolution with potential during CV (Figure IV-32 (b)).

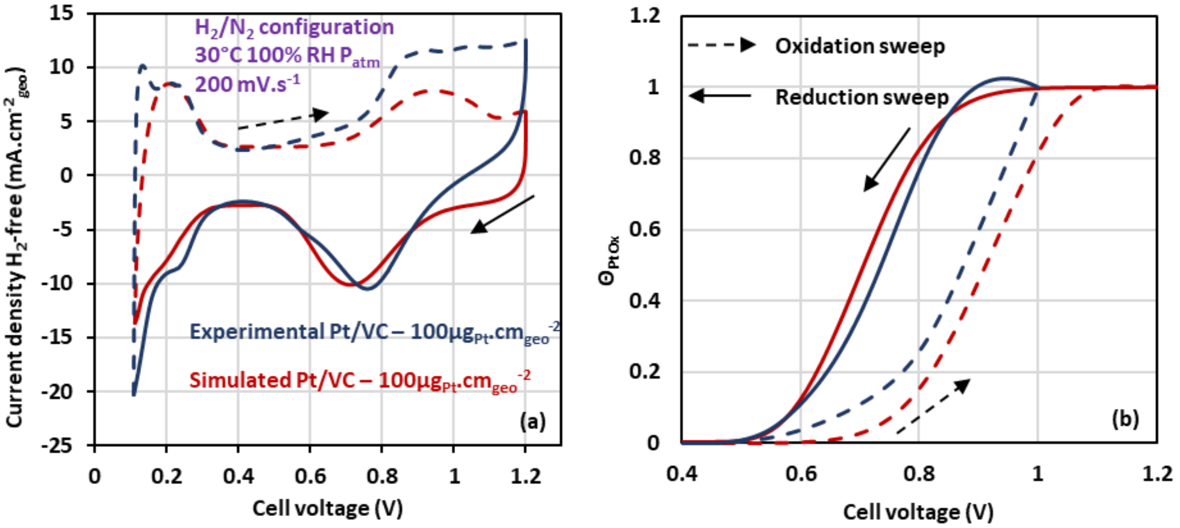

Figure IV-32 : Comparison between (a) Experimental and simulated cyclic voltammetries corrected from H_2 crossover current of 100 $\mu g_{Pt}.cm_{geo}^{-2}$ catalyst layers and (b) Pt oxides coverage ratio evolution with potential during CV.

Figure IV-33 (a) shows a comparison of simulated cyclic voltammetries normalized by the ECSA value, determined from the H_{UPD} region from the simulated CV, between 20 $\mu g_{Pt}.cm_{geo}^{-2}$ and 100 $\mu g_{Pt}.cm_{geo}^{-2}$ catalyst layers. First, the coulommetry of proton desorption is almost the same between the two loadings, which is in agreement with the experiment, whereas the proton adsorption coulommetry is higher in the case of the 100 $\mu g_{Pt}.cm_{geo}^{-2}$ loading, which is not the case for the experiment. The differences may come from the proton activity, which is involved in the reactions occurring on the reduction sweep. As for experiment, the Pt oxidation and Pt oxides reduction coulometries seem to be more important in the case of 100 $\mu g_{Pt}.cm_{geo}^{-2}$ catalyst layer. This was also observed experimentally: more Pt sites leads to more oxides formation and thus oxides reduction because of better water trapping in thick CL. However, the latter observation is not reflected on the Pt oxides coverage ratio evolution (Figure IV-33 (b) to (d)) and on the free Pt coverage ratio evolution (Figure IV-33 (e)). Indeed, there are almost no differences between the two loadings regarding the different coverage ratio, which may be due to the absence of water production under nitrogen atmosphere. Another explanation may be that the 0D version of the model may not be suitable to perform cyclic voltammetry with thicker/more loaded catalyst layer.

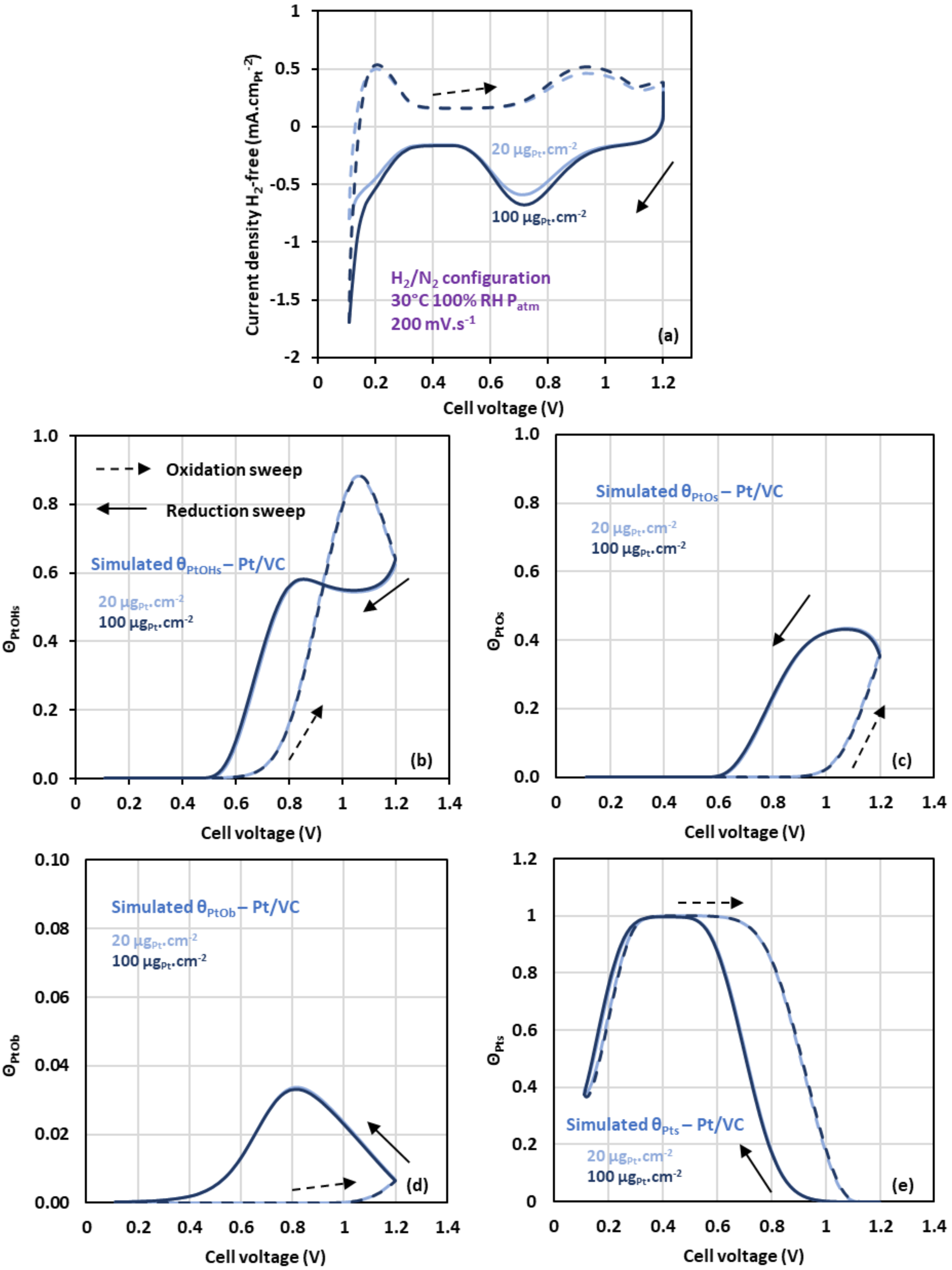

Figure IV-33 : Comparison between 20 µg$_{Pt}$.cm$_{geo}^{-2}$ and 100 µg$_{Pt}$.cm$_{geo}^{-2}$ catalyst layer of simulated (a) cyclic voltammetries with the current normalized by the ECSA value and (b) θ_{PtOHs} (c) θ_{PtOs} (d) θ_{PtOb} and (e) θ_{Pts} evolution with potential.

From these different results, even though some global trends from the model are in agreement with experiment, one can conclude that the transition to the 1D catalyst layer description is not achieved. In a first approach, it seems that the issues come from a lack or inaccurate description of transport phenomena (motion of water in the ionomer phase for instance) and the inaccurate description of the kinetic parameters of different reactions from the multi-steps ORR mechanism (kinetic constant as a function of temperature for instance). This is also confirmed by the different parametric studies, that shown that the simulations under various operating conditions does not accurately describe the different results obtained experimentally. However, some of the global trends still match what is observed experimentally. The transition to the 1D catalyst layer being not achieved, the performance simulation of a complex MEA such as the FURTHER MEA, which is optimized and representative of what can be commercialized, is not possible at the moment.

IV.6 Conclusion

A multi-steps ORR mechanism was proposed in this work, including the formation of Pt surface and bulk oxides as intermediates species, in order to better describe the electrochemical and physico-chemical phenomena that take place in the catalyst layer during operation. This new description introduces new parameters such as the different coverage ratio evolution of the oxides species (surface and 'bulk') and the free Pt surface. These parameters allow to have insights into the surface state of Pt, and better describe the surface structural change of Pt, which seems to play a crucial role in the ORR mechanism and the performance of the PEMFC. Compared to the initial electrochemical description from the work of Randrianarizafy [30], the multi-steps ORR mechanism captures quite well the main features related to Pt oxides formation and reduction observed on the experimental characterization under nitrogen or oxygenated atmosphere (hysteresis observed on experimental polarization curve, Pt oxides formation and reduction response on cyclic voltammetries) with only one single set of kinetic parameters for both descriptions. However, the model used in this work still needs to be improved to overcome a rigorous validation process under various operating conditions, as well as to capture the transition to real catalyst layer, including the thickness of the latter. Only with such improvements, will it be able to predict the performance in a reliable way of different electrode compositions. Further investigations on reaction order, and Tafel plots for instance would have been helpful in order to validate the multi-step ORR mechanism and the kinetic parameters chosen [43]. Finally, it is important to describe as accurately as possible the ORR mechanism, to further implement/improve the reversible degradation mechanism (performance loss due to Pt oxides formation) and irreversible degradation mechanism (Pt corrosion occurring through Pt oxidation and Pt oxides reduction).

References of Chapter IV

[1] T. Jahnke, G. Futter, A. Latz, T. Malkow, G. Papakonstantinou, G. Tsotridis, P. Schott, M. Gérard, M. Quinaud, M. Quiroga, A.A. Franco, K. Malek, F. Calle-Vallejo, R. Ferreira de Morais, T. Kerber, P. Sautet, D. Loffreda, S. Strahl, M. Serra, P. Polverino, C. Pianese, M. Mayur,W.G. Bessler and C. Kompis, “Performance and degradation of Proton Exchange Membrane Fuel Cells: State of the art in modeling from atomistic to system scale,” *J. Power Sources*, vol. 304, pp. 207–233, Feb. 2016, doi: 10.1016/j.jpowsour.2015.11.041.

[2] S. Mazumder and J. V. Cole, “Rigorous 3-D mathematical modeling of PEM fuel cells II. Model predictions with liquid water transport,” *J. Electrochem. Soc.*, vol. 150, no. 11, pp. A1510–A1517, 2003, doi: 10.1149/1.1615609.

[3] J. K. Nørskov, J. Rossmeisl, A. Logadottir, L. Lindqvist, J. R. Kitchin, T. Bligaard and H. Jonsson, “Origin of the Overpotential for Oxygen Reduction at a Fuel-Cell Cathode,” *J. Phys. Chem. B*, vol. 108, no. 46, pp. 17886–17892, Nov. 2004, doi: 10.1021/jp047349j.

[4] R. Ferreira de Morais, A. A. Franco, P. Sautet and D. Loffreda, “Interplay between Reaction Mechanism and Hydroxyl Species for Water Formation on Pt(111),” *ACS Catal.*, vol. 5, no. 2, pp. 1068–1077, Feb. 2015, doi: 10.1021/cs5012525.

[5] P. Costamagna, “Transport phenomena in polymeric membrane fuel cells,” *Chem. Eng. Sci.*, vol. 56, no. 2, pp. 323–332, Jan. 2001, doi: 10.1016/S0009-2509(00)00232-3.

[6] Y. Wang and C.-Y. Wang, “Transient analysis of polymer electrolyte fuel cells,” *Electrochimica Acta*, vol. 50, no. 6, pp. 1307–1315, Jan. 2005, doi: 10.1016/j.electacta.2004.08.022.

[7] Y. Wang and C.-Y. Wang, “Dynamics of polymer electrolyte fuel cells undergoing load changes,” *Electrochimica Acta*, vol. 51, no. 19, pp. 3924–3933, May 2006, doi: 10.1016/j.electacta.2005.11.005.

[8] S. Um and C.Y. Wang, “Three-dimensional analysis of transport and electrochemical reactions in polymer electrolyte fuel cells,” *J. Power Sources*, vol. 125, no. 1, pp. 40–51, Jan. 2004, doi: 10.1016/j.jpowsour.2003.07.007.

[9] T. E. Springer, T. A. Zawodzinski and S. Gottesfeld, “Polymer Electrolyte Fuel Cell Model,” *J. Electrochem. Soc.*, vol. 138, no. 8, pp. 2334–2342, Aug. 1991, doi: 10.1149/1.2085971.

[10] S. Ge, X. Li, B. Yi and I-M. Hsing, “Absorption, Desorption, and Transport of Water in Polymer Electrolyte Membranes for Fuel Cells,” *J. Electrochem. Soc.*, vol. 152, no. 6, p. A1149, 2005, doi: 10.1149/1.1899263.

[11] P. W. Majsztrik, M. B. Satterfield, A. B. Bocarsly and J. B. Benziger, “Water sorption, desorption and transport in Nafion membranes,” *J. Membr. Sci.*, vol. 301, no. 1–2, pp. 93–106, Sep. 2007, doi: 10.1016/j.memsci.2007.06.022.

[12] J. H. Chun, K. T. Park, D. H. Jo, S. G. Kim and S. H. Kim, “Numerical modeling and experimental study of the influence of GDL properties on performance in a PEMFC,” *Int. J. Hydrog. Energy*, vol. 36, no. 2, pp. 1837–1845, Jan. 2011, doi: 10.1016/j.ijhydene.2010.01.036.

[13] T. Koido, T. Furusawa and K. Moriyama, “An approach to modeling two-phase transport in the gas diffusion layer of a proton exchange membrane fuel cell,” *J. Power Sources*, vol. 175, no. 1, pp. 127–136, Jan. 2008, doi: 10.1016/j.jpowsour.2007.09.029.

[14] P. P. Mukherjee, Q. Kanga and C.-Y. Wang, “Pore-scale modeling of two-phase transport in polymer electrolyte fuel cells—progress and perspective,” *Energy Env. Sci*, vol. 4, no. 2, pp. 346–369, 2011, doi: 10.1039/B926077C.

[15] X. Zhang, Y. Gao, H. Ostadi, K. Jiang and R. Chen, “Modelling water intrusion and oxygen diffusion in a reconstructed microporous layer of PEM fuel cells,” *Int. J. Hydrog. Energy*, vol. 39, no. 30, pp. 17222–17230, Oct. 2014, doi: 10.1016/j.ijhydene.2014.08.027.

[16] J. Ma, X. Zhang, Z. Jiang, H. Ostadi, K. Jiang and R. Chen, “Flow properties of an intact MPL from nano-tomography and pore network modelling,” *Fuel*, vol. 136, pp. 307–315, Nov. 2014, doi: 10.1016/j.fuel.2014.07.040.

[17] F. C. Cetinbas, S. G. Advani and A. K. Prasadz, “A Modified Agglomerate Model with Discrete Catalyst Particles for the PEM Fuel Cell Catalyst Layer,” *J. Electrochem. Soc.*, vol. 160, no. 8, pp. F750–F756, 2013, doi: 10.1149/2.017308jes.

[18] F. C. Cetinbas, S. G. Advani and A. K. Prasadz, “An Improved Agglomerate Model for the PEM Catalyst Layer with Accurate Effective Surface Area Calculation Based on the Sphere-Packing Approach,” *J. Electrochem. Soc.*, vol. 161, no. 6, pp. F803–F813, 2014, doi: 10.1149/2.116406jes.

[19] G. Wang, P. P. Mukherjee and C.-Y. Wang, “Optimization of polymer electrolyte fuel cell cathode catalyst layers via direct numerical simulation modeling,” *Electrochimica Acta*, vol. 52, no. 22, pp. 6367–6377, Jun. 2007, doi: 10.1016/j.electacta.2007.04.073.

[20] A. Suzuki, U. Sen, T. Hattori, R. Miura, R. Nagumo, H. Tsuboi, N. Hatakeyama, A. Endou, H. Takaba, M. C. Williams and A. Miyamoto, “Ionomer content in the catalyst layer of polymer electrolyte membrane fuel cell (PEMFC): Effects on diffusion and performance,” *Int. J. Hydrog. Energy*, vol. 36, no. 3, pp. 2221–2229, Feb. 2011, doi: 10.1016/j.ijhydene.2010.11.076.

[21] A. Z. Weber and J. Newman, “Transport in Polymer-Electrolyte Membranes,” *J. Electrochem. Soc.*, p. 16.

[22] Q. Yan and J. Wu, “Modeling of single catalyst particle in cathode of PEM fuel cells,” *Energy Convers. Manag.*, vol. 49, no. 8, pp. 2425–2433, Aug. 2008, doi: 10.1016/j.enconman.2008.01.021.

[23] S. Jomori, N. Nonoyama and T. Yoshida, “Analysis and modeling of PEMFC degradation: Effect on oxygen transport,” *J. Power Sources*, vol. 215, pp. 18–27, Oct. 2012, doi: 10.1016/j.jpowsour.2012.04.069.

[24] J. X. Wang, J. Zhang and R. R. Adzic, “Double-Trap Kinetic Equation for the Oxygen Reduction Reaction on Pt(111) in Acidic Media,” *J. Phys. Chem. A*, vol. 111, no. 49, pp. 12702–12710, Dec. 2007, doi: 10.1021/jp076104e.

[25] B. Jayasankar and K. Karan, “O2 electrochemistry on Pt: A unified multi-step model for oxygen reduction and oxide growth,” *Electrochimica Acta*, vol. 273, pp. 367–378, May 2018, doi: 10.1016/j.electacta.2018.03.191.

[26] A. Damjanovic, M. A. Genshaw and J. O'M. Bockris, “The Mechanism of Oxygen Reduction at Platinum in Alkaline Solutions with Special Reference to H2O2,” J. Electrochem. Soc. **114** 1107, 1967

[27] A. Damjanovic and V. Brusic, “Electrode kinetics of oxygen reduction on oxide-free platinum electrodes,” *Electrochimica Acta*, vol. 12, no. 6, pp. 615–628, Jun. 1967, doi: 10.1016/0013-4686(67)85030-8.

[28] T. Jahnke, G. A. Futter, A. Baricci, C. Rabissi and A. Casalegno, “Physical Modeling of Catalyst Degradation in Low Temperature Fuel Cells: Platinum Oxidation, Dissolution, Particle Growth and Platinum Band Formation,” *J. Electrochem. Soc.*, vol. 167, no. 1, p. 013523, Nov. 2019, doi: 10.1149/2.0232001JES.

[29] G. Maranzana, A. Lamibrac, J. Dillet, S. Abbou, S. Didierjean and O. Lottina, “Startup (and Shutdown) Model for Polymer Electrolyte Membrane Fuel Cells,” *J. Electrochem. Soc.*, vol. 162, no. 7, pp. F694–F706, 2015, doi: 10.1149/2.0451507jes.

[30] B. Randrianarizafy, “Multi-physics modeling of startup and shutdown of a PEM fuel cell and study of the carbon support degradation: mitigation strategies and design optimization,” Thèse, Université Grenoble Alpes, CEA Grenoble, 2018. [Online]. Available: https://tel.archives-ouvertes.fr/tel-02140284

[31] B. Randrianarizafy, P. Schott, M. Chandesris, M. Gerard and Y. Bultel, “Design optimization of rib/channel patterns in a PEMFC through performance heterogeneities modelling,” *Int. J. Hydrog. Energy*, vol. 43, no. 18, pp. 8907–8926, May 2018, doi: 10.1016/j.ijhydene.2018.03.036.

[32] F. Nandjou, “Etude locale de la thermique dans les piles à combustibles pour application automobile. Corrélation à la durée de vie,” Thèse, Université Grenoble Alpes, CEA Grenoble, 2015. [Online]. Available: https://tel.archives-ouvertes.fr/tel-01267255

[33] J. B. Young and B. Todd, “Modelling of multi-component gas flows in capillaries and porous solids,” *Int. J. Heat Mass Transf.*, vol. 48, no. 25–26, p. 5338, 2005, doi: doi:10.1016/j.ijheatmasstransfer.2005.07.034.

[34] J.-P. Poirot-Crouvezier, “Modélisation dynamique des phénomènes hydrauliques, thermiques et électriques dans un groupe électrogène à pile à combustible destiné à l’application automobile,” Thèse, Institut National Polytechnique de Grenoble, CEA Grenoble, PSA Peugeot Citroën, 2000. [Online]. Available: https://tel.archives-ouvertes.fr/tel-02907129

[35] T. A. Zawodzinski, Jr., M. Neeman, L. O. Sillerud and S. Gottesfeld, "Determination of water diffusion coefficients in perfluorosulfonate ionomeric membranes," *J. Phys. Chem.*, vol. 95, no. 15, pp. 6040–6044, Jul. 1991, doi: 10.1021/j100168a060.

[36] F. Meier and G. Eigenberger, "Transport parameters for the modelling of water transport in ionomer membranes for PEM-fuel cells," *Electrochimica Acta*, vol. 49, no. 11, pp. 1731–1742, Apr. 2004, doi: 10.1016/j.electacta.2003.12.004.

[37] G. Lin and T. Van Nguyen, "A Two-Dimensional Two-Phase Model of a PEM Fuel Cell," *J. Electrochem. Soc.*, vol. 153, no. 2, p. A372, 2006, doi: 10.1149/1.2142267.

[38] A. Kusoglu and A. Z. Weber, "New Insights into Perfluorinated Sulfonic-Acid Ionomers," *Chem. Rev.*, vol. 117, no. 3, pp. 987–1104, Feb. 2017, doi: 10.1021/acs.chemrev.6b00159.

[39] V. A. Saveleva, V. Papaefthimiou, M. K. Daletou, W. H. Doh, C. Ulhaq-Bouillet, M. Diebold, S. Zafeiratos and E. R. Savinova, "*Operando* Near Ambient Pressure XPS (NAP-XPS) Study of the Pt Electrochemical Oxidation in H_2O and H_2O/O_2 Ambients," *J. Phys. Chem. C*, vol. 120, no. 29, pp. 15930–15940, Jul. 2016, doi: 10.1021/acs.jpcc.5b12410.

[40] I. Martens, R. Chattot, M. Rasola, M. Valeria Blanco, V. Honkimäki, D. Bizzotto, D. P. Wilkinson and J. Drnec, "Probing the Dynamics of Platinum Surface Oxides in Fuel Cell Catalyst Layers Using in Situ X-ray Diffraction," *ACS Appl. Energy Mater.*, vol. 2, no. 11, pp. 7772–7780, Nov. 2019, doi: 10.1021/acsaem.9b00982.

[41] B. E. Conway, "Electrochemical oxide film formation at noble metals as a surface-chemical process," *Prog. Surf. Sci.*, vol. 49, no. 4, pp. 331–452, Aug. 1995, doi: 10.1016/0079-6816(95)00040-6.

[42] B. E. Conway, B. Barnett, H. Angerstein-Kozlowska and B. V. Tilak, "A surface-electrochemical basis for the direct logarithmic growth law for initial stages of extension of anodic oxide films formed at noble metals," *J. Chem. Phys.*, vol. 93, no. 11, pp. 8361–8373, Dec. 1990, doi: 10.1063/1.459319.

[43] M. Moore, A. Putz and M. Secanell, "Investigation of the ORR Using the Double-Trap Intrinsic Kinetic Model," *J. Electrochem. Soc.,* vol. 160, no. 6, *pp. F670*-F681, Apr. 2013, doi: 10.1149/2.123306jes.

Conclusion & perspectives

The PEMFC technology is enough mature to be commercialized for automotive application (commercial systems are on the market, for instance Hyundaï Nexo, Toyota Miraï and Honda Clarity). However, there is still significant technological limitations that need to be overcome, such as the stack/systems cost and durability, to enable wide-commercialization of the technology. These limitations mainly come from the cathode catalyst layer, where the electrochemical oxygen reduction reaction takes place. It uses carbon-supported Pt-based catalyst and a polymer-based protonic conductor. The electrode must ensure several properties to enable an efficient operation and reach the desired high power density. Its operation requires a complex interplay between numerous physico-chemical and electrochemical phenomena occurring concomitantly in this layer. Thus, the understanding of the cathode catalyst layer operation is mandatory to optimize the design of the electrode, as well as to reduce the quantity of the materials used. Identifying the limiting phenomena is also an important step to elaborate mitigation strategies regarding the degradation of the materials and ultimately, to overcome the technological limitations. This work pursues this objective, and therefore couples both experimental and simulation approaches that are relevant to that goal.

On the one hand, state-of-the-art electrocatalysts were characterized from the scale of the raw Pt/C materials up to the complete catalyst layer, to gather as much information as possible and better understand the electrocatalyst operation and its utilization/effectiveness in catalyst layers. This is achieved by making the link between the micro-structure, the nature of the electrocatalyst and the different electrochemical response measured under various operating conditions. To do so, Rotating Disk Electrode and Differential Cell setups were used to perform the electrochemical measurements. The importance of the catalyst layer fabrication step and related parameters must be taken into account to control the fabrication process and provide well-designed and controlled catalyst layers. The RDE setup was used to assess the intrinsic electrocatalytic features of the Pt/C materials and make the link with the nature of the latter. The DC setup was then used to better understand the electrocatalyst working properties in an environment that is more relevant of the real PEMFC operation. The choice of the different components as well as electrochemical measurement procedures were also investigated and justified to make the measurements in the most reliable and relevant way. It was found that the RDE setup may lead to underestimation of the activity recorded at high potential (from 0.85 to 0.95 V), which means that the activity in RDE may not always be representative of the catalyst layer configuration for all the electrocatalysts (case of Pt/HSAC). Regarding the DC, the activities at 0.6 V for all the electrocatalysts studied seem to be close, which may be explained by the fact that at this potential, the formulation/catalyst layer structure mainly drives the performance, and this was observed even for very thin layers (20 and 100 μg_{Pt} cm_{geo}^{-2}). The different electrochemical characterizations using the differential cell setup were also performed to investigate the behaviour of the electrocatalyst and catalyst layer under various operating conditions in terms of temperature and relative humidity, but also to estimate the impact of the catalyst loading on the performance. Finally, these experimental characterizations were gathered to build a reliable dataset to support the description improvement of the model, to simulate as accurately as possible the relevant processes that take place during PEMFC operation and to predict the performance of a given electrode composition.

As a perspective of this experimental work, it would be interesting to investigate the behaviour of the catalyst layer during potentiostatic operation. Indeed, such operation leads to reversible performance loss in major cases, but also to irreversible degradation, due to Pt oxidation phenomena. Potentiostatic measurements should enable to obtain more insights into the Pt oxides formation/reduction, thus into the ORR mechanism and the catalyst layer response. To contribute to the better understanding of the ORR mechanism and of the degradation it may induce of the Pt-based catalysts, one may consider advanced *in situ* characterizations such as time-resolved high-energy powder X-ray diffraction measurements or *operando* characterisations such as near ambient pressure X-ray photoelectron spectroscopy measurements at large scale facilities. This would help to unveil the definition (state of surface, crystallinity, degree of oxidation) of the Pt/C catalyst under potential control. However, such characterizations are not easy to put into practice.

On the other hand, modeling is a powerful tool to quantify the contribution of each mechanism by giving access to local operating conditions and taking into account all the couplings, which is rarely possible experimentally. The former model description (which is at the basis on this thesis) allowed quite accurate performance simulations. However, the electrochemical description of the ORR, in a one single step, was not sufficient to understand the phenomena occurring during the catalyst layer operation. In particular, the ORR process is much more complex and involves several intermediate species. These reaction intermediates are surface species ($PtOH_s$ and PtO_s) that are formed via the oxidation of platinum, which are also partly responsible of the degradation processes of the cathode catalyst layers, during long-term operation or potential cycling. To cope with these effects, a multi-steps ORR mechanism has been implemented; it covers the different formation of the surface intermediates, as well as the so-called place exchange phenomenon, resulting in the formation of Pt ‘bulk’ oxide (PtO_b). Each reaction is described by direct kinetic equation, which introduces new parameters that enable the simulation of the surface coverage ratio of the different intermediate species. Under H_2/O_2 configuration, this new description leads to encouraging outcomes, with more insights into the surface processes involved during ORR, under the reference operating conditions (80°C, 80% RH, 1.34 bar abs.). With the new description, simulations allow monitoring the coverage ratio evolution of the different surface oxide species and ‘bulk’ oxide PtO_b that partly account for the performance hysteresis observed on polarization curve between the forward and backward sweeps, and thus are partly responsible of the reversible performance loss. Under H_2/N_2 configuration, the multi-steps mechanisms of Pt oxides formation/reduction and proton adsorption/desorption allow to simulate and rather well capture the electrochemical response during cyclic voltammetry simulation at and 30°C, 100% RH, P_{atm}. The simulation of H_2/N_2 operation was very helpful to fit the reaction kinetics of the oxide formation. Parametric studies under various operating conditions were also performed to validate the new description. They give global good trends according to temperature, relative humidity or sweeping rate parameters, which are in agreement with the experimental results. They also reveal that the simulation does not match the experimental data in all conditions. Nevertheless, these results have been very useful to identify the physics that are still not accurately described or lacking in the model, which open the doors for further improvements.

Among the improvements possible, one should focus on the kinetic parameters' description, that might actually follow an Arrhenius law, and on the water and proton transport description in the catalyst layer. As a result, even though the electrochemical multi-steps ORR mechanism and transport properties are largely improvable, it gives, in a first approach, good insights into the catalyst layer performance and behaviour under nitrogen atmosphere at reference operating conditions, thanks to the description of the surface evolution of Pt with potential. In addition, the Pt surface description which has been developed in this work is a necessary step for realistic implementation of degradation mechanism, or to take into account the presence of contaminants, a very actual issue if PEMFCs are to be spread on the road.

Abstract

In the interests of ecological transition and reducing the use of fossil fuels, greenhouse gas emitters, the Proton Exchange Membrane Fuel Cell (PEMFC) is a promising candidate as a clean and efficient energy converter in transport and stationary applications. It converts hydrogen and oxygen into electrical energy, heat and water via electrochemical reactions. The PEMFC can exploit the advantages of the hydrogen carrier if its production is decarbonised, which remains a challenge in terms of the cost of hydrogen production and storage facilities. Despite many improvements, PEMFC systems still suffer technological limitations, some of which being linked to the materials' cost, performance and durability of the cathode catalyst layer. In that extent, this work focuses on coupling modeling with experimental characterizations of PEMFCs at the electrode scale to better understand the active layer operation (microstructure, performances and limiting phenomena). Physico-chemical and electrochemical measurements are performed from the scale of the raw Pt/C materials up to the complete catalyst layer, to gather as much information as possible on the catalytic layer micro-structure and its operating properties. Based on this experimental work and data sets, the behaviour of the Pt/C electrocatalysts has been studied in order to introduce new electrocatalytic features in one-dimensional models, especially the Pt surface oxide formation and reduction through basic reactions linked to the surface state of Pt as well as to 'bulk' Pt oxide formation via chemical place exchange reaction. A complete performance model has been developed for the O_2 reduction reaction at the cathode, which better describes the physical and electrochemical phenomena involved in catalyst layer during its operation under oxygen atmosphere, and potential cycling under nitrogen atmosphere. The aim is to characterize and predict performances of a PEMFC in the most reliable and possible way.

Résumé

Dans un souci de transition écologique et de diminution de l’utilisation de combustibles fossiles, émetteurs de gaz à effet de serre, la pile à combustible à membrane échangeuse de protons (PEMFC pour Proton Exchange Membrane Fuel Cell) est une candidate prometteuse comme convertisseur d’énergie propre et efficace dans les applications des transports et stationnaires. Elle convertit l’hydrogène et l’oxygène en énergie électrique, en chaleur et en eau via des réactions électrochimiques. La PEMFC permet d’exploiter les avantages du vecteur hydrogène si sa production est décarbonée, ce qui reste un défi en termes de coût des installations de production et de stockage de l’hydrogène. Malgré de nombreuses améliorations, les systèmes PEMFC souffrent encore de limitations technologiques, dont certaines sont liées au coût des matériaux, aux performances et à la durabilité de la couche catalytique cathodique. Dans ce contexte, ce travail de thèse se concentre sur le couplage de la modélisation avec des caractérisations expérimentales des PEMFC à l'échelle de l'électrode pour mieux comprendre le fonctionnement de la couche active (microstructure, performances et phénomènes limitants). Des mesures physico-chimiques et électrochimiques sont effectuées depuis l'échelle des matériaux bruts Pt/C jusqu'à la couche catalytique complète, afin de recueillir le plus d'informations possible sur la microstructure de la couche catalytique et ses propriétés de fonctionnement. Sur la base de ce travail expérimental et de ces ensembles de données, le comportement des électrocatalyseurs Pt/C a été étudié afin d'introduire de nouvelles caractéristiques électrocatalytiques dans les modèles unidimensionnels, en particulier la formation et la réduction d’oxydes de surface du Pt, par des réactions de base liées à l'état de surface du Pt ainsi qu'à la formation d'oxyde dit ‘bulk’ via une réaction chimique d'échange de place. Un modèle de performance complet a été développé pour la réaction de réduction du dioxygène à la couche catalytique cathodique, qui décrit mieux les phénomènes physiques et électrochimiques impliqués dans la couche active pendant son fonctionnement sous dioxygène, et des cycles en potentiel sous azote. L'objectif est de caractériser et de prédire les performances d'une PEMFC de la manière la plus fiable possible.